Ground and Excited State Electron Transfer Dynamics

Jennifer L. Brennan, B.Sc.(Hons)

A thesis submitted for the degree of Doctor of Philosophy

Supervisor: Prof. Robert J. Forster,
School of Chemical Sciences,
Dublin City University.

August 2002

I hereby certify that this material, which I now submit for assessment on the program of study leading to the award of Doctor of Philosophy is entirely my own work and has not been taken from the work of others save and to the extent that such work has been cited and acknowledged within the text of my work.

Signed: Jennifer Brennan ID No.: 98970755

Date: 12/9/04

"One's mind, once stretched by a new idea, never regains its original dimensions"

Oliver Wendall Holmes

Acknowledgements

I would like to express my sincere thanks to my supervisor, Robert Forster, for all the help, advice and guidance that he has given me over the past four years. Thank you for teaching me to never stop questioning and most of all, to never accept mediocrity in my work, or myself.

Many thanks to all the technical staff - Mick, Damien, Maurice, Ambrose, Vinny, Mary, Veronica and Ann for all their help with my many questions and queries. Special thanks to Maurice for drilling the cuvettes that I needed for my laser work. Thanks also to all the secretarial, faculty office and lecturing staff that were of assistance to me during my postgrad years.

A special mention for all the members of the Forster Reseach Group, past and present – Conor, Dominic, Egbert, Edna, Richard, Darren, Lorraine, Mary, Johan, Sonia, Lynn and Darragh. Thanks for all the great conversations, even better nights out and interesting Christmas dinners! Special thanks to Dominic and Conor for all their help in those early months, when I hadn't got a clue. To Johan and Darren for the many interesting conversations, both chemistry and non-chemistry related – I've learned so much from you both. Thanks to Mary for being the best lab buddy a girl could ask for. Lastly, thanks to Richard for always making me see the funny side of things and for never letting me take myself too seriously.

Thanks to all the former and present chemistry postgrads in DCU, without whom, doing this PhD would have been a very dull experience! There are too many names to mention, but a special thanks has to go to those who have been such great friends – Carol, Mairead, Helen, Davnat, Edel, Richard, Colm, Ben, Conor, Scott, Ger and Shaggy – especially the girlies, who deserve special mention for all those great chats, tea breaks and girl's nights out. Thanks to all the members of the HVRG who gave me such a lot of help with my synthetic work – Scott, Adrian, Christine, Anthea, Helen, Wesley and of course, Marco (couldn't have done those NMR's without you!). A special shout out to my fellow PGAC reps. - hope you've enjoyed being a thorn in the side of the staff as much as I have – keep up the good work!

To all my non-DCU friends – Su, Siobhan, Eimer, Grace, Caroline, Orla, Janet, Sarah, Jenny Mac, Jenny Broph and Aisling – thanks for being there for me and for being the great people that you are. Thanks to "The Linsay Singers" and "Saddle and Spurs" for giving me something else to think about besides' chemistry!

And last but not least, to the people that matter the most – Mum, Dad, Andrew, Nana and Niall. Special thanks to Mum and Dad - without you this could never have happened. Thanks for all the sacrifices that you have made so that I can follow my dreams. To Niall, thank you for being you, and for being so patient over these last few months, when I've practically disappeared from your life to write this thesis. I love you all more than words can say.

This thesis is dedicated to my parents

TABLE OF CONTENTS

"GROUND AND EXCITED STATE ELECTRON TRANSFER DYNAMICS"

Jennifer L. Brennan, B.Sc.

The focus of this work is the investigation of the factors controlling electron transfer in molecular electronic systems, in particular those affecting electron transfer to and from electronically excited states. To achieve this, a number of mono- and tri-metallic osmium and ruthenium complexes were synthesised and characterised. Monolayers of an osmium polypyridyl complex bound to a platinum microelectrode via a *trans*-1,2-bis-(4-pyridyl)ethylene bridge were formed to probe ground state electron transfer dynamics. This is compared to the rate of photoinduced oxidative electron transfer quenching which occurs in a trimetallic osmium complex where the metal centres are linked by the same bridging ligand. The rate constant for this quenching is 1.3×10^8 s^{-1}, compared to 2×10^6 s^{-1} for the ground state process with the same driving force. These investigations show that the strength of coupling across the bpe ligand is higher when it links two metal centres as opposed to when it bridges a metal centre and an electrode. Extensive experiments were carried out to quantify the effect of laser pulses on an unmodified electrode surface. Laser activation improves the heterogeneous kinetics of a solution phase redox probe by removing polishing debris and other adsorbed impurities. Laser-induced current transients observed following a single laser pulse are due to a rapid (μs) restructuring of the double-layer followed by a slow (ms) thermal decay within the metal electrode. A mathematical model has yielded values of the thermal diffusion coefficient as a function of applied potential. To investigate excited state heterogeneous electron transfer, monolayers of a ruthenium polypyridyl complex containing the bridging ligand, 2,2′:4,4″:4′,4″-Quarterpyridyl are used. Using Rehm-Weller calculations, the excited state redox potentials occur at –0.71 and +1.05 V for oxidation and reduction respectively. Laser excitation of these monolayers in conjunction with high-speed cyclic voltammetry was utilised to attempt to *directly* measure the excited state redox potentials of this complex. This experiment has not been entirely successful and suggestions for improvements to the experiment are discussed.

Chapter 1

Literature Survey and Theoretical Framework

"If I have seen further, it is by standing on the shoulders of giants"

Isaac Newton

1.1 Introduction – Applications of Electron Transfer

Electron transfer reactions are of great importance to nearly every sub-discipline of chemistry. The simple transfer of a single electron has been shown repeatedly to be a common activating mode for organic, inorganic and biological molecules.[1] The focus of this thesis is the investigation of the factors controlling electron transfer in molecular electronic systems, in particular those affecting electron transfer to and from electronically excited states.

One important goal of this investigation is the development of a method allowing the *direct* measurement of the excited state redox potentials of a ruthenium polypyridine complex. This opening chapter contains a detailed discussion of current theory describing electron transfer and a review of the experimental methods used to investigate electron transfer in the ground and electronically excited state. Also discussed are the methods previously used to experimentally determine excited state redox potentials and the factors which must be taken into account when designing an experiment to *directly* measure the excited state redox potentials of a material.

Chapter 2 details the synthesis and characterisation of the osmium and ruthenium polypyridyl complexes used in this thesis to investigate electron transfer. In Chapter 3, ground and excited state electron transfer is compared and contrasted. This is accomplished using adsorbed osmium polypyridyl monolayers to probe ground state electron transfer and a trimetallic osmium complex, which undergoes intramolecular electron transfer quenching of the electronically excited state created upon adsorption of a photon, to investigate excited state (photoinduced) electron transfer. Chapter 4 presents the results of detailed experiments which probe the effect of laser radiation on unmodified electrode surfaces. Chapter 5 describes the evaluation of a ruthenium complex for use in an experiment to *directly* measure the excited state redox potentials of this complex. The experiment is based on high-speed cyclic voltammetry applied to monolayers of a fluorescent molecules immobilised on a microelectrode, during laser irradiation of the monolayer. In using laser irradiation to electronically excite monolayers adsorbed on an electrode, an important control experiment is to quantify the effect of the laser radiation on the underlying metal substrate.

Our interest in electron transfer stems from the role that it plays in processes such as corrosion inhibition, charging and discharging of batteries, electroanalysis and medical device operation, all of which involve electron transfer across an interface consisting of metallic and molecular species.[2] Another significant area involving electron transfer is the field of molecular electronics, notably the development of computing and information storage that takes places on a molecular level. Progress towards this goal demands the use of highly ordered materials[3] and an understanding of the processes that affect the rate of heterogeneous electron transfer between these materials and an experimentally addressable interface, e.g., a metal surface. Supramolecular assemblies of electroactive molecules provide a simple way to create highly-ordered electronically conducting materials, which make them suitable for developing molecular electronic devices.

Excited state electron transfer is important due to the many "real world" applications which involve electronically excited states. The fact that many excited states are more easily oxidised and reduced than their ground state precursors,[4] has been exploited in a diverse range of research areas, including optical memory and display devices,[5,6,7] photoelectrochromic materials,[8,9] chemical sensors,[10] molecular shift registers,[11,12] DNA recognition sensors,[13,14,15] industrial waste treatment,[16,17] solar energy conversion[18,19] and the development of artificial photosynthesis.[20,21] The following paragraphs describe, in more detail, some of the important applications of photoinduced electron transfer. These examples illustrate the many diverse applications of electron transfer and emphasise why there is considerable interest in controlling the dynamics and energetics of electron transfer, both in the ground and the electronically excited state.[22,23]

One of the most extensively researched applications of photoinduced electron transfer is the development of artificial photosynthetic systems. Photosynthesis is the natural process where sunlight is converted into chemical energy (food, firewood, and fossil fuels).[24] This process, which maintains life on earth, is based on photoinduced energy and electron transfer processes. In green plants, light is absorbed by ordered arrays of pigments and the resulting excitation energy is channelled to specific reaction centers, where a charge separation takes place. The reducing and oxidising species obtained give rise to secondary chemical reactions that lead to the final products.[24] A long standing challenge has been the development of artificial photosynthetic systems

capable of mimicking the biological system described above, i.e., the use of sunlight to drive the reaction of an abundant material that is thermodynamically uphill in the ground state to drive selected chemical reactions.[20]

Many approaches have been taken to design synthetic molecules or cells that mimic the major steps involved in photosynthesis – light harvesting,[21] charge separation[25,26,27] and production of a fuel.[26,28] Light harvesting is mainly achieved via artificial antenna systems of chromophoric molecules, which absorb incident light and channel the excitation energy towards an acceptor component.[21] Strategies for charge separation include triad systems of donor-chromophore-acceptor molecules[29] and the use of colloidal catalyst-coated semiconductors.[26] The production of fuel has mainly focused on water oxidation to produce hydrogen and oxygen,[20,30] and photosensitised reduction of CO_2 to organic molecules such as methane[28] and formate.[31] A schematic representation of a system for the generation of H_2 and methane from CO_2, developed by Zengerle and co workers[28] is shown in Fig.1.1.1. This system is composed of Ru(II)tris(bipyridine), $Ru(bpy)_3^{2+}$, as photosensitiser, triethanolamine, TEOA, as electron donor and a bipyridinium charge relay. As shown in the diagram, illumination of this system under an atmosphere of CO_2 in the presence of Os or Ru colloids results in the formation of methane and ethylene and in the evolution of H_2. The CO_2 reduction is achieved by a photosensitised electron transfer reaction and is catalysed by the interaction of CO_2 with the metal colloid surface.

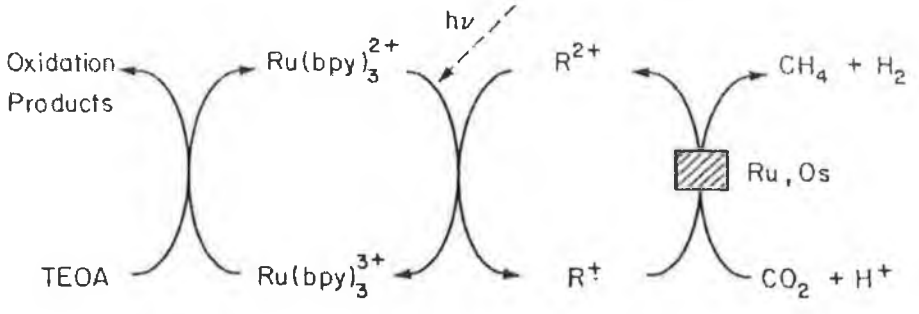

Figure 1.1.1 Schematic cycle for photosensitised H_2 evolution and CO_2 reduction using bypyridinium electron relays (R^{2+}). Reproduced from Reference 28.

The conversion of solar energy to electrical energy is an area of great interest and has become somewhat of a "holy grail" of chemical research.[20] The most successful approach to date has been the dye-sensitised photovoltaic cell developed by Grätzel and co-workers.[18,19] The device is based on a 10 μm thick, optically transparent film of nanometer-size titanium dioxide particles, coated with a monolayer of a charge-transfer dye to sensitise the film for light harvesting. As shown in Figure 1.1.2, current is generated when a photon absorbed by the dye molecule gives rise to electron injection into the conduction band of the semiconductor. To complete the circuit, the dye is regenerated by electron transfer from a redox species in solution which is then reduced at the counter electrode. The cell achieves a light-to-electric energy conversion yield of 12% in direct sunlight. This high conversion level, coupled with good stability and low cost, make this a viable cell for practical applications. However, one possible drawback is the use of an organic solvent (80/20 v/v ethylene carbonate/acetonitrile) as the liquid medium for the iodide/triiodide redox electrolyte. Even though the solvent is present in very small amounts (μL), it may still raise environmental concerns as to the safety of the cell.

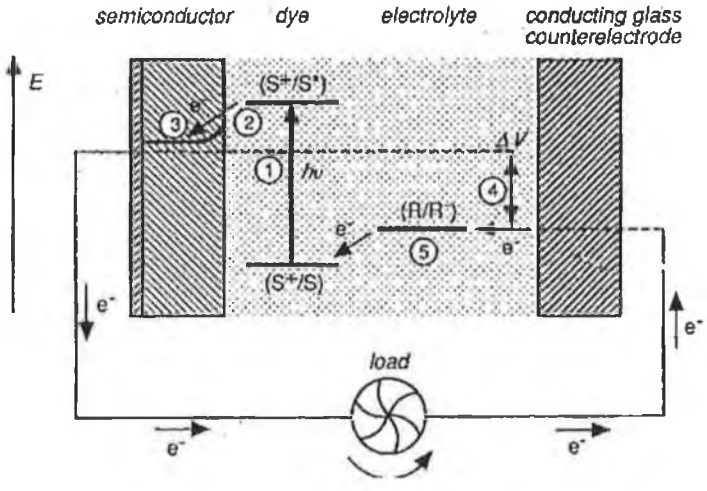

Figure 1.1.2 Schematic representation of the Grätzel cell. The cell voltage observed under illumination corresponds to the difference, ΔV, between the quasi-Fermi level of TiO_2 under illumination and the electrochemical potential of the electrolye. The latter is equal to the Nernst potential of the redox couple (R/R^-) used to mediate charge transfer between the electrodes. Reproduced from Reference 19.

Photoinduced electron transfer is also important in the development of systems capable of collecting and storing electrons. Brewer et al.[32,33] have synthesised a complex of the form $\{[(bpy)_2Ru(dpb)]_2IrCl_2\}(PF_6)_5$, where bpy is 2,2'-bipyridine and dpb is 2,3-bis(2-pyridyl)benzoquinoxaline), Figure 1.1.3. This trimetallic species, which incorporates two light absorbing Ru moieties coupled to a central iridium core, forms the basis of a photochemical molecular device for photoiniated electron collection. Photolysis of the complex in the presence of a sacrificial electron donor leads to the formation of the doubly reduced species $\{[(bpy)_2Ru(dpb^-)]_2IrCl_2\}^{3+}$, in which both bridging ligands coordinated to the central iridium center have been photoreduced by one electron. The central iridium fragment has been shown to be capable of delivering the electrons "stored" on the bridging ligand π^* orbitals to a substrate. It functions as an electrocatalyst for the reduction of carbon dioxide to formate.[33]

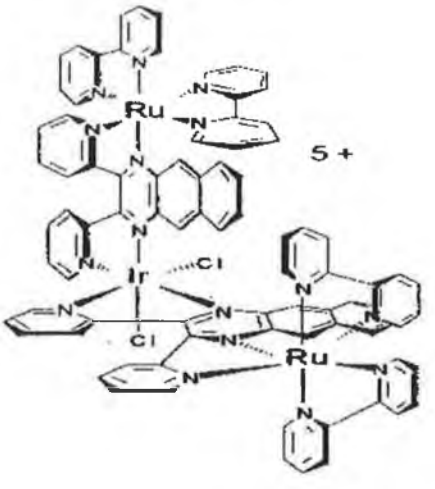

Figure 1.1.3 Structure of $\{[(bpy)_2Ru(dpb)]_2IrCl_2\}^{5+}$.Reproduced from Reference 32.

1.2 Electron Transfer Models

The most widely used and successful theory of electron transfer (ET), is that introduced and developed by Marcus.[34,35,36,37,38,39] The classical theory and its derivatives apply equally well to photoinduced, interfacial and thermally driven electron transfers. The main difference between these three processes lies in the driving force for electron transfer. Heterogeneous electron transfer allows the driving force to be controlled externally through an applied potential, whereas in homogeneous and photoinduced electron transfer, it is dictated by the electronic nature of the two reactant species.

1.2.1 Homogeneous Electron Transfer

Marcus – Hush[40,41] semi - classical theory is conventionally used for outer sphere ET reactions between a donor D and an acceptor A. The term "outer sphere" denotes a reaction between two species in which the original coordination spheres are maintained in the activated complex i.e., electron transfer from one primary bond system to another.[43] If either D or A is in the excited state, the process is a photoinduced electron transfer (PET). Excepting a change in the initial energies, the principles of Marcus theory apply equally well to both photoinduced and ground state electron transfer processes.[42] If D and A are separate molecules, the reactants must diffuse together to form an outer – sphere *precursor complex* before electron transfer is possible. However, as is the case for the photoinduced electron transfer reactions discussed in this thesis, D and A can be linked by a bridge, L, which may be a physical linkage or a through-space interaction. In this case, the homogeneous electron transfer process may be represented by:

$$D - L - A \rightarrow D^{+} - L - A^{-} \qquad (1.2.1)$$

Figure 1.2.1 illustrates the classical model in which simple parabolas of equal curvature are used to represent the free energies of the reactant and product states. Parabolas are used since Marcus theory assumes that the reaction coordinates conform to a simple harmonic oscillator model.[40] The reaction is considered to occur on a multidimensional surface which defines the standard free energy of the system in terms of the nuclear coordinates (i.e., the relative positions of the atoms) of the reactant, product and solvent.[43] In general, two factors influence the rate at which an electron transfer

occurs. The first is the Franck Condon Principle, which states that electronic transitions are faster than vibrational or nuclear transitions, therefore electron transfer is an instantaneous process, and no change in nuclear configuration, either inner or outer sphere can occur during the actual electron transfer event itself.[44] The second is the first law of thermodynamics, which states that energy must be conserved, therefore electron transfer is an isoenergetic process. For both these rules to be observed, electron transfer must only occur at the crossover point on the intersecting parabolas of Figure 1.2.1.[44]

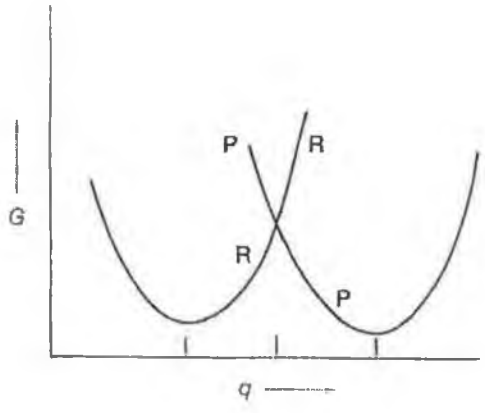

Figure 1.2.1 Plot of the free energy of the reactant (R) state (D-L-A) and product (P) state (D^+-L-A^-) vs. the reaction coordinate. Reproduced from Reference 40.

First, consider a ground-state reaction where $\Delta G° < 0$. $\Delta G°$ is the difference in Gibbs energy between the equilibrium configurations of the product and reactant states. The first-order rate constant for electron transfer, k_{ET}, is given by

$$k_{ET} = \kappa_{el} \nu_n \exp\left[\frac{-\Delta G^{\neq}}{RT}\right] \qquad (1.2.2)$$

where κ_{el} is the electronic transmission coefficient, which is a measure of the probability of electron transfer once the transition state has been reached; ν_n is the frequency of passage (nuclear motion) through the intersection point of the product and reactant parabolas, that is generally associated with bond vibrations and solvent

motion;[43] $\Delta G^{\neq}$ is the Gibbs free energy of activation for forward electron transfer; R is the gas constant and T is the temperature.

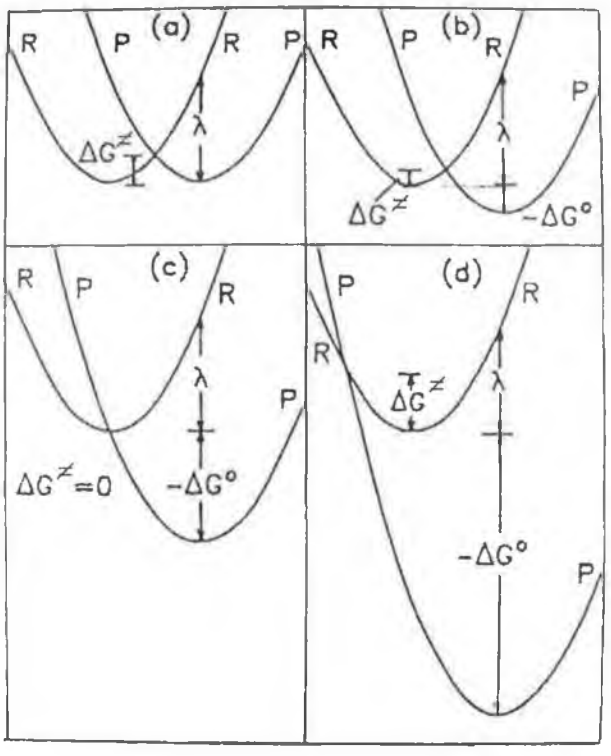

Figure 1.2.2 Diagrams showing the intersection of the Gibbs energy surfaces for the reactant (R) state (D-L-A) and the product (P) state (D^+-L- A^-): (a) an isoenergonic reaction with $\Delta G° = 0$; (b), the normal region where $0 \leq -\Delta G° \leq \lambda$; (c), the condition for maximum rate constant where $-\Delta G° = \lambda$; (d), the inverted region where $-\Delta G° > \lambda$. Reproduced from reference 42.

Figure 1.2.2 illustrates the parabolic Gibbs energy surfaces as a function of reaction coordinate for a variety of conditions. In Marcus theory, the curvature of the reactant and product surfaces is assumed to be the same. The important quantities in this diagram are the *reorganisation energy*, λ, defined as the change in Gibbs energy if the reactant state were to distort to the equilibrium configuration of the product state without transfer of the electron; $\Delta G^{\neq}$, the Gibbs energy for forward electron transfer; and $\Delta G°$, the difference in Gibbs energy between the equilibrium configurations of the product and reactant states. It is assumed that $\Delta G°$ represents the Gibbs energy of reaction when the donor and acceptor are a distance of d_0 (i.e., Van der Waals distance) apart.[42]

Figure 1.2.2a represents the situation for electron transfer between species where $\Delta G^\circ = 0$. The parabolic surfaces are identical in this case, except that the product surface is displaced along the reaction coordinate with respect to the reactant surface. It follows from the properties of parabolas that for a self-exchange reaction or other reaction where ΔG° is zero:

$$\Delta G^{\neq} = \frac{\lambda}{4} \qquad (1.2.3)$$

This analysis ignores any work terms that describe the Gibbs free energy associated with electrostatic barriers e.g., of ion association. For reactions where $\Delta G^\circ \neq 0$, as in Figure 1.2.2b, it is usually assumed that the product surface simply shifts vertically by ΔG° with respect to the reactant surface. Again it follows from the geometry of intersecting parabolas that:

$$\Delta G^{\neq} = \frac{(\lambda + \Delta G^\circ)^2}{4\lambda} \qquad (1.2.4)$$

The zero of Gibbs energy is taken as that of the reactant at the reaction distance of d_0. Inserting Equation 1.2.4 into Equation 1.2.2 yields the semi - classical Marcus equation

$$k_{ET} = \kappa_{el} \nu_n \exp\left[\frac{-(\lambda + \Delta G^\circ)^2}{4\lambda RT}\right] \qquad (1.2.5)$$

Equations 1.2.4 and 1.2.5 and Figure 1.2.2 show that for moderately exergonic reactions $\Delta G^{\neq}$ will decrease and k_{ET} will consequently increase, as ΔG° becomes more negative. When $-\Delta G^\circ = \lambda$, as in Figure 1.2.2c, $\Delta G^{\neq} = 0$ and k_{ET} reaches its maximum value of $\kappa_{el}\nu_n$. However, as ΔG° becomes ever more negative in a highly exergonic reaction, the intersection point of the R and P surfaces moves to the left of the centre of the R surface, as shown in Figure 1.2.2d. This shift indicates that $\Delta G^{\neq}$ should increase again. Thus the striking prediction of Equation 1.2.5 is that k_{ET} will decrease as the reaction becomes highly exergonic in what is known as the Marcus *inverted region*. Physically, this indicates that the product will be formed in an increasingly distorted and high-energy state.

Until 1984, attempts to detect the inverted region had failed. The first definitive observations where made in 1984 by Closs and Miller et al.[45] on the intermolecular charge-shift reactions between a biphenyl radical anions and various acceptors in a rigid low-temperature glass. Since then, several other workers have found strong evidence for the existence of the inverted region.[46,47] However, the search for the inverted region in bimolecular photoinduced electron transfer reactions has yielded a constant diffusion-controlled value at very negative $\Delta G°$, known as Rehm-Weller behaviour. The possible reasons for this are several-fold: masking by diffusion control, the existence of alternative mechanisms, such as reaction via exciplexes, atom transfer, or the formation of electronically excited products, which reduces the magnitude of $\Delta G°$ for the electron transfer step. More recently however, Ganguly and others[48] have demonstrated a decrease of k_{ET} with increasing $\Delta G°$ for a series of photoinduced electron transfer reactions of organic donors and acceptors, indicating that the inverted region is observable in bimolecular photoinduced electron transfer.

1.2.1.1 Reorganisation Energy

The total reorganisation energy, λ, is the sum of an "internal" reorganisation λ_{in} which is related to the change in molecular geometry on going from the initial species to the final product and an "external" reorganisation of the solvent shell which becomes polarised around the charged product molecules, λ_{out}.[49]

$$\lambda = \lambda_{in} + \lambda_{out} \qquad (1.2.6)$$

The inner reorganisation energy is associated with changes in the molecular geometry of the reactant as it reaches the product state and is defined in Equation 1.2.7, where f^r_j is the j^{th} normal mode force constant in the reactant species and f^p_j is the j^{th} normal mode force constant in the product species, and Δq_j is the equilibrium displacement of the j^{th} normal coordinate.[50]

$$\lambda_{in} = \sum_j \frac{f_j^r f_j^p}{f_j^r + f_j^p} (\Delta q_j)^2 \qquad (1.2.7)$$

The outer reorganisation energy, which is by far the predominant term in the electron transfer processes considered in this work, can be calculated by the expression:

$$\lambda_{out} = \Delta e^2 \left(\frac{1}{\varepsilon_{op}} - \frac{1}{\varepsilon_s} \right) \left(\frac{1}{2r_R} + \frac{1}{2r_P} - \frac{1}{d} \right) \qquad (1.2.8)$$

where Δe is the electronic charge transferred during the reaction, ε_{op} and ε_s are the optical and static dielectric constants of the solvent, r_R and r_P are the radii of the reactants and products, respectively, and d is the interreactant centre-to-centre distance.[23] This equation illustrates that λ_{out} is dependant on the solvent used, the distance between the reactants and, to a lesser extent, temperature, as ε_{OP} and ε_S vary with temperature.[42] Therefore, it is possible to vary the reorganisation energy, and hence the rate of electron transfer, by varying the solvent used and by manipulating the distance between reactant centers; for example, by varying the length of the bridging ligand between metal centers in a transition metal complex,[51,52] or by immobilisation of a monolayer of an electroactive species onto an electrode in electrochemical electron transfer reactions.[53]

1.2.1.2 Electronic Coupling and Frequency Factors

The electronic transmission coefficient in Equation 1.3.7 is related to the detailed shape of the potential energy curves in the intersection region. The magnitude of electronic interaction between the reactant and product states is denoted by H_{rp}, the electronic coupling energy, which is related to κ_{EL} and ν_n via the following equation:[23,61]

$$\kappa_{EL} = 2\left[1 - \exp(-\nu_{el}/2\nu_n)\right] / \left[2 - \exp(\nu_{el}/2\nu_n)\right] \qquad (1.2.9)$$

where ν_{el} is the electron hopping frequency in the complex and ν_n is the nuclear frequency factor as introduced earlier. ν_{el} may be defined as follows: [61,64]

$$\nu_{el} = \left(2H_{rp}^{\ 2}/h\right)\left(\pi^3/\lambda RT\right)^{1/2} \qquad (1.2.10)$$

where h is Planck's constant. These equations give rise to two limiting cases, depending on the magnitude of the electronic interaction between the donor and acceptor moieties. The two cases are illustrated in Figure 1.2.3.

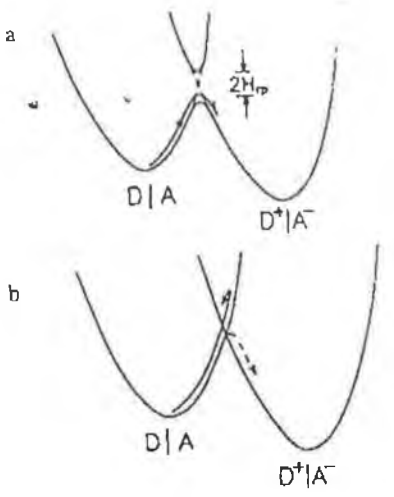

Figure 1.2.3 Adiabatic (a) and nonadiabatic (b) electron transfer. See text for further details. Reproduced from Reference 42.

If H_{rp} is small, which means that the reactant and product surfaces do not interact strongly electronically, $\nu_{el} << \nu_n$ and $\kappa_{EL} << 1$ indicating that the probability of crossover between the product and reactant surfaces is small. In this case, the ET reaction is said to be *nonadiabatic*. The transition state appears as a sharp cusp and the system must cross over the transition state onto a new potential energy surface in order for electron transfer to occur (Figure 1.2.3b). If H_{rp} is moderately large, $\nu_{el} >> \nu_n$ and $\kappa_{EL} = 1$. The Gibbs energy surfaces interact as shown in Figure 1.2.3a, showing significant flattening of the reaction hypersurface close to the transition state. In this case, the rate of crossing the barrier is reduced, but the value of κ_{EL}, the probability of electron transfer once the transition state has been reached, is now unity and the electron transfers across a single energy surface in passing from reactant to product. The value of H_{rp} depends on the overlap between the wave functions of the donor and acceptor groups, and is expected to decrease exponentially with increasing donor acceptor distance. Hence, varying this distance allows the probability of electron transfer, and so k_{ET}, to be systematically altered. [23,42]

1.2.1.3 Influence of the bridge on the rate of homogeneous electron transfer

Supramolecular chemistry has provided materials which make it possible to study the parameters which control electron transfer, such as driving force, transfer distance and the electronic nature of the bridge. Extensive study of supramolecular donor – acceptor systems in the solution phase,[23,54] has highlighted the importance of the ligand used to bridge the donor and acceptor sites in controlling the extent and rate of electron transfer. The origin of this distance dependence is in the magnitude of H_{rp}, the electronic coupling matrix element, previously mentioned in Section 1.2.1.2. A useful model which describes the decay of H_{rp} over distance between the donor and acceptor moeties is described by Equation 1.2.11, which describes electron tunnelling through a one-dimensional square barrier.[50]

$$H_{rp}(d) = H_{rp}(d_0)\exp\left[\frac{-\beta(d-d_0)}{2}\right] \qquad (1.2.11)$$

where $H_{rp}(d_0)$ is the coupling element when donor and acceptor are at the van der Waals distance, d_0, d ($\geq d_0$) is the centre-to-centre distance between donor and acceptor moieties, and β is the tunnelling parameter, a constant which describes the rate of decay of coupling with distance.

Studies on electron transfer rates in supramolecular systems have shown that experimental electron transfer rates decrease exponentially with increasing donor – acceptor distance. This behaviour is described in Equations 1.2.12 and 1.2.13.

$$H_{rp} \propto \exp\left(-(1/2)\beta_{rp}d\right) \qquad (1.2.12)$$

$$k_{et} \propto \exp(\beta d) \qquad (1.2.13)$$

H_{rp} is also influenced by the electronic nature of the bridge and the relative orientation of donor, bridge and acceptor and it has been demonstrated that the π-bonds in aromatic or conjugated covalent bridges support fast electron transfer.[50] H_{RP} values can be estimated from analysing intervalence transfer bands observed in UV-visible spectra of dimetallic mixed-valence supramolecular complexes, using an Equation developed by Hush:[55,56]

$$H_{RP} = \sqrt{\frac{4.2 \times 10^{-4} \varepsilon_{max} \Delta \bar{\upsilon}_{1/2} E_{abs}}{d^2}} \qquad (1.2.14)$$

where ε_{max} is the molar extinction coefficient (M^{-1} cm^{-1}) at the absorption maximum E_{abs} (cm^{-1}), $\Delta\upsilon_{1/2}$ is the bandwidth at half-height (cm^{-1}) and d is the metal-metal separation distance(cm).

Electron transfer is also mediated through solvent. Recent studies have involved bridges which are flexible and allow the donor and acceptor sites to approach each other in a U – shaped configuration. This minimises through – bridge electron transfer, and has shown that interaction between the donor and acceptor moieties in a flexible bridge may be mediated via the solvent molecules and not the bridge.[57]

1.2.2 Heterogenous Electron Transfer

In Section 1.2.1, the concept of homogeneous electron transfer in a generic donor acceptor supermolecule, D – L – A was introduced. In this section, heterogeneous electron transfer is discussed. In this case, D is now an electrode which is characterised by continuous or semi-continuous density of states and A remains a molecular moiety, characterised by molecular orbitals. The most common model used to describe heterogeneous electron transfer is the Butler – Volmer model of electrode kinetics.[43] However, this model has a number of limitations, the most important being its inability to predict how changes in the electron transfer distance, structure of the redox centre, electrode materials or solvent will affect the values of k^o. Also, it has been shown that the Butler – Volmer prediction that the rate constant will increase exponentially with increasing driving force, agrees with experiment only over a limited range of overpotentials.[22,58] In contrast, Marcus theory does not exhibit these limitations and so will be used to model the experimental data presented in this thesis.

1.2.2.1 Marcus Theory of Heterogeneous Electron Transfer

Similar to homogeneous electron transfer as described in Section 1.2.1, the rate of heterogeneous electron transfer is controlled by two factors. According to the Franck – Condon principle, at the moment of electron transfer, the redox centre switches from

oxidised to reduced forms while maintaining its internal structure and solvation shell. The electron transfer must also obey the First Law of Thermodynamics, in that energy cannot be transferred into, or out of, the surrounding medium. Therefore, as discussed in Section 1.2.2.1, the energy of the reactants and products must be identical.

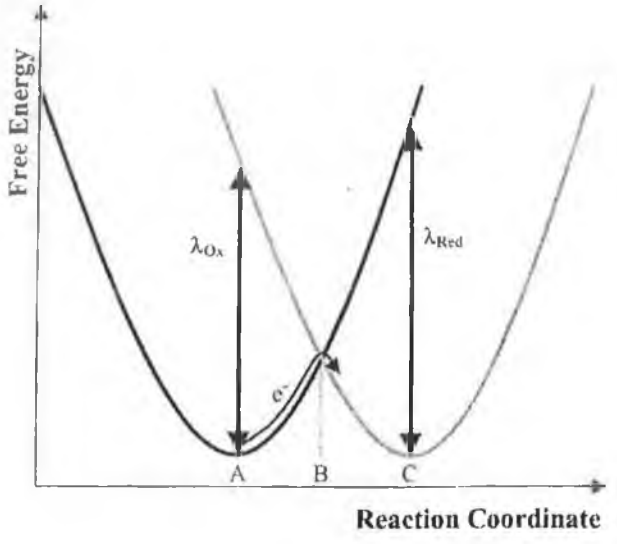

Figure 1.2.4 Plot of the free energy of the oxidised and reduced forms as a function of normalised reaction coordinate. A, B and C denote the equilibrium nuclear configurations of Ox, the transition state and Red, respectively. The diagram represents the situation in which the potential energies of Ox and Red are identical.

Firstly, the standard rate constant for heterogeneous electron transfer, k^0, when the electrochemical driving force is zero, is considered. Transition state theory focuses on the intersection or crossover point of the free energy curves for the oxidised and reduced forms illustrated in Figure 1.2.4.[43] In this model, the rate of the reaction is found to depend on two factors; the number of molecules with sufficient energy to reach the transition state at a particular instant in time and the probability at which they cross over the transition state. The number of molecules which are at the transition state depends on the free energy of activation, ΔG°, the difference in free energy between the donor and acceptor states. Hence the rate constant for heterogeneous electron transfer is given by Equation 1.2.15.

$$k^o = \nu_n \kappa_{el} \sigma \exp\left(\frac{-\Delta G^{\neq}}{RT}\right) \qquad (1.2.15)$$

where ν_n is the average nuclear frequency factor, κ_{el} is the electronic transmission coefficient (both defined previously in Section 1.2.1) and σ is a factor introduced into the expression which is an equivalent reaction – layer thickness and is expressed in units of cm.

The outer sphere component of the free energy of activation arises due to the change in the charge of the redox centre which occurs during electron transfer. It depends on both the static and optical dielectric constants as described in Equation 1.2.16:

$$\Delta G_{OS} = \frac{n^2 e^2}{8\pi\varepsilon_0 r}\left(\frac{1}{\varepsilon_{op}} - \frac{1}{\varepsilon_s}\right) \qquad (1.2.16)$$

where n is the number of electrons transferred, e is the electronic charge, ε_0 is the permittivity of free space, r is the molecular radius and ε_{op} and ε_s are the optical and static dielectric constants, respectively.[59] This explains why the Marcus formulation, unlike the Butler – Volmer theory, is sensitive to both the structure of the redox centre and the solvent.

1.2.2.2 Potential Dependent Heterogeneous Electron Transfer

The standard heterogeneous electron transfer rate constant, k^0, depends on both a frequency factor and a Franck – Condon barrier:[60,61,62,63]

$$k^o = A_{el} \exp\left(-\Delta G^{\neq}/RT\right) \qquad (1.2.17)$$

where A_{et} is the pre-exponential factor and $\Delta G^{\neq}$ is the electrochemical free energy of activation.[64] For an *adiabatic* reaction, the pre-exponential factor is given by the product of κ_{el}, the electronic transmission coefficient and ν_n, the average nuclear frequency factor. In contrast, for a *nonadiabatic* reaction, $\kappa_{el} << 1$ and the pre-

exponential factor is dictated by the electron hopping frequency in the activated complex, ν_{el}, as defined earlier in Equation 1.2.10.

One approach to decoupling the contribution to k^o from electronic coupling, A_{et}, and free energies of activation, $\Delta G^{\neq}$, is to use temperature resolved measurements of k^o to measure the free energy of activation, $\Delta G^{\neq}$, therefore allowing A_{et} to be determined. In this manner, information about the strength of electronic coupling can be obtained.[58,65] A second method involves measuring electron – transfer rate constants at a single temperature over a range of driving forces. For example, Finklea and Hanshew[66] have developed a through – space electron tunnelling model which provides a good description of electron tunnelling across monolayers. In the model, the cathodic rate constant is described by the integral over energy, ε, of three functions (a) the Fermi function for the metal, n(ε), (b) a Gaussian distribution of energy levels for the acceptor states in the monolayer, $D_{OX}(\varepsilon)$, and a probability factor describing electron tunnelling at a given energy, P(ε):[66]

$$k_{OX}(\eta) = A\int_{-\infty}^{\infty} D_{OX}(\varepsilon)n(\varepsilon)P(\varepsilon)d\varepsilon \qquad (1.2.18)$$

The zero point of energy is the Fermi level of the metal and the particular overpotential of interest (η). The Fermi function of the metal describes the distribution of occupied states within the metal and is defined by:[50,66]

$$n(\varepsilon) = \left(\frac{1}{1+\exp\left[\varepsilon - \varepsilon_f / k_b T\right]}\right) \qquad (1.2.19)$$

where k_b is the Boltzmann constant. The density of acceptor states in the molecule is derived from Marcus theory[34,38] and can be represented by Equation 1.2.20:

$$D_{OX}(\varepsilon) = \exp\left[-\frac{(\varepsilon+\eta-\lambda)^2}{4k_b\lambda T}\right] \qquad (1.2.20)$$

where λ is the reorganisation energy. The probability of direct elastic tunnelling[67,68] through a trapezoidal energy barrier of height E_B can be approximated by Equation 1.2.21:[66]

$$P(\varepsilon) = (E_B - \varepsilon + e\eta/2)\exp(-\beta d) \qquad (1.2.21)$$

where E_B is the average barrier height at zero overpotential and d is the electron distance. β is the tunnelling constant and is given by[66]

$$\beta = \left(2(2m)^{1/2}/\hbar\right)(E_B - \varepsilon + e\eta/2)^{1/2} \qquad (1.2.22)$$

where m is the mass of the electron.

Chidsey,[69] Creager[70] and Murray[71] have modelled *nonadiabatic* heterogeneous electron transfer for long-chain alkane-thiol monolayers using an expression similar to Equation 1.2.18, except that the energy dependent pre-factor in the tunnelling probability expression is excluded. Following Chidsey,[69] the potential dependent rate constants for monolayer reduction, $k_{Red,\eta}$ and oxidation, $k_{Ox,\eta}$, are given by

$$k_{Red,\eta} = \kappa_{el}\,\rho\,k_B T \int_{-\infty}^{\infty} \frac{\exp\left\{-(x-(\lambda+\eta)/k_B T)^2/(k_B T/4\lambda)\right\}}{1+\exp(x)}\,dx \qquad (1.2.23)$$

$$k_{Ox,\eta} = \kappa_{el}\,\rho\,k_B T \int_{-\infty}^{\infty} \frac{\exp\left\{-(x-(\lambda-\eta)/k_B T)^2/(k_B T/4\lambda)\right\}}{1+\exp(x)}\,dx \qquad (1.2.24)$$

where x is the electron energy relative to the Fermi level, κ_{el} is the distance dependent electronic coupling between the electrode and the redox sites, ρ is the density of electronic states in the metal electrode, k_B is the Boltzmann constant, T the absolute temperature, and λ is the reorganization energy.

Irrespective of the electron transfer model used, the voltammetric current for the reaction of an immobilized redox centre following first order kinetics is given by:[71]

$$i_F = nFA(k_{Ox,\eta}\,\Gamma_{Red,\eta} - k_{Red,\eta}\,\Gamma_{Ox,\eta}) \qquad (1.2.25)$$

where $\Gamma_{Red,\ \eta}$ and $\Gamma_{Ox,\ \eta}$ are the instantaneous surface coverages of the oxidized and reduced species and $k_{Ox}(\eta)$ and $k_{red}(\eta)$ are the reaction rate constants given by Equation 1.2.18, or its complement, in which $n(\varepsilon)$ is replaced by $(1-n(\varepsilon))$ and $-\lambda$ is replaced by $+\lambda$, with or without a tunnelling probability function.

The sensitivity of the heterogeneous rate constant to the applied overpotential depends on the strength of electronic coupling between the reactant and the electrode.[43] For an *adiabatic* process, where the electrode and reactant are strongly coupled, electron transfer occurs through states near the Fermi level of the electrode. For *nonadiabatic* systems, electrons with energies below the Fermi level may be transferred and one must sum over all electron energies, rather than just at the Fermi level.[43] The effects of the strength of electronic coupling on the rate constant only become apparent at high overpotentials, where the overpotential is more than half the reorganisation energy. The result of this is curvature in Tafel plots of $\ln k^o$ vs. η at high values of η. For extremely large driving forces, k no longer depends on overpotential and reaches a maximum value when η is equal to λ, this is equivalent to the *Marcus Inverted Region* seen in homogeneous electron transfer reactions.[50] However, the rate of electron transfer does not decrease with increasing driving force as in homogeneous electron transfer, rather it becomes independent of driving force. This reflects the fact that the entire distribution of redox – active molecules with states available for electron transfer is matched by states in the electrode that are also able to transfer electrons. Increasing the driving force does not make any new states available for electron transfer and so the rate does not change. Behaviour of this type has been reported by Weber and Creager[70] in data obtained for a series of scan rates carried out on a ferrocene-alkanethiol monolayer. Using the equations for the Marcus theory as described above, they have prepared theoretical plots of $\ln(k_{red} + k_{ox})$ vs η for specific k^o and a range of reorganisation energies. These show a plateau region at high driving force where the sum of k_{red} and k_{ox} is nearly independent of potential and agree well with the observed experimental data.

1.3 Experimental Investigations of Electron Transfer in Ground and Electronically Excited States

The experimental investigation and probing of the existing theories of electron transfer as described in Section 1.2, has received considerable attention in recent years.[22,66,69,71,72,84,85,86] The advent of ultrafast electrochemical instrumentation and microelectrodes, whose short response times allow electron transfer reactions with fast heterogeneous kinetics to be probed, has resulted in the use of self – assembled monolayers of redox – active molecules immobilised on microelectrodes to investigate ground state electron transfer reactions. Electron transfer in the electronically excited state has mainly focused on the use of dimeric species, where redox centres are separated by a ligand bridge, and efficient photoinduced electron transfer occurs between the centres on the creation of an excited state at one centre by light excitation.

1.3.1 Adsorbed monolayers

Self-assembled monolayers offer a number of distinct advantages for the investigation of heterogeneous kinetics. When immobilised on a surface, the redox species no longer needs to diffuse to the electrode surface for electron transfer, which eliminates the influence of mass transfer when trying to measure large rate constants. Also, the redox species is preconcentrated on the electrode surface, with typical surface coverages of 10^{-10} mol cm^{-2}, giving rise to larger currents than are observed at microelectrodes using solution phase reactants at mM concentrations. These currents are easier to detect at the short experimental timescales needed to accurately measure rapid heterogeneous kinetics.[50] Moreover, every redox-active group is attached to the electrode via the same bridging group and the local chemical microenvironment surrounding the redox-active groups can be controlled.[70]

For a number of years, there has been a focus on the use of functionalised alkane-thiols, $HS(CH_2)_n$, where $5 \leq n \leq 16$, to form self – assembled monolayers. Various authors have demonstrated that functionalised alkane-thiol monolayers, when formed in conjunction with a suitable diluent, exhibit close to ideal reversible electrochemical behaviour under a wide variety of experimental conditions of timescale, temperature, solvent and electrolyte.[66,69,70,71,72] Self-assembled monolayers formed using

oligophenylenevinylene "molecular wire" bridges, functionalised at one end with a ferrocene moiety and tethered to the electrode at the opposite end with a thiol group, have exhibited similar ideal electrochemical responses.[73,74] These studies have investigated the effects of electron transfer distance, tunnelling medium and other factors on heterogeneous electron transfer dynamics. Most importantly, they have provided the necessary detailed experimental data to thoroughly test the Marcus theory of heterogeneous electron transfer kinetics.

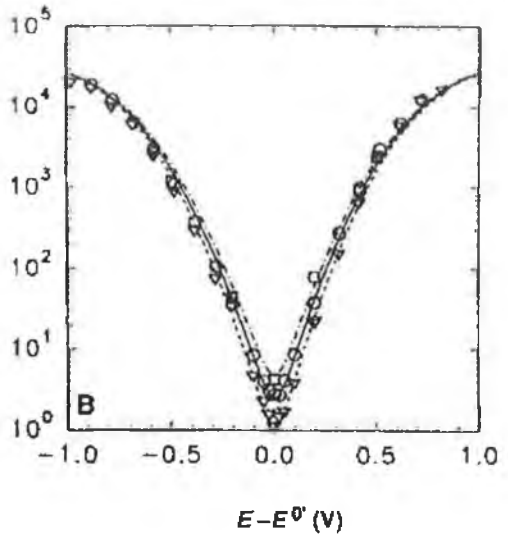

Figure 1.3.1 Semilog plot of the measured decay rate constants for a mixed self-assembled monolayer containing $HS(CH_2)_{16}OOC$-Ferrocene and $HS(CH_2)_{15}CH_3$ in 1.0 M $LiClO_4$ at 1°C (triangles), 25°C (circles) and 47 °C (squares); and calculated decay constants using $\lambda = 0.85$ eV and $\nu\rho = 6.73 \times 10^4$ s^{-1} eV^{-1}. Reproduced from Reference 69.

These studies have revealed three major insights into heterogeneous electron transfer kinetics. First, as demonstrated by Finklea,[75] Creager,[76] and Smalley,[77] a plot of the logarithm of the standard heterogeneous rate constant, k^0, vs. the number of methylene units in an alkane chain, is linear. This result correlates well with the Marcus theory, which predicts that tunnelling rates decay exponentially with increasing distance. The slope of this plot provides an estimate of the tunnelling parameter, β, which for an alkane – thiol monolayer is 1.0 – 1.1 $Å^{-1}$. Second, a plot of the potential dependent heterogeneous electron transfer rate constant, k, vs. the overpotential, η, is not linear

for all driving forces. [66,69] As predicted by the Marcus theory, when the overpotential becomes comparable to the reorganisation energy of the redox couple, curvature is observed and k eventually becomes independent of the driving force.[50] Third, using temperature dependent measurements of k and the formal potential, E^o, the activation enthalpy and reaction entropy can be obtained, which can then be used to calculate the free energy of activation and, providing k^o is known, the pre – exponential factor.[62]

Creager[70] and Murray[71] have modelled *nonadiabatic* heterogeneous electron transfer for long-chain alkane-thiol monolayers using the potential dependent Marcus theory expressions described in Section 1.2.2.2. Creager has prepared working curves of peak potential relative to the formal potential ($E_p - E^o$) vs. logarithm of scan rate, and has used a Simplex algorithm to perform least -squares minimisation between the calculated curves and experimental cyclic voltammetric peak potential data.[70] This method has provided an efficient means of calculating both the heterogeneous electron transfer rate constant, k^o, and λ, the reorganisation energy and has allowed the authors to simulate voltammograms showing the effect of a distribution of rate constants on the cyclic voltammograms obtained. Similarly, Murray has prepared working curves of peak current vs. logarithm of ν/k^o, and has used these curves to yield values of the rate constant for experimental data.[71] A working curve of normalised peak current vs. logarithm of the ratio of scan rate and k^o has been used to estimate values of λ, although the authors have found that simulating the entire current-potential curve is more reliable for estimates of reorganisation energy than the use of peak currents alone.

Beyond the extensive use of functionalised alkane-thiol monolayers, considerable attention has been given to monolayers of osmium and ruthenium polypyridyl complexes with surface – active ligands as suitable probes for the investigation of heterogeneous electron transfer.[22,58,65,78,79,80] These materials display a number of properties which make them attractive systems for probing electron transfer. They allow the formation of highly ordered monolayer assemblies on microelectrodes, which assemble rapidly from solution.[78,81] The films formed are highly stable due to their low rate of desorption and, for osmium monolayers in particular, their photochemical stability.[82] By careful choice of the type of surface-active bridging ligand, the electron transfer distance and tunnelling medium may be controlled and systematically varied and the complexes also exhibit inherent electrochemical reversibility.[22,83]

Forster and Faulkner have presented two seminal contributions in the field of heterogeneous electron transfer kinetics in osmium polypyridyl monolayers.[22,53] In the first, the effects of solvent, electrolyte and temperature on the electrochemical response of monolayers of $[Os(bpy)_2(pNp)Cl]^+$, where bpy is 2,2'-bipyridyl and pNp is 4,4'-bipyridyl, 1,2-bis(4-pyridyl)ethane or 4,4'-trimethylenedipyridine, has been investigated and the heterogeneous rate constant, k^o, for the $Os^{2+/3+}$ reaction has been evaluated using nanosecond timescale chronoamperometry. Well-defined voltammetric responses are obtained for the metal–based redox processes. The effect of solvent on the monolayers has been evaluated by determining the slope of plots formal potential vs. logarithm of electrolyte concentration, with the results showing that oxidation of the monolayers in organic solvents causes the association of an extra anion, while in aqueous solution, two extra anions are bound to the oxidised centres. The temperature dependence of the formal potential over the temperature range –5 to 40 °C has shown that the reaction entropy, $\Delta S_{rc}°$, is positive, indicating increased ordering in the higher oxidation state.

However, most importantly, these monolayers have proved to be ideal probes for investigating heterogeneous electron transfer. Nanosecond timescale chronoamperometry has demonstrated that the rate constant for electron transfer, k^o, is sensitive to the distance of the $Os^{2+/3+}$ metal centre from the electrode, with values of 70×10^4 s^{-1} obtained for the shorter p0p ligand in acetonitrile, as compared to 1.8×10^4 s^{-1} for the p3p ligand in the same solvent. Estimates of the tunnelling parameter, β, have shown that it is independent of the solvent used, yielding a value of 1.6 ± 0.2 $Å^{-1}$. This value is consistent with those calculated by Finklea for through-space tunnelling in metal/monolayer interfaces (1.3-1.8 $Å^{-1}$).[66] However, their measurements on functionalised alkane-thiol monolayers have yielded a value of 1.06 ± 0.4 $Å^{-1}$ for β, more consistent with values expected for through-bond tunnelling,[66] indicating that the electron transfer mechanism in osmium polypyridyl monolayers is different than that observed for monolayers of functionalised alkane-thiols. In common with Chidsey's measurements of functionalised alkane-thiol monolayers,[69] Tafel plots for all monolayers studied exhibit the curvature at high overpotentials predicted on the basis of the Marcus theory. These results demonstrate the excellent suitability of these monolayer systems, in conjunction with high – speed nanosecond timescale chronoamperometry, for the investigation of current electron transfer theory.

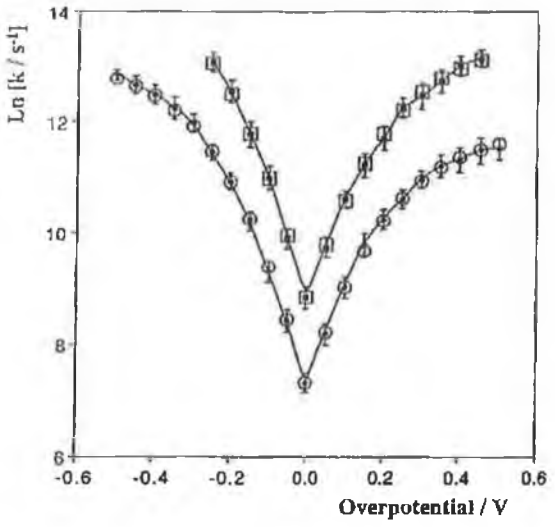

Figure 1.3.2 Tafel plot for $[Os(bpy)_2(p2p)Cl]^+$ and $[Os(bpy)_2(p3p)Cl]^+$ monolayers. The supporting electrolyte is 0.1 M TBAP in chloroform. Solid squares (top) and circles (bottom) denote the experimental p2p and p3p experimental data, respectively. Open squares and circles denote fitted data using $\beta = 1.5$ Å^{-1} and $\lambda = 27.7$ and 26.4 kJ mol^{-1} for the p2p and p3p monolayers respectively. Reproduced from Reference 22.

The second contribution builds on the previous report to investigate the effects of solvent, potential and temperature on the heterogeneous electron transfer dynamics and uses these measurements to test the validity of existing formulations of electrode kinetics.[53] Temperature resolved measurements of k have been used to determine the electrochemical enthalpy, $\Delta H^{\ddagger}$, and have demonstrated that the electrical component of $\Delta H^{\ddagger}$ is considerably less sensitive to potential than is predicted by the Butler – Volmer formulation. The authors have shown that this response is due to the potential-dependent pre-exponential factor described by the Marcus theory. Measurements of the reaction entropy, in conjunction with the enthalpy measurements have allowed the electrochemical free energy of activation, $\Delta G^{\neq}$, to be calculated as a function of solvent. The free energy values obtained agree well with those calculated for solvent reorganisation using the corresponding Marcus theory expression and have provided a means to determine the electronic transmission coefficient, κ_{el}, from the pre – exponential factor. κ_{el} is considerably less than unity, suggesting that the electron

transfer reaction is nonadiabatic. The experimental observation that κ_{el} is increases as the electron transfer distance is reduced is consistent with a reaction rate that is influenced by the spatial overlap of electronic orbitals between the electrode and the redox centre. The interesting conclusion of this work is that the electrode kinetics depend strongly on solvent dynamics, as demonstrated in a strong solvent dependence of $\Delta G^{\neq}$, despite the nonadiabatic character of the reaction.

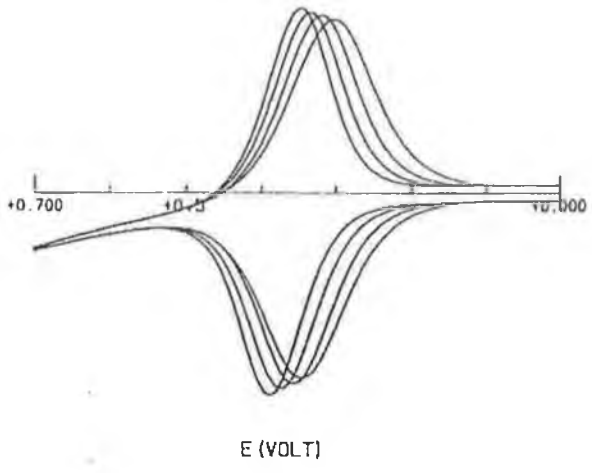

Figure 1.3.3 Effect of temperature on the cyclic voltammetry of a monolayer of $[Os(bpy)_2(p0p)Cl]^{2+}$ in aqueous 0.1 M $LiClO_4$. The temperatures are, from right to left, 37, 25, 15 and 7 ° C, respectively. The scan rate is 51 V s^{-1}. Reproduced from Reference 22.

High-speed chronoamperometry has also been exploited to investigate the heterogeneous kinetics of metal- and ligand -based redox reactions within adsorbed monolayers of $[Os(bpy)_2(py)(p3p)]^{+}$, where bpy is 2,2'-bipyridyl, py is pyridine and p3p is 4,4'-trimethlyenedipyridine.[83] Well-defined voltammetric responses are obtained for the metal- and ligand-based redox processes, at positive and negative potentials, respectively. The chronoamperometry responses are similarly ideal over a range of timescales and potentials, allowing the effect of mediating electronic states of the bridging ligand on charge tunnelling to be investigated.

Tafel plots of ln k vs. overpotential for both metal and ligand based processes display the characteristic Marcus curvature at high overpotentials. Extrapolation of these plots to zero overpotential yielded values of $4.8\pm0.3 \times 10^4$ s^{-1}, $2.2\pm0.2 \times 10^5$ s^{-1} and $3.3\pm0.3 \times 10^4$ s^{-1} for $k°_{3+/2+}$, $k°_{2+/1+}$, and $k°_{1+/0}$, respectively. Significantly, temperature resolved

measurements of k demonstrate that the electrochemical activation enthalpy, $\Delta H^{\ddagger}$, decreases from 43.1±2.8 kJ mol^{-1} for the 3+/2+ reaction to 25.8±1.9 kJ mol^{-1} for the 1+/0 process. The reaction entropy, $\Delta S_{rc}°$, has been determined by temperature resolved measurements of the formal potential, with the value depending on the charge state of the monolayer (211±18, 119±9 and 41±5 J mol^{-1} K^{-1} for 3+/2+, 2+/1+ and 1+/0, respectively). The entropy and enthalpy values have been used to calculate the electrochemical free energy of activation, $\Delta G^{\neq}$, 11.5±0.8, 14.2±1.2 and 19.8±1.3 kJ mol^{-1} for for 3+/2+, 2+/1+ and 1+/0, respectively. That $\Delta G^{\neq}$ depends on the charge state emphasises the importance of considering the difference in reaction energetics when evaluating the degree of donor/acceptor coupling from rate data.

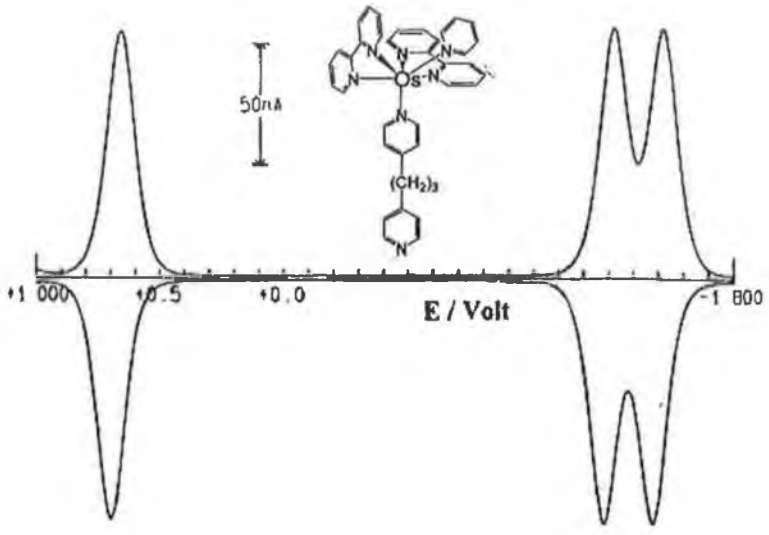

Figure 1.3.4 Cyclic voltammogram of a spontaneously adsorbed $[Os(bpy)_2py(p3p)]^{2+}$ monolayer. The scan rate is 50 V s^{-1}, the surface coverage is 9.5×10^{-11} mol cm^{-2}. The supporting electrolyte is 0.1 M $TBABF_4$ in acetonitrile. The radius of the Pt microelectrode is 25 μm. Cathodic currents are up and anodic currents are down. The initial potential is 1.000 V. Reproduced from Reference 83.

The electronic transmission coefficients, κ_{el}, are all less than unity, suggesting that the electron transfer reaction for all redox processes within these monolayers is nonadiabatic, indicating weak electronic coupling between the electrode and the redox moiety. However, the pre – exponential factors calculated for the first and second bpy reductions, 22.9±8.3 and 24.4±9.9 $\times 10^6$ s^{-1}, are more than a magnitude larger than

those observed for the metal – based reaction, $1.5\pm1.7 \times 10^6$ s^{-1}, suggesting that electronic coupling between the redox moiety and the electrode is stronger for the ligand reduction process. This observation indicates that traditional two-state models that consider just the donor and the acceptor, may not account for important factors that influence that rate of heterogeneous electron transfer across metal/monolayer interfaces.

In another contribution, Forster and co-workers have utilised high – speed cyclic voltammetry to compare heterogeneous electron transfer through conjugated and non-conjugated bridges, using monolayers of $[Os(bpy)_2(bpe)Cl]^+$, where bpe is the conjugated bridge *trans*-1,2-(4-pyridyl)ethylene[79] and comparing the results to those previously published for the non-conjugated 1,2-bis(4-pyridyl)ethane (p2p) bridging ligand.[22,53] Cyclic voltammograms have been obtained at scan rates between 1000 and 6000 V s^{-1}, in the range where the time constants for the voltammetric experiment and heterogeneous electron transfer become comparable. The heterogeneous electron transfer rate constant, k^o, and the reorganisation energy, λ, for the electron transfer reaction have been determined by least -squares minimisation between the experimental voltammograms and theoretical voltammograms generated using the through-space electron tunnelling model proposed by Finklea,[66] as described in Section 1.2. The least-squares minimisation was performed using the Nelder and Mead Simplex algorithm. Figure 1.3.5 shows the comparison between the model and the experimental data, demonstrating that the electron transfer response is quite well described by the through – space tunnelling mechanism. The fit yields values of 9.4×10^3 s^{-1} and 11.4 kJ mol^{-1} for k^o and $\Delta G^{\neq}$, respectively, where $\Delta G^{\neq} = \lambda / 4$. For the p2p monolayer, values of 300×10^3 s^{-1} for k^o and 1.2 kJ mol^{-1} for $\Delta G^{\neq}$ were obtained, which are indistinguishable from those obtained by potential step chronoamperometry.[22] Using these results to calculate the pre-exponential factor demonstrates that electronic coupling is significantly stronger for the non-conjugated bridge, suggesting that the p2p bridge has sufficient flexibility to reduce its electron transfer distance below the value of 10 Å expected on the basis of a rigid rod model. Overall, this work demonstrates the powerful contribution that Marcus modelling of high-speed cyclic voltammograms can make to elucidating heterogeneous electron transfer dynamics.

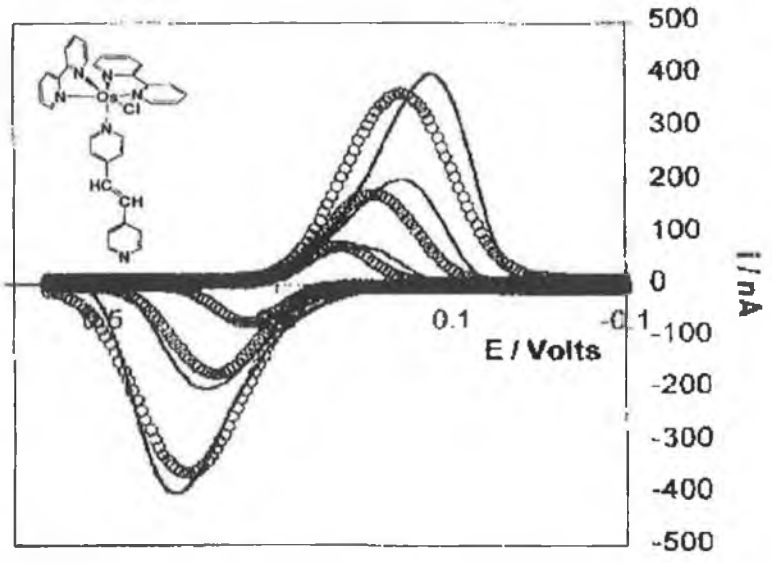

Figure 1.3.5 Experimental (-) and theoretical (O) voltammograms generated using the method of Finklea, for a spontaneously adsorbed $[Os(bpy)_2(bpe)Cl]^{2+}$ monolayer on a 25 μm radius Pt electrode. From top to bottom, the scan rates are 6000, 3000 and 1000 V s^{-1}. Reproduced from Reference 80.

A combination of high speed chronoamperometry and high scan rate cyclic voltammetry has been exploited to investigate the effect of electrode density of states on the heterogeneous electron transfer dynamics of monolayers of $[Os(Ome\text{-}bpy)_2(p3p)Cl]^{+}$, where Ome-bpy is 4,4'-dimethyoxy-2,2'-bipyridyl and p3p is 4,4'-trimethylenedipyridine.[80] Stable monolayers of this complex have been formed onto platinum, mercury, gold, silver, carbon and copper microelectrodes and the voltammetric response at scan rates above 2000 V s^{-1} has been modelled using the nonadiabatic model described in the previous paper.[79] This modelling shows that the rate constant, k^o, depends on the identity of the electrode material, e.g., k^o is 6×10^4 and 4×10^3 s^{-1} for platinum and carbon electrodes, respectively. Chronoamperometry, utilised to probe the potential dependence of the rate constant, yields values of $4.0\pm0.2 \times 10^4$ and $3.0\pm0.3 \times 10^3$ s^{-1} on going from platinum to carbon electrodes. Significantly, temperature resolved chronoamperometry and cyclic voltammetry reveals that the electrochemical enthalpy, $\Delta H^{\ddagger}$, and reaction entropy, ΔS_{rc}°, are independent of electrode material, having values of 11.1 ± 0.5 kJ mol^{-1} and 29.6 ± 2.4 J mol^{-1} K^{-1},

respectively. The authors have carried out an analysis of the experimental pre-exponential factor which indicates that electron transfer is controlled by a nonadiabatic mechanism and that ν_{el}, the electron hopping frequency, is sensitive to the identity of the electrode material. This data has been used to probe the validity of electron transfer models which predict that the extent of electronic coupling between the redox species and the electrode is higher for platinum than gold. These models, developed by Marcus and co-workers, also predict that the higher density of states (the electronic states in the metal available to participate in an electron transfer reaction, having units of (area-energy)$^{-1}$, such as $cm^{-2}eV^{-1}$ [43]) in platinum vs. gold leads causes a proportional increase in ν_{el}. The analysis found that the ratio of the prefactors for platinum and gold is 2.9 ± 0.7, compared with a ratio of 7.5 for the density of states and leads the authors to conclude that the nonadiabatic rate of heterogeneous electron transfer does not simply depend on the density of states within the electrode.

High-speed cyclic voltammetry has again been utilised as a means to probe heterogeneous electron transfer, in this case the effect of protonation on electron transfer via a superexchange mechanism.[84] Monolayers of $[Os(bpy)_2(4\text{-tet})Cl]^+$, where bpy is 2,2'-bipyridyl and 4-tet is 3,6-bis(4-pyridyl)-1,2,4,5-tetrazine, have been formed on gold microelectrodes and have exhibited well-defined voltammetric responses for the $Os^{2+/3+}$ redox reaction over the pH range 0.5 – 8.0. The tetrazine bridge linking the osmium centre to the electrode may be reversibly protonated and deprotonated by varying the solution pH, and pH dependent measurements of the interfacial capacitance has indicated that the pK_a is 2.7 ± 0.3. Cyclic voltammograms at scan rates of up to 4000 V s^{-1} for the protonated and deprotonated monolayers have been modelled using the nonadiabatic mechanism utilised in the previous papers.[79,80] Interestingly, the modelling shows that protonating the bridge decreases the electron transfer rate constant, k^o, from 1.1×10^4 to 1.2×10^3 s^{-1}, while the $\Delta G^{\neq}$ values obtained are the same for the protonated and unprotonated bridge. However, for this system the quality of the model fit is not particularly sensitive to the value of $\Delta G^{\neq}$, i.e., increasing $\Delta G^{\neq}$ by 25% increases the value of the model sum squared residuals by less than 10%, suggesting that the values of $\Delta G^{\neq}$ obtained are mere approximations of the true value. The observation that k^o for the reaction decreases upon protonation of the tetrazine bridge indicates that the redox switching process is influenced by mediating electronic states within the bridging ligand (superexchange) and that the hole transfer is mediated

through the highest unoccupied molecular orbital of the tetrazine ligand. Protonating the bridge increases the energy difference between the bridge states and the Os metal centre and therefore causes the standard rate constant to decrease.

1.3.2 Di- and Tri-metallic molecules

As described in Section 1.1 of this chapter, electronically excited states are of considerable interest due to their many diverse applications, including strategies for artificial photosynthetic systems[20,21] and solar energy conversion.[18,19] As a consequence, there is a large body of research which focuses on elucidating the factors which affect electron transfer to and from electronically excited states. In the context of these studies, ligand – bridged dimetallic and trimetallic polypyridyl complexes of ruthenium and osmium are well suited, because the redox sites are held in a well-defined geometry to one another and they exhibit facile, reversible electrochemical responses.[85] Considerable investigations into electron transfer between metal centres have been carried out utilising both dimeric homo- and hetero-metallic complexes of osmium, ruthenium and other metals such as rhenium, iridium and rhodium and some comprehensive reviews on the subject are available.[23,86,87,88]

Many significant contributions in this area have been made by Meyer and various authors, who have extensively investigated the electron transfer properties of homo-metallic dimers of osmium[85,89,90] and ruthenium,[91,92] bridged using polypyridyl-type ligands, with particular emphasis on intramolecular electron transfer quenching in mixed – valence dimers. In one contribution, they have reported on osmium –osmium dimetallic complexes of the type $[(bpy)_2(CO)Os^{II} - L - Os^{II}(Cl)(phen)(dppe)](PF_6)_3$ where bpy is 2,2'-bipyridyl, phen is 1'10'-phenanthroline, dppe is cis-$Ph_2PCH{=}CHPPh_2$ and L is 4,4'-dipyridyl or 1,2-bis(4-pyridyl)ethane.[85] Using transient emission spectrocopy, they observed a reduction in the lifetime of the bpy based excited state in the dimer compared to the parent monomer species, which has been attributed to reductive electron-transfer quenching of the bpy based excited state by the phen-dppe osmium centre. The rate constant for this electron transfer quenching is estimated to be of the order of 10^7 s^{-1}. Related work has shown that the likelihood of electron transfer in such dimeric species is enhanced by having the metal centres as close together as possible, i.e., by controlling the length of the bridging ligand employed.[91]

In a more recent contribution, Meyer et al. have studied the near-infrared spectroscopy of the mixed-valence osmium dimers, $[(bpy)_2(Cl)Os^{III}(BL)Os^{II}(Cl)(bpy)_2]^{3+}$ and $[(tpy)(bpy)Os^{III}(BL)Os^{II}(bpy)(tpy)]^{5+}$, where bpy is 2,2'-bipyridyl, tpy is 2,2';6',2''-terpyridine and BL is a bridging ligand, either 4,4'-bipyridyl or pyrazine.[90] The complexes exhibit weak bands in the near-infrared region of the spectrum, due to intervalence transfer (IT) transitions, in which light absorption results in electron transfer between orbitals on different sites. Using the theory developed by Hush,[55,56] the IT bands have been analysed in terms of ε_{max}, the molar absorptivity (M^{-1} cm^{-1}), E_{abs}, the absorption maximum (cm^{-1}) and $\Delta\upsilon_{1/2}$, the bandwidth at half height (cm^{-1}) and these parameters have been used to calculate the electronic coupling factor, H_{rp} and $\Delta G^{\neq}$, the free energy change for the reaction. For example, for the pyrazine bridged dimers, the analysis yields values of 247 cm^{-1} (0.03 eV) for H_{rp} and 408 cm^{-1} (0.05 eV) for $\Delta G^{\neq}$, for the lowest energy IT transition, consistent with an adiabatic electron transfer reaction.[42] Using Marcus-Hush theory, these values are used to estimate values of 8.3×10^{10} s^{-1} for k_{ET}, the electron transfer rate constant and 2620 cm^{-1} (0.32 eV) for λ, the reorganisation energy.

With a focus on the development of photonic molecular devices and testing current theoretical treatments of electron transfer, Balzani and co-workers have carried out a number of investigations into the photoinduced energy and electron transfer processes of same- and mixed-valence dimers of osmium and ruthenium.[93,94,95,96] A significant paper describes the synthesis of heterometallic complexes of ruthenium and osmium linked by the bridging ligand 1,4-bis[2-(2,2'-bipyridin-5-yl)ethenyl]bicyclo[2.2.2]octane (bpy-S-bpy, Figure 1.3.6).[93] The length of the rigid spacer, S, is 9 Å and the centre-to-centre separation distance in the complexes is 17 Å. On the basis of luminescence and transient emission spectroscopy measurements, the authors demonstrate that efficient energy transfer quenching from the osmium to the ruthenium unit occurs in the same-valence dimers, while quenching is dominated by an electron-transfer mechanism in the mixed-valence dimers. The rate of electron transfer quenching is rapid, e.g., k_{ET} is 8.7×10^9 s^{-1} for the Ru^{II}(bpy-s-bpy)Os^{III} species. This value has been used to calculate a value of 1.3×10^{10} s^{-1} for ν_{el}, the electron hopping frequency, using Marcus-Hush theory. These values seem reasonable and suggests strong electronic coupling across the bpy-S-bpy bridge.

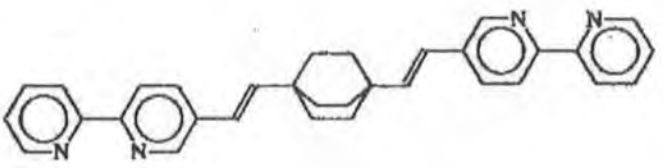

Figure 1.3.6 Schematic representation of the bridging ligand bpy-S-bpy. Reproduced from Reference 93.

Fagalde and Katz have investigated the distance dependence of intramolecular electron transfer parameters in mixed valence asymmetric complexes of ruthenium.[97] The complexes are of the general form $[(terpy)(bpy)Ru^{II}\text{-}L\text{-}Ru^{III}(NH_3)_5]^{5+}$, where terpy is 2,2';6',2''-terpyridine, bpy is 2,2'-bipyridyl and L is CN^-, pyrazine, 4-cyanopyrazine, 4,4'-bipyridyl or trans-1,2-bis(4-pyridyl)ethylene (bpe). A range of metal-to-metal distances, d, from 5 to ≅ 14 Å is encompassed when going from L = CN^- to L = bpe. Each of these compounds exhibits intervalence transfer (IT) bands in the near-infrared spectra. These bands have been analysed via the method described by Hush,[55,56] and utilised by Meyer,[90] to yield values of H_{rp}, $\Delta G^{\neq}$ and λ for each compound. For example, the bpe bridged compound has values of 189 cm^{-1} (0.023 eV) for H_{rp}, 0.89 eV for $\Delta G^{\neq}$ and 1.34 eV for λ. Forster et al. obtained a value of 0.47 eV for λ for heterogeneous electron transfer across the same bpe bridge in the case when it links a metal electrode and an osmium polypyridine centre.[79] λ for the homogeneous reaction should be approximately twice λ for a heterogeneous reaction.[43] The reorganisation energy demonstrates the dependence with 1/r expected on the basis of Marcus-Hush theory. A plot of 2 ln H_{rp} vs. d yields a value of 0.40 $Å^{-1}$ for β, considerably smaller than the value of 1.6 $Å^{-1}$ previously observed for heterogeneous electron transfer across the BPE bridge.[79] These differences in reorganisation energy and tunnelling parameter demonstrate the considerable difference between the conditions of homogeneous and heterogeneous electron transfer, even when it takes place across the same ligand bridge.

Recent reports have shown that trimetallic species can function as useful photonic molecular devices.[98,99] Abrana and Abruña have reported on the synthesis and electrochemical investigation of $Os(tppz)_2(Ru(tpy))_2(PF_6)_6$, a trimetallic complex of two ruthenium-terpyridine centres with a central osmium core, bridged with the ligand tetra-2-pyridyl-1,4-pyrazine (tppz). They have found that the tppz ligand allows the

rapid construction of transition metal complexes and suggest that this ligand may allow for the construction of molecular wires with potentially useful electronic properties.[98] Zahavy and Fox have described the behaviour of a trimetallic complex with a sequence of redox-active metal sites (Os^{II}-Ni^{II}-Pd^{II}), synthesised in an attempt to develop an electro-switchable-photoinduced-electron-transfer device(ESPET).[99] In this complex, the Os^{II} centre is the light-harvesting component, the Pd^{II} site is the electron acceptor and the Ni^{II} site functions as the electro-switchable intervening spacer. Combined electrochemical and lifetime measurements have shown that selective reduction of the Ni^{II} centre permits regulation of the photoinduced electron transfer from the excited state Os^{II} site to the Pd^{II}. This is demonstrated in single photon counting transients of the complex. In the oxidised form of the complex, the short-lived (major) component of the observed biexponential emission decay is due to the partial oxidative quenching of the Os^{II} centre by Ni^{II}, while the long-lived (minor) component is due to the unquenched Os^{II}* site. In the reduced form, direct oxidative quenching by the Pd^{II} site is a possible pathway as the direct oxidation by Ni^{II} is significantly reduced and the lifetime of the Os^{II}* site is extended. In this manner, the complex has an "off" (quenching by Ni^{II}, short lifetime) and an "on" mode (quenching by Pd^{II}, long lifetime). While this trimetallic species does not function in the exact manner required of an ESPET, it nevertheless demonstrates that electrochemical switching of the redox state of a spacer between a donor-acceptor pair can dictate the type of the observable charge separation and the lifetime of the resulting charge-separated ion pair.

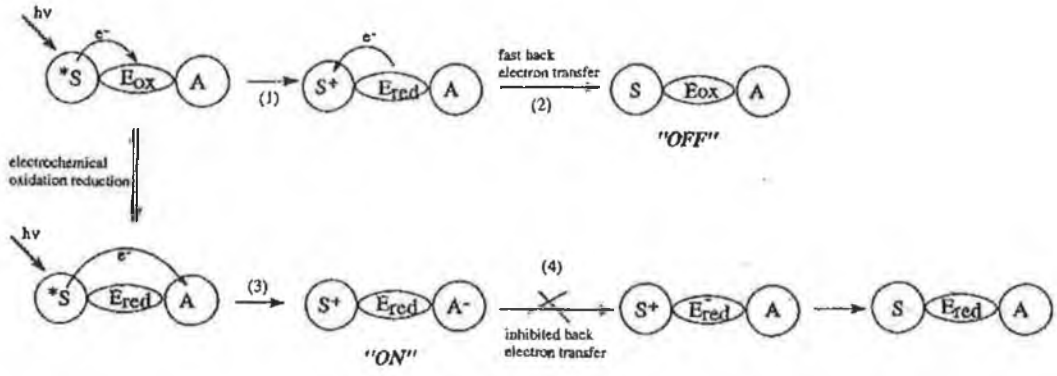

Figure 1.3.7 The operational principle of an electro-switchable-photoinduced-electron-transfer (ESPET). S is the light harvesting component, A is the electron acceptor and E is an intervening electro-switchable component, stable in both the oxidised and reduced forms. Reproduced from Reference 99.

Brewer and co-workers have carried out significant investigations in the synthesis and spectroscopic and electrochemical investigation of trimetallic complexes.[32,33,100,101,102,103] Most notable is the development of a mixed-metal trimetallic complex, $\{[(bpy)_2Ru(dpb)]_2IrCl_2\}(PF_6)_5$, where bpy is 2,2'-bipyridine and dpb is 2,3-bis(2-pyridyl)benzoquinoxaline (c.f. Figure 1.1.3), which is capable of photoinitiated electron collection.[32] The authors suggest that the lowest excited state of the complex is $Ru(d\pi) \rightarrow dpb(\pi)^*$ in nature, however the reasoning for this conclusion is not well explained. Accepting the hypothesis that the LUMO is on the dpb ligand, photolysis of the complex in the presence of dimethylaniline as a sacrificial electron donor leads to the formation of the doubly-reduced species, $\{[(bpy)_2Ru(dpb^-)]_2IrCl_2\}^{3+}$, in which both bridging ligands have been photoreduced by one electron, described here as a "photoinitiated electron collection" process. This is shown by the disappearance of the $Ru(d\pi) \rightarrow dpb(\pi^*)$ band at 660 nm in the UV-visible absorption spectrum of the complex during the photolysis. Further investigations have shown that this complex functions as an efficient catalyst for the electrocatalytic reduction of CO_2 to CO.[33]

Finally, a combination of monolayer electrochemistry and spectroscopy has allowed Forster and Keyes to compare electrochemical and photoinduced electron transfer.[104] They utilised a dimeric complex of [p0p $Os(bpy)_2$ 4-tet $Os(bpy)_2Cl]^{3+}$, where p0p is 4,4'-bipyridyl, bpy is 2,2'-bipyridyl and 4-tet is 3,6-bis(4-pyridyl)-1,2,4,5-tetrazine. By spontaneously forming adsorbed monolayers of this complex onto platinum microelectrodes, the rate constant for both the "inner" $[p0pOs(bpy)_2$ 4-tet$]^{2+}$ and "outer" [4-tet $Os(bpy)_2Cl]^+$ heterogeneous electron transfers have been determined using high-speed chronoamperometry and high-scan rate cyclic voltammetry modelled using the Marcus theory. The rates are $1.3\pm0.2 \times 10^6$ and $1.1\pm0.1 \times 10^4$ s^{-1} for the "inner" and "outer" electron transfer reactions respectively and the reorganisation energy λ is estimated to be at least 0.6 eV. Transient emission spectroscopy has allowed the determination of the rate constant for photoinduced electron transfer quenching within the metal complex. The results show that the rate constant for PET ($1.6\pm0.1 \times 10^6$ s^{-1}) is faster than that for ground state electron transfer at the same driving force ($4.0\pm0.2 \times 10^4$ s^{-1}). Using these values and the experimental estimations of λ, has allowed the pre-exponential factor for the ground and excited state electron transfer to be calculated, which is related to the magnitude of electronic coupling between the donor and acceptor states in the electron transfer reaction. The interesting conclusion drawn from

these calculations is that the strength of electronic coupling across the tetrazine bridge is significantly greater for two metal centres than for a metal electrode and a remote redox moiety.

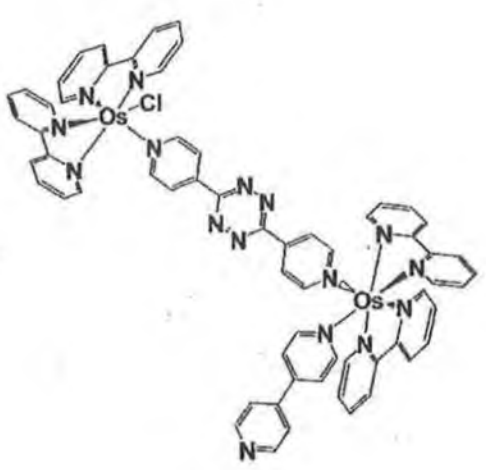

Figure 1.3.8 Schematic representation of [p0p $Os(bpy)_2$ 4-tet $Os(bpy)_2$ $Cl]^{3+}$. See text for details of abbreviations. Reproduced from Reference 104.

The discussion presented in this section have shown that both alkane-thiol and osmium/ruthenium polypyridine monolayers provide a powerful means of testing contemporary heterogeneous electron transfer theory as it occurs in the ground state. Similarly, dimetallic complexes allow the probing of the Marcus-Hush homogeneous electron transfer theory as it applies to excited state electron transfers. Significantly, while trimetallic complexes have been investigated as photonic molecular devices, they have not to date been used extensively to probe the dynamics and energetics of photoinduced excited state electron transfer. The final example detailed in this section has shown that combining ground state monolayer and photoinduced excited state electron transfer measurements can provide insights as to the fundamental differences between electron transfer in the ground and excited state. However, notable by their absence from this section is reports which use monolayers to probe excited state electron transfer characteristics. The reasons for this lack of available literature, and a discussion as to why these kinds of measurements are viable is presented in the following sections, 1.4 and 1.5.

1.4 Direct Experimental Determination of Excited State Redox Potentials

The importance of electronically excited states in the development of photonic molecular devices was emphasised in Section 1.1. This importance is due to the fact that electronically excited states are simultaneously better electron donors and acceptors that their ground state counterparts.[4] While ground state redox potentials are easily obtained by conventional electrochemical means such as cyclic voltammetry, the transient nature and short lifetimes of excited states traditionally precludes the use of such methods for the direct determination of excited state redox potentials.

Traditionally, excited state redox potentials have been estimated in two ways. The first and most common, is the approach of Rehm and Weller,[105] which uses the excited state energy E^{0-0} to correct the ground-state redox potentials:

$$E^*_{1/2}{}^{ox} = E_{1/2}{}^{ox} - E^{0-0} \qquad (1.4.1)$$

$$E^*_{1/2}{}^{red} = E_{1/2}{}^{red} + E^{0-0} \qquad (1.4.2)$$

where $E_{1/2}{}^{red}$ and $E_{1/2}{}^{ox}$ are the potentials for the first reduction and oxidation, respectively, and E^{0-0} is the energy gap between the zeroth vibrational levels of the ground and excited states, estimated from emission spectra obtained at cryogenic temperatures. This method has been widely used for the calculation of excited state redox potentials.[4,23,106] However, the values obtained by this method are only estimates of the true potentials and typically contain uncertainties of 100 mV or more, due to the inaccuracies involved in using ground state parameters to approximate excited state characteristics. For example, in the case of ruthenium and osmium polypyridyl complexes, the vibrational fine structure is never well resolved,[65] making it difficult to accurately determine E^{0-0}

The second approach is an indirect measurement based on kinetic studies of quenching data for Ru(tris-bipyridine) and a series of nitroaromatics, aromatic amines and bipyridinium ions. An example of the use of this method is demonstrated by Bock and Meyer et al.[107] Their approach is based on a modification of the kinetic scheme for fluorescence quenching proposed by Rehm and Weller.[105] To estimate the excited state

redox potentials, plots of ln k_q vs. E^o for a series of related quenchers (k_q is the rate constant for electron transfer quenching, obtained from transient emission experiments) are prepared. The authors define a potential, $E^o(0)$, as the formal potential at a hypothetical quencher couple where the driving force is zero, $k_q(0)$. Their theoretical treatment of the quenching mechanism allows the calculation of ln $k_q(0)$ from the self-exchange rate constants of the quencher and excited state couples and the work terms involved in bringing together the reactants. Based on their theory, $E^o(0)$ is the quencher potential for which ln k_q (calculated) equals ln k_q (plotted from experimental data). Correcting $E^o(0)$ for the electrostatic energies required to bringing together the reactant and product species allows the excited state redox potentials to be calculated. In this manner, the excited state redox potentials for $Ru(bpy)_3^{2+}$ in acetonitrile at room temperature are estimated to be -0.81 $\pm$ 0.07 V for $Ru(bpy)_3^{3+/2+*}$ and +0.77 $\pm$ 0.07 V for $Ru(bpy)_3^{2+*/1+}$. This method has also been used by Ballardini et al, yielding a value of +0.79 V for the $Ru(bpy)_3^{2+*/1+}$ redox couple.[108]

Both these methods, while widely used and theoretically sound,[109,110,111] never the less have their drawbacks. In the first method, the inherent inaccuracies in using ground state parameters to approximate excited-state characteristics cause uncertainties in the values calculated of 100 mV or more. The bimolecular quenching method involves extremely detailed and time-consuming experiments utilising a large range of oxidative and reductive quenchers and is only applicable in the case where energy transfer does not compete with electron transfer. From these points, it is easy to conclude that a *direct* method of determining excited state redox potentials highly desirable.

To date, only two examples of direct experimental determination are to be found in literature. The first was proposed by Jones and Fox[112] in 1994 and is based on a modified phase-modulated voltammetry (PMV) system (Figure 1.4.1). PMV had been used previously to measure the oxidation and reduction potentials of organic radical species.[113,114] The PMV system uses an argon laser tuned to 350 mW output at 457.9 nm as a light source to create a transient population of the unstable species to be interrogated within an electrochemical cell. By modulating the light source sinusoidally (using a sine wave generated by a 10 MHz function generator coupled to an electrooptic voltage modulator), the concentration of the photogenerated transient species of interest is modulated in parallel. If the applied potential is sufficient to induce electron transfer, the resulting change in concentration can be observed

electrochemically as an alternating (ac) component to the current output. By using a phase- and frequency-sensitive detector, it is possible to "lock in" on the resulting ac signal and discriminate against high-frequency noise and low-frequency background currents. From the observed phase shift of the electrochemical signal, it is also possible to determine the lifetime of the analyte. However, this approach proves to be experimentally challenging due to low equilibrium concentration of excited state species and other experimental limitations, including an error of $\pm 2°$ in determining the phase shift with the lock-in amplifier, the inherent time resolution of the potentiostat and the possibility of efficient excited state quenching by the gold electrode, and therefore the lifetime values obtained differ significantly from literature values.

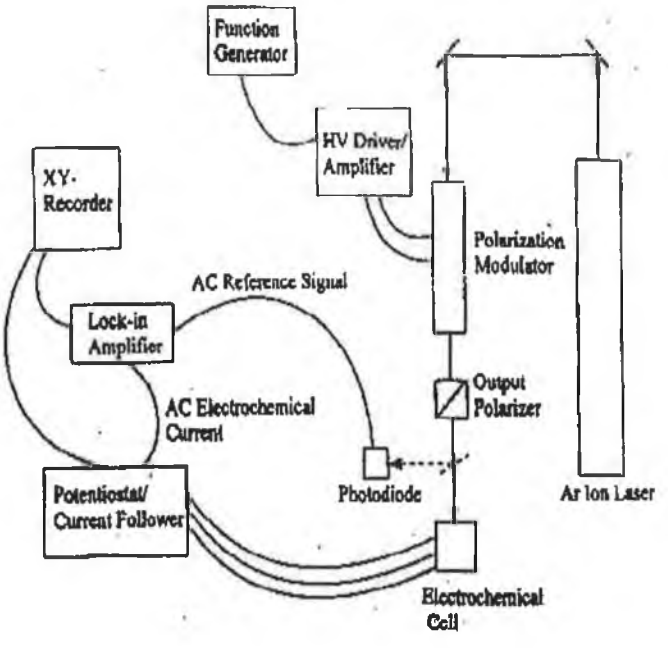

Figure 1.4.1 Phase – modulated voltammetry apparatus. Reproduced from Reference 112.

The PMV system described has been used to determine the excited state redox potentials, lifetimes and excited state energies of a range of ruthenium polypyridine complexes. The excited state reduction and oxidation potentials of $Ru(bpy)_3^{2+}$ have been determined to be +0.83 V and –0.79 V respectively, which are in good agreement with the theoretical Rehm-Weller values. However, the values obtained for the excited state oxidation potentials are less accurate than those for the excited state reduction potentials, attributed to the inability of the experiment to detect the photocurrents which

correspond to oxidation for compounds with excited state lifetimes of less than < 800 ns. Another limitation of the experiment is the need for extensive drying of the solvent used to reduce significant background photocurrent from the gold electrode, caused by charge transfer to residual water in organic solvents. However, aside from these limitations, the system is capable of the *direct* determination of excited state reduction potentials and to less accurate extent, excited state oxidation potentials, although no information as to the dynamics of excited state electron transfer is obtained with this experimental procedure.

The second method for the direct measurement of excited state redox potentials has been developed by Forster and Keyes.[65] This approach is based on measuring high – speed cyclic voltammograms of a redox active, luminescent monolayer immobilised on a microelectrode. The rationale for this lies approach is that if an adsorbate displays a relatively long emissive lifetime (≈ 1 μs), and the kinetics of electron transfer occur on a shorter time-scale than the excited state lifetime, then theoretically, if the potential is swept sufficiently fast, it should be possible to observe the oxidation and reduction of the excited state. The long lifetime also ensures that when the species is located close to the metal electrode, the emission is capable of competing with energy and electron transfer quenching by the electrode surface.

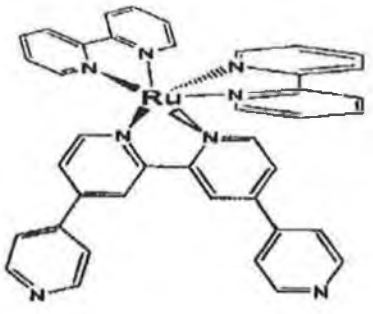

Figure 1.4.2 Schematic diagram of $[Ru(bpy)_2(Qbpy)]^{2+}$. Reproduced from Reference 65.

In order to carry out these measurements, a complex of $[Ru(bpy)_2(Qbpy)]^{2+}$, where bpy is 2,2'-bipyridine and Qbpy is 2,2':4,4'':4',4''-quarterpyridyl (Figure 1.4.2) was synthesised. This complex is capable of forming spontaneously adsorbed monolayers

on a clean platinum microelectrode. Chronoamperometry on a microsecond time scale indicates that the standard heterogeneous electron transfer rate constants of the complex are rapid ($5.1\pm0.3 \times 10^5$ s^{-1} and $3.0\pm0.1 \times 10^5$ s^{-1} for the ground state $Ru^{2+/3+}$ and $Ru^{2+/1+}$ reactions, respectively). However, the value of κ_{el} for the electron transfer, evaluated from Tafel plots of ln k vs overpotential is significantly less than unity, indicating that electron transfer takes place via a nonadiabatic mechanism. This low κ_{el} value suggests that electronic coupling between the monolayer redox centres and the electrode is weak.[23]

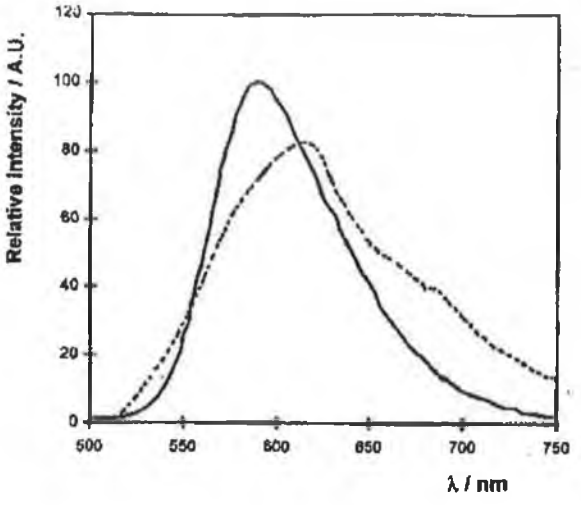

Figure 1.4.3 Room temperature emission spectra for $[Ru(bpy)_2(Qbpy)]^{2+}$ dissolved in 4:1 ethanol:methanol (—) and as a spontaneously adsorbed monolayer (---). The y-axes are normalised relative to each peak's maximum intensity. Reproduced from Reference 65.

The complex exhibits a long luminescence lifetime of microsecond order in solution at both room and at liquid nitrogen temperatures, and significantly, as shown in Figure 1.4.3, upon laser excitation at 355 nm, the monolayers fluoresce. This emission indicates that despite having the excited state located close to a metal surface energy transfer does not completely quench the excited state, a phenomenon which will be discussed in more detail in Section 1.5. The transient emission decays display bi-exponential behaviour, which is not unusual for luminescent species immobilised within polymer films or sol – gels and may reflect discrete local microenvironments within the monolayer.[115] However, the most interesting result obtained from these

lifetime measurements is the observation that the excited-state lifetime of the adsorbate is approximately three times longer than that found for the complex in solution (6.2 μs vs. 1.4 μs) and is indistinguishable from that observed for the complex in an ethanol:methanol glass at cryogenic temperatures. The authors have attributed this phenomenon to the solid-like microenvironment within the monolayer. Fluorescence enhancement has previously been observed for dye molecules located near to rough metal surfaces (c.f. Section 1.5).[126,127] The observed increase in lifetime could be due to this enhancement effect, as the electrode upon which the monolayer is immobilised is significantly rough on a microscopic scale (roughness factors of 1.3 to 1.6 are typical).

For the excited state redox potentials to be experimentally observed within a potential sweep, it is important that the timescale of electron transfer is shorter than the excited state lifetime. For these complexes, it has been previously shown that the same orbital is populated by ligand-based reduction and photoexcitation. Using this fact, the rate of electron transfer from the bpy-localised excited state has been likened to the rate at which the reduced $bpy^{\bullet-}$ ligand can be reoxidised. The authors have used data reported by Strekas and Baker on the excited state lifetimes of $[Ru(bpy)_2(Qbpy)]^{2+}$ and its methylated derivative, $[Ru(bpy)_2(Qbpyme_2)]^{2+}$,[116] to calculate the rate of quenching of the bpy-localised excited state by the viologen electron acceptor as 1.5×10^7 s^{-1} where the driving force is approximately 0.32 V. By extrapolating the potential dependent rate constant data for the reoxidation of the reduced $bpy^{\bullet-}$ ligand to this driving force, a rate constant of 6.6×10^8 s^{-1} is obtained for the ground state oxidation of the $bpy^{\bullet-}$ species. The authors acknowledge that this analysis has its limitations, but suggest that it provides a reasonable estimate of the rate of excited state oxidation. This analysis leads to the conclusion that the time constant for electron transfer from the excited state is approximately 300 ns under conditions of zero driving force, compared to an emission lifetime of approximately 6 μs.

The fact that the complex is capable of forming electroactive films with rapid heterogeneous electron transfer kinetics, and that these monolayers are capable of efficient fluorescence, indicates that this complex is suitable for the *direct* determination of excited state redox potentials via direct high – speed cyclic voltammetry. For electrochemistry at short timescales, the authors have utilised a

custom-built function generator-potentiostat, capable of MV s^{-1} scan rates. Laser excitation of the monolayers is used to optically trigger the voltammetric scan so that it commences simultaneously with the arrival of an incident laser pulse on the electrode surface. The voltammetric response obtained in this experiment at a scan rate of 22,000 V s^{-1} is shown in Figure 1.4.4. The authors have found that the response obtained in this experiment depends markedly on the scan rate employed, with too slow a scan rate yielding only the CV expected for a ground state monolayer. The current oscillation seen in Figure 1.4.4 is attributed to the oxidation of Ru^{2+}* to Ru^{3+} and the rapid reduction of Ru^{3+} to Ru^{2+}, as Ru^{3+} will be highly unstable in this potential region. It is qualitatively consistent with the response anticipated for an electronically excited state, as is the peak potential and voltammetric time-scale over which the transient response is observed for monolayer modified electrodes. The experiment yields a value of –0.42 V for the excited state oxidation potential, which agrees to within 180 mV to that predicted by the Rehm – Weller equation. The difference may be accounted for by the influence of the dynamics of heterogeneous electron transfer on the experimentally determined value of the excited state redox potential. These results indicate that a careful choice of probe redox species, and the use of microelectrodes and high – speed electrochemical techniques makes it feasible to directly determine excited state redox potentials.

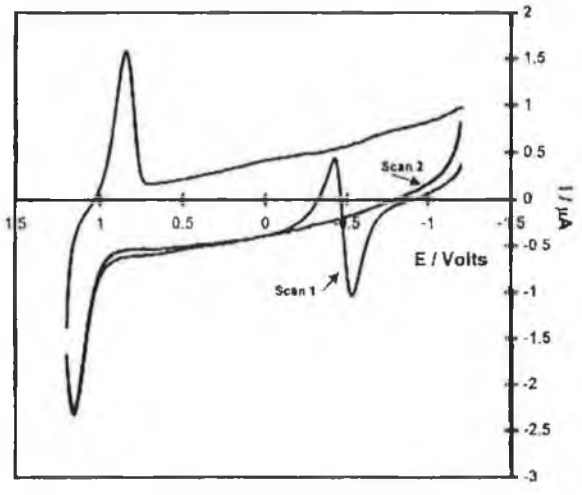

Figure 1.4.4 Cyclic voltammetry of a 5 μm radius platinum microelectrode modified with an $[Ru(bpy)_2(Qbpy)]^{2+}$ monolayer following laser excitation at 355 nm. The scan rate is 22,000 V s^{-1}, the surface coverage is 1.1×10^{-10} mol cm^{-2}, and the supporting electrolyte is 0.1 M $TBABF_4$ in acetonitrile. The initial potential is – 1.2 V. Reproduced from Reference 65.

1.5 Emission at Interfaces

In order to electrochemically measure the excited state redox potentials of a monolayer immobilised on a platinum microelectrode, the excited state must exhibit emission with sufficient lifetime to allow the heterogeneous electron transfer to take place. Conventional theory postulates that excited states near to metal surfaces are efficiently quenched and therefore emission is unobservable.[117] In contrast, excited states are known to persist near semiconductor surfaces and this process forms the basis of many of the photonic molecular devices discussed in Section 1.1.[8,19]

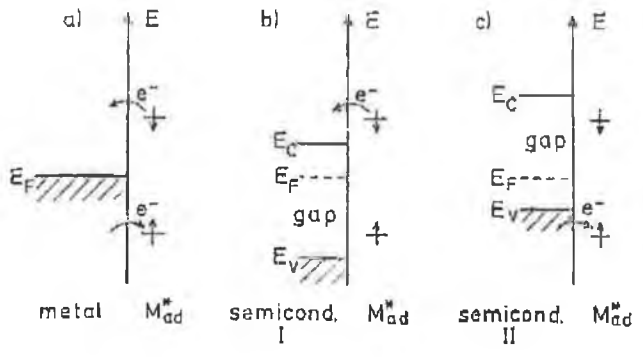

Figure 1.5.1 Typical situations for electron transfer between an electronically excited molecule and metal or semiconductor electrodes. Reproduced from Reference 117.

An explanation for the persistence of excited states near semiconductors, which does not traditionally occur near metals, is illustrated in Figure 1.3.1. Case (a) shows that an excited molecule near a metal electrode is efficiently quenched by mutual electron exchange. If the absorption spectrum of the electrode and excited molecule overlap, resonance energy transfer provides another quenching pathway. In sharp contrast, for an excited molecule near a semiconductor electrode, depending on the relative positions between the energy bands and the redox orbitals of the excited molecule, either electron injection into the conduction band, resulting in an observable anodic photocurrent (Figure 1.5.1(b)), or electron extraction from the valence band, resulting in a cathodic photocurrent will occur. This model suggests that excited states can exist for long periods of time near semiconductors, but not near metals. However, the investigations

presented in the following section show that excited states are observable near metals and in many cases are sufficiently long-lived to permit significant photoactivity.

Some of the first investigations of the observation of emission at metal surfaces were carried out by Drexhage,[118,119] who, using systems of long-chain fatty-acid molecules modified to contain a fluorescent dye moiety at the end of the chain, probed the effect of binding these fatty acid layers to a silver mirror, and increasing the distance between the emitter and the silver mirror, on the observed fluorescence. The results are presented in Figure 1.5.2 and show that the lifetime of the emission oscillates as a function of distance from the silver mirror. This is attributed to the reflection of part of the emitted light wave by the mirror, which results in constructive and destructive interference with the non-reflected part. Disagreement with the results occurs at very small distances, where energy transfer from the emitter to the mirror is thought to occur efficiently.[120]

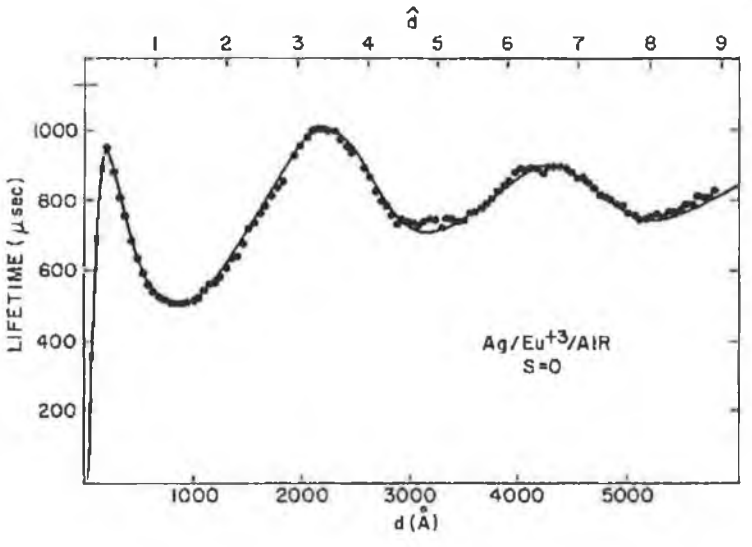

Figure 1.5.2 Lifetime versus distance for the Ag/Eu^{3+}/air system. Experimental data from Drexhage et al.[118,119] The solid curve represents the best fit of the oscillating dipole model to the experimental data. Reproduced from Reference 125.

Extensive experimental and theoretical investigations in this area have been carried out by Chance, Prock, Silbey and co-workers,[121,122,123,124] resulting in a comprehensive mathematical treatment describing the lifetime of an excited molecule near a metal mirror.[125] The authors applied the classical theory of an oscillating charge distribution near a dielectric interface to the problem of molecules fluorescing near a surface and investigated the role of resonant coupling between the emitter and surface plasmon modes of the metal surface. Their mathematical treatment supported Drexhage's theory of the metal surface acting as a mirror for the electric field of the emitter and showed that the large decrease in lifetime at small distance from the metal is due to nonradiative energy transfer from the excited state to the metal. The most important conclusion to be drawn from this work is that the distance of the emitter from the metal, in the case of a mirrored surface, is very important in controlling the lifetime of the emission.

The effect on the optical properties of emitting molecules near *rough, non-mirrored* surfaces has been examined by a small number of groups.[126,127,128] These investigations have focused on the *increase in quantum yield of emission* observed for Basic Fuschin (BF) and Rhodamine 6G (R6G) dye molecules adsorbed on silver island films on silica[127] and the distance dependence of the emission.[126] The observed enhancement in fluorescence (Figure 1.5.3) was found to depend on the quantum efficiency (QE) of the dye molecule, with molecules of low QE (BF) demonstrating an increase of a factor of 10 and molecules of high QE (R6G) showing a decrease in intensity due to enhanced nonradiative damping of molecules of high QE by the silver islands. The observed enhancement is attributed to interactions between the optical fields of the adsorbed molecules and electronic plasma resonances localised on the roughness features of the metal surfaces.[127] The observed strong distance dependence of the fluorescent enhancement of BF was explained by a competition between enhanced absorption/emission by local field amplification, which involves coupling of the dye molecule to the surface plasmon of the silver island films, and loss of excitation by radiationless energy transfer.[126]

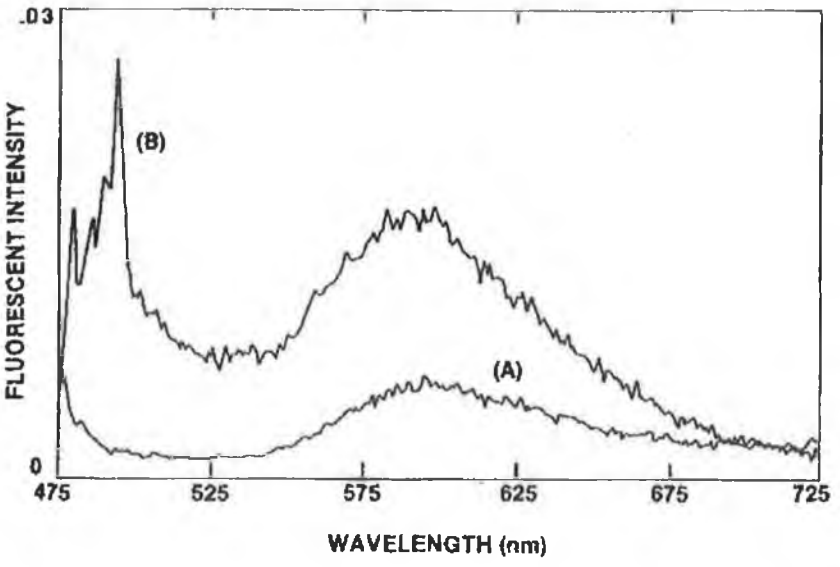

Figure 1.5.3 Fluorescence spectra of Basic Fuschin excited at 458 nm on (A) silica and (B) silver – island films on silica. Reproduced from Reference 126.

The observation of emission near metal surfaces via electrogenerated chemiluminescence (ECL) has been reported. A number of authors have observed ECL from layers of surfactant derivatives of ruthenium tris-bipyridine immobilised on gold and semiconductor electrodes.[129,130,131] In particular, Bard and Obeng[130] have observed efficient ECL for layers of $[Ru(bpy)_2(bpy')]^{2+}$, where bpy' is 4-methyl-(dodecyl-1-thiol)-2,2'-bipyridine, in the presence of $C_2O_4^{2-}$, on indium-doped tin oxide (ITO) and polycrystalline gold electrodes, although the emission intensity is decreased for the gold electrodes in comparison to the ITO. These experimental observations indicate that emission from molecules with relatively long lifetimes (≈ 1 μs) can compete effectively with quenching by the metal surface when the monolayer is under potential control. However, in general, no attempts were made to determine a critical distance for the observation of ECL of reasonable intensity.

Similarly, ECL has been observed from films of ruthenium polymers on both gold and platinum electrodes.[132,133,134,135,136] For example, Abruña and Bard have formed films of varying thickness (≈ 40 Å to ≈ 1 μm) of tris(4-vinyl-4'-methyl-2,2'-bipyridyl)ruthenium(II) by electroreduction onto a platinum flag electrode. They report on the observation of efficient ECL from these layers, irrespective of film thickness,

which contain, on average, 2×10^{-8} mol cm^{-2} of electroactive species, via an electron transfer reaction between electrogenerated +1 and +3 centres. A number of authors, utilising many types of ruthenium polymers, films of varying thickness and a range of different electrode types, from thin metal films on silica to polycrystalline metals, have reported similar results.[133,134,135,136] This reinforces the observation that emission from long-lived species can compete with quenching from the metal surface. Thick films may also benefit from the distance dependence effect described by Chance et al,[125] as many of the emitting Ru^{2+*} centres in the film would be located at a distance where energy transfer to the metal surface does not efficiently occur.

A number of reports have described the observation of emission from fluorescent organic dye monolayers on metallic electrodes.[137,138,139,140,141,142] Strategies for the preparation of such monolayers include modifying thiols to contain a fluorescent dye at the end of the thiol chain and forming a self-assembled monolayer,[137,138,139] or modifying the surface of an electrode firstly by attaching alkane or sulfur spacers and then attaching the dye to the end of the spacer molecules.[140,141,142] The use of a spacer molecule provides sufficient dielectric shielding to suppress electronic coupling between the dye excited state and the metal, and hence, allow for competitive emission.[139] These investigations have also shown that the observed emission displays a distance dependence and a strong potential dependence when the electrode is placed under potential control.[138,141,142] In the case of measurements carried out by Pope and Buttry,[138] the fluorescent probe displays a roughly linear dependence of the maximum emission wavelength and emission intensity on the applied potential. This has been attributed to a number of factors, including a potential dependence of the rate of quenching by the metal surface, influences of ion-pairing on the fluorescence intensity, potential dependent probe orientation, which can influence quenching behaviour of fluorophores near metal surfaces, as well as others not described in detail here.[138] However these experiments do not allow an unambiguous determination of the influence of each of these factors on fluorescence intensity.[138] Significantly, these authors have also concluded that a short fluorescence lifetime is necessary for the observation of efficient fluorescence, as emission is then competitive with the metal quenching processes.

In conclusion, the discussion presented above has highlighted that emission from fluorophores is observable under a number of conditions. The molecule must be

located at a sufficient distance from the metal to block quenching via energy transfer. The presence of a spacer molecule such as an alkyl thiol chain between the emitter and the electrode is advantageous in observing efficient emission, as the intervening alkyl chains provide sufficient dielectric shielding to cause weak electronic coupling between the metal and the fluorophore. This suppresses energy and electron transfer quenching from the metal surface. Fluorescence enhancement is possible at both mirror-like and atomically rough electrodes. Recent experiments have shown that under potential control, significant enhancement is possible, as the driving force for electron transfer quenching can be controlled by the potential applied to the electrode. Finally, the lifetime of the fluorescent probe has been demonstrated to play a critical role in the observation of emission at metal interfaces, with probes of extremely short (100 ps) and relatively long (1 μs) lifetime demonstrating the ability to compete with quenching by the metal surface via both energy and electron transfer.

1.6 The Effect of Laser Radiation on Unmodified Electrode Surfaces.

In proposing to utilise nanosecond laser pulses to electronically excite a monolayer of a redox active species immobilised on a metal electrode, an important control experiment is to consider the effect of the laser pulse on the underlying metal surface. The use of lasers in electrochemistry has been investigated by a small number of groups, with the research focusing mainly on electroanalytical applications, investigations of the electrical double layer and probing heterogeneous kinetics.

McCreery and co-workers have thoroughly evaluated the laser activation of glassy carbon,[143,144,145,146] highly ordered pyrolytic graphite (HOPG)[147,148] and platinum electrodes.[149,150] For example, they have utilised *in-situ* pulses of 10 ns, 1064 nm light of 20 – 70 MW cm^{-2} intensity from a Nd:YAG laser during cyclic and differential pulse voltammetry of redox probes such as potassium ferricyanide, ascorbic acid and dopamine. The results have shown that laser activation results in an increase in the heterogeneous electron transfer rate constant, k^o, for a solution phase redox probe, and is capable of removing passivating layers formed during potential cycling. Electrochemical and surface science (SEM, STM) investigations of these phenomena have shown that the laser activation is due to the temperature assisted desorption of passivating adsorbed material from the electrode surface, which then allows fast heterogeneous electron transfer to take place.

More recently, Watanabe and co-workers[151] have utilised high-intensity ($\approx$ 360 MW cm^{-2}) pulses of infrared laser light (1064 nm) to produce clean electrode surfaces for the electro-oxidation of ascorbic acid, by periodically ablating the top layer of a gold electrode surface during the potential sweep, known as *laser ablation voltammetry*. However, this method is extremely damaging to the electrode surface and therefore limits the lifetime of the electrode. Compton et al. have adapted this method to utilise lower-intensity 532 nm light during the potential sweep, which causes less damage to the electrode surface. Using this *laser activation voltammetry* technique,[152] they have obtained reproducible steady-state voltammograms at gold and platinum electrodes for a range of electroactive species. The authors propose that thermoelastic stresses are induced in the electrode by adsorption of laser energy, together with localised heating and solution convection currents, which in turn, maintain a diffusion layer at the

electrode surface and facilitate the observed steady mass-transport limited current. The steady-state response is described by a model for mass-transport of electroactive species to the electrode, based on a uniform Nernst diffusion layer thickness that is light intensity dependent. The model is of the form:

$$I_{LAV} = \frac{nAFD[X]_0}{\delta} \qquad (1.6.1)$$

where I_{LAV} is the mass-transport limited current, D is the diffusion coefficient of the species, X, of bulk concentration $[X]_0$, δ is the diffusion layer thickness and A, F and n have their usual significance. Values of δ, calculated assuming D has its bulk value, are seen to decrease as the laser intensity is increased, i.e., as the laser-induced thermal convection increases. The laser activation technique as described also allows electrochemistry to take place in passivating media, as the laser pulse periodically removes any material deposited on the electrode during electrochemical experiments,[153] and has allowed these authors to electrochemically analyse a wide range of species.[154,155,156]

Low energy laser pulses which cause only a slight transient increase of the electrode surface temperature were used by Barker and Cloke to study the electrical double layer on mercury electrodes.[157,158] In a preliminary investigation,[157] laser pulses of 694.3 nm wavelength and 20 ns duration from a Q-switched ruby laser, when applied to a flowing mercury pool electrode held at constant potential, resulted in a sharp change of potential, which decayed slowly to the baseline with a millisecond timescale. The decay has been attributed to the gradual return after the laser pulse of the interfacial temperature to its initial value, and the concomitant relaxation of the double layer structure. In a subsequent publication,[158] a 700 nm filtered light pulse of 200 μs duration from a 20 J domestic photographic flash unit was applied to a mercury electrode. The current decay resulting from the perturbation of the electrical double layer by the light pulse was monitored as a function of applied potential. The measurements show that there exists a potential of zero response (pzr), where no current decay is observed. This pzr is, for all electrolyte types and concentrations studied, approximately 100 to 150 mV negative of the potential of zero charge (pzc) of the electrode, as determined by conventional means. This displacement of the pzr is discussed by the authors on the assumption that water molecules, close to the pzc, are

oriented with the negative end of the water dipole pointing towards the electrode surface. A temperature increase lessens this preferred orientation and thus produces at potentials close to the pzc, an increase in the inner potential of the electrode with respect to the solution. The authors also point out that thermal diffusion potentials connected with transient temperature gradients in the solution and mercury phases may affect the observed current response, but their analysis of published Soret coefficients and thermodynamic temperature coefficients suggests that the effect would be similar to the influence of experimental error ($\pm$ 20 mV). However, the calculations are not described in the paper so no comment can be made as to their validity. Overall, they conclude that the pzc can be identified with the potential at which the influence of water dipole reorientation when the temperature is raised, is nullified by the effect of increasing diffuseness in the double layer structure. Further experiments show that for all electrolytes studied, at low potentials (< 0.8 V vs. SCE), the peak value of the current decay displays a linear dependence on applied potential. However, an explanation for this behaviour is not presented in the publication.

Benderskii et al[159] have used the temperature jump provided by pulses from a Rhodamine 6G dye laser (595 nm, 4 ns) to investigate the electrical double layer (EDL) at a mercury electrode. They have developed a system to measure the voltage response on electrode heating by the laser pulse, V_h. The dependence of this parameter on time, $V_h(t)$, and potential, $V_h(\varphi)$, where φ is the applied potential, have been determined. Using a thermodynamic analysis, they have shown that V_h can be related to the specific surface entropy, ΔS^σ, by the following equation:

$$\frac{V_h}{\Delta T} = -\left(\frac{\delta \Delta S^\sigma}{\delta q}\right)_T = \left(\frac{\delta \varphi_0}{\delta T}\right)_{q=0} + \int_0^q \frac{\delta}{\delta T}\left(\frac{1}{c}\right) dq \qquad (1.6.2)$$

where $(d\varphi_0/\delta T)_{q=0}$ is the inner potential drop at the potential of zero charge (pzc) and $(d(1/c)/\delta T)$ is the temperature coefficient of the double layer capacity. The potential φ^* (potential of zero response, pzr), where $V_h = 0$ is shown to correspond to the maximum of the entropy of EDL formation, ΔS^σ, which can be determined by numerical integration of the measured curves of $V_h(\varphi)$. They have shown that their analysis of plots of $V_h(\varphi)$ yields values of $(d(1/c)/\delta T)$ and $(d\varphi_0/\delta T)_{q=0}$ which agree well with previously published values. Also demonstrated is the fact that in solutions that do not

contain appreciable amounts of H_3O^+ and OH^- ions, thermodiffusion does not contribute to $V_h(\varphi)$ and φ^*. The large thermodiffusion potentials associated with H_3O^+ and OH^- ions is due to their anomalously high transport entropy and therefore high mobility in solution. With respect to the time dependence of V_h, they have observed that the relaxation time of V_h, τ, exhibits a maximum at the pzr. The existence of this large relaxation time near the pzr, as well as the coincidence of the pzr with the potential of maximum entropy of the EDL, suggest that at the pzr there is maximum disorder of the adsorbed water molecules and that the measured relaxation time refers to their reorientation time. This observation is consistent with conventional theory, which states that reorientation of solvent molecules causes redistribution of charge in the EDL. This process is so fast that the electrode potential variation following this redistribution is determined by the relaxation rate of the solvent dipoles. At the point where there is maximum disorder of the solvent dipoles, naturally, a higher relaxation time will be observed. This is consistent with the experimental response described here.

In a later paper,[160] the authors have used the same technique to determine the temperature coefficient of potential drop, $(d\varphi_0/\delta T)_{q,\mu}$ where μ is the chemical potential, and the excess entropy of EDL formation, ΔS^σ, at the boundary between mercury and aqueous solutions of NaF, KF, LiCl, KCl and CsCl. In dilute solutions, they have found that $(d\varphi_0/\delta T)_{q,\mu}$ and ΔS^σ are equal to the sum of two quantities corresponding to the compact and diffuse parts of the EDL. The first is determined by orientational polarisation of the aqueous monolayer in the inner EDL region and is independent of salt concentration. The second corresponds to the value calculated from Gouy-Chapman theory for the case where specific adsorption is absent. The measured EDL relaxation times do not depend on electrolyte concentration up to 14 M (for all the salts listed above), or the structure of the diffuse layer and are shown to be due to the reorientation of water dipoles.

Benderskii and co-workers have also investigated the laser activation of the rates of hydrogen evolution at nickel electrodes and anodic dissolution of a range of metal electrodes.[161,162,163,164] All the measurements have been made using 530 nm pulses from a 15 ns, 12.5 Hz neodymium laser. The authors have developed a model for the maximum temperature excursion caused by the laser pulse, T_m, (assuming negligible

penetration depth of the light, i.e., all the nonreflected radiation is instantaneously converted into heat at the electrode surface), and the decay of the temperature increase as a function of time, T(t):

$$\Delta T_m = \frac{2(1-R)q}{\sqrt{\pi\kappa cd} + \sqrt{\pi\kappa_{Soln} c_{Soln} d_{Soln}}} \sqrt{t_0} \qquad (1.6.3)$$

$$\Delta T(t) = \frac{1}{2} \Delta T_m \sqrt{\frac{t_o}{t}} \qquad (1.6.4)$$

where R is the reflection coefficient of the metal, q is the laser intensity, t_0 is the laser pulse length, κ, c and d and κ_{Soln}, c_{Soln}, and d_{soln} are the thermal conductivity, thermal capacity and density of gold and the aqueous electrolyte solution, respectively. The model assumes a gaussian spatial intensity distribution for the laser pulse and neglects the possibility of metal melting and evaporation. This model shows that the 10^7 to 10^8 W cm^{-2} laser pulse is sufficient to heat the electrode to a temperature of 10^3 K, which causes deformation waves with stresses exceeding the threshold of plasticity of the metal, but does not melt it. The observed electrochemical activation upon laser irradiation is attributed to these deformations and the enhancement of the rate of reactant transport from solution.

Jaworski and McCreery have studied laser-induced transient currents resulting from the application of 9 ns, 1064 nm laser pulses onto a glassy carbon electrode.[165] The transient current depends on both the potential applied to the electrode during the application of the laser pulses and the nature of the electrolyte solution. The transients were found to consist of three exponential decays. The two longest decays of ms timebase have been attributed to the restructuring of the double layer following the temperature perturbation of the surface by the laser pulse. However, the shortest decay (< 40 μs) is not well explained by the authors and is tentatively attributed to a thermal or even electronic effect. The charge under the transients, Q, has been determined and a potential of zero transient (pzr), where Q = 0, is observed. In common with Barker and Cloke, the pzr has been related to the potential of zero charge (pzc) of the electrode. The ability of this laser transient technique to probe double layer structure has been evaluated by determining the pzr for the electrode while varying the

electrolyte cation and anion. In analogous behaviour to the pzc, the pzr shifts in a positive direction with adsorption of cations on the electrode, with the strength of interaction decreasing in the order $H^+ > Li^+ > Na^+ > K^+ > Et_4N$. However, there is no such significant trend observed for the variation of the electrolye anion. The authors are unable to fully explain the observed dependence of the pzr on the nature of the electrolyte cation, but suggest that it is perhaps due to interaction of the cations with anionic groups on the surface of the electrode.

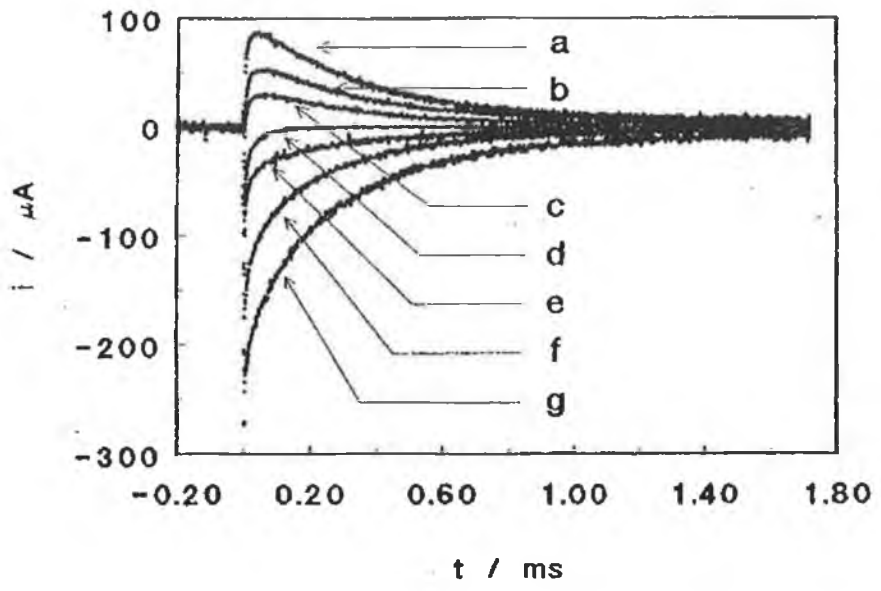

Figure 1.6.1 The effect of applied potential on the laser-induced current transients on a glassy carbon electrode in 0.1 M KCl at 10 MW cm^{-2} power density. The applied potential was: a, -0.2; b, -0.1; c, 0.0; d, 0.1; e, 0.2; f, 0.3; and g, 0.4 V. Reproduced from Reference 165.

Using the *laser ablation voltammetry* technique described earlier, the potential of zero charge of a molybdenum electrode has been determined by Hinoue et al.[166] Time-resolved voltammograms were obtained by holding the electrode at a constant potential and measuring the observed laser-induced current decay every 50 μs from the decay. By stepping the potential by 10 mV and repeating the measurement, an i – E curve for each delay time (from 50 to 1500 μs) is obtained. They have observed a potential of zero response at 0.54 V in this time-resolved voltammogram during laser ablation in phosphate buffer at pH 6.97. This potential corresponds with that at which a

differential capacitance component showed a minimum in a corresponding phase-selective ac-voltammogram of the molybdenum electrode free from ablation. This leads the authors to conclude that the potential of zero response in the time-resolved voltammogram corresponds to the potential of zero charge of the electrode. It is interesting to note that these authors do not see a small shift of the value of the pzc from that of the pzr, as has been demonstrated by previous authors. However, this could be due to the uncertainty of pzc values determined by traditional means and not due to an inaccuracy in this work.

In a recent contribution,[167] Compton and co-workers have described the analysis of laser induced *current* transients on a Au(111) single crystal electrode as a general method for the measurement of potentials of zero charge of solid electrodes. They have measured the current decays immediately following the application of a single pulse from a 10 ns, 532 nm Nd:YAG laser on the single crystal electrode in 0.01 M solutions of sulphuric and perchloric acid. Using the theory proposed by Benderskii,[164] they have calculated the temperature rise in the metal induced by the laser pulse to be 120 K. The current transients have been explained as due to the recovery of the double layer capacity after the sudden rise of temperature. It has been shown that there is a correlation between the sign of the current transient and the sign of the double layer charge and that the potential where no transient is observed is coincident with the potential of zero charge. Interestingly, although Benderskii's equations predict a rapid decay of the temperature increase, i.e., 10 μs after the pulse, the temperature is only 2 K above the equilibrium, the transients obtained from these experiments exhibit decay lifetimes of ms order. This has been shown to be due to the inherent time constant of the cell and indicates the limitation of the technique in studying the kinetics of the double layer relaxation processes if they are faster than the time constant of the cell.

Following on from this work, the same authors have investigated laser induced *potential* transients by following the evolution of the open circuit potential of Au(111)[168] and Pt(111)[169] single crystal electrodes during the relaxation of the temperature increase caused by a laser pulse. Adapting the theories presented by Benderskii to their own experiments,[159] they have been able to obtain a relative measurement of the entropy of formation of the double layer by integrating a plot of the slopes of the potential change vs. $1/\sqrt{t}$ as a function of the double layer charge. They have used these plots to correlate the electrode potential where the transient is zero with

the potential of maximum entropy of formation of the double layer. For the Au(111) electrode,[168] in both perchloric and sulphuric acid solutions, the potential of maximum entropy (pme) is located slightly negative to the pzc, which has been explained using conventional models of the double layer as due to a net negative contribution of the water-dipole moments to the electrode-solution drop. The authors have also noted that the results at low pH must be corrected for a thermodiffusion potential, due to the very high entropy of transport of H_3O^+ions.

These experimental methods have been used to probe the rate of hydrogen adsorption and potential of maximum entropy of a Pt(111) single crystal electrode in acidified potassium perchlorate or sulphate solutions.[169] At low pH, the potential transients in the hydrogen adsorption region (0 – 0.3 V vs. Pd/H_2) display a bipolar shape, which is explained by the influence of the rate of hydrogen adsorption on the temperature relaxation. Using an analysis developed from conventional adsorption isotherms, the rate constant for hydrogen adsorption has been estimated to be approximately 8×10^6 M^{-1} s^{-1}. Increasing the pH to reduce the rate of hydrogen adsorption effectively removes its contribution to the measured relaxation and has allowed the double-layer response to be decoupled from the hydrogen adsorption process. As before,[168] the potential of maximum entropy has been correlated with the potential of zero transient and has yielded a value of 0.42 V vs. Pd/H_2, in the double-layer region. This value compares favourably with some of the previously published values, notably those obtained by CO_2 charge displacement (0.34 V vs RHE), but does not agree with others, such as those obtained by immersion methods (0.84 V vs. RHE). This fact emphasises the difficulty in obtaining accurate estimates of the pzc of Pt electrodes, due to the presence of hydrogen and anion adsorption reactions.

In a variation on the laser temperature jump methods described previously, Feldberg and co-workers have reported on the development of the *indirect laser-induced temperature-jump method* (ILIT).[170,171] In the ILIT method, the (front) surface of a thin metal foil or film electrode is placed in contact with an electrolyte solution, while the other (back) surface contacts either air or some dielectric support. The laser pulse irradiates the *back-side* of the electrode. Some of the energy of the laser pulse is absorbed by the metal and is quickly (within ca. 10^{-12} s) degraded into heat, which diffuses across the electrode and induces a change in temperature at the front surface (i.e., the electrode-electrolyte interface). The interfacial temperature change perturbs

interfacial equilibria, thereby causing a redistribution of charge (ions, electrons, dipoles) and altering the open-circuit potential, which is the measured response. ILIT has several advantages over front illumination methods including the elimination of the possibility of any laser-induced photochemical processes in solution, elimination of the possibility of photoelectric emission of electrons into the solution and an interfacial temperature change which approximates a step function more closely than the corresponding change associated with direct irradiation of a thick electrode.

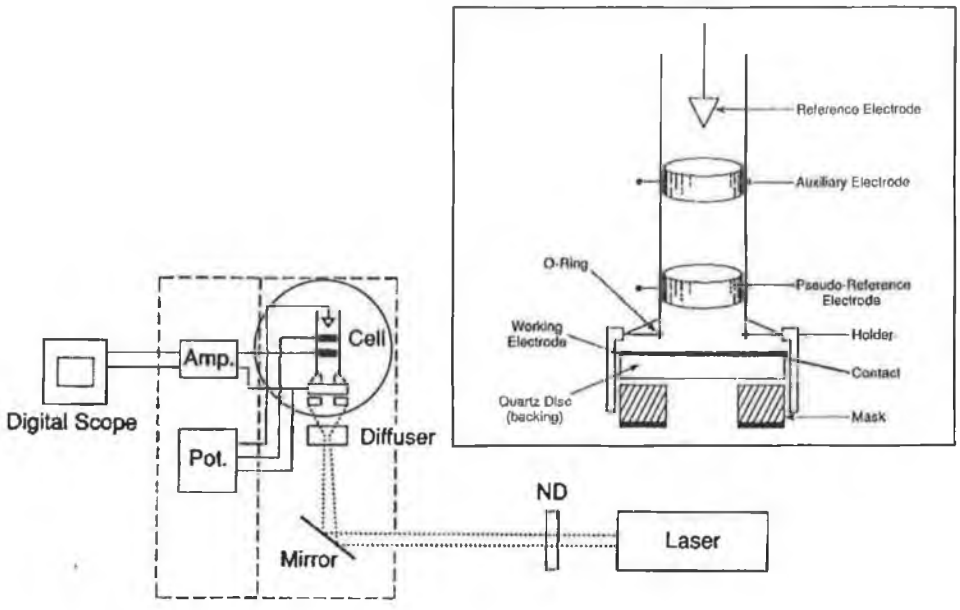

Figure 1.6.2 L.H.S. Block diagram of the ILIT apparatus: ND, neutral density filters; Amp., amplifier; Pot., potentiostat. The broken line indicates a Faraday cage. R.H.S. Diagram of the ILIT cell. Reproduced from Reference 171.

This method has been used by the authors to investigate a number of redox processes.[77,170,171,172,173] In one report, the heterogeneous rate constant of ferri/ferrocyanide has been determined using a flashlamp-pumped dye laser (width at half max 0.35 μm) and a 25 μm Pt-foil electrode.[170] The value obtained for k° is 1.64×10^{-2} cm s^{-1}, which is in good agreement with literature values. ILIT has also been used to provide evidence for the adsorption of ferri/ferrocyanide on gold.[171] The addition of ferricyanide to a 1 M KF solution was shown to effect a significant change in the response of the open-circuit potential to a rapid change in the interfacial temperature, effected by backside illumination of an electrode by 1064 nm light from a Nd:YAG Q-switched laser. The authors show that the ILIT method changes the interfacial

temperature fast enough (within a few nanoseconds), so that electron transfer does not have time to occur. This leads to the conclusion that the only explanation for the observed change the ILIT response is that the ferricyanide adsorbs onto the gold surface and effects a change in the structure, and therefore the thermal response, of the double layer. The method has also been utilised in the determination of rate constants that are too fast to be measured by conventional chronoamperometry at a macroelectrode (limited to rate constants $\leq 10^4$ s^{-1}), such as the kinetics of electron transfer through ferrocene-terminated alkanethiol monolayers on gold.[77,172] The surface pK_a of 11-mercaptoundecanoic acid monolayers on gold has also been evaluated by ILIT, with values of 5.7 $\pm$ 0.2 at 0.1 M ionic strength and 4.4 $\pm$ 0.2 at 1.0 M ionic strength being obtained.[173] The method is suitable for the measurement of the pK_a of a surface-attached acid, because the magnitude of the ILIT response is related to the potential gradient at the electrode/electrolyte interface, which is, in turn, related to the extent of ionisation of the acid. The relatively large variation in pK_a with ionic strength is explained by the fact that the interfacial potential at the monolayer surface becomes smaller as the ionic strength of the electrolyte solution increases. In other words, the Coulombic attraction between the hydrogen cations in the solution and the carboxylate anions on the monolayer surface is decreasing as a function of ionic strength, so that the carboxylic acid group becomes a stronger acid when the ionic strength of the electrolyte solution increases. The validity of this theory is enforced via reference to other work where this interfacial potential shift has been used to explain shifts in the pK_a's of acids adsorbed on charged interfaces such as micelles.[174]

The final effect of lasers on unmodified electrode surfaces to be discussed here, is the phenomenon of photoemission of electrons from the electrode into the electrolyte solution. In the experiments described in this section, the majority of authors have discounted the effect of photoelectron emission on the observed experimental response, by stating that the wavelength of light chosen is considerably longer than that needed to eject photoelectrons.[158,159,167] Using the Einstein photoelectric equation,[175] the threshold wavelength of electron emission, λ_{th}, is given by:

$$hc/\lambda_{th} = \phi \qquad (1.6.5)$$

where c is the speed of light in vacuum, h is Planck's constant and ϕ is the work function of the metal (typically 4 to 6 eV[176]). Using gold as an example, with a workfunction of 5.31 eV, the threshold wavelength for photoemission is 233 nm. Light of wavelength higher than this value does not have sufficient energy to eject photoelectrons from the surface. Similarly, for platinum, the threshold wavelength is 219 nm.

However, some controversy exists as to the similarity between the conditions for vacuum photoemission and the situation for an electrode in contact with a liquid electrolyte. Sass and Gerischer[177] have shown that the threshold energy for photoelectron emission can be varied by changing the voltage applied to the electrode. This behaviour is described by the following equation:

$$\Delta E_e = V_e^0 - \varepsilon_F + e\Delta V \qquad (1.6.6)$$

where ΔE_e is the threshold energy for photoemission, V_e^0 is the potential of the lowest free electron in the electrolyte, ε_F is the Fermi level and ΔV is the applied voltage. Therefore, the principle effect of the applied voltage ΔV is to vary the threshold height ΔE_e. As $\Delta E_e = hf_0$, where f_0 is the threshold frequency for photoelectron emission, Equation 1.6.6 may be rewritten as

$$hf_0 = V_e^0 - \varepsilon_F + e\Delta V \qquad (1.6.7)$$

Gurevich et al. have developed an expression which relates the observed photoemission current to the excess photon energy above the threshold energy hf_0:

$$j \propto \left(hf - hf_0\right)^{5/2} \qquad (1.6.8)$$

Inserting Equation 1.6.7 into Equation 1.6.8 yields an expression which predicts a linear relationship between $j^{0.4}$ and ΔV.

$$j^{0.4} \propto hf - V_e^0 + \varepsilon_F - e\Delta V \qquad (1.6.9)$$

Experimental observations have shown that there exists a potential where j = 0, $\Delta V_{j=0}$, where hf is equal to hf_0. Setting hf_0 = hf for j = 0 in equation 1.6.9 allows the energy dependence of the threshold potential to be determined:

$$e\Delta V_{j=0} = hf - V_e^0 + \varepsilon_F \qquad (1.6.10)$$

Using this equation and experimental plots of j vs. ΔV extrapolated to j = 0, the threshold value of hf for ΔV = 0 can be calculated and turns out to be 3.15 eV vs. NHE. Interestingly, this value is, contrary to the vacuum workfunction, independent of the nature of the metal.

While the overall indication of this work is that the threshold energy for photoelectron emission from a metal electrode into an electrolyte solution can be varied by changing the potential applied to the electrode, this result does not seriously complicate the experiments as carried out by Barker,[158] Benderskii[159,160] and Compton.[167,168,169] The reason for this is quite simple and is due to the fact, as pointed out by Sass and Gerischer,[177] that the observation of a substantial, measureable photocurrent, requires the presence of an electron scavenger such as H^+ or N_2O in the electrolyte solution. The scavenger has the added effect of preventing recapture of the emitted electron by the electrode, a phenomenon which substantially reduces the photocurrent observed in the experiment. Overall, it may be concluded from this short discussion, that while ejection of electrons is very likely to occur during the application of laser radiation of a suitable wavelength to an electrode surface in contact with an electrolyte, and the probability of this occurring is increased by holding the electrode at a high potential, significant photocurrents are unlikely to be observed unless a suitable scavenger is present in solution.

1.7 Conclusions

The discussion presented here has outlined the importance of understanding the nature of electron transfer, both in the ground and electronically excited state. Electron transfer has been shown to underpin a range of "real world" applications, including the development of artificial photosynthetic systems, molecular computing and electrochromic devices. Therefore, an understanding of the dynamics of electron transfer both to and from excited states would be advantageous in the development of high-performance, stable and commercially viable photonic molecular devices.

The Marcus theory of electron transfer, and its modified versions, have proved to be powerful models of the fundamentals of electron transfer. For both homogeneous and heterogeneous electron transfer, the theory has shown itself capable of predicting the effects of solvent, temperature and inter-reactant distance on the rate of electron transfer. For homogeneous electron transfer, the rate and probability of electron transfer depends mainly on the electronic nature of the two reactant species and the inter-reactant distance. Heterogeneous electron transfer allows the driving force, and therefore the rate of electron transfer, to be controlled externally by an applied potential. This type of electron transfer (between an electrode and a redox moiety) also depends on the density of acceptor states in the molecule, the distribution of occupied states in the electrode and the probability of electron tunnelling, which itself depends on the distance between the electrode and the redox moiety. Qualitative analysis predicts that heterogeneous electron transfer depends strongly on the type of electrode, the nature of the redox moiety and the inter-reactant distance (therefore the nature of the bridging ligand in an electrode-monolayer system). The theory also predicts that electron transfer is affected by the solvent used.

Successful strategies for probing the Marcus theory of heterogeneous electron transfer have focused mainly on the use of adsorbed monolayers on metallic electrodes because of the need to eliminate mass transfer limitations. In conjunction with computer modelling, electrochemical measurements carried out on monolayers of functionalised alkane-thiol or osmium and ruthenium polypyridyl complexes, have allowed the predictions of Marcus theory to be investigated. For example, many authors have observed that the heterogeneous electron transfer rate constant becomes independent of

the applied overpotential as the overpotential is increased to large values. Measurements on adsorbed monolayers have also allowed the effects of such factors as inter-reactant distance, temperature, solvent, electrode density of states and the nature of the ligand bridge on the electrochemical rate constant to be explored. Moreover, parameters such as λ, the reorganisation energy, $\Delta H^{\ddagger}$, the enthalpy of electron transfer, $\Delta G^{\neq}$, the free energy of electron transfer and β, the tunnelling constant have been directly determined experimentally.

Hetero- and homo-dimetallic species of metals such as osmium, ruthenium, rhodium, rhenium and iridium have been extensively used to explore the factors controlling homogeneous excited state electron transfer. This widespread use is due to their facile, reversible redox responses and the fact that the metal redox sites are held in a well-defined geometry to each other. The dimetallic species commonly undergo rapid intramolecular electron transfer by one of the metal sites, upon photoexcitation of the other. The resulting intervalence transfer (IT) bands in the near-infrared region of the spectrum can be analysed in terms of the molar absorptivity, the absorption maxium and the bandwidth at half-height. These parameters can, using Marcus theory, be used to calculate the electronic coupling factor and the free energy change for the electron transfer reaction. In this manner, the factors affecting electron transfer can be probed and the accuracy of Marcus theory in predicting the effect of these factors can be investigated. Interestingly, while trimetallic species have been used to develop photonic molecular devices, to date these species have not been used extensively to investigate electron transfer theories. Presented in Chapter 3 of this thesis are experiments combining adsorbed monolayers and trimetallic species, which allow the investigation of both heterogeneous and homogeneous Marcus electron transfer theory.

While ground state electron transfer is easily electrochemically investigated using adsorbed monolayers, and photoinduced excited state electron transfer may be probed by spectroscopic measurements on dimetallic species, few reports exist of the *direct* electrochemical measurement of electron transfer to and from electronically excited states, due to their transient nature and short lifetimes. The determination of excited state redox potentials has been traditionally estimated using the Rehm-Weller equation, or by an indirect measurement based on kinetic studies of quenching data for the redox species in question and a series of organic quencher molecules, as presented in Section 1.4. One of the objectives of the investigations reported here was to extend the *direct*

measurement of excited state redox potentials using the experimental procedure reported in Section 1.4 by Forster and Keyes.[65] In this approach, an immobilised monolayer is electronically excited by a nanosecond laser pulse, a high-speed cyclic voltammogram is recorded. If the monolayer species displays a relatively long emissive lifetime ($\approx$ 1 μs) and the kinetics of heterogeneous electron transfer occur on a shorter time-scale than the excited state lifetime, then it should be possible to observe the oxidation and reduction of the excited state.

When proposing to excite monolayers of a compound bound to a metal electrode with a laser, it is important to consider two factors; the likelihood of observing emission from the adsorbed compound and the effects of the laser on the underlying electrode surface. Although conventional theory states that electronically excited states near metals will be efficiently quenched by both energy and electron transfer from the metal to the emitter, the discussion presented in Section 1.5 has illustrated that excited states can exist for long periods near metal electrode surfaces. The observation of near-metal emission depends on the distance of the emitter from the surface, its excited state lifetime and in the case where the electrode is under potential control, the potential applied to the electrode. Consideration of the effect of the laser radiation on the underlying metal is important, because even if there is 100% creation of excited states in the monolayer by the laser pulse, a significant portion of the laser light may still penetrate to the electrode surface. The discussion presented in Section 1.6 has shown the effects of laser light on an electrode surface can vary considerably with the wavelength and mostly, the intensity of the light chosen. Laser treatment of electrodes has been shown to be a powerful tool for the investigation of heterogeneous electron transfer kinetics and the electrical double layer. In Chapter 4, the results of a series of experiments on the effect of laser pulses from a 10 Hz Nd:YAG laser at 355 nm on the surface of gold electrodes will be presented and these results will be discussed in terms of contemporary theory. Beyond issues of excited state electrochemistry, the importance of laser activation of electrodes extends to the use of laser pulses to provide clean, reproducible electrodes for analytical applications.

The experimental chapters of this thesis will make use of, and investigate the theories and experimental methods presented here. Chapter 2 details the synthesis and characterisation of the redox- active species utilised in these investigations. In Chapter 3, an experimental comparison of ground and excited state electron transfer using

adsorbed monolayers and a trimetallic species is presented. Chapter 4 presents the investigation of the effect of nanosecond laser pulses on unmodified electrode surfaces. Finally, Chapter 5 details the results of experiments which probe the suitability of a ruthenium complex, $[Ru(dpp)_2(Qbpy)](PF_6)_2$, where dpp is 4,7-diphenyl-1,10-phenanthroline and Qbpy is 2,2';4,4'';4',4''-quarterpyridyl, for use in the excited state electrochemistry experiment described above. These investigations have helped to bridge the gap between electrochemical and spectroscopic theory, and will assist in the development of devices based on photoinduced electron transfer.

REFERENCES

(1) Fox M. A.; Chanon, M. "Photoinduced Electron Transfer", Elsevier, Amsterdam, **1988**.

(2) Bard, A. J.; Abruña, H. D.; Chisdey, C. E. D.; Faulkner, L. R.; Feldberg, S. W.; Itaya, K.; Majda, M.; Melroy, O. S.; Murray, R. W.; Porter, M. D.; Soriaga, M. P.; White, H. S. *J. Phys. Chem.* **1993**, *97*, 7147.

(3) Ulman, A. "An Introduction to Ultra-thin Organic Films – From Langmuir Blodgett to Self-Assembly", Academic Press, San Diego, CA, 1991.

(4) Juris, A.; Balzani, V.; Barigelletti, F.; Campagna, S.; Belser, P.; von Zelewsky, A. *Coord. Chem. Rev.* **1988**, *84*, 85.

(5) Bruinink, J.; Kregting, C. G. A.; Ponjee, J. J. *J. Electrochem. Soc.* **1977**, *124*, 1854.

(6) Tsivgoulis, G. M.; Lehn, J. M. *Angew. Chem. Int. Ed.* **1995**, *34*, 1119.

(7) Mejiritski, A.; Polykarpov, A. Y.; Sarker, A. M.; Neckers, D. C. *Chem. Mat.* **1996**, *8*, 1360.

(8) Gregg, B. A. *Endeavour* **1997**, *21*, 52.

(9) Kim, Y.; Teshima, K.; Kobayashi, N. *Electrochimica Acta* **2000**, *45*, 1549.

(10) Demas, J. N.; DeGraff, B. A. *Coord. Chem. Rev.* **2001**, *211*, 317.

(11) Hopfield, J. J.; Onuchic, J. N.; Beratan, D. N. *Science* **1988**, *241*, 817.

(12) Hopfield, J. J.; Onuchic, J. N.; Beratan, D. N. *J. Phys. Chem.* **1989**, *93*, 6350.

(13) Barton, J. K. *Science* **1986**, *253*, 727.

(14) Homlin, R. E.; Stemp, E. D. A.; Barton, J. K. *J. Am. Chem. Soc.* **1996**, *118*, 5236.

(15) Homlin, R. E.; Stemp, E. D. A.; Barton, J. K. *Inorg. Chim. Acta* **2000**, *297*, 88.

(16) Hoffman, M. R.; Martin, S. T.; Choi, W.; Bahnemann, D. W. *Chem. Rev.* **1995**, *95*, 69.

(17) Pichat, P.; Fox, M. A. in "Photoinduced Electron Transfer – Vol.D", Eds. Fox, M. A.; Chanon, M., Elsevier, Amsterdam,**1988**, p. 241.

(18) Nazeeruddin, M. K.; Kay, A.; Rodicio, I.; Humphry-Baker, R.; Muller, E.; Liska, P.; Vlachopoulos, N.; Grätzel, M. *J. Am. Chem. Soc.* **1993**, *115*, 6382.

(19) O'Regan, B.; Grätzel, M. *Nature* **1991**, *353*, 737.

(20) Bard, A. J.; Fox, M. A. *Acc. Chem. Res.* **1995**, *28*, 141.

(21) Balzani, V.; Scandola, F. in "Comprehensive Supramolecular Chemistry", Vol.10, Eds. Atwood, J. L.; Davies, E. D. D.; MacNicol, D. D.; Vögtle, F., Pergamon, London, **1996**, p. 687.

(22) Forster, R. J.; Faulkner, L. R. *J. Am. Chem. Soc.*, **1994**, *116*, 5444.

(23) Balzani, V.; Juris, A.; Venturi, M.; Campagna, S.; Serroni, S. *Chem. Rev.*, **1996**, *96*, 759.

(24) Balzani, V. *Tetrahedron* **1992**, *48*, 10443.

(25) Meyer, T .J. *Acc. Chem. Res.* **1989**, *22*, 163.

(26) Tricot, Y. M.; Fendler, J. H. *J. Am. Chem. Soc.* **1984**, *106*, 7359.

(27) Wasielewski, M. R. *Chem. Rev.* **1992**, *92*, 435.

(28) Wilner, I.; Maidan, R.; Mandler, D.; Durr, H.; Dorr, G.; Zengerle, K. *J. Am. Chem. Soc.* **1987**, *109*, 6080.

(29) Gust, D.; Moore, T. A.; Liddell, P. A.; Nemeth, G. A.; Makings, L. R.; Moore, A. L.; Barrett, D.; Pessiki, P. J.; Benasson, R. V.; Rougee, M.; Chachaty, C.; De Schryver, F. C.; Van der Auweraer, M.; Holzwarth, A. R.; Connolly, J. S. *J. Am. Chem. Soc.* **1987**, *109*, 846.

(30) Rotzinger, F. P.; Munavalli, S.; Comte, P.; Hurst, J. K.; Grätzel, M.; Pern, F. J.; Frank, A. J. *J. Am. Chem. Soc.* **1987**, *109*, 6619.

(31) Hawecker, J.; Lehn, J. M.; Ziessel, R. *J. Am. Chem. Soc. Chem. Comm.* **1985**, 56.

(32) Molnar, S. M.; Nallas, G.; Bridgewater, J. S.; Brewer, K. J. *J. Am. Chem. Soc.* **1994**, *116*, 5206.

(33) Nallas, G. N. A.; Brewer, K. J. *Inorganica Chimica Acta* **1996**, *253*, 7.

(34) Marcus, R. A. *J. Chem. Phys.* **1956**, *24*, 966.

(35) Marcus, R. A. *Faraday. Discuss. Chem. Soc.* **1960**, *29*, 21.

(36) Marcus, R. A. *J. Chem. Phys.* **1957**, *26*, 867.

(37) Marcus, R. A. *J. Chem. Phys.* **1957**, *26*, 872.

(38) Marcus, R. A. *J. Chem. Phys.* **1965**, *43*, 679.

(39) Marcus, R. A. *Faraday Discuss. Chem. Soc.* **1982**, *74*, 7.

(40) Marcus, R. A. *Angew. Chem. Int. Ed. Eng.* **1993**, *32*, 1111.

(41) Hush, N. S. *Trans. Farad. Soc.* **1992**, *57*, 557.

(42) Bolton, J. R.; Archer, M. D. in "ET in Inorganic, Organic, and Biological Systems", Eds. Bolton, J. R.; Mataga, N.; McLendon, G., American Chemical Society, Washington D.C., **1999**.

(43) Bard, A. J.; Faulkner, L. R. "Electrochemical Methods: Fundamentals and Applications", 2nd Ed., Wiley, New York, **2001**.

(44) Atkins, P. W. "Physical Chemistry", Oxford University Press, Oxford, **1978**.

(45) Miller, J. R.; Calcaterra, L. T.; Closs, G. L. *J. Am. Chem. Soc.* **1984**, *106*, 3047.

(46) Gould, I. R.; Moser, J. E.; Ege, D.; Farid,S. *J. Am. Chem. Soc.* **1988**, *110*, 1991.

(47) Ohno, T.; Yoshimura, A.; Mataga, N. *J. Phys. Chem.* **1986**, *90*, 3295.

(48) Sinha, S.; De, R.; Ganguly, T. *J. Phys. Chem.* **1997**, *101*, 2852.

(49) Suppan, P. "Chemistry and Light", Royal Society of Chemistry, Cambridge, **1994**.

(50) Forster, R. J.; Keyes, T. E.; Vos, J. G. "Interfacial Supramolecular Assemblies: Electrochemical and Photophysical Properties", Wiley, New York, 2002.

(51) Richardson, D. E.; Taube, H. *J. Am. Chem. Soc.* **1983**, *105*, 40.

(52) Wasielewski, M. R. in "Photoinduced Electron Transfer", Eds. Fox, M. A.; Chanon, M., Elsevier, New York, **1988**.

(53) Forster, R. J.; Faulkner, L. R. *J. Am. Chem. Soc.* **1994**, *116*, 5453.

(54) De Cola, L.; Belser, P. *Coord. Chem. Rev.* **1998**, *177*, 301.

(55) Hush, N. S. *Coord. Chem. Rev.* **1985**, *64*, 135.

(56) Hush, N. S. *Electrochimica Acta* **1968**, *13*, 1005.

(57) Han, H.; Zimmt, M. B. *J. Am.Chem. Soc.* **1996**, *118*, 2299.

(58) Forster, R. J.; O'Kelly, J. P. *J. Phys. Chem.* **1996**, *100*, 3695.

(59) Miller, C. J. in "Physical Electrochemistry: Principles, Methods and Applications", Ed. Rubenstein, I., Marcel Dekker, New York, **1995**.

(60) Bagchi, B. *Ann. Rev. Phys. Chem.* **1989**, *40*, 115.

(61) Sutin, N. *Acc. Chem. Res.* **1982**, *15*, 275.

(62) Barr, S. W.; Guyer, K. L.; Li, T. T-T.; Liu, H. Y.; Weaver, M. J. *J. Electrochem. Soc.* **1984**, *131*, 1626.

(63) Weaver, M. J. *Chem. Rev.* **1992**, *92*, 463.

(64) Brunschwig, B. S.; Sutin, N. *Coord. Chem. Rev.* **1999**, *187*,233.

(65) Forster, R. J.; Keyes, T. E. *J. Phys. Chem. B.* **1998**, *102*, 10004.

(66) Finklea, O. H.; Hanshew, D. D. *J. Am. Chem. Soc.* **1992**, *114*, 3173.

(67) Schmickler, W. *J. Electroanal. Chem.* **1986**, *204*, 3143.

(68) Miller, R. J. D.; McLendon, G. L.; Nozik, A. J.; Schmickler, W.; Willig, F. "Surface Electron Transfer Processes", VCH, New York, **1995**.

(69) Chidsey, C. E. D., *Science* **1991**, *251*, 919.

(70) Weber, K., Creager, S. E., *Anal. Chem.* **1994**, *66*, 3164.

(71) Tender, L., Carter, M. T., Murray, R. W., *Anal. Chem.* **1994**, *66*, 3173.

(72) Sumner, J. J.; Creager, S. E.; *J. Am. Chem. Soc.* **2000**, *122*, 11914.

(73) Creager, S.; Yu, C. J.; Bamdad, C.; O'Connor, S.; MacLean, T.; Lam, E.; Chong, Y.; Olsen, G. T.; Luo, J.; Gozin, M.; Kayyem, J. F. *J. Am. Chem. Soc.* **1999**, *121*, 1059.

(74) Sikes, H. D.; Smalley, J. F.; Dudek, S. P.; Cook, A. R.; Newton, M. D.; Chidsey, C. E. D.; Feldberg, S. W. *Science*, **2001**, *291*, 1519.

(75) Finklea, H. O.; Liu, L.; Ravenscroft, M. S.; Punturi, S. *J. Phys. Chem.* **1996**, *100*, 188852.

(76) Weber, K.; Hockett, L.; Creager, S. E. *J. Phys. Chem. B* **1997**, *101*, 8286.

(77) Smalley, J. F.; Feldberg, S. W.; Chidsey, C. E. D.; Linford, R.; Newton, M. R.; Liu, Y-P. *J. Phys. Chem.* **1995**, *99*, 13141.

(78) Acevedo, D.; Abruña, H. *J. Phys. Chem.* **1991**, *95*, 9590.

(79) Forster, R. J.; Figgemeier, E.; Loughman, P.; Lees, A.; Hjelm, J.; Vos, J. G.; *Langmuir* **2000**, *16*, 7871.

(80) Forster, R. J.; Loughman, P.; Keyes, T. E.; *J. Am. Chem. Soc.* **2000**, *122*, 11948.

(81) Forster, R. J.; O'Kelly, J. P. *J. Electrochem. Soc.*, **2001**, *148*, E31.

(82) Forster, R. J.; Figgemeier, E.; Lees, A. C.; Hjelm, J.; J. Vos, J.G. *Langmuir*, **2000**, *16*, 7867.

(83) Forster, R.J. *Inorg. Chem.* **1996**, *35*, 3394.

(84) Walsh, D. A.; Keyes, T. E.; Hogan, C. F.; Forster, R. J. *J. Phys. Chem.* **2001**, *105*, 2792.

(85) Schanze, K. S.; Meyer, T. J. *Inorg. Chem.* **1985**, *24*, 2123.

(86) De Cola, L.; Belser, P. *Coord. Chem. Rev.* **1998**, *177*, 301.

(87) Ward, M. D. *Chem. Soc. Rev.* **1995**, *24*, 121.

(88) Sauvage, J-P.; Collin, J.-P.; Chambron, J-C.; Guillerez, S.; Coudret, C.; Balzani, V.; Barigelletti, F.; De Cola, L.; Flamigni, L. *Chem. Rev.* **1994**, *94*, 993.

(89) Schanze. K. S.; Neyhart, G. A.; Meyer, T. J. *J. Phys. Chem.* **1986**, *90*, 2182.

(90) Demadis, K. D.; Neyhart, G. A.; Kober, E. M.; White, P. S.; Meyer, T. J. *Inorg. Chem.* **1999**, *38*, 5948.

(91) Powers, M. J.; Meyer, T. J. *J. Am. Chem. Soc.* **1980**, *102*, 1289.

(92) Curtis, J. C.; Bernstein, J. S.; Meyer, T. J. *Inorg. Chem.* **1985**, *24*, 385.

(93) De Cola, L.; Balzani, V.; Barigelletti, F.; Flamigni, L.; Belser, P.; von Zelewsky, A.; Frank, M.; Vögtle, F. *Inorg. Chem.* **1993**, *32*, 5228.

(94) Barigelletti, F.; Flamigni, L.; Balzani, V.; Collin, J-P.; Sauvage, J-P.; Sour, A.; Constable, E. C.; Thompson, A. M. W. C. *J. Am. Chem. Soc.* **1994**, *116*, 7692.

(95) Balzani, V.; Barigelletti, F.; Belser, P.; Bernhard, S.; De Cola, L.; Flamigni, L. *J. Phys. Chem.* **1996**, *100*, 16786.

(96) Frank, M.; Nieger, M.; Vögtle, F.; Belser, P.; von Zelewsky, A.; De Cola, L.; Balzani, V.; Barigelletti, F.; Flamigni, L. *Inorg. Chim. Acta* **1996**, *242*, 281.

(97) Fagalde, F.; Katz, N. E. *Polyhedron*, **1995**, *14*, 1213.

(98) Arana, C. R.; Abruña, H. D. *Inorg. Chem.* **1993**, *32*, 194.

(99) Zahavy, E.; Fox, M. A. *Chem. Eur. J.* **1998**, *4*, 1647.

(100) Richter, M. M.; Brewer, K. J. *Inorg. Chem.* **1993**, *32*, 5762.

(101) Molnar, S. M.; Jensen, G. E.; Vogler, L. M.; Jones, S. W.; Laverman, L.; Bridgewater, J. S.; Richter, M. M.; Brewer, K. J. *J. Photochem. Photobiol. A: Chem.* **1994**, *80*, 315.

(102) Nallas, G. N. A.; Jones, S. W.; Brewer, K. J. *Inorg. Chem.* **1996**, *35*, 6974.

(103) Brauns, E.; Jones, S. W.; Clark, J. A.; Molnar, S. M.; Kawanishi, Y.; Brewer, K. J. *Inorg. Chem.* **1997**, *36*, 2861.

(104) Forster, R. J.; Keyes, T. E. *J. Phys. Chem.* **2001**, *105*, 8829.

(105) Rehm, D.; Weller, A. *Isr. J. Chem.* **1970**, *8*, 259.

(106) Vlcek, A. A.; Dodsworth, E. S.; Pietro, W. J.; Lever, A. B. P. *Inorg. Chem.* **1995**, *34*, 1906.

(107) Bock, C. R.; Connor, J. A.; Gutierrez, A. R.; Meyer, T. J.; Whitten, D. G.; Sullivan, B. P.; Nagle, J. K. *J. Am. Chem. Soc.* **1979**, *101*, 4815.

(108) Ballardini, R.; Varani, G.; Indelli, M. T.; Scandola, F.; Balzani, V. *J. Am. Chem. Soc.* **1978**, *100*, 7219.

(109) Paw, W.; Cummings, S. D.; Mansour, M. A.; Connick, W. B.; Geiger, D. K.; Eisenberg, R. *Coord. Chem. Rev.* **1998**, *171*, 125.

(110) Wing-Wah Yam, V.; Lai, T-F.; Che, C-M. *J. Chem. Soc. Dalton Trans.* **1990**, *12*, 3747.

(111) Furue, M.; Maruyama, K.; Oguni, T.; Naiki, M.; Kamachi, M. *Inorg. Chem.* **1992**, *31*, 3792.

(112) Jones, W. E., Fox, M. A., *J. Phys. Chem.* **1994**, *98*, 5095.

(113) Wayner, D. D. D.; McPhee, D. L.; Griller, D. *J. Am. Chem. Soc.* **1988**, *110*, 132.

(114) Nagoaka, T.; Griller, D.; Wayner, D. D. M. *J. Phys. Chem.* **1991**, *95*, 6264.

(115) Kalayasundaram, K. in "Photochemistry in Organized and Constrained Media", Eds. Ramamurthy, V., VCH Publishers, New York, **1991**.

(116) Bierig, K.; Morgan, R. J.; Tysoe, S.; Gafney, H. D.; Strekas, T.; Baker, A. D. *Inorg. Chem.* **1991**, *30*, 4898.

(117) Gerischer, H., *J. Electrochem. Soc.* **1978**, *125*, 218C.

(118) Drexhage, K. H. *Sci. Amer.* **1970**, *222*, 108.

(119) Drexhage, K. H. *J. Lumin.* **1970**, *1 – 2*, 693.

(120) Kuhn, H. *J. Chem. Phys.* **1970**, *53*, 101.

(121) Chance, R. R.; Prock, A.; Silbey, R. *J. Chem. Phys.* **1974**, *60*, 2184.

(122) Chance, R. R.; Prock, A.; Silbey, R. *J. Chem. Phys.* **1974**, *60*, 2744

(123) Chance, R. R.; Prock, A.; Silbey, R. *J. Chem. Phys.* **1975**, *62*, 771.

(124) Chance, R. R.; Miller, A. H.; Prock, A.; Silbey, R. *J. Chem. Phys.* **1975**, *63*, 1589.

(125) Chance, R. R.; Prock, A.; Silbey, R. in "Advances in Chemical Physics", Eds. Prigogine, I.; Rice, S. R., Wiley, New York, **1978**.

(126) Wokaun, A.; Lutz, H. P.; Wild, U. P.; Ernst, R. R. *J. Chem. Phys.* **1983**, *79*, 509.

(127) Weitz, D. A.; Garoff, S.; Gersten, J. I.; Nitzan, A. *J. Chem. Phys.* **1983**, *78*, 5234.

(128) Gersten, J.; Nitzan, A. *J. Chem. Phys.* **1981**, *75*, 1139.

(129) Zhang, X.; Bard, A. J. *J. Phys. Chem.* **1988**, *92*, 5566.

(130) Obeng, Y. S.; Bard, A. J. *Langmuir* **1991**, *7*, 195.

(131) Sato, Y.; Uosaki, K. *J. Electroanal. Chem.* **1995**, *384*, 57.

(132) Abruña, H. D.; Bard, A. J. *J. Am. Chem. Soc.* **1982**, *104*, 2641.

(133) Maness, K. M.; Terrill, R. H.; Meyer, T. J.; Murray, R. W.; Wightman, R. M. *J. Am. Chem. Soc.* **1996**, *118*, 10609.

(134) Westmoreland, T. D.; Calvert, J. M.; Murray, R. W.; Meyer, T. J. *J. Chem. Soc. Chem. Comm.* **1983**, 65.

(135) Xu, X. H.; Bard, A. J. *J. Am. Chem. Soc.* **1995**, *117*, 2627.

(136) Hamaguchi, M.; Nambu, H.; Ohsawa, T.; Yoshino, K. *J. Appl. Phys.* **1997**, *36*, 679.

(137) Chen, S. H.; Frank, C. W. *Langmuir* **1991**, 7, 1719.

(138) Pope, J. M.; Buttry, D. A. *J. Electroanal. Chem.* **2001**, *498*, 75.

(139) Fox, M. A.; Li, W.; Wooten, M.; McKerrow, A.; Whitesell, J. K. *Thin Solid Films* **1998**, *329*, 477.

(140) Naujok, R. R.; Duevel, R. V.; Corn, R. M. *Langmuir* **1993**, *9*, 1771.

(141) Li, L.; Ruzgas, T.; Gaigalas, A. K. *Langmuir* **1999**, *15*, 6358.

(142) Li, L.; Meuse, C.; Silin, V.; Gaigalas, A. K. *Langmuir* **2000**, *16*, 4672.

(143) Hershenhart, E.; McCreery, R. L.; Knight, R. D. *Anal. Chem.* **1984**, *56*, 2256.

(144) Rice, R. J.; Pontikos, N. M.; McCreery, R. L. *J. Am. Chem. Soc.* **1990**, *112*, 4617.

(145) Rice, R. J.; McCreery, R. L. *J. Electroanal. Chem.* **1991**, *310*, 127.

(146) Jaworski, R. K.; McCreery, R. L. *J. Electroanal. Chem.* **1994**, *369*, 175.

(147) Rice, R. J.; McCreery, R. L. *Anal. Chem.* **1989**, *61*, 1637.

(148) Bowling, R. J.; Packard, R. T.; McCreery, R. L. *J. Am. Chem. Soc.* **1989**, *111*, 1217.

(149) Poon, M.; McCreery, R. L. *Anal. Chem.* **1987**, *59*, 1615.

(150) Huang, W.; McCreery, R. L. *J. Electroanal. Chem.* **1992**, *326*, 1.

(151) Hinoue, T.; Kuwamoto, N.; Watanabe, I. *J. Electroanal. Chem.* **1999**, *466*, 31.

(152) Akkermans, R. P.; Suárez, M. F.; Roberts, S. L.; Fulian, Q.; Compton, R. G. *Electroanalysis* **1999**, *11*, 1192.

(153) Fulian, Q.; Compton, R. G. *Anal. Chem.* **2000**, *72*, 1830.

(154) Akkermans, R. P.; Wu, M.; Bain, C. D.; Fidel-Suárez, M.; Compton, R. G. *Electroanalysis*, **1998**, *10*, 613.

(155) Fulian, Q.; Compton, R. G.; Marken, F.; Wilkins, S. J.; Goeting, C. H.; Foord, J. S. *Anal. Chem.* **2000**, *72*, 2362.

(156) Fulian, Q.; Compton, R. G. *Analyst* **2000**,*125*, 531.

(157) Barker, G. C.; Cloke, G.; Bottura, G. *J. Electroanal. Chem.* **1973**, *45*, 21.

(158) Barker,G. C.; Cloke, G. *J. Electroanal. Chem.* **1974**, *52*, 468.

(159) Benderskii, V. A.; Velichko, G. I. *J. Electroanal. Chem.* **1982**, *140*, 1.

(160) Benderskii, V. A.; Velichko, G. I.; Kreitus, I. *J. Electroanal. Chem.* **1984**, *181*, 1.

(161) Efimov, I. O.; Krivenko, A. G.; Benderskii, V. A. *Sov. Electrochem.* **1989**, *24*, 1092.

(162) Efimov, I. O.; Krivenko, A. G.; Benderskii, V. A. *Sov. Electrochem.* **1991**, *27*, 401.

(163) Efimov, I. O.; Krivenko, A. G.; Benderskii, V. A. *Sov. Electrochem.* **1989**, *24*, 1097.

(164) Benderskii, V. A.; Efimov, I. O.; Krivenko, A. G. *J. Electroanal. Chem.* **1991**, *315*, 29.

(165) Jaworski, R. K.; McCreery, R. L. *J. Electrochem. Soc.* **1993**, *140*, 1360.

(166) Nakamura, K; Ohno, M.; Umemoto, K.; Hinoue, T. *Chem. Letts.* **2000**, 1050.

(167) Climent, V.; Coles, B. A.; Compton, R. G. *J. Phys. Chem. B* **2001**, *105*, 10669.

(168) Climent, V.; Coles, B. A.; Compton, R. G. *J. Phys. Chem. B* **2002**, *106*, 5258.

(169) Climent, V.; Coles, B. A.; Compton, R. G. *J. Phys. Chem. B* **2002**, *106*, 5988.

(170) Smalley, J. F.; Krishnan, C. V.; Goldman, M.; Feldberg, S. W.; Ruzic, I. *J. Electroanal. Chem.* **1988**, *248*, 255.

(171) Smalley, J. F.; Geng, L.; Feldberg, S. W.; Rogers, L. C; Leddy, J. *J. Electroanal. Chem.* **1993**, *356*, 181.

(172) Sachs, S. B.; Dudek, S. P.; Hsung, R. P.; Sita, L. R.; Smalley, J. F.; Newton, M. D.; Feldberg, S. W.; Chidsey, C. E. D. *J. Am. Chem. Soc.* **1997**, *119*, 10563.

(173) Smalley, J. F.; Chalfant, K.; Feldberg, S. W.; Nahir, T. M.; Bowden, E. F. *J. Phys. Chem. B* **1999**, *103*, 1676.

(174) Creager, S. E.; Clarke, J. *Langmuir* **1994**, *10*, 3675.

(175) Jones, E. R.; Childers, R. L. "Contemporary College Physics", 2nd Ed., Addison-Wesley, Reading, Massachusetts, 1993.

(176) Haas, G. in "American Institute of Physics Handbook", 3rd Ed., Ed. Gray, D. E., McGraw Hill, New York, 1972.

(177) Sass, J. K.; Gerischer, H. in "Photoemission and the Electronic Properties of Surfaces", Eds. Feuerbacher, B.; Fitton, B.; Willis, R. F., Wiley and Sons, Chichester, 1978.

Chapter 2

Synthesis and Characterisation of Osmium and Ruthenium Polypyridyl Complexes

"Insanity: doing the same thing over and over again and expecting different results"

Albert Einstein

2.1 Introduction

In the development of devices based on photoinduced electron transfer, much use has been made of osmium and ruthenium polypyridyl complexes.[1,2,3] Moreover, as they exhibit close to ideal reversible electrochemical properties, they may be used as models to probe electron transfer within ground and electronically excited states.

Osmium and Ruthenium polypyridyl complexes with surface-active ligands make attractive model compounds with which to investigate electron transfer. These materials allow the formation of highly ordered monolayer and multilayer assemblies on microelectrodes, which assemble rapidly from solution. The films formed are highly stable due to their low rate of desorption and photochemical stability. By careful choice of the type of surface-active bridging ligand, the electron transfer distance and tunnelling medium may be controlled and systematically varied. The complexes also exhibit inherent electrochemical reversibility. Therefore, although many authors have focused on the use of ferrocene alkanethiols to investigate heterogeneous electron transfer,[4,5,6,7] the advantages detailed above have resulted in their use by a small number of research groups for the study of heterogeneous electron transfer between an electrode surface and an intimately bound electro-active layer.[8,9,10,11,12]

Ligand bridged homo- and hetero - metallic dimers of osmium and ruthenium have been widely used for the study of photoinduced electron transfer between molecular excited states localised within the complexes.[13,14,15,16,21] These systems are useful because the metal sites are held in a well –defined geometry relative to each other and electron transfer between sites is a reversible process. Transient emission measurements can be made on these systems to estimate the rate of intramolecular electron transfer quenching of excited states within the complex, which are created by the absorption of a photon. Varying the length or type of bridging ligand joining the metal sites in the complex allows the strength of electronic coupling, and therefore the likelihood of electron transfer, within the complex to be controlled. Trimetallic species of osmium and ruthenium have been synthesised and utilised in photonic molecular devices,[17,18,19,20] but to date, no reports have focused in detail on the investigation of photoinduced electron transfer within localised metal sites in trimetallic compounds.

Trimetallic compounds exhibit the same well-defined electrochemical and spectroscopic responses as dimetallic complexes and therefore make equally attractive systems for the investigation of intramolecular photoinduced electron transfer quenching.

Within this chapter is a description of the synthesis and characterisation of osmium and ruthenium polypyridyl complexes, which in later chapters will be utilised to investigate photoinduced electron transfer within a trimetallic species and both ground and excited state electron transfer in a monolayer immobilised on a metal electrode.

Scheme 1 Schematic representation of the osmium compounds where bpy is 2,2'-dipyridyl and bpe is *trans*-1,2-bis-(4-pyridyl)ethylene.

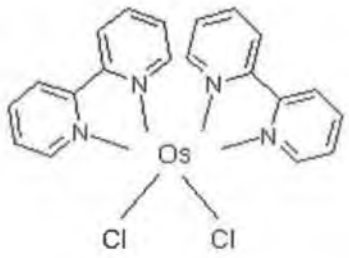

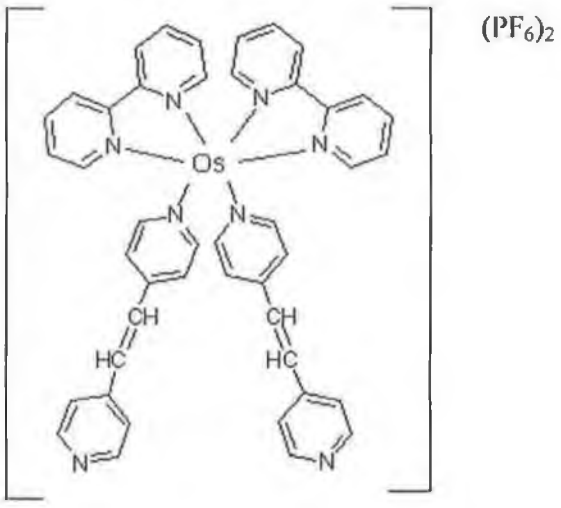

$[Os(bpy)_2Cl_2]$ **$[Os(bpy)_2(bpe)_2](PF_6)_2$**

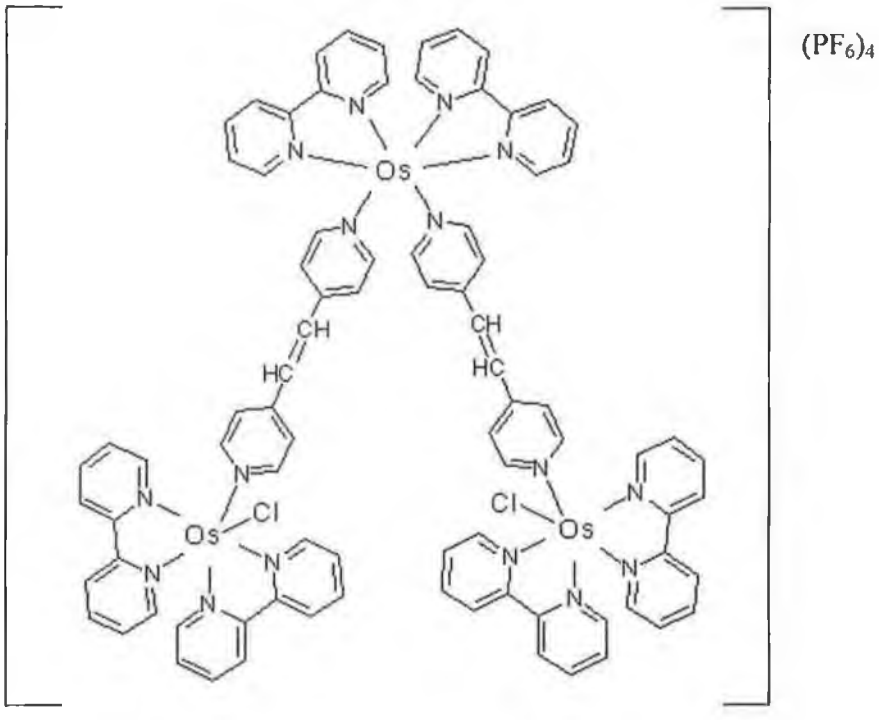

$\{[Os(bpy)_2(bpe)_2][Os(bpy)_2Cl]_2\}(PF_6)_4$

Scheme 2. Schematic representation of the ruthenium compounds where dpp is 4,7-diphenyl-1,10-phenanthroline and Qbpy is 2,2';4,4'';4',4''-Quarterpyridyl.

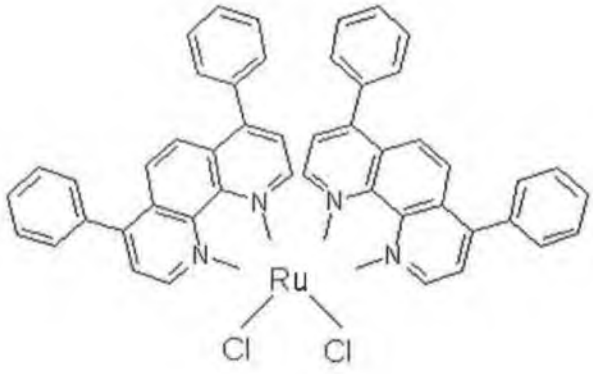

$[Ru(dpp)_2Cl_2]$

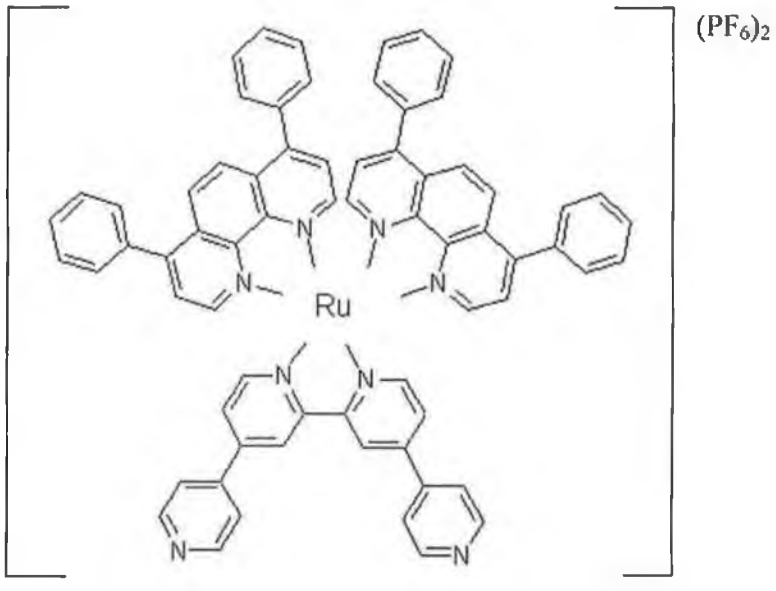

$[Ru(dpp)_2Qbpy](PF_6)_2$

2.2 Apparatus and Materials

High performance liquid chromatography was carried out using a Varian Prostar Model 230 HPLC pump equipped with a 20 μl injection loop. The column stationary phase was a partisil P10 SCX 3092 radical PAK cation exchange cartridge. A Varian Prostar photodiode array detector, used at a detection wavelength of 280 nm and interfaced with a Dell personal computer with Varian Star Hichrom Cation Exchange software, Version 5.3, was used for peak detection and readout. The mobile phase consisted of 80:20 (v/v) acetonitrile:water and 0.08 M $LiClO_4$ employed as an ion-pairing agent. A flow rate of 1.8 ml min^{-1} was utilised.

Proton magnetic resonance spectra were carried out using a Bruker 400 NMR spectrometer. Measurements were carried out in deuterated dimethylsulfoxide (d_6-DMSO) or deuterated chloroform (d_3-chloroform).

Analysis for total carbon, hydrogen and nitrogen content was carried out at the Microanalytical Laboratory, Chemical Services Unit, University College Dublin, Belfield, Dublin 4.

Ultraviolet-visible spectra were recorded using a Shimadzu UV-3100 diode array spectrometer. Room temperature emission spectra were recorded using a Perkin Elmer LS50 B luminescence spectrometer, equipped with a red sensitive Hamamatsu R928 detector. Samples were prepared at concentrations of 10^{-5} to 10^{-6} M in spectroscopic grade butyronitrile or acetonitrile. For room temperature measurements, 1 cm quartz cells were used. The excitation and emission slits were 2 nm for all experiments.

Cyclic voltammetry was performed using a CH Instruments Model 660A Electrochemical Workstation and a conventional three-electrode cell. All solutions were deoxygenated thoroughly using argon, and a blanket of argon was maintained over the solution during all experiments. Potentials are quoted with respect to a CH Instruments Ag/Ag^+ organic reference electrode filled with anhydrous acetonitrile/0.1M TBAP/10 mM $AgNO_3$. The potential of the ferrocene/ferrocenium couple obtained using this reference electrode was 0.0725 V. All experiments were performed at room temperature (22±3 °C).

2.3 Synthesis of Osmium Complexes

$[Os(bpy)_2Cl_2]$ was kindly provided by Dominic O'Hanlon of Dublin City University and was used following confirmation of purity by cation – exchange HPLC and ^1H – NMR.

$[Os(bpy)_2(bpe)_2](PF_6)_2$ was provided by Dominic O' Hanlon of Dublin City University. The synthesis was carried out as follows:

$$Os(bpy)_2Cl_2 + 2\ bpe \xrightarrow{MeOH,H_2O,\Delta} [Os(bpy)_2(bpe)_2](PF_6)_2$$

172 mg (0.3 mmol) of $Os(bpy)_2Cl_2$ was placed in 40 cm^3 of methanol and refluxed for 10 minutes to ensure complete dissolution. A solution of 110 mg (0.6 mmol) of *trans*–1,2-bis-(4-pyridyl)ethylene dissolved in 10 cm^3 of methanol was added, together with 40 cm^3 of water and the solution was refluxed for 15 hr. The progress of the reaction was monitored using HPLC and cyclic voltammetry. After the reaction was complete, the volume was reduced to 5 cm^3 by rotary evaporation. Ammonium hexafluorophosphate (95+%, Aldrich) was then added, and the dark green-black product was collected by filtration and washed with diethylether. The product was recrystallised from aqueous methanol to give dark green-black crystals. Elemental analysis: Calculated for $C_{44}H_{36}N_8OsP_2F_{12}$, C:45.67%, H:3.11%, N:9.68%. Found C:45.43%, H:3.20%, N:9.62%.

$\{[Os(bpy)_2(bpe)_2][Os(bpy)_2Cl]_2\}(PF_6)_4$

$$[Os(bpy)_2(bpe)_2](PF_6)_2 + 2\ Os(bpy)_2Cl_2 \xrightarrow{EtOH,\ \Delta} \{[Os(bpy)_2(bpe)_2][Os(bpy)_2Cl]_2\}(PF_6)_4$$

$[Os(bpy)_2(bpe)_2](PF_6)_2$ (100 mg, 0.0865 mmol) was dissolved in 20 cm^3 ethanol and refluxed for 10 minutes to ensure complete dissolution. A solution of $[Os(bpy)_2Cl_2]$ (99.2 mg, 0.173 mmol) dissolved in 10 cm^3 of ethanol was added and the mixture was refluxed for 72 hours. The solvent was removed to a volume of 10 cm^3, and was added drop wise with constant stirring to a solution of concentrated aqueous NH_4PF_6. The

resulting black solid was collected by filtration and recrystallised from acetone/water (2/1 v/v) by slow evaporation to give black crystals. Elemental analysis (Calculated: For $Os_3C_{84}H_{68}N_{16}P_4F_{24}Cl_2$; C, 39.99%; H, 2.72%; N, 8.88%. Found: C, 38.16%; H, 2.28%; N, 8.20%).

2.4 Characterisation of Osmium Complexes

2.4.1 High-performance liquid chromatography

Figure 2.1 illustrates the chromatogram obtained for $[Os(bpy)_2Cl_2]$ and shows a single peak with a retention time of 1.51 min and a peak area of 100%, consistent with the compound being uncharged. The chromatogram of $[Os(bpy)_2(bpe)_2](PF_6)_2$ detailed in Figure 2.2 shows one significant peak of 98.7% area at 4.78 mins, consistent with the compound having a charge of +2 and therefore being more strongly retained on the column than the uncharged $[Os(bpy)_2Cl_2]$ complex. The Varian Star software used to analyse this data allows the chromatogram to be displayed as a "purity parameter" versus time. By monitoring the full UV-VIS spectrum of every point on the chromatogram, this "purity parameter" plot determines if a single peak consists of two separate compounds which elute at the same time. For both compounds analysed, the single peaks detected proved to consist of a single species.

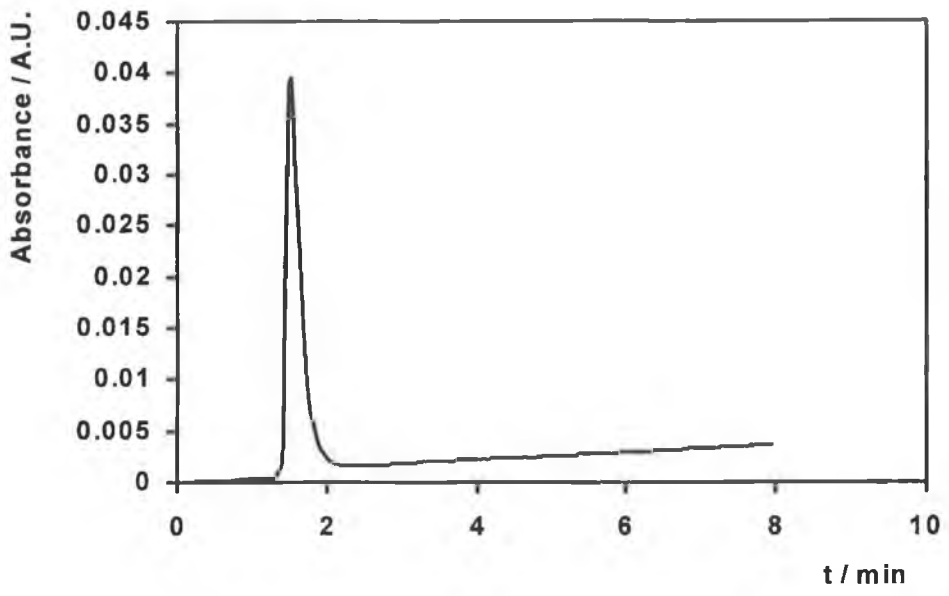

Figure 2.1 Chromatogram of $[Os(bpy)_2Cl_2]$ obtained using cation-exchange HPLC at a flow rate of 1.8 ml min^{-1}. The mobile phase was 80:20 (v/v) ACN/H_2O, 0.08 M $LiClO_4$

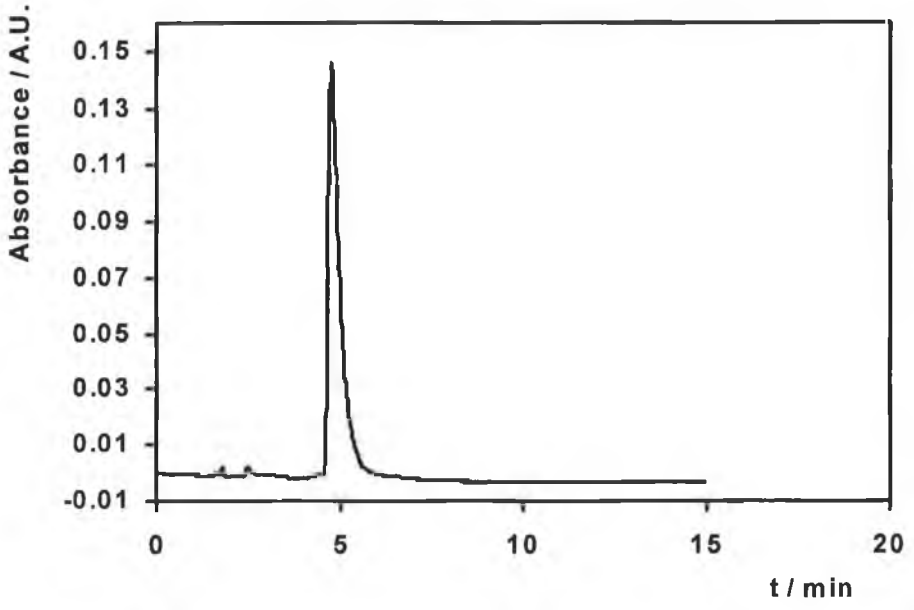

Figure 2.2 Chromatogram of $[Os(bpy)_2(bpe)_2](PF_6)_2$ obtained using cation-exchange HPLC at a flow rate of 1.8 ml min^{-1}. The mobile phase was 80:20 (v/v) ACN/H_2O, 0.08 M $LiClO_4$.

2.4.2 ^{1}H – NMR

An important feature of low-spin d_6 systems is that the complexes are diamagnetic and sharp NMR spectra can be obtained. Proton magnetic resonance spectra for the trimer, $\{[Os(bpy)_2(bpe)_2][Os(bpy)_2Cl]_2\}(PF_6)_4$ and the two parent monomers, $Os(bpy)_2Cl_2$ and $[Os(bpy)_2(bpe)_2](PF_6)_2$ are presented in Figures 2.3 to 2.5. Scheme 3 illustrates the hydrogen numbering which is referred to in the text.

The bands for the monomers were assigned by obtaining Aromatic COSY proton coupling spectra for the compounds and are as follows:

$[Os(bpy)_2Cl_2]$ ^{1}H-NMR δ (d_6-DMSO): 6.75 ppm (2H, t, H5), 7.25 ppm (2H, t, H4), 7.30 ppm(2H, d, H6'), 7.50 ppm (2H, t, H5'), 7.60 ppm (2H, t, H4'), 8.30 ppm (2H, d, H3), 8.50 ppm (2H, d, H3'), 9.70 ppm (2H, d, H6).

$[Os(bpy)_2(bpe)_2](PF_6)_2$ ^{1}H-NMR δ (d_6-DMSO): 7.39 ppm (1H, t, H_D), 7.50 ppm (3H, 2 x d, $H_{D'}$ (1H), H_4 (2H)), 7.55 ppm (2H, d, H_2), 7.82 ppm (3H, q, H_B, H_C, $H_{C'}$), 7.98 ppm (1H, t, $H_{B'}$), 8.35 ppm (2H, d, H_3), 8.60 ppm (2H, t, H_1), 8.65 ppm (1H,d, $H_{A'}$), 8.90 ppm (1H, d, H_A). Peaks for vinylic hydrogens are expected in the region of 2 to 4 ppm, but are obscured by solvent and water peaks.

The sheer number and the overlap of the 1H signals present make the structural investigation by ^{1}H-NMR of osmium polypyridyl complexes containing more than one metal centre difficult.[21] The spectrum of $\{[Os(bpy)_2(bpe)_2][Os(bpy)_2Cl]_2\}(PF_6)_4$ presented in Figure 2.5 shows a large number of overlapping signals due to the six bpy ligands and 2 bpe ligands on the complex. A closer examination of the spectrum shows that it is a convolution of the two parent monomer spectra. However, it is not possible to assign the bands present to individual hydrogens with any degree of certainty. The structural identity of the complex is confirmed on the basis of CHN and cyclic voltammetry results.

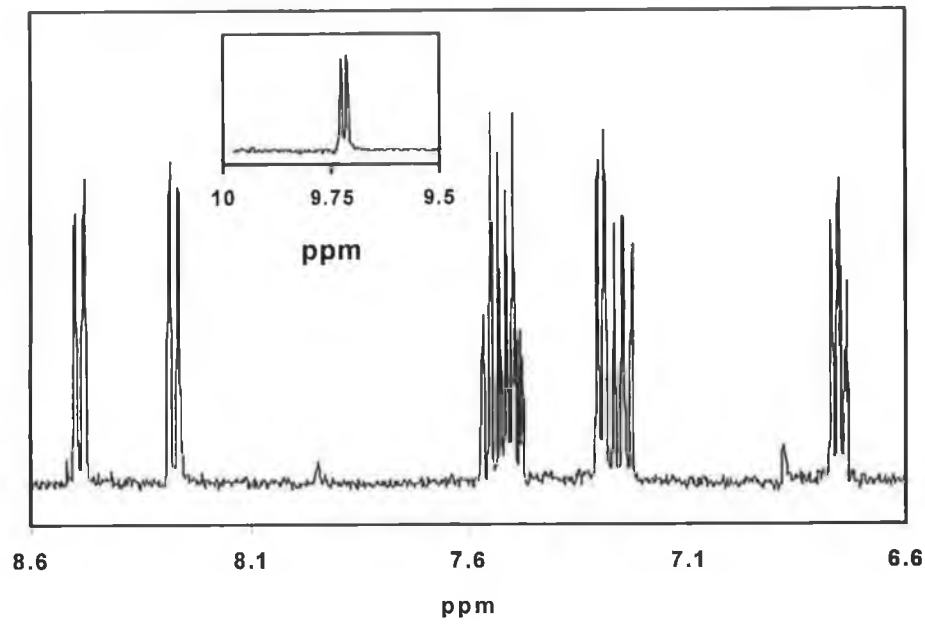

Figure 2.3 ^{1}H-NMR of $[Os(bpy)_2Cl_2]$ in d_6-dimethylsulfoxide. Inset: ^{1}H-NMR peak at 9.70 ppm.

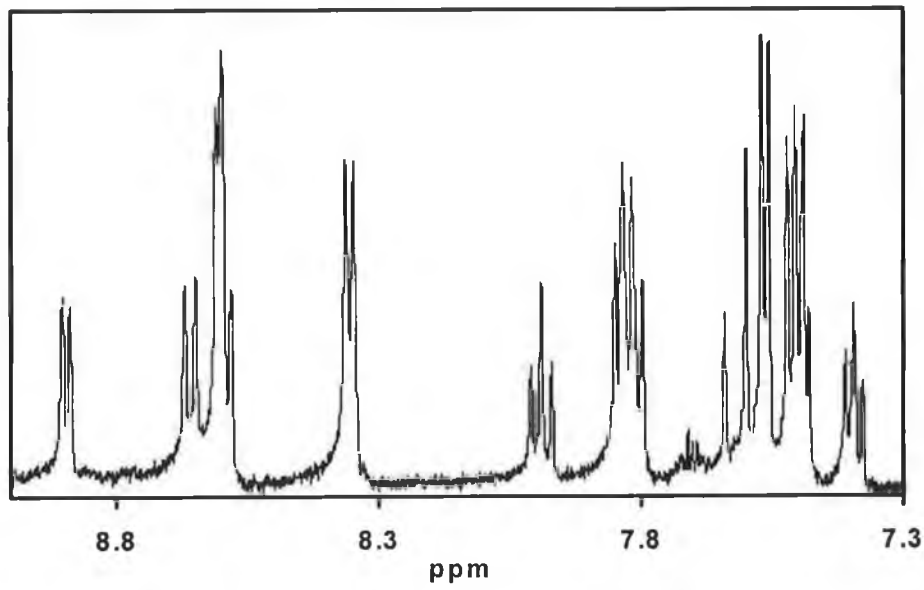

Figure 2.4 ^{1}H-NMR of $[Os(bpy)_2(bpe)_2](PF_6)_2$ in d_6-dimethylsulfoxide.

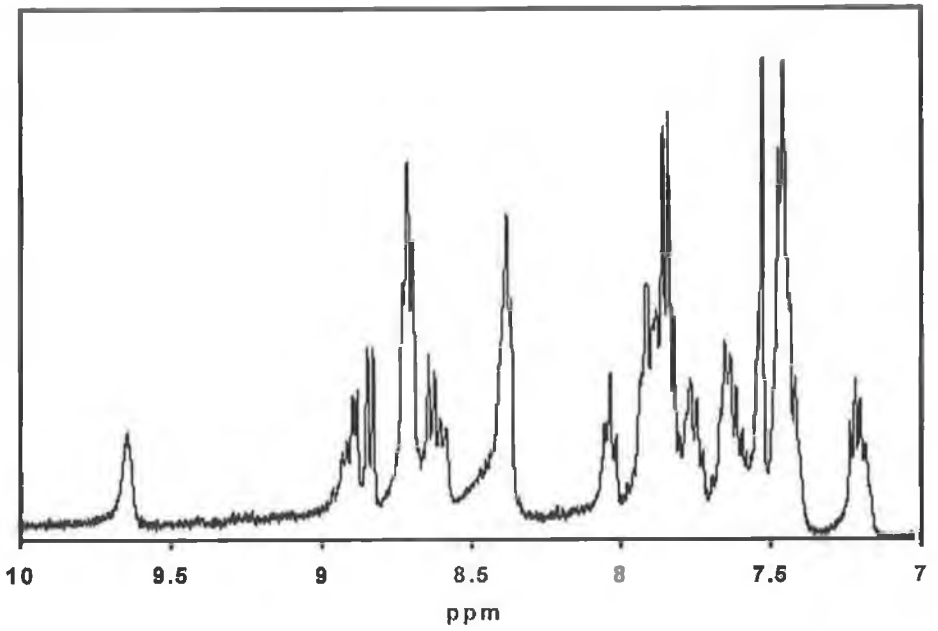

Figure 2.5 ^{1}H-NMR of $\{[Os(bpy)_2(bpe)_2][Os(bpy)_2Cl]_2\}(PF_6)_4$ in d_6-dimethylsulfoxide.

Scheme 3 Schematic representations of osmium compounds including hydrogen numbering system used in the ^{1}H-NMR analysis.

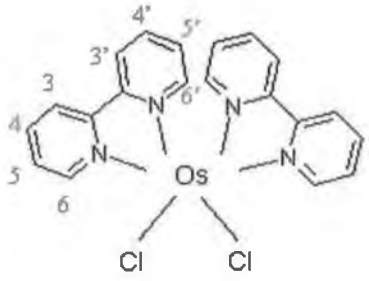

$[Os(bpy)_2Cl_2]$

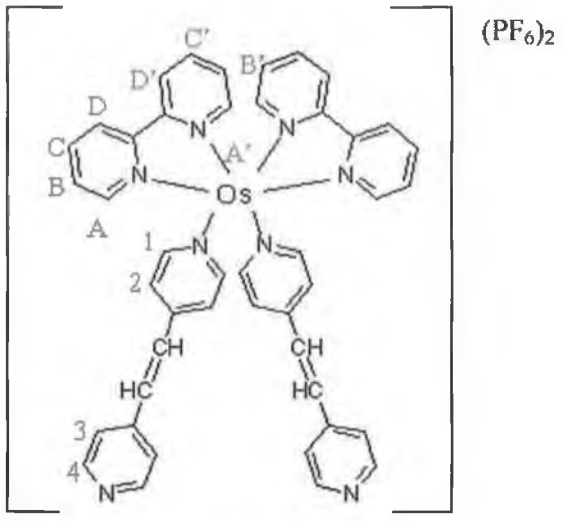

$[Os(bpy)_2(bpe)_2](PF_6)_2$

2.4.3 UV-Vis Spectroscopy

Ultraviolet-visible spectra of transition metal complexes provide insights into the electronic transitions within the complex. Figure 2.6 depicts the absorption spectra of $[Os(bpy)_2(bpe)_2](PF_6)_2$ and $\{[Os(bpy)_2(bpe)_2][Os(bpy)_2Cl]\}(PF_6)_4$. Both compounds exhibit intense bands representing ligand – based $\pi \rightarrow \pi^*$ transitions in the high-energy near - UV region of the spectrum[22] (200 – 380 nm) and spin-allowed metal – to – ligand charge transfer (MLCT) bands in the low–energy visible region[22] (380 – 780 nm). These absorption bands are typical of the UV-Vis spectra of osmium and ruthenium polypyridyl complexes.[2,21] $[Os(bpy)_2(bpe)_2](PF_6)_2$ exhibits two bands in the visible region of the spectrum at 395 and 480 nm, which correspond to $d\pi(Os^{II}) \rightarrow \pi^*(bpe)$ and $d\pi(Os^{II}) \rightarrow \pi^*(bpy)$ MLCT, respectively.[14] In the spectrum of $\{[Os(bpy)_2(bpe)_2][Os(bpy)_2Cl]\}(PF_6)_4$, the visible region contains bands at 440 and 490 nm, corresponding to $d\pi(Os^{II}) \rightarrow \pi^*(bpe)$ and $d\pi(Os^{II}) \rightarrow \pi^*(bpy)$ MLCT, respectively.[14] The difference in energy of the $d\pi(Os^{II}) \rightarrow \pi^*(bpe)$ band in the $[Os(bpy)_2(bpe)_2](PF_6)_2$ monomer in comparison to the same band in the $\{[Os(bpy)_2(bpe)_2][Os(bpy)_2Cl]\}(PF_6)4$ trimer species, has been previously demonstrated for osmium dimers incorporating a similar bridging ligand, 1,2-bis(4-pyridyl)ethane, p2p.[14] The shift has been attributed to a change in the band gap energy of the $d\pi(Os^{II}) \rightarrow \pi^*(p2p)$ band caused by binding to the second osmium centre. Similarly, the shift in energy of the $d\pi(Os^{II}) \rightarrow \pi^*(bpe)$ band in this trimer complex is caused by binding of the $[Os(bpy)_2Cl]$ centre to the bpe ligand. Table 2.1 contains a summary of the UV-Vis data for the complexes.

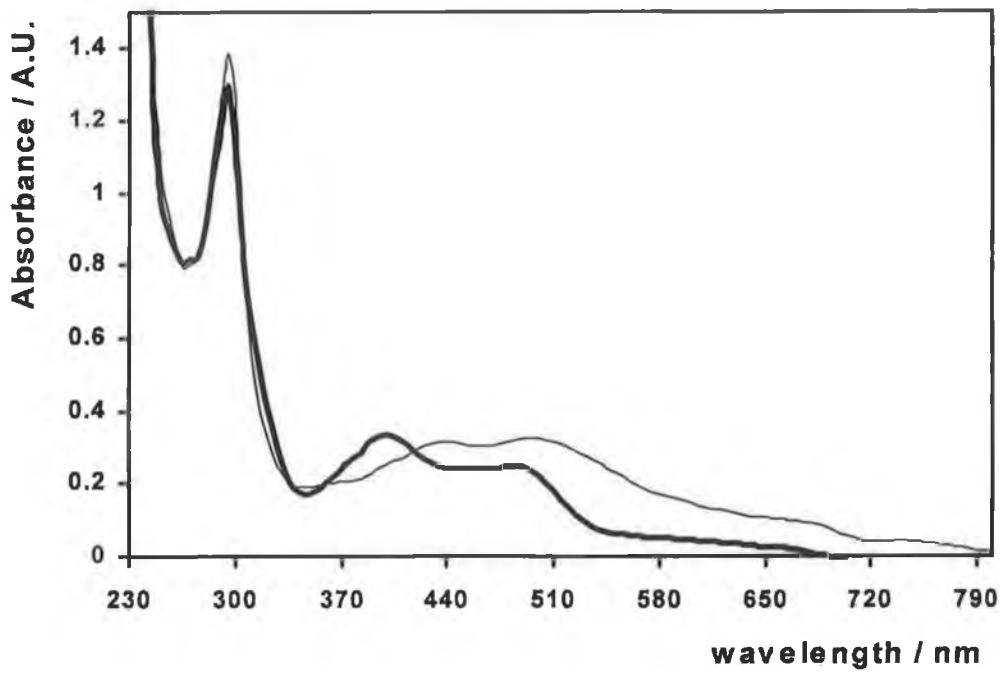

Figure 2.6 Overlaid UV-vis spectra of 2×10^{-5} M $[Os(bpy)_2(bpe)_2](PF_6)_2$ (thick line), and $\{[Os(bpy)_2(bpe)_2][Os(bpy)_2Cl_2]\}(PF_6)_4$ (thin line). In both cases the solvent is deoxygenated butyronitrile.

Table 2.1 UV – Vis Absorption Data and Assignments

Complex	λ_{max} [nm]	ε [M^{-1} cm^{-1}]	Assignment
$[Os(bpy)_2(bpe)_2](PF_6)_2$	295	6.4×10^4	$\pi \rightarrow \pi^*$
	395	1.7×10^4	$d\pi(Os^{II}) \rightarrow \pi^*(bpe)$
	480	1.3×10^4	$d\pi(Os^{II}) \rightarrow \pi^*(bpy)$
$\{[Os(bpy)_2(bpe)_2][Os(bpy)_2Cl]_2\}(PF_6)_4$	295	6.9×10^4	$\pi \rightarrow \pi^*$
	440	1.6×10^4	$d\pi(Os^{II}) \rightarrow \pi^*(bpe)$
	490	1.6×10^4	$d\pi(Os^{II}) \rightarrow \pi^*(bpy)$

2.4.4 Emission Spectroscopy

Emission spectra for $\{[Os(bpy)_2(bpe)_2][Os(bpy)_2Cl]_2\}(PF_6)_4$ and $[Os(bpy)_2(bpe)_2](PF_6)_2$ were obtained at room temperature in deoxygenated butyronitrile. The resulting spectra are displayed in Figure 2.7. The observation that the $[Os(bpy)_2\ (bpe)_2](PF_6)_2$ complex is highly luminescent is consistent with the known photophysical properties of $[Os(N)_6]^{2+}$ complexes, where N represents a nitrogen donor such as pyridine or bpy.[23] Absorption of light by these complexes causes an MLCT transition, where an electron is promoted from the HOMO of the complex (usually a metal-centred d-d orbital) into the LUMO of the complex (usually a ligand π^* orbital) creating an MLCT excited state, which decays to the ground state with a characteristic luminescence.[21,26] The λ_{max} of emission for $[Os(bpy)_2\ (bpe)_2](PF_6)_2$ is 750 ± 2 nm.

The trimer emission is centred at the maximum emission wavelength of the $[Os(bpy)_2(bpe)_2](PF_6)_2$ monomer, within experimental error. However, it exhibits less than 2% of the intensity shown by the monomer species under identical conditions. It is not expected that emission will be observed from the $[Os(bpy)(bpe)Cl]^+$ centres in the trimer, as $[Os(N)_5Cl]^+$ complexes are only weakly emissive, even at liquid nitrogen temperatures, due to vibrational interactions which provide a fast non-radiative decay pathway.[24] The fact that both complexes have a similar maximum emission wavelength, indicates that emission in both species is originating from the same chromophore, namely the $[Os(bpy)_2(bpe)_2]^{2+}$ centre. The observation that the emission intensity is dramatically lower for the trimer than the $[Os(bpy)_2(bpe)_2](PF_6)_2$ complex suggests that the $[Os(bpy)(bpe)Cl]^+$ centres quench the luminescence of the electronically excited $[Os(bpy)_2(bpe)_2]^{2+*}$ centre within the trimer. This phenomenon will be further discussed in Chapter 3 of this thesis.

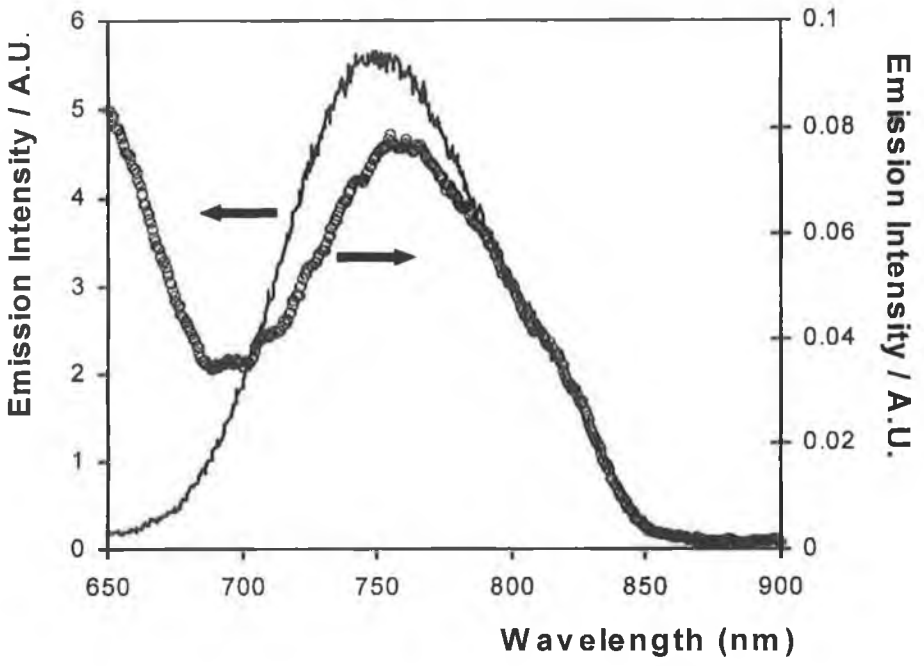

Figure 2.7 Emission spectra at 298 K of $[Os(bpy)_2(bpe)_2]$ $(PF_6)_2$ (solid line) and $\{[Os(bpy)_2(bpe)_2][Os(bpy)_2Cl_2]\}(PF_6)_4$ (open circles). In both cases the solvent is deoxygenated butyronitrile. Both spectra were processed using a 5-point moving average smooth.

2.4.5 Cyclic Voltammetry

Potential sweep methods such as cyclic voltammetry provide a quick and straightforward assessment of the redox behaviour of molecular systems.[25] In particular, cyclic voltammetry in nonaqueous, aprotic, solvents has been adopted as the method of choice for the electrochemical analysis of supramolecular complexes.[26] Figure 2.8 illustrates a solution phase cyclic voltammogram of the trimer complex, $\{[Os(bpy)_2(bpe)_2][Os(bpy)_2Cl_2]\}(PF_6)_4$, overlaid with that of $[Os(bpy)_2(bpe)_2](PF_6)_2$. This figure illustrates the oxidation and reduction of the osmium metal centres within the two complexes and the formal potentials are consistent with those previously measured for the metal-based oxidation of osmium polypyridyl complexes.[11,21,27]

$[Os(bpy)_2(bpe)_2](PF_6)_2$ demonstrates one metal-based oxidation at 0.433 V, consistent with an osmium complex containing six N-donor ligands. The trimer, $\{[Os(bpy)_2(bpe)_2][Os(bpy)_2Cl_2]\}(PF_6)_4$, exhibits two oxidations at 0.039 and 0.464 V. The values of the anodic and cathodic peak currents of the voltammograms are equal and the separation between the anodic and cathodic peak potentials of 61 ± 2 mV is close to the ideal of 59 mV, indicating the reversibility of the metal – based redox reactions in both complexes.[28] The redox peak at 0.039 V has approximately twice the area of the peak at 0.464 V, indicating that the two $[Os(bpy)_2Cl]^+$ centres are the first to be oxidised. This is expected on the basis of the known strong σ-donating properties of the chloride ligand.[29] It is interesting to note that the formal potential of the $[Os(bpy)_2(bpe)_2]^{2+}$ oxidation is not significantly changed upon binding to the two $[Os(bpy)_2Cl]^+$ centres in the trimer complex, indicating that minimal electrostatic interactions exist within the complex.[17,21]

The location of the first excited state within a metal complex can be often be inferred from the first reduction wave, if as described by Koopman's theorem,[30] the π_L^* orbital involved in the reduction process is the same as that involved in the MLCT transitions. Figure 2.9 illustrates a CV of the trimer complex, showing both the metal-based oxidations and the reductions of the ligands. Formal potentials are reproducible to within 10 mV. The potential for the first reduction is –1.500 V. The voltammogram for $[Os(bpy)_2(bpe)_2](PF_6)_2$ shows evidence of adsorption, commonly seen in the ligand reduction voltammograms of surface-active complexes.[31] However, the results are adequate to allow the potential of the first reduction wave to be estimated from the

cathodic peak potential, to yield a value of –1.700 V. A summary of the formal potentials for both complexes is presented in Table 2.2.

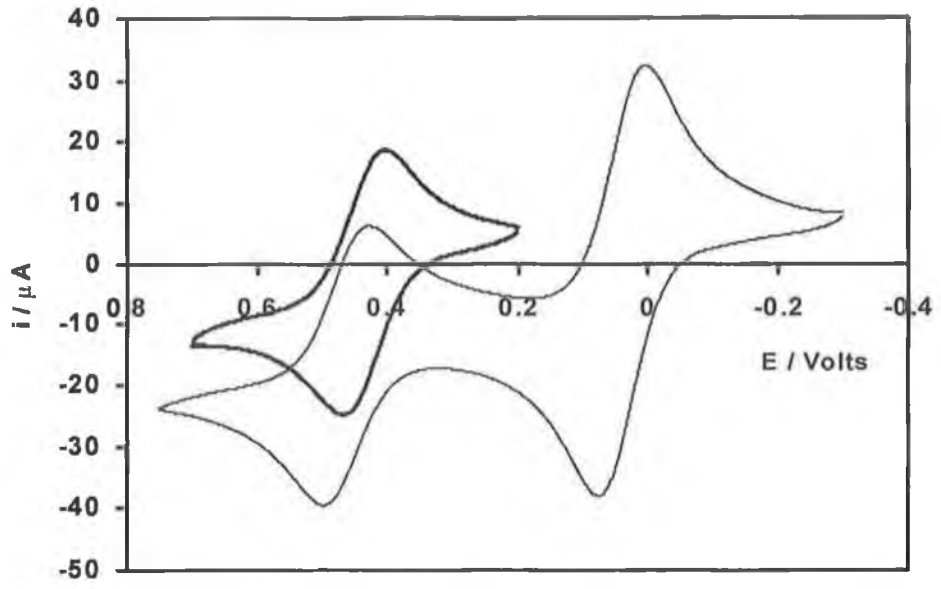

Figure 2.8 Cyclic voltammograms of 5 mM $[Os(bpy)_2(bpe)_2](PF_6)_2$ (thick line) and $\{[Os(bpy)_2(bpe)_2][Os(bpy)_2Cl_2]\}(PF_6)_4$ (thin line) dissolved in deoxygenated acetonitrile/ 0.1 M TBAP. Potentials are versus Ag/Ag^+. The working electrode is a 2 mm diameter platinum disc. The scan rate for both voltammograms is 0.1 V s^{-1}. The initial potentials are 0.2 and –0.3 V for $[Os(bpy)_2(bpe)_2](PF_6)_2$ and $\{[Os(bpy)_2(bpe)_2][Os(bpy)_2Cl_2]\}(PF_6)_4$, respectively.

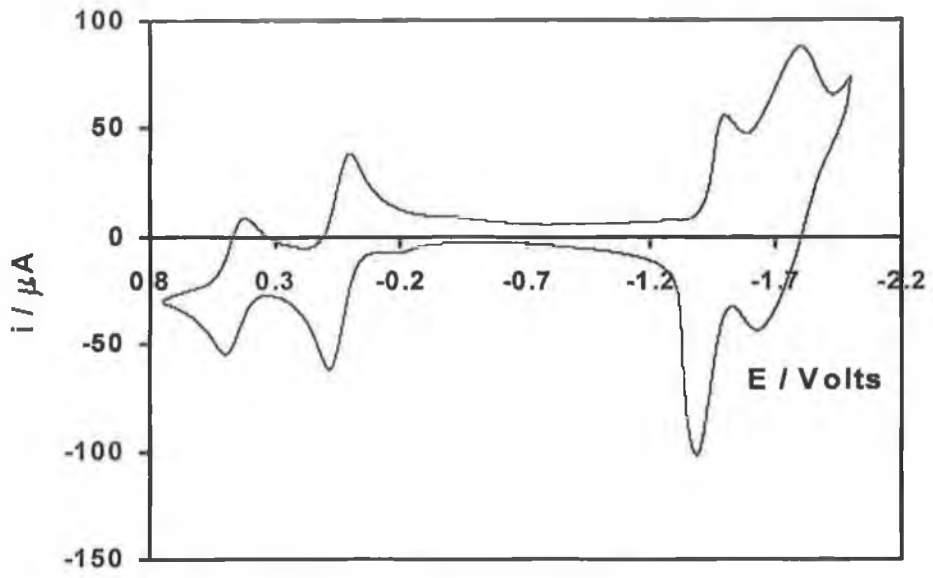

Figure 2.9 Segments 5 and 6 of a cyclic voltammogram of 5 mM $\{[Os(bpy)_2(bpe)_2][Os(bpy)_2Cl_2]\}(PF_6)_4$ dissolved in deoxygenated acetonitrile/ 0.1 M TBAP. Potentials are versus Ag/Ag^+. The working electrode is a 2 mm diameter platinum disc. The scan rate is 0.1 V s^{-1} and the initial potential is – 0.3 V.

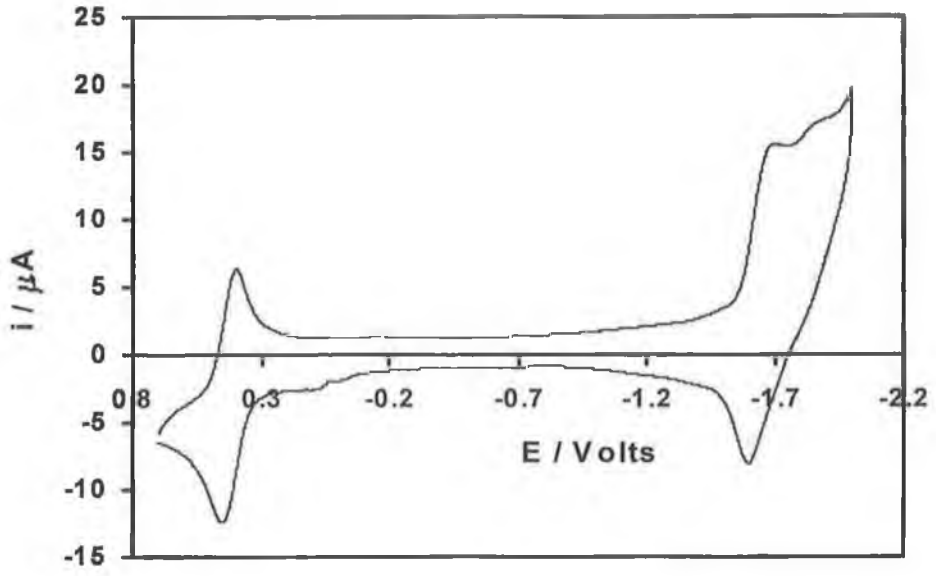

Figure 2.10 Segments 5 and 6 of a cyclic voltammogram of 5 mM $[Os(bpy)_2(bpe)_2](PF_6)_2$ dissolved in deoxygenated acetonitrile/ 0.1 M TBAP. Potentials are versus Ag/Ag^+. The working electrode is a 2 mm diameter gold disc. The scan rate is 0.1 V s^{-1} and the initial potential is 0.0 V.

Table 2.2 Formal Potentials for Monomeric and Trimeric Metal Complexes.[a]

Complex	$E^{o'}_{Os2+/3+}$ / V[b]	$E^{o'}_{bpy\ /\ bpy^{\bullet -}}$ / V[b]
$\{[Os(bpy)_2(bpe)_2][Os(bpy)_2Cl]_2\}^{4+}$	0.039, 0.464	-1.500
$[Os(bpy)_2(bpe)_2](PF_6)_2$	0.433	-1.700

[a] All measurements were made in acetonitrile containing 0.1 M TBABP as supporting electrolyte.

[b] Formal potentials are reproducible to within ±10 mV.

[c] Potentials are quoted versus Ag/Ag^+.

2.5 Synthesis of Ruthenium Complexes

$[Ru(dpp)_2Cl_2]$

$$RuCl_3 + 2\,dpp \xrightarrow{DMF,\ \Delta} Ru(dpp)_2Cl_2$$

$RuCl_3$ (250 mg, 1.2 mmol) was dissolved in DMF (40 cm^3) and heated for 30 mins. 4,7-diphenyl-1,10-phenanthroline (761.2 mg, 2.3 mmol) was dissolved in 10 cm^3 DMF and gradually added to the reaction mixture over a 1 hour period. To prevent the formation of carbonyl substituted product, LiCl (2 g) was added to the initial reaction mixture and the reaction was carried out under a constant purge of N_2. The reaction was heated to just under reflux at 135 °C (b.p. DMF is 153 °C) for 5 hours, then made up to 400 cm^3 with acetone and stored overnight in the freezer. The product was collected by vacuum filtration, washed with copious amounts of water and diethyl ether to remove un-reacted starting materials and dried overnight.

2,2′:4,4″:4′,4″-Quarterpyridyl (Qbpy) was kindly provided by Dr. Tia Keyes from Dublin Institute of Technology, Kevin Street and was used following confirmation of purity by ^{1}H-NMR.

$[Ru(dpp)_2(Qbpy)](PF_6)_2$

$$[Ru(dpp)_2Cl_2] + 2\,Qbpy\ (xs) \xrightarrow{1{:}1\ (v/v)\ EtOH/\ H_2O,\Delta} [Ru(dpp)_2(Qbpy)](PF_6)_2$$

$[Ru(dpp)_2Cl_2]$ (0.25g, 0.298 mmol) and 2,2′:4,4″:,4′,4″-quarterpyridyl (0.1854g, 0.5974 mmol, xs.) were dissolved in 50 cm^3 of 50:50 ethanol/water and heated to reflux for 8 hours. The solvent was removed to a volume of 10 cm^3 and precipitated by addition of an aqueous solution of concentrated NH_4PF_6. High performance liquid chromatography (HPLC) showed that the crude red-orange material was 70 % pure (70% product, 20% un-reacted Qbpy ligand, 10% other Ru compounds). This 10% consisted of two peaks, of approximately 4 and 6 % intensity. The UV-Vis spectra of these peaks are characteristic of ruthenium polypyridine complexes. As the starting materials for the reaction ($[Ru(dpp)_2Cl_2]$ and Qbpy) were both of 100 % purity, the

origin of these Ru impurities remains unclear. A possible explanation is that some of the Qbpy ligand is degrading into 4,4'-dipyridyl ligand (p0p). This free p0p ligand could then react with the $[Ru(dpp)_2Cl_2]$ complex to form $[Ru(dpp)_2(p0p)Cl](PF_6)$ and $[Ru(dpp)_2(p0p)_2](PF_6)_2$. However, no concrete evidence is available to support this hypothesis and the origin of these impurities is not considered further.

A number of purification strategies based on adsorption chromatography were carried out on the complex, but none were successful in separating the required product from the impurities. Table 2.3 contains the experimental details and results of each of the purification attempts. The resulting samples were analysed by HPLC or thin layer chromatography (TLC) on silica plates using 80/20 Acetonitrile/Water, saturated with KNO_3 as a mobile phase. In all cases, elution of the bands from the columns was difficult, due to the tendency of the free nitrogens on the Qbpy ligand to bind strongly to the stationary phase. For example, in the case of the Sephadex C25 ion-exchange resin column, the band did not elute from the column using the usual NaCl solution as the mobile phase, but was washed off with acetone saturated with ammonium hexafluorophosphate (NH_4PF_6).

The most successful purification method proved to be fractional recrystallisation, in which 100 mg of the complex was dissolved in 30 mls 2:1 (v/v) acetone:water. The solution was left to stand in the refrigerator. Every two days, any solid was filtered from the solution, whereupon the filtrate was returned to the refrigerator and left to stand for another two days. This was repeated three times (a total of six days). Each solid fraction recovered was washed with water and diethylether and analysed by HPLC. The third and final fraction was found to be of 90 % purity. This proved to be the best possible purity obtainable for this complex using standard purification methods. This sample of complex was used for the analysis detailed in the following section.

Table 2.3 Details and results of purification attempts carried out on $[Ru(dpp)_2(Qbpy)](PF_6)_2$

	Stationary Phase	Mobile Phase (Packing)	Mobile Phase (Eluent)	HPLC or TLC[a] Results
1	Alumina (neutral, activated)	ACN[b] / 2% MeOH[c]	ACN with increasing concn. of MeOH	76% product 1.5% ligand 18 % other MLCT
2	Sephadex LH20 (size exclusion resin)	MeOH	MeOH	70% product 18% ligand 10.4% other MLCT
3	Sephadex C25 (ion-exchange resin)	H_2O	(1) 0.01 – 2M aq. NaCl (2) Acetone/ NH_4PF_6	52% product 29% ligand 13% other MLCT
4	Silica	80/20 ACN/H_2O, sat. KNO_3	80/20 ACN/H_2O, sat. KNO_3	68% product 17% ligand 17% other MLCT
5	Alumina (neutral, unactivated (15% H_2O))	CH_2Cl_2	CH_2Cl_2 with increasing concn. MeOH	4 cm - product 3.6 cm - other MLCT 1.8 cm - ligand
6	Preparative Silica TLC plate (20 cm × 20 cm)	80/12/8 ACN/H_2O/sat KNO_3	80/12/8 ACN/H_2O/sat KNO_3	4 cm - product 5.5 cm – other MLCT

[a] 10 cm long silica TLC plate. Mobile phase: 80/12/8 ACN/H_2O/sat. KNO_3

[b] HPLC grade acetonitrile

[c] HPLC grade methanol

2.6 Characterisation of Ruthenium Complexes

2.6.1 High Performance Liquid Chromatography

Figure 2.11 illustrates a HPLC of $[Ru(dpp)_2Cl_2]$. The chromatogram exhibits a single peak at 2.3 min, with a peak area of 100 %. The visible region λ_{max} in the UV-vis spectrum of this peak is 550 nm. It may be concluded from the HPLC chromatogram that this compound contains no un-reacted starting materials.

Figure 2.12 illustrates a HPLC of $[Ru(dpp)_2(Qbpy)](PF_6)_2$. This HPLC contains three peaks at 2.51, 3.48 and 4.90 min. The peak areas are 7.50, 2.50 and 90.0 % respectively. The UV-Vis spectrum of the peak at 2.51 min contains bands in the UV – region of the spectrum (200 – 380 nm[22]) only, indicating that this is un-reacted Qbpy free ligand. The peak at 3.48 min displays the characteristic $\pi \rightarrow \pi^*$ and MLCT bands of a ruthenium polypyridyl complex, with λ_{max} = 470 nm. This wavelength is lower than the λ_{max} of the $[Ru(dpp)_2Cl_2]$ peak (550 nm), which leads to the conclusion that this peak is not un-reacted $[Ru(dpp)_2Cl_2]$. The final peak at 4.90 min displays a UV-Vis spectrum with an MLCT λ_{max} = 450 nm, similar to that reported previously for its analogue, $[Ru(bpy)_2(Qbpy)](PF_6)_2$, where the dpp ligand is replaced by bpy, 2,2'-dipyridyl.[32] This similarity, coupled with the fact that this is the largest peak in the chromatogram, leads to the conclusion that this peak corresponds to the required $[Ru(dpp)_2(Qbpy)](PF_6)_2$ complex. The complex is therefore present in 90 % purity, with some unreacted ligand (7.50 %) and an unknown ruthenium polypyridyl impurity (2.50 %). The identity of the major band is confirmed later by ^{1}H-NMR.

The Varian Star software used to analyse the HPLC data allows the chromatogram to be displayed as a "purity parameter" versus time. By monitoring the full UV-VIS spectrum of every point on the chromatogram, this "purity parameter" plot determines if a single peak consists of two separate compounds which elute at the same time. For both compounds analysed, the individual peaks detected proved to consist of a single species.

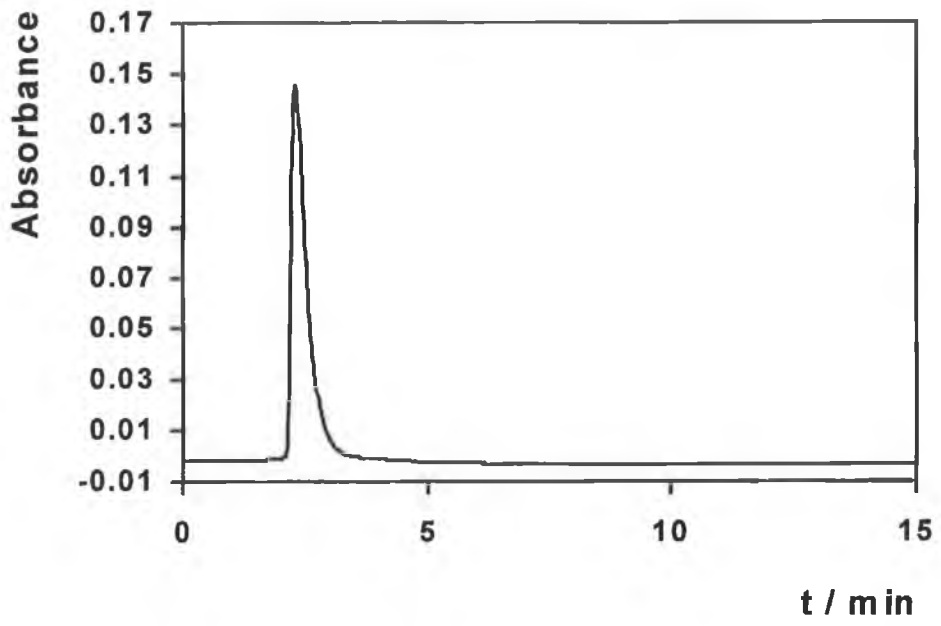

Figure 2.11 Chromatogram of $[Ru(dpp)_2Cl_2]$ obtained using cation-exchange HPLC at a flow rate of 1.8 ml min^{-1}. The mobile phase was 80:20 (v/v) ACN/H_2O, 0.08 M $LiClO_4$.

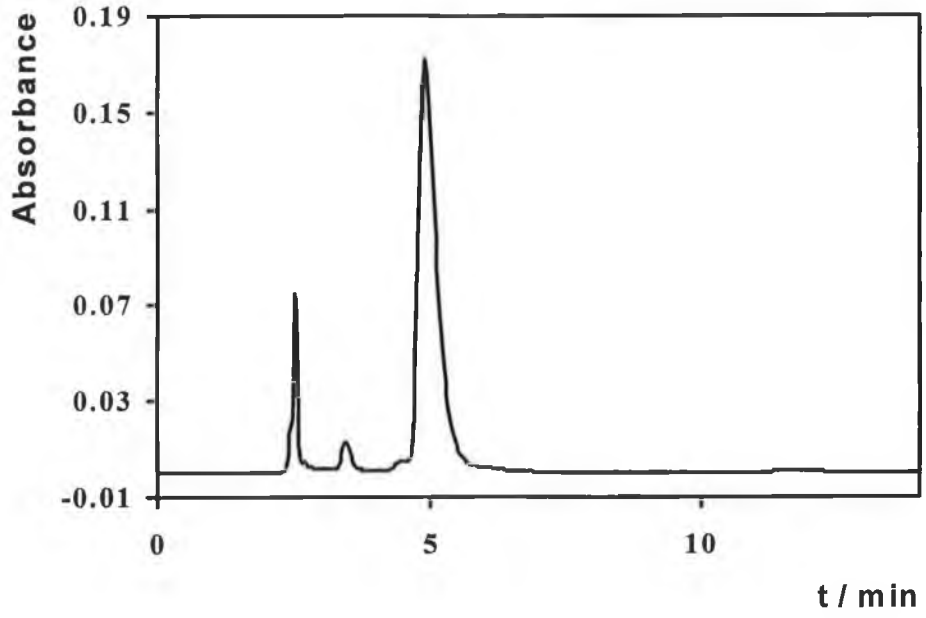

Figure 2.12 Chromatogram of $[Ru(dpp)_2(Qbpy)](PF_6)_2$ obtained using cation-exchange HPLC at a flow rate of 1.8 ml min^{-1}. The mobile phase was 80:20 (v/v) ACN/H_2O, 0.08 M $LiClO_4$.

2.6.2 ^{1}H – NMR

An important feature of low-spin d_6 systems is that the complexes are diamagnetic and sharp NMR spectra can be obtained. Proton magnetic resonance spectra for $[Ru(dpp)_2Cl_2]$, 2,2′:4,4″:4′,4″-Quarterpyridyl and $[Ru(dpp)_2(Qbpy)](PF_6)_2$ are presented in Figures 2.13 to 2.15. Scheme 4 illustrates the hydrogen numbering which is referred to in the text.

The bands for the monomers were assigned by obtaining Aromatic COSY proton coupling spectra for the compounds and are as follows:

$[Ru(dpp)_2Cl_2]$ ^{1}H-NMR. δ (d_6-DMSO): 7.47 (2H, d, $H_{A'}$), 7.63 (10H, s, $H_{C'}$. $H_{D'}$, $H_{E'}$, $H_{F'}$, $H_{G'}$), 7.74 (2H, d, H_E), 7.80 (4H, t, H_D, H_F), 7.92 (4H, d, H_C, H_G), 8.12, (2H, d, $H_{B'}$), 8.14 (2H, d, $H_{H'}$), 8.30 (2H, d, H_H), 8.33 (2H, d, H_B), 10.5 (2H, d, H_A).

2,2′:4,4″:4′,4″-Quarterpyridyl ^{1}H-NMR. δ ($CDCl_3$): 7.55 (2H, d, H_F, $H_{F'}$), 7.64 (4H, d, H_C, $H_{C'}$, H_D, $H_{D'}$), 8.69 (4H, d, H_A, $H_{A'}$, H_B, $H_{B'}$), 8.71 (2H, s, H_E, $H_{E'}$), 8.77 (2H, d, H_G, $H_{G'}$).

$[Ru(dpp)_2(Qbpy)](PF_6)_2$ ^{1}H-NMR. δ ($CDCl_3$): 7.50 (20H, m, H_{Ph}), 7.63 (2H, d, H_H), 7.76 (4H, d, H_F, $H_{F'}$), 7.78 (4H, d, H_A, $H_{A'}$), 7.83 (2H, d, H_C), 8.22 (4H, d, H_B, $H_{B'}$), 8.24 (2H, s, $H_{C'}$), 8.43 (2H, d, H_G), 8.65 (4H, d, H_E, $H_{E'}$), 8.69 (2H, d, H_D).

The spectrum of $[Ru(dpp)_2(Qbpy)](PF_6)_2$ shows some indications of the two impurities identified by the HPLC analysis. These are represented in the ^{1}H-NMR spectrum by small peaks, of approximately 10 % intensity when compared to the main peaks listed above. For example, the doublet at 8.43 ppm has smaller peaks located either side of the main peak. Also, the numerical integration of the peak area for the doublets corresponding to H_F and $H_{F'}$, and H_A and $H_{A'}$, at 7.76 and 7.78 ppm, respectively, do not correspond to exactly 4 protons in each case. These facts correlate well with the HPLC result and confirm that the $[Ru(dpp)_2(Qbpy)](PF_6)_2$ material contains approximately 10 % impurities.

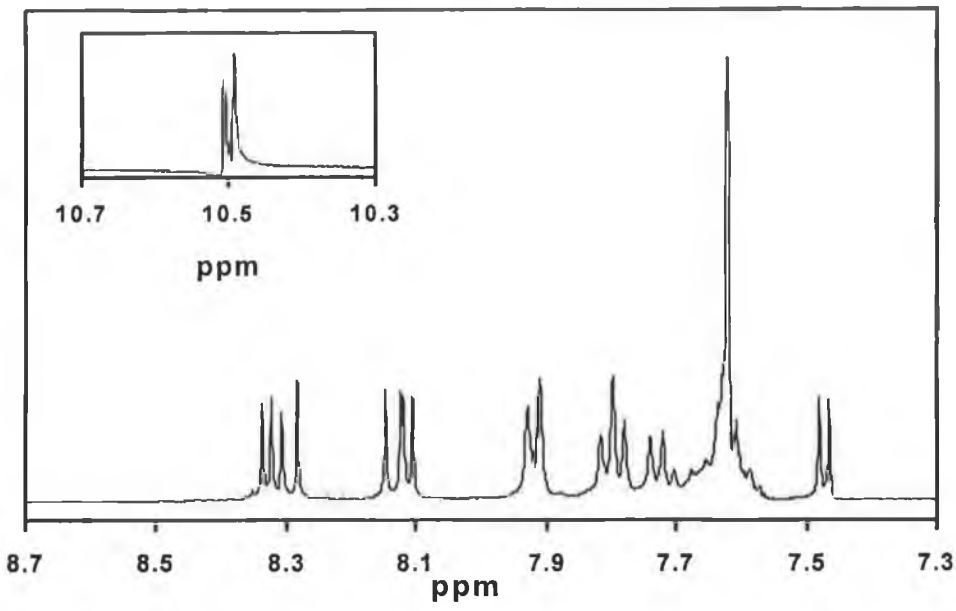

Figure 2.13 ^{1}H – NMR spectrum of $[Ru(dpp)_2Cl_2]$ in d_3-chloroform. Inset: ^{1}H-NMR peak at 10.5 ppm.

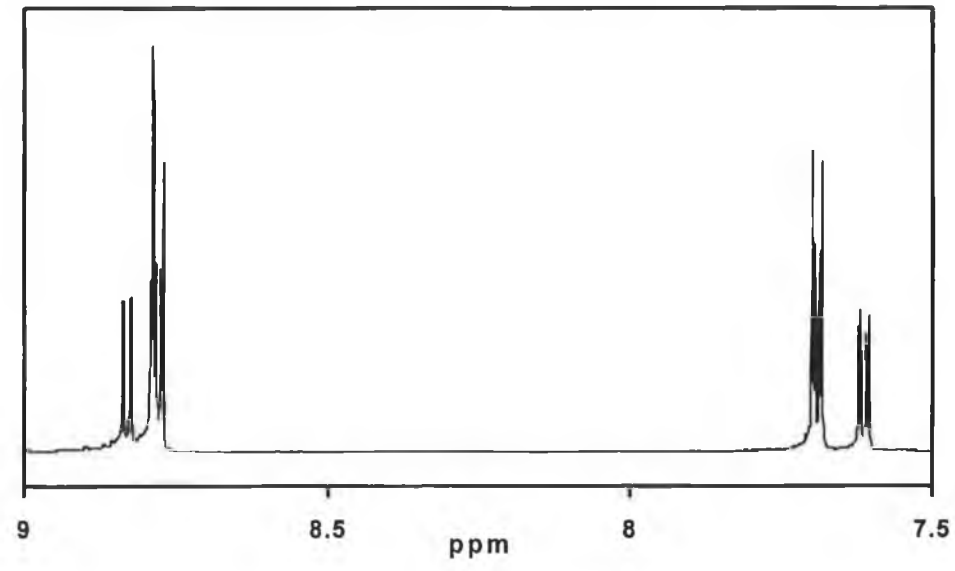

Figure 2.14 ^{1}H-NMR of 2,2′:4,4″:4′,4″-Quarterpyridyl in d_3-chloroform.

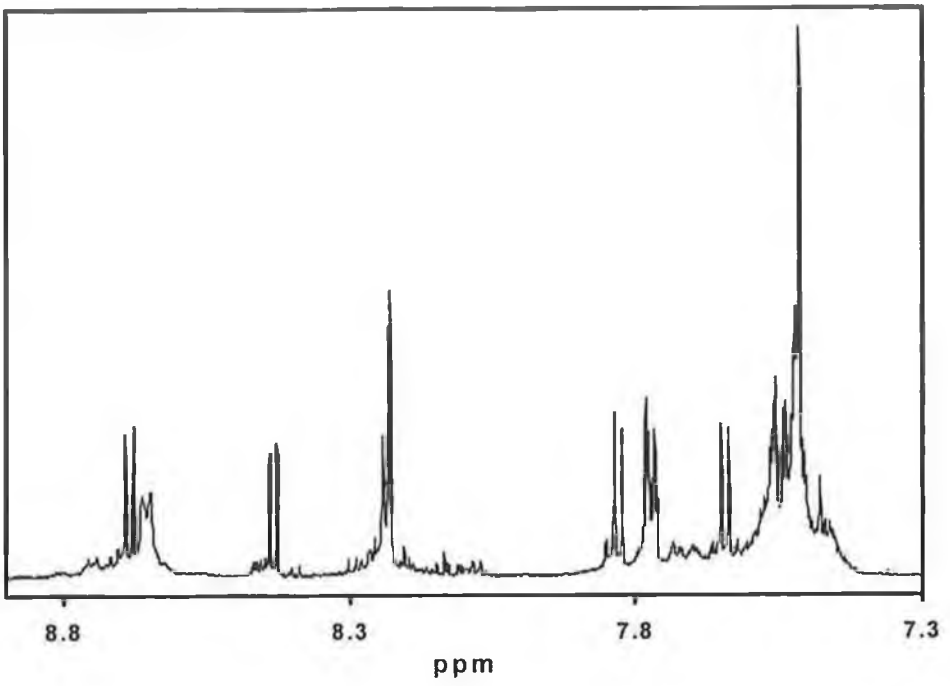

Figure 2.15 ^{1}H – NMR spectrum of $[Ru(dpp)_2(Qbpy)](PF_6)_2$ in d_3-chloroform.

Scheme 4 Schematic representation of ruthenium compounds including hydrogen numbering system used in the ^{1}H-NMR analysis.

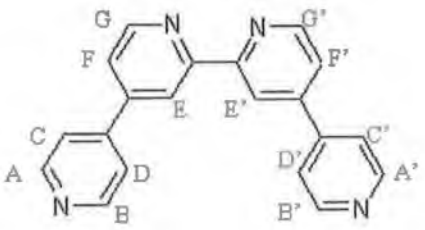

2,2':4,4'':4',4''-Quarterpyridyl (Qbpy)

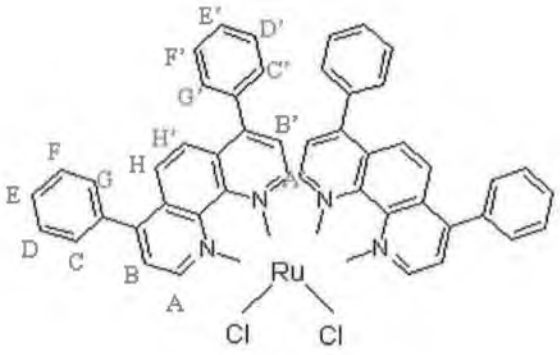

$Ru(dpp)_2Cl_2$

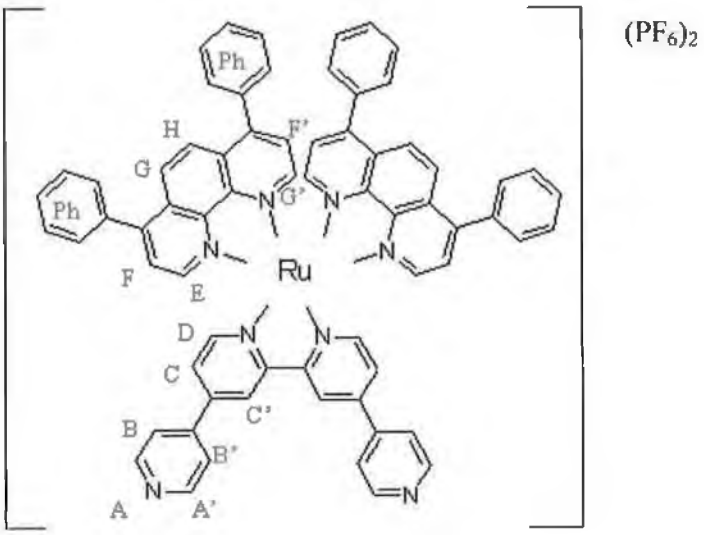

$(PF_6)_2$

$[Ru(dpp)_2(Qbpy)](PF_6)_2$

2.6.3 UV - Vis Spectroscopy

The recording of an ultraviolet-visible spectrum of a complex allows insights into the electronic transitions within the complex. Shown in Figure 2.16 are the UV-Vis spectra of $[Ru(dpp)_2Cl_2]$ and $[Ru(dpp)_2(Qbpy)](PF_6)_2$ in spectroscopic grade acetonitrile. Both compounds exhibit intense bands representing ligand – based $\pi \rightarrow \pi^*$ transitions in the high-energy near - UV region of the spectrum[22] (200 – 380 nm) and spin-allowed metal – to – ligand charge transfer (MLCT) bands in the low–energy visible region[22] (380 – 780 nm). These absorption bands are typical of the UV-Vis spectra of osmium and ruthenium polypyridyl complexes.[2,21]

For $[Ru(dpp)_2(Qbpy)](PF_6)_2$ the visible region $d\pi(Ru^{II}) \rightarrow \pi^*(dpp)$ and $d\pi(Ru^{II}) \rightarrow \pi^*(Qbpy)$ metal-to ligand charge transfer (MLCT) bands are seen in a broad region at approximately 430 – 460 nm, while the shoulder at approximately 310 nm may correspond to metal-centered (MC) transitions.[26] Comparison to published results for $[Ru(bpy)_2(Qbpy)](PF_6)_2$, an analogous complex where the dpp ligand is replaced by 2,2'-bipyridine, and its derivative, $[Ru(bpy)_2(Qbpy\text{-}me)](PF_6)_2$, containing a methylated Qbpy ligand,[32] indicate that the broad absorption at 430 – 460 nm can be resolved into two bands at 432 and 465 nm, corresponding to $d\pi(Ru^{II}) \rightarrow \pi^*(dpp)$ and $d\pi(Ru^{II}) \rightarrow \pi^*(Qbpy)$ respectively. A strong MLCT band is also seen at 275 nm, while the other bands between 200 and 300 nm correspond to ligand-centered $\pi \rightarrow \pi^*$ transitions.[26] Similar bands are found in the spectrum of $[Ru(dpp)_2Cl_2]$, however the visible region MLCT band is red – shifted to 550 nm, due to the strong electron donating properties of the chloride ligands,[29] which narrows the energy gap between the d-d orbital of the ruthenium metal and the π^* orbital of the ligand, shifting the MLCT band to lower energy, and therefore a higher wavelength.[33]

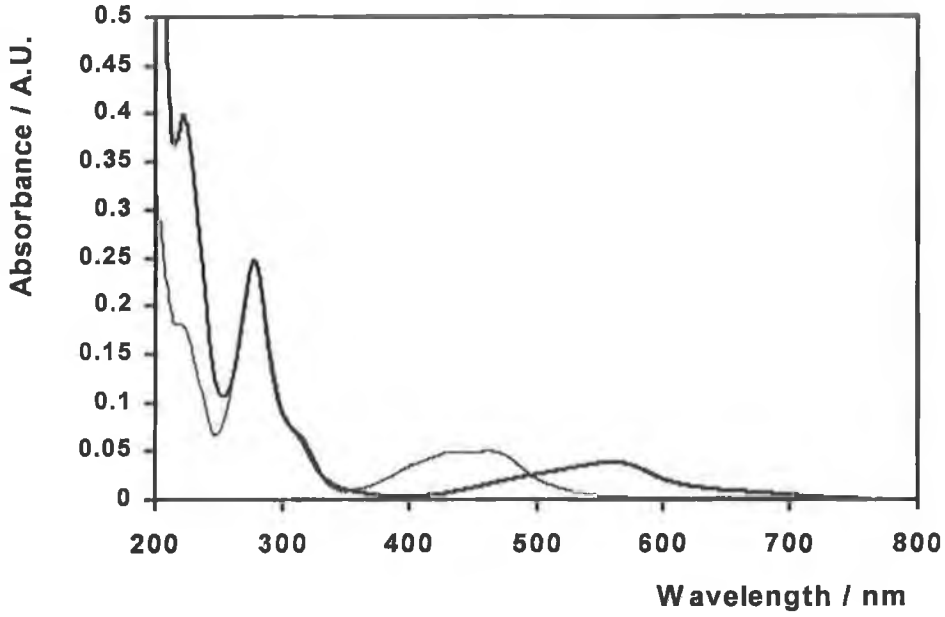

Figure 2.16 Overlaid UV-Vis absorbance spectra of 2×10^{-6} M $Ru(dpp)_2Cl_2$ (thick line) and $[Ru(dpp)_2Qbpy](PF_6)_2$ (thin line). In both cases, the solvent is deoxygenated acetonitrile.

Table 2.4 UV – Vis Absorption Data and Assignments

Complex	λ_{max} [nm]	ε [M^{-1} cm^{-1}]	Assignment
$[Ru(dpp)_2Cl_2]$	275	1.3×10^5	$\pi \rightarrow \pi^*$
	550	2.0×10^3	$d\pi(Ru^{II}) \rightarrow \pi^*(dpp)$
$[Ru(dpp)_2(Qbpy)](PF_6)_2$	275	1.2×10^5	$\pi \rightarrow \pi^*$
	432	2.5×10^4	$d\pi(Ru^{II}) \rightarrow \pi^*(dpp)$
	465	2.5×10^4	$d\pi(Ru^{II}) \rightarrow \pi^*(Qbpy)$

2.6.4 Emission Spectroscopy

Excitation of a ruthenium complex into any of its absorption bands leads to a luminescence emission which occurs from a set of three closely spaced MLCT levels.[26] The theoretical description of the luminescent levels continues to be a matter of debate, but current opinion favours a description which assumes a triplet character and a single ligand localised excitation.[21,26] Figure 2.17 details an emission spectrum of $[Ru(dpp)_2(Qbpy)](PF_6)_2$ obtained in room temperature in acetonitrile. The complex exhibits an emission maximum at approximately 615 nm, consistent with the known photophysical properties of $[Ru(N)_6]^{2+}$ complexes, where N represents a nitrogen donor such as pyridine or bpy.[23] No emission is observed for $[Ru(dpp)_2Cl_2]$, as the strong electron-donating properties of the chloride ligands result in an energy gap between the ground and excited state which is small enough to allow the rate of nonradiative decay to be considerably faster than the radiative rate, and therefore no emission is observable.[33]

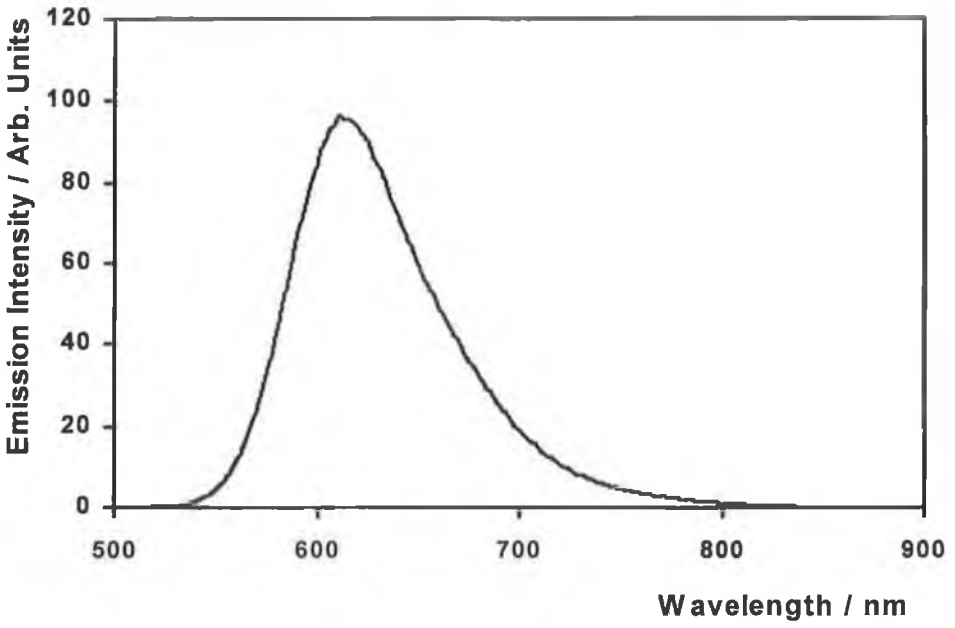

Figure 2.17 Emission spectrum of 4×10^{-6} M $[Ru(dpp)_2(Qbpy)](PF_6)_2$. The solvent is deoxygenated acetonitrile.

2.6.5 Cyclic Voltammetry

Ruthenium complexes are well known for the reversibility of their metal based redox processes in the ground state and a wealth of information is now available on the electrochemical behaviour of ruthenium-polypyridine complexes.[21] Figure 2.18 illustrates a CV of $[Ru(dpp)_2(Qbpy)]^{2+}$, showing the metal-based oxidations within the complex. $E^{o'}$ for the oxidation of the $Ru^{2+/3+}$ process is 0.503 V vs. Ag/Ag^+. The values of the anodic and cathodic peak currents of the voltammogram are equal and the separation between the anodic and cathodic peak potentials of 59 mV is ideal, indicating the reversibility of the metal – based redox reactions in the complex.[28]

Reduction of Ru(II) complexes may in principle involve either a metal-centered or a ligand-centered orbital, depending on the relative energy ordering. When the ligand field is sufficiently strong, and/or the ligands can be easily reduced, reduction takes place on a ligand π^* orbital. This is the commonly observed behaviour of Ru(II) polypyridine complexes.[26,30] The added electron appears to be localised on a single ligand and several reduction steps can often be observed in the accessible potential range. The identity of the first excited state of a complex can often be inferred from the potential of the first reduction wave, if, as described by Koopman's theorem,[30] the π_L^* orbital involved in the reduction process is the same as that involved in the MLCT transitions.

In Figure 2.19, a cyclic voltammogram of $[Ru(dpp)_2Cl_2]$ is presented. The CV shows one metal-based redox couple at 0.006 V and two ligand reduction redox couples at –1.77 and –1.90 V. For the metal-based redox couple, the values of the anodic and cathodic peak currents of the voltammograms are equal and the separation between the anodic and cathodic peak potentials of 61±2 mV is close to the ideal of 59 mV, indicating the reversibility of the metal-based redox reactions in the complex.

Figure 2.20 illustrates a CV of $[Ru(dpp)_2(Qbpy)](PF_6)_2$, showing both the metal-centered oxidations and the ligand reductions of the complex. The peaks for the metal-based redox couple are ill-defined when compared to the ligand reduction peaks. This was consistently observed for a number of experiments using solutions of different concentration and a number of different electrodes. However, the ligand reduction peaks are sufficiently well resolved to determine the potentials of the first two

reductions. They are observed at −1.46 and −1.63 V. Significantly, although the HPLC and ^{1}H-NMR results indicate that this complex is of 90 % purity, there is no trace of the impurities (7.5% Qbpy ligand, 2.5% unknown Ru-polypyridine) in the cyclic voltammograms detailed here. This leads to the conclusion that the impurities are either not redox – active or are present at such small levels, that they do not interfere with the voltammetry of $[Ru(dpp)_2(Qbpy)](PF_6)_2$.

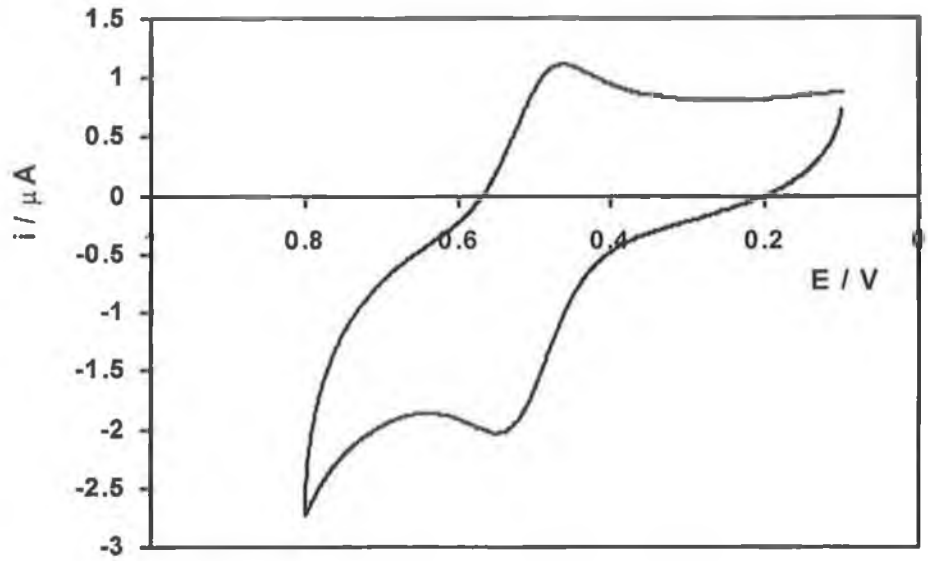

Figure 2.18 Cyclic voltammogram of 5 mM $[Ru(dpp)_2Qbpy](PF_6)_2$ dissolved in de-aerated acetonitrile/ 0.1 M TBAP. Potentials are versus Ag/Ag^+. The working electrode is a 3 mm diameter glassy carbon disc. The scan rate is 0.1 V s^{-1} and the initial potential is 0.1 V.

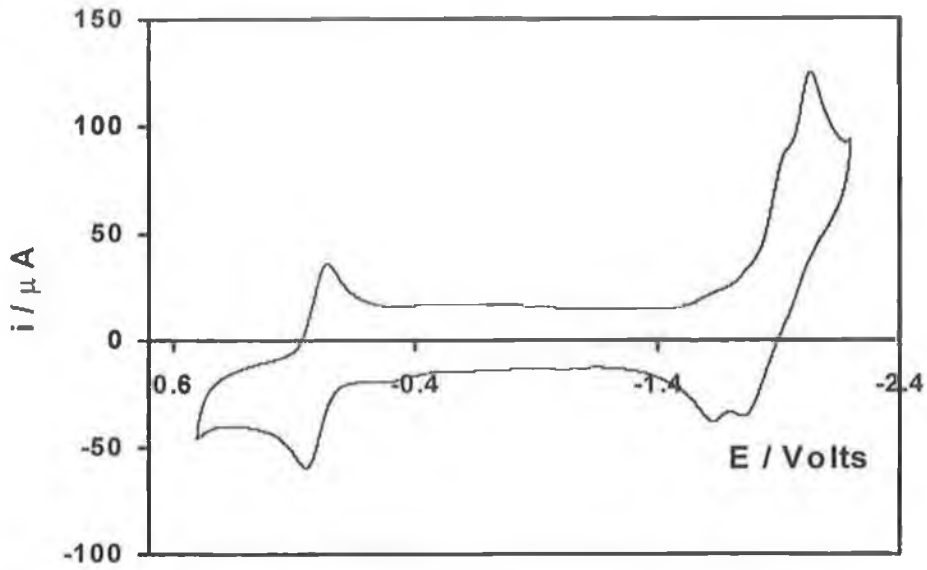

Figure 2.19 Segments 5 and 6 of a cyclic voltammogram of 5 mM $[Ru(dpp)_2Cl_2]$ dissolved in de-aerated acetonitrile/ 0.1 M TBAP. Potentials are versus Ag/Ag^+. The working electrode is a 3 mm diameter glassy carbon disc. The scan rate is 0.1 V s^{-1} and the initial potential is – 0.4 V.

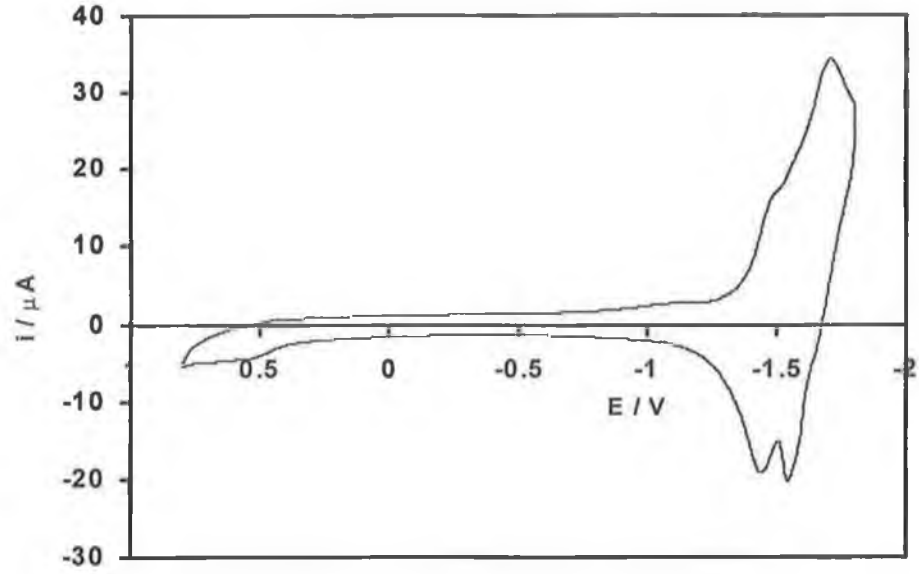

Figure 2.20 Segments 5 and 6 of a cyclic voltammogram of 2 mM $[Ru(dpp)_2Qbpy](PF_6)_2$ dissolved in de-aerated acetonitrile/ 0.1 M TBAP. Potentials are versus Ag/Ag^+. The working electrode is a 3 mm diameter glassy carbon disc. The scan rate is 0.1 V s^{-1} and the initial potential is 0.0 V.

Table 2.5 Formal Potentials for Monomeric Metal Complexes.[a,b]

Complex	$E^{\circ\prime}_{Ru2+/3+}$ / V	$E^{\circ\prime}_{bpy\,/\,bpy^{\bullet-}}$ / V
$[Ru(dpp)_2Cl_2]$	0.006 V[b]	-1.77 V, -1.90 V
$[Ru(dpp)_2(Qbpy)](PF_6)_2$	0.503 V[b]	-1.46 V, -1.63 V

[a] All measurements were made in acetonitrile containing 0.1 M TBABP as supporting electrolyte.

[b] Potentials are quoted versus Ag/Ag^+.

2.7 Conclusions

A number of osmium and ruthenium polypyridyl complexes have been synthesised. Purification was performed by recrystallisation from acetone:water solutions and column chromatography. A thorough characterisation of these complexes has been performed using a variety of spectroscopic and chromatographic techniques. Elemental analysis was employed to confirm the % content of carbon, nitrogen and hydrogen. The oxidation and reduction potentials of each redox-active complex was found using electrochemistry.

The osmium complexes described in Sections 2.3 and 2.4 exhibit properties which make them ideal for the study of ground and excited state electron transfer. Both display well – defined electrochemical responses and a characteristic emission from a bpy-based MLCT state. It is also possible to probe the electronic structure of the complexes using UV-Vis spectroscopy. The emission spectra of both $[Os(bpy)_2(bpe)_2](PF_6)_2$ and $\{[Os(bpy)_2(bpe)_2][Os(bpy)_2Cl]_2\}(PF_6)_4$ show that emission in both complexes occurs from the same $[Os(bpy)_2(bpe)_2]^{2+}$ centre. However the emission intensity of the trimetallic complex is drastically reduced, indicating that the emission is quenched. In Chapter 3, we will use transient laser spectroscopy and single photon counting to probe the emission lifetime of the complexes and provide an estimate of the rate of electron-transfer quenching of the emissive state. Monolayers of $[Os(bpy)_2(bpe)_2](PF_6)_2$ will be used to determine the rate of ground state heterogeneous electron transfer. Comparing the rate of ground and photo-excited electron transfer, will allow the extent of electronic coupling across a ligand bridge in the instance where it links two metal centres, and in that where the identical bridge links a metal centre to an electrode, to be compared.

Similarly, $[Ru(dpp)_2(Qbpy)](PF_6)_2$ displays ideal, reversible electrochemical responses and a highly emissive MLCT excited state. Although it has been shown that the $[Ru(dpp)_2(Qbpy)](PF_6)_2$ material contains 10% impurities, these are not visible in the cyclic voltammetry data. This indicates that they are either not redox active, or are present in such small amounts, that they do not interfere with the electrochemical properties of the $[Ru(dpp)_2(Qbpy)](PF_6)_2$ material. Monolayers of this species will be used to probe the ground state electron transfer dynamics of this complex. The emission lifetime of the complex will also be fully investigated and the suitability of the

complex for the *direct* determination of the excited state redox potentials of the complex via a combination of laser excitation and high – speed cyclic voltammetry will be explored.

REFERENCES

(1) Balzani, V.; Scandola, F. in "Comprehensive Supramolecular Chemistry Vol. 10 – Supramolecular Technology", Eds. Atwood, J.L.; Davies, E.D.D.; MacNicol, D.D.; Vögtle, F. Pergamon Press, London, **1996**.

(2) Kalyanasundaram, K. *Coord. Chem. Rev.* **1982**, *46*, 159.

(3) Demas, J. N.; DeGraff, B. A. *Coord. Chem. Rev.* **2001**, *211*, 317.

(4) Chidsey, C. E. D. *Science* **1991**, *251*, 919.

(5) Tender, L.; Carter, M. T.; Murray, R. W. *Anal. Chem.* **1994**, *66*, 3173.

(6) Sikes, H. D.; Smalley, J.; Dudek, S. P.; Cook, A. R.; Newton, M. D.; Chidsey, C. E. D.; Feldberg, S. W. *Science* **2001**, *291*, 1519.

(7) Sumner, J. J.; Creager, S. E. *J. Phys. Chem. B.* **2001**, *105*, 8739.

(8) Acevedo, D.; Abruña, H. *J. Phys. Chem.* **1991**, *95*, 9590.

(9) Forster, R. J.; Faulkner, L. R. *J. Am. Chem. Soc.* **1994**, *116*, 5444.

(10) Forster, R. J. *Inorg. Chem.* **1996**, *35*, 3394.

(11) Forster, R. J.; Figgemeier, E.; Loughman, P.; Lees, A.; Hjelm, J.; Vos, J. G. *Langmuir* **2000**, *16*, 7871.

(12) Forster, R. J.; Loughman, P.; Keyes, T. E. *J. Am. Chem. Soc.* **2000**, *122*, 11948.

(13) Powers, M. J.; Meyer, T. J. *J. Am. Chem. Soc.* **1980**, *102*, 1289.

(14) Schanze, K. S.; Neyhart, G. A.; Meyer, T. J. *J.Phys. Chem.* **1986**, *90*, 2182.

(15) Fischer, H.; Tom, G. M.; Taube, H. *J. Am. Chem. Soc.* **1976**, *98*, 5512.

(16) De Cola, L.; Balzani, V.; Barigelletti, F.; Flamigni, L.; Belser, P.; von Zelewsky, A.; Frank, M.; Vögtle, F. *Inorg. Chem.* **1993**, *32*, 5228.

(17) Arana, C. R.; Abruña, H. D. *Inorg. Chem.* **1993**, *32*, 194.

(18) Zahavy, E.; Fox, M. A. *Chem. Eur. J.* **1998**, *4*, 1647.

(19) Richter, M. M.; Brewer, K. J. *Inorg. Chem.* **1993**, *32*, 5762.

(20) Molnar, S. M.; Nallas, G.; Bridgewater, J. S.; Brewer, K. J. *J. Am. Chem. Soc.* **1994**, *116*, 5206.

(21) Balzani, V.; Juris, A.; Venturi, M.; Campagna, S.; Serroni, S. *Chem. Rev.* **1996**, *96*, 759.

(22) Christian, G. D. "Analytical Chemistry", 5th Ed., Wiley, New York, **1994**.

(23) Meyer, T. J. *Prog. Inorg. Chem.* **1983**, *30*, 389.

(24) Barigelletti, F.; Flamigni, L.; Balzani, V.; Collin, J-P.; Sauvage, J-P.; Sour A.; Constable, E. D.; Thompson, J. *J. Am. Chem. Soc.* **1994**, *116*, 7692.

(25) Kaifer, A. E.; Gómez-Kaifer, M. "Supramolecular Electrochemistry", Wiley – VCH, Weinheim, **1999**.

(26) Juris, A.; Balzani, V.; Barigelletti, F.; Campagna, S.; Belser, P.; Von Zelewsky, A. *Coord. Chem. Rev.* **1988**, *84*, 85.

(27) Rodriguez, M.; Bard, A. J. *Anal. Chem.* **1990**, *62*, 2658.

(28) Bard, A. J.; Faulkner, L. R. "Electrochemical Methods: Fundamentals and Applications", 2nd Ed., Wiley, New York, **2001**.

(29) Morrison, R. T.; Boyd, R. N. "Organic Chemistry", 6th Ed., Prentice Hall, New Jersey, **1992**.

(30) De Armond, M. K.; Carlin, C. M. *Coord. Chem. Rev.* **1981**, *36*, 325.

(31) Nallas, G. N. A.; Jones, S. W.; Brewer, K. J. *Inorg. Chem.* **1996**, *35*, 6974.

(32) Bierig, K.; Morgan, R. J.; Tysoe, S.; Gafney, H. D.; Strekas, T. C.; Baker, A. D. *Inorg. Chem.* **1991**, *30*, 4898.

(33) Huheey, J. E.; Keiter, E. A.; Keiter, R. L. "Inorganic Chemistry: Principles of Structure and Reactivity", 4th Ed., Harper Collins College Publishers, New York, **1993**.

Chapter 3

Ground vs. Excited State Electron Transfer: Adsorbed Monolayers and Trimers in Solution

"Discovery consists of seeing what everybody has seen and thinking what nobody has thought"

Albert Szent-Georgyi

3.1 Introduction

As discussed in the literature review in Chapter 1 of this thesis, electron transfer reactions are of great importance to nearly every sub-discipline of chemistry.[1] It has been demonstrated that electron transfer reactions play pivotal roles in areas as diverse as dye sensitisation for solar energy conversion,[2] information storage[3] and artificial photosynthesis.[4,5] Electronically excited states, created upon absorption of a photon, play pivotal roles in many of these applications. As such, there is widespread interest in the investigation of the factors controlling electron transfer in molecular electronic systems, within both ground and electronically excited states.[6,7] This chapter presents an investigation into the electrochemistry, photophysics and ultimately, the rates of electron transfer quenching of photoexcited states within a novel osmium trimer complex, $\{[Os(bpy)_2(bpe)_2][Os(bpy)_2Cl]_2\}^{4+}$ (Scheme 3.1), where bpy is 2,2'-bipyridyl and bpe is *trans* –1,2-bis-(4-pyridyl)ethylene. Also detailed here are the heterogeneous kinetics of related osmium monomers $[Os(bpy)_2(bpe)_2]^{2+}$ and $[Os(bpy)_2(bpe)$ pyridine$]^{2+}$ (Scheme 3.1) adsorbed as a monolayer onto platinum microelectrodes. These monomers are linked to the electrode via the same bpe bridging ligand that links the osmium centres in the trimer complex. Using the same bridging ligand allows the comparison of photoinitiated (excited state) homogeneous electron transfer within metal centres in a supramolecular species, with ground state heterogeneous electron transfer between a monolayer and the electrode to which it is adsorbed.

As discussed in Section 1.3 of Chapter 1, in the investigation of ground state electron transfer reactions, there has been a focus on the use of monolayers of surface-active osmium polypyridyl complexes immobilised on microelectrodes.[6,8,9] This is due to their ability to spontaneously form highly ordered monolayers and their well-defined, reversible electrochemical responses.

In the context of studies of electron transfer to and from electronically excited states, ligand – bridged dimeric polypyridyl complexes of ruthenium and osmium are well suited, because the redox sites are held in a well-defined geometry to one another (depending on the bridging ligand structure) and they exhibit facile, reversible electrochemical responses.[10] Considerable investigations into electron transfer between metal centres have been carried out utilising both dimeric homo- and hetero-metallic complexes of osmium, ruthenium and other metals such as rhenium, iridium and

rhodium and some comprehensive reviews on the subject are available.[7,11,12] Most notable is the research of Meyer and various authors, who have extensively investigated the electron transfer properties of homo-metallic dimers of osmium[10,13] and ruthenium,[14,15] bridged using polypyridyl-type ligands, with particular emphasis on the observation of intramolecular electron transfer quenching in mixed – valence dimers. They have observed reductive electron-transfer quenching of a bpy based excited state within an osmium-osmium dimeric complex with 4,4'-dipyridyl and 1,2-bis(4-pyridyl)ethane bridging ligands.[10] The rate constant for this electron transfer quenching is estimated to be of the order of 10^7 s^{-1}, based on transient emission spectroscopy results. Related work has shown that the likelihood of electron transfer in such dimeric species is enhanced by having the metal centres as close together as possible, e.g., by controlling the length of the bridging ligand employed.[14]

Balzani and co-workers have also carried out considerable investigations into electron transfer in ruthenium and osmium dimers[7,16,17] and their research has shown that the electrochemical and photophysical properties of these dimers depend heavily on the type of bridging ligand used. In particular, they have observed direct intramolecular electron transfer quenching of emission from the Ru(II) centre by the Os(III) centre in a mixed – valence Ru – Os dimer.[17] The rate constant for this quenching reaction is of the order of 10^6 s^{-1}.

Forster and Keyes have compared the rates of electrochemical and photoinduced electron transfer within a dimeric complex of $[p0p\ Os(bpy)_2\ 4\text{-}tet\ Os(bpy)_2Cl]^{3+}$, where p0p is 4,4'-bipyridyl, bpy is 2,2'-bipyridyl and 4-tet is 3,6-bis(4-pyridyl)-1,2,4,5-tetrazine.[18] By forming spontaneously adsorbed monolayers of this complex onto platinum microelectrodes, the rate constant for the heterogeneous electron transfer has been determined using high-speed chronoamperometry. Transient emission spectroscopy has allowed the determination of the rate constant for photoinduced electron transfer quenching (PET) within the metal complex. The results show that the rate constant for PET is faster than that for ground state electron transfer at the same driving force and that the strength of electronic coupling across the tetrazine bridge is significantly greater for two metal centres than for a metal electrode and a remote redox moiety.

Recent reports in the literature have shown that trimetallic complexes of osmium and ruthenium can function as useful photonic molecular devices. Zahavy and Fox have reported on the use of an osmium – nickel – palladium complex as an electro-switchable-photoinduced-electron-transfer device (ESPET).[19] Brewer and co-workers have extensively investigated the properties of trimeric hetero-metallic osmium, ruthenium and iridium polypyridyl complexes.[20,21] They have synthesised a ruthenium – iridium – ruthenium complex (c.f. Figure 1.1.3) which functions as a device for photoiniated electron collection, whereby the bridging ligands linking the two ruthenium centres to the iridium core are photoreduced by one electron and the electrons are delivered to a substrate.[22] This complex has been shown to act as a catalyst for the reduction of carbon dioxide to formate.[23] Abrana and Abruña have reported on a series of trimetallic complexes of ruthenium and osmium bridged with the ligand tetra-2-pyridyl-1,4-pyrazine (tppz). They have found that the tppz ligand allows the rapid construction of transition metal complexes with electronic properties that are attractive for constructing molecular wires.[24]

While many of these reports investigate the mechanisms of electron transfer between metal centres in a trimer complex, there is little mention of the measurement of the rates of these electron transfers, or the elucidation of the driving forces behind electron transfer to and from excited states created within these molecular species by the absorption of a photon. Transition metal trimer complexes of this kind make useful probes to investigate photoinduced electron transfer, as they are exhibit well-defined electrochemical and spectroscopic behaviour. Also, when compared to dimeric species, the synthesis of these complexes is relatively simple and they require minimal purification following the initial synthetic step.

Scheme 3.1 Schematic representation of a monomeric osmium compound used in this study. Refer to Scheme 2.1 for the other monomeric and trimeric osmium compounds utilised.

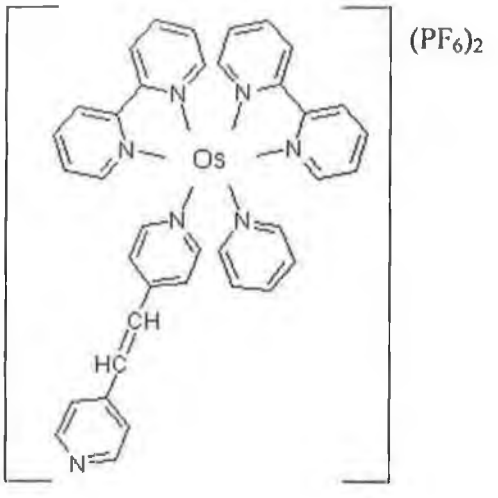

[Os(bpy)$_2$ bpe pyridine](PF$_6$)$_2$

3.2 Apparatus

Ultraviolet-visible spectra were recorded using a Shimadzu UV-3100 diode array spectrometer. Room temperature emission spectra were recorded using a Perkin Elmer LS50 B luminescence spectrometer, equipped with a red sensitive Hamamatsu R928 detector. Samples were prepared at concentrations of 10^{-4} to 10^{-5} M in spectroscopic grade butyronitrile. For room temperature measurements, 1 cm quartz cells were used. The excitation and emission slits were 2 nm for all experiments.

Luminescent lifetimes and low temperature emission spectra for the monomeric complexes were measured using the third harmonic (355 nm) of a Spectron Q-switched Nd-YAG laser for excitation. Emission was detected in a right-angled configuration to the laser using an Oriel model IS520 gated intensified CCD coupled to an Oriel model MS125 spectrograph. With suitable signal averaging, this configuration allows a complete emission spectrum (spectral range 250 nm) to be obtained within times as short as 10 ns. The emission spectra were typically recorded using the average of twenty laser shots. The gatewidth, i.e., the exposure time of the CCD, was never more than 5% of the excited state lifetime. The step size, i.e., the time between the acquisition of discrete spectra, was typically 5 % of the excited state half-life.

The excited state lifetime of the trimer was determined using an Edinburgh Analytical Instruments Single Photon Counter in a T setting using J – ya monochromators. The light source in this system is an nF 900 Nanosecond Flashlamp filled with nitrogen, with a profile of 1 ns. The detector is a Single Photon Photomultiplier Detection system, Model S300, with a Norland N5000 MCA card and a Cd900 serial PC interface. The program used for the data correlation and manipulation is an F900 program, Version 5.13. The excitation wavelength was 337 nm and the lifetimes were collected and determined by analysing the emission decay at λ_{max}.

Dilute solutions of the complex in acetonitrile (298 K) or butyronitrile (77K) (10^{-4} to 10^{-5} M) were de-aerated for 20 minutes under nitrogen prior to use. Low temperature emission lifetime studies were carried out using an Oxford Instruments gas-exchange cryostat equipped with an ITC502 temperature controller. Standard iterative techniques were employed to determine the lifetimes of emission.[25]

Cyclic voltammetry was performed using a CH Instruments Model 660A Electrochemical Workstation and a conventional three-electrode cell. All solutions were degassed thoroughly using argon, and a blanket of argon was maintained over the solution during all experiments. Potentials are quoted with respect to a CH Instruments Ag/AgCl reference electrode filled with saturated KCl which had a potential of +0.190 V with respect to the normal hydrogen electrode. The potential of the ferrocene/ferrocenium couple at this electrode was 0.340 V. All experiments were performed at room temperature (22±3 °C).

Microelectrodes were fabricated from platinum microwires of radii between 2.5 and 50 μm (Goodfellows Metals Ltd.) by sealing them in soft glass using a procedure described previously.[26] Microdisk electrodes were exposed by removing excess glass using 600 grit emery paper, followed by succesive polishing with 12.5, 5, 1, 0.3 and 0.05 μm alumina. The polishing material was removed between changes of particle size by sonicating the electrodes in deionised water for at least 1 minute. Electrochemical cleaning of the electrodes was carried out by cycling in 0.1 M H_2SO_4 between potential limits chosen to initially oxidize and then reduce the surface of the platinum electrode. Excessive cycling was avoided in order to minimize the extent of surface roughening. The real surface area of the electrodes was determined by calculating the charge under the platinum oxide reduction peak.[27] Typically surface roughness values were between 1.6 and 2.0. Determining the real, as opposed to the geometric area of the electrodes is important if the area of occupation of the adsorbate is to be accurately determined. The final step in the cleaning procedure was repetitive cycling between – 0.2 and + 1.0 V in 0.1 M $LiClO_4$ until hydrogen desorption was complete and a flat background was obtained.[28]

Spontaneously adsorbed monolayers of $[Os(bpy)_2(bpe)_2]^{2+}$ and $[Os(bpy)_2$ bpe pyridine$]^{2+}$ were formed *in-situ* using a 50 μM solution of the metal complex in the electrolyte solution. A low concentration of the surface-active complex in solution minimizes the diffusional contribution to the overall current in chronoamperometry or cyclic voltammetry and improves the stability of the monolayers. The complex is stable towards aerial oxidation and no precautions were taken to exclude atmospheric oxygen during monolayer formation.

3.3 Materials

The synthesis of $[Os(bpy)_2(bpe)_2]^{2+}$ and $\{[Os(bpy)_2(bpe)_2][Os(bpy)_2Cl]_2\}^{4+}$ is described in Chapter 2. $[Os(bpy)_2$ bpe pyridine$]^{2+}$ was available from a previous study and was used following confirmation of purity by cation – exchange HPLC and ^1H – NMR.

3.4 Results and discussion

3.4.1 Photoinduced Charge Transfer

Spontaneously adsorbed and self-assembled monolayers that incorporate redox active centres provide important insights into the energetics and dynamics of electron transfer. In particular, tunnelling across an organic bridge, e.g., an alkane chain, that links the continuum of states in the electrode and the localised molecular orbitals of the redox centres, has been investigated in considerable detail.[29,30,31] However, relatively few studies have compared this situation with the dynamics of photoinduced electron transfer between two molecular components across the same bridge. For example, by comparing the rates of photochemically and electrochemically triggered electron transfer across the *trans*–1,2-bis-(4-pyridyl)ethylene bridge, insight can be obtained into the effect of swapping an electronically localized redox centre for an electronically delocalized metal electrode on the strength of electronic coupling. Here, this issue is probed by considering photo induced charge transfer within a trimeric metal complex, $\{[Os(bpy)_2(bpe)_2][Os(bpy)_2Cl]_2\}^{4+}$ and comparing the behaviour with that found for ground state electron transfer across a monolayer/electrode interface.

3.4.1.1 UV-Vis Absorption Spectroscopy

The recording of an ultraviolet-visible spectrum of a transition metal complex traditionally provides insights into the electronic transitions within the complex. In a complex containing more than one metal centre, such as the trimetallic species considered here, a comparison of the absorption spectrum of the complex with that of the parent monomeric species can provide an insight into the extent of electronic coupling between the metal centers.[10,32]

Figure 3.1 illustrates the UV-visible absorption spectra of $[Os(bpy)_2(bpe)_2]^{2+}$ and $\{[Os(bpy)_2(bpe)_2][Os(bpy)_2Cl]\}^{4+}$ in deoxygenated acetonitrile at 298 K. The spectrum of an $[Os(bpy)_2$ bpe $Cl]^{1+}$ complex is also shown to allow the degree of electronic coupling between the $Os(bpe)_2$ metal centre and the two peripheral Os(bpe)Cl centres to be determined. All complexes exhibit intense bands representing ligand-based $\pi \rightarrow \pi^*$ transitions in the high-energy UV region of the spectrum and metal-to-ligand charge transfer (MLCT) bands in the low-energy visible region. These absorption

bands are typical of the UV-Vis spectra of osmium and ruthenium polypyridyl complexes.[7,33] $[Os(bpy)_2(bpe)_2]^{2+}$ exhibits two bands in the visible region of the spectrum at 395 and 480 nm, which correspond to $d\pi(Os^{II}) \rightarrow \pi^*(bpe)$ and $d\pi(Os^{II}) \rightarrow \pi^*(bpy)$ MLCT, respectively.[13] The spectrum of $[Os(bpy)_2$ bpe $Cl]^{1+}$ also contains two MLCT bands, at 440 and 500 nm, which are again due to $d\pi(Os^{II}) \rightarrow \pi^*(bpe)$ and $d\pi(Os^{II}) \rightarrow \pi^*(bpy)$ MLCT.[13]

The trimer spectrum is a composite of the absorption bands of the component monolayers, indicating that the metal centres within the trimer are at best weakly interacting.[10,13] The visible portion of the spectrum is dominated by $d\pi(Os^{II}) \rightarrow \pi^*(bpe)$ and $d\pi(Os^{II}) \rightarrow \pi^*(bpy)$ MLCT transitions at the $[Os(bpy)_2(bpe)_2]^{2+}$ and $[Os(bpy)_2$ bpe $Cl]^+$ centres, but there are subtle changes in the band shapes and energies of the transitions.[10,34] In the classification system of Robin and Day[35], mixed-valence complexes can be grouped as class I (localised oxidation states, no interaction), class II (localised, with an interaction) and class III (delocalised). If localised, the odd electron is in an orbital on one site. If delocalised, the electron is in a molecular orbital delocalised over both sites and it is not possible to assign integral oxidation states. On the basis of the UV-vis spectral data detailed here, this complex displays Class II behaviour, where the oxidation states are localised, but there is an interaction between them. Strong electronic coupling has been observed in osmium dimers, for example, Taube et al. have observed a series of sharp bands in the near-infrared spectrum of $[(NH_3)_5Os^{II.5}\text{-}(N_2)\text{-}Os^{II.5}(NH_3)_5]^{5+}$ arising from transitions between delocalised molecular levels.[36] However, Meyer et al. has observed similar UV-vis behaviour to that reported here in mixed-valence dimers of osmium and/or ruthenium linked by a range of polypyridyl bridging ligands, including the same bpe bridging ligand as reported on here, i.e., the spectra of the dimers are a composite of the parent monomer species, but with subtle shifts in shape and the energy of the bands.[13,14,15] This result indicates that the dominant behaviour of mixed-valence complexes bridged by the bpe ligand is described as Class II. The overall conclusion to be drawn from this discussion is that the UV-vis spectral properties of the $[Os(bpy)_2(bpe)_2]^{2+}$ complex are relatively unaffected by binding to the two $[Os(bpy)_2Cl]$ centres and hence, little electronic communication is exhibited between the redox centres in the trimer complex.

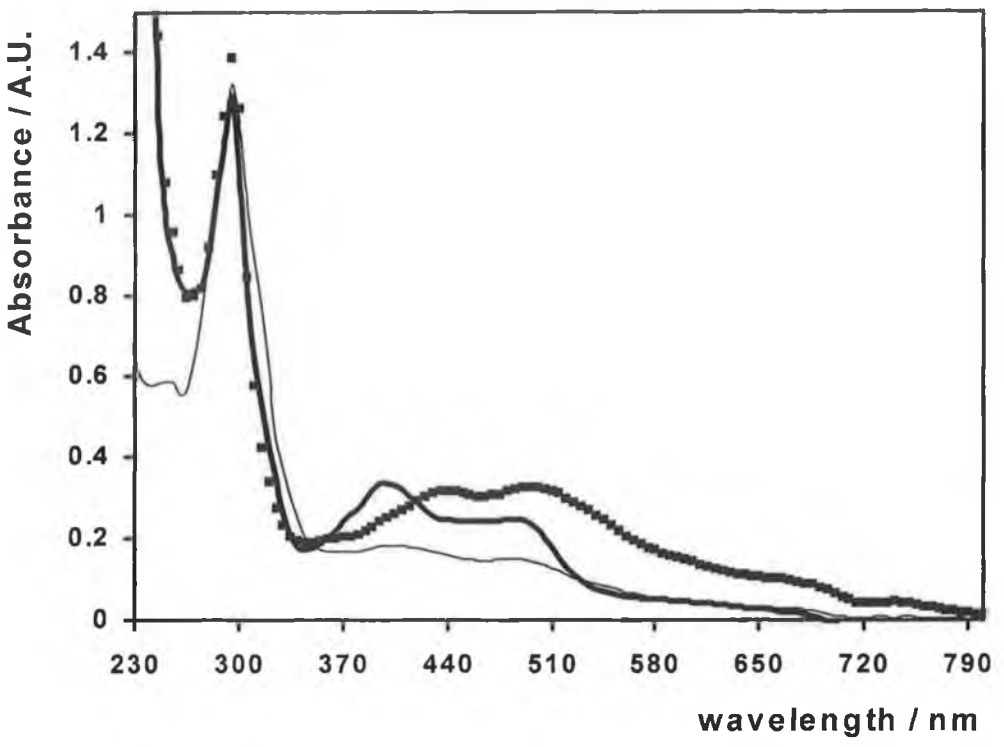

Figure 3.1 Overlaid UV-vis spectra of 2×10^{-5} M $[Os(bpy)_2\ bpe\ Cl]^+$ (thin line), $\{[Os(bpy)_2(bpe)_2][Os(bpy)_2Cl_2]\}^{4+}$ (solid squares) and $[Os(bpy)_2(bpe)_2]^{2+}$ (thick line). In all cases the solvent is deoxygenated butyronitrile.

3.4.1.2 Emission Spectroscopy

Figure 3.2 shows emission spectra for $[Os(bpy)_2(bpe)_2]^{2+}$ and $\{[Os(bpy)_2(bpe)_2][Os(bpy)_2Cl]_2\}^{4+}$ at room temperature in deoxygenated butyronitrile. The observation that the $[Os(bpy)_2\ (bpe)_2]^{2+}$ complex is highly luminescent is consistent with the known photophysical properties of $[Os(N)_6]^{2+}$ complexes, where N represents a nitrogen donor such as bpy.[32] In contrast, $[Os(N)_5Cl]^+$ complexes are only weakly emissive, even at liquid nitrogen temperatures, due to vibrational interactions which provide a fast non-radiative decay pathway.[37] Therefore, we do not expect to observe emission from the $[Os(bpy)(bpe)Cl]^+$ centres in the trimer. Within experimental error, the complexes exhibit the same emission wavelength. This suggests that emission in both species is originating from the same chromophore, namely the $[Os(bpy)_2(bpe)_2]^{2+}$ centre, but the trimer exhibits less than 2% of the intensity shown by the corresponding emitting centre in the monomer complex, $[Os(bpy)_2(bpe)_2]^{2+}$. The observation that the emission intensity is dramatically lower for the trimer than the model $[Os(bpy)_2(bpe)_2]^{2+}$ complex suggests that the $[Os(bpy)_2Cl]^+$ centres play an important role in quenching the luminescence of the electronically excited $[Os(bpy)_2(bpe)_2]^{2+*}$ centre within the trimer.

Emission spectra for monomer and trimer were obtained at 80 K in butyronitrile glass. The spectra are displayed in Figure 3.3 with the axes normalised to illustrate the similarity of the maximum emission wavelength of both complexes, again demonstrating that emission occurs from the $[Os(bpy)_2(bpe)_2]^{2+}$ centre in both the trimer and the monomer species. An estimate of the relative intensities of the two emissions is made difficult due to the need to significantly increase the signal gain of the iCCD to improve signal to noise ratios in the capture of the trimer spectra, but based on the room temperature results, it is expected that the emission of the trimer will again be less intense than that of the monomer. The low temperature emission spectrum of the trimer may be used to calculate $E^{0\text{-}0}$, the energy difference between the lowest vibrational level of the ground and excited states. The value of $E^{0\text{-}0}$, as obtained from the wavelength of maximum emission at 80 K (737 nm) is 1.68 eV.

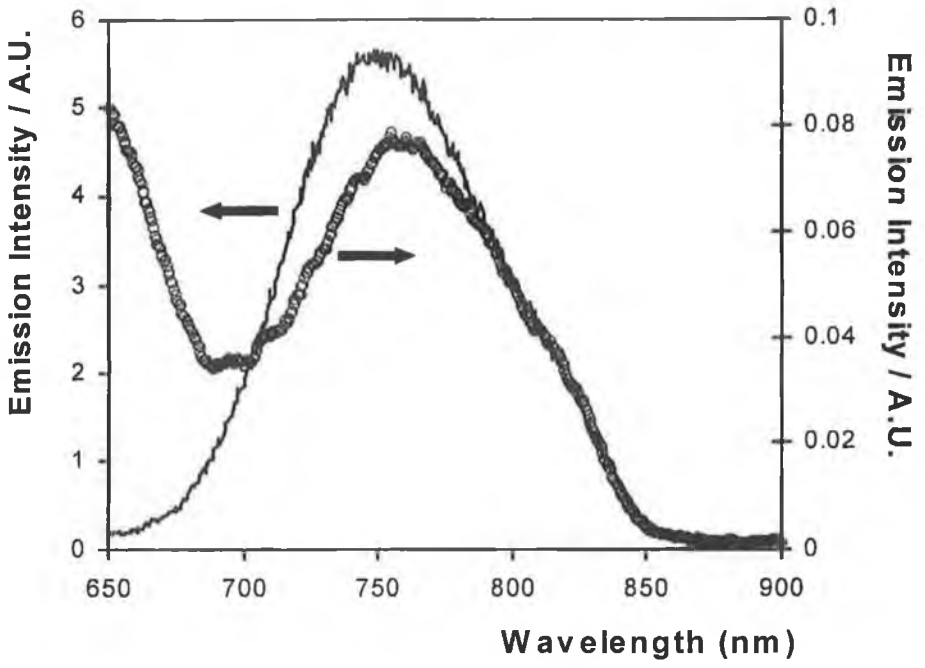

Figure 3.2 Emission spectra at 298 K of $[Os(bpy)_2(bpe)_2]^{2+}$ (solid line) and $\{[Os(bpy)_2(bpe)_2][Os(bpy)_2Cl_2]\}^{4+}$ (open circles). In both cases the solvent is deoxygenated butyronitrile and the solutions are 1×10^{-5} M. Both spectra were processed using a 5-point moving average smooth.

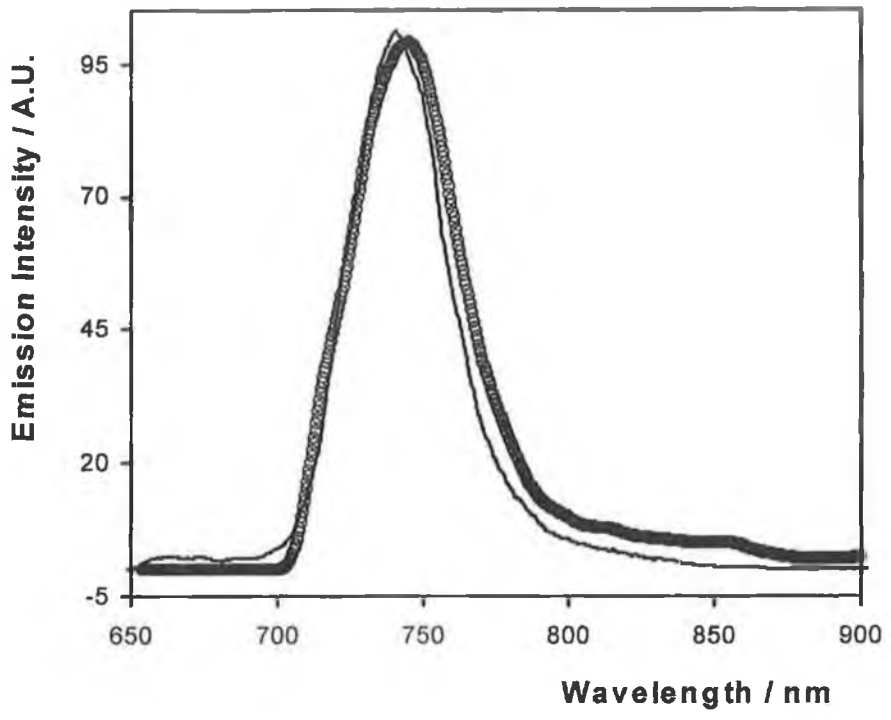

Figure 3.3 Emission spectra at 80 K of $[Os(bpy)_2(bpe)_2]^{2+}$ (solid line) and $\{[Os(bpy)_2(bpe)_2][Os(bpy)_2Cl_2]\}^{4+}$ (open circles). In both cases the solvent is deoxygenated butyronitrile and the solutions are 1×10^{-5} M. Both spectra were processed using a 5-point moving average smooth. In both cases, the emission is normalised to 100 % at λ_{max}.

The fluorescence lifetime of a substance represents the average amount of time the species remains in the excited state prior to its return to the ground state. Fluorescence is typically a unimolecular process and therefore the excited state population established by an impulse of exciting light will generally decay exponentially according to first order kinetics.[38] In these experiments the lifetime of the complex is estimated by monitoring the decay of emission as a function of time and plotting the natural log of emission versus time. The lifetime (τ) may be determined from the slope as follows:

$$\ln(I/I_O) = -kt \qquad (3.1)$$

$$k = 1/\tau \qquad (3.2)$$

The emission lifetime of $[Os(bpy)_2(bpe)_2]^{2+}$ was obtained in deoxygenated butyronitrile at a range of temperatures from 80 to 298 K using transient laser spectroscopy. Figure 3.4 details the emission decay observed at 80 K in butyronitrile glass. The lifetime of the emission is the inverse of the slope of the semilog plot in the inset of Figure 3.4 and at 80 K is 550 $\pm$ 12 ns.

A list of the lifetimes obtained over the full temperature range is detailed in Table 3.1 and demonstrates that as temperature increases, the emission lifetime decreases. This change may be attributed to (a) an activated surface crossing to another excited state (usually from ^{3}MLCT to ^{3}MC) or (b) the role of vibrational modes that favour radiationless decay.[39] These vibrational modes are prevented at low temperature because of the frozen molecular environment. An Arrhenius plot of the lifetime data shown in Figure 3.5 clearly illustrates an inflection point at approximately 100 – 200 K (the melting point[40] of the butyronitrile solvent is 161 K).

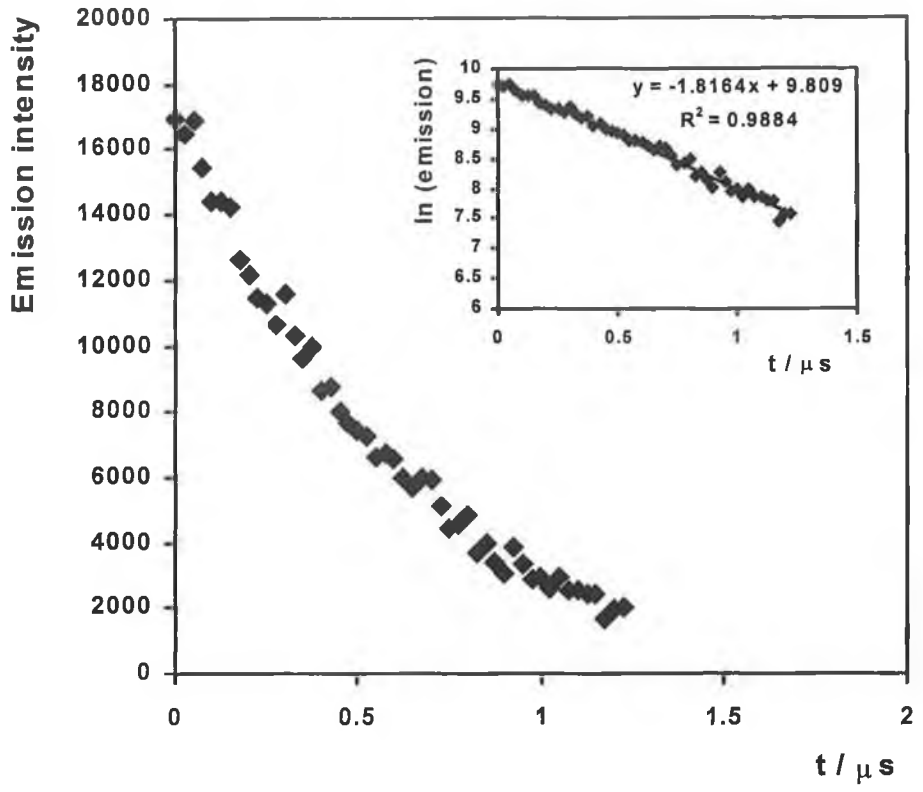

Figure 3.4 Emission decay for 1×10^{-5} M $[Os(bpy)_2(bpe)_2]^{2+}$ obtained in deoxygenated butyronitrile glass at 80 K using transient emission spectroscopy. The excitation wavelength is 355 nm and the detection wavelength is 737 nm. Inset: semilog plot of the decay.

Table 3.1 Lifetime versus temperature data for 1×10^{-5} M $[Os(bpy)_2(bpe)_2]^{2+}$ in butyronitrile. The excitation wavelength is 355 nm.

Temperature / K	Lifetime / ns
80	550 ± 12.1
95	450 ± 8.8
110	389 ± 8.9
130	252 ± 6.2
150	216 ± 6.4
165	166 ± 5.8
180	103 ± 5.2
200	75.4 ± 4.1
235	50.9 ± 3.8
275	42.2 ± 3.6
298	40.3 ± 2.4

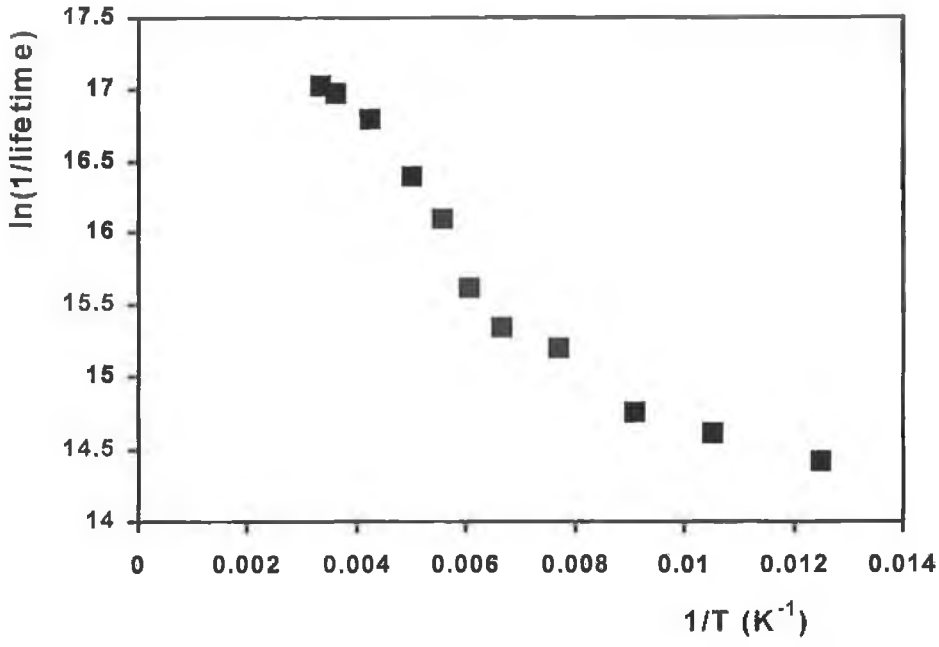

Figure 3.5 Arrhenius plot of ln(k) vs 1/T for 1×10^{-5} M $[Os(bpy)_2(bpe)_2]^{2+}$ in deoxygenated butyronitrile obtained at a range of temperatures from 80 to 298 K using transient emission spectroscopy.

Due to the low emission intensity of the trimer, the signal – to noise ratio of the decays obtained using transient laser spectroscopy was extremely low and therefore compromised the accuracy of this method for determining the emission lifetime of the trimer. To overcome this problem, Time–Correlated Single Photon Counting was used to determine the lifetime of $\{[Os(bpy)_2(bpe)_2][Os(bpy)_2Cl]_2\}^{4+}$ in deoxygenated butyronitrile. This technique counts photons which are time-correlated to the excitation pulse employed, building up a histogram of counts versus time channels, which represents the intensity decay of the sample. TCSPC uses the rising edge of a photoelectron pulse for timing which allows phototubes of nanosecond width to provide subnanosecond resolution and therefore allows lifetimes of nanosecond timescale to be accurately determined. As the method counts individual photons rather than measuring the overall fluorescence intensity as a function of time as in transient laser spectroscopy, it can determine the lifetime of samples with relatively low fluorescence intensity.[41]

The transients obtained are reproduced in Figure 3.6, overlaid with the single exponential fit applied to the data by the instrument's F900 program, following automatic subtraction of the N_2 lamp profile, to obtain the lifetime of the decay. A lifetime of 42.4 $\pm$ 0.6 ns for $[Os(bpy)_2(bpe)_2]^{2+}$ was obtained by this method. This agrees well with that obtained by transient laser spectroscopy (40.3 $\pm$ 12 ns). Significantly, the data reveals that the lifetime of the trimer species is significantly shorter (6.5 $\pm$ 1.4 ns) than that of the monomer (42.4 $\pm$ 0.6 ns). The intensity of the emission is again considerably lessened and this fact, coupled with the lifetime data, leads to the conclusion that the $[Os(bpy)_2$ bpe $Cl]^+$ moiety quenches the excited $[Os(bpy)_2(bpe)_2]^{2+*}$ centre.

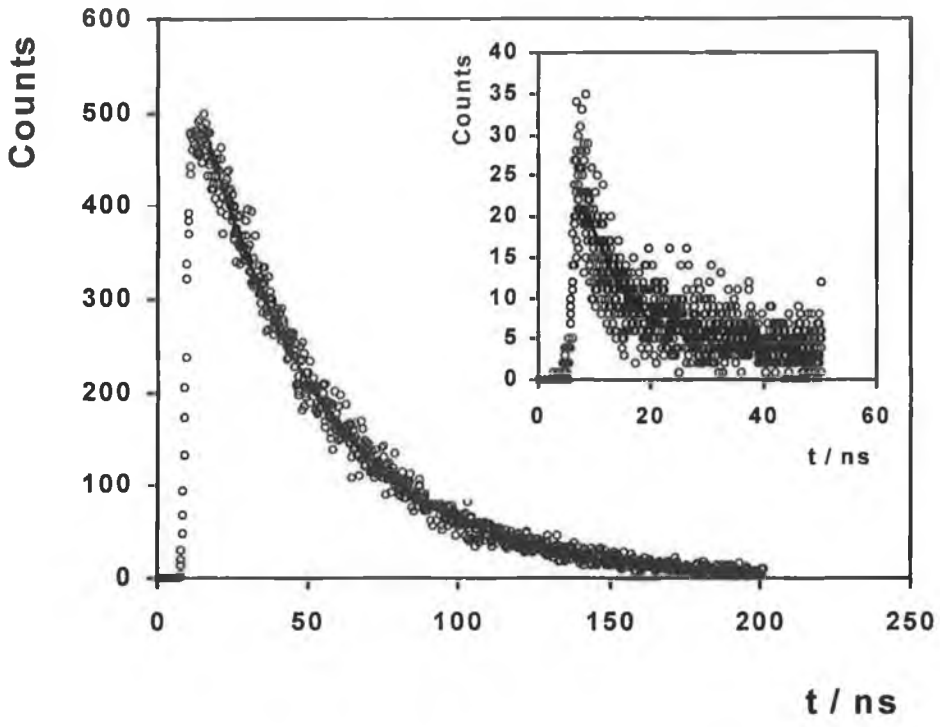

Figure 3.6 Emission transients following correction for the lamp profile for $[Os(bpy)_2(bpe)_2]^{2+}$ and $\{[Os(bpy)_2(bpe)_2][Os(bpy)_2Cl_2]\}^{4+}$ (inset) recorded using time correlated single photon counting (TCSPC) approaches. In both cases the solvent is deoxygenated butyronitrile. χ^2 values are 1.015 and 1.208 for $[Os(bpy)_2(bpe)_2]^{2+}$ and $\{[Os(bpy)_2(bpe)_2][Os(bpy)_2Cl_2]\}^{4+}$, respectively.

In a system of this kind, energy or electron transfer are possible quenching mechanisms.[13,42] However, for efficient Förster energy transfer[43] dipole-dipole coupling must occur, requiring significant overlap of the absorption and emission spectra of the two species. From an examination of the UV-vis and emission spectra detailed in Figures 3.1 and 3.2, the overlap of the emission and absorbance spectra for the $[Os(bpy)_2(bpe)_2]^{2+}$ and $[Os(bpy)_2$ bpe $Cl]^+$ is very weak, given that $\lambda_{max,em}$ and $\lambda_{max,abs}$ are approximately 750 and 450 nm, respectively. Therefore, in common with related systems,[13,18,44] it appears that Förster *energy* transfer involving dipolar coupling is not the dominant quenching mechanism in the trimer. In contrast, *electron* transfer to or from the $[Os(bpy)_2$ bpe $Cl]^+$ to the $[Os(bpy)_2(bpe)_2]^{2+*}$ excited state is the more likely mechanism.

The photoinduced electron transfer rate constant, k_{PET}, can be estimated using Equation 3.3:

$$k_{PET} = \frac{1}{\tau} - \frac{1}{\tau^o} \qquad (3.3)$$

where τ and τ^o are the luminescence lifetimes in the presence and absence of a linked quencher. Inherent in this equation is the assumption that the other nonradiative decay pathways in the monomer and trimer complexes are identical and therefore can be ignored. Using the lifetime values of 6.5±1.4 ns and 42.4±0.6 ns obtained by single photon counting for the lifetimes of the trimer and monomer respectively, yields a rate constant of $1.3\pm0.1 \times 10^8$ s^{-1} at 298 K for this intramolecular charge transfer process, suggesting that quenching takes place efficiently across the 10 Å *trans*-1,2-bis-(4-pyridyl)ethylene bridge. Similar behaviour has been observed in other osmium complexes, notably in $[(bpy)_2(CO)Os\text{-}p2p\text{-}Os(phen)(dppe)Cl]^{3+}$, where bpy is 2,2'-dipyridyl, phen is 1,10-phenanthroline, dppe is 1,2-bis(diphenylphosphino)-*cis*-ethene and the p2p bridging ligand is 1,2-bis(4-pyridyl)ethane.[13] The lifetime of the bpy-based excited state in the complex at 77 K is 45 ns, in comparison to 5430 ns for the parent monomer $[(bpy)_2(CO)Os(p2p)]^{2+}$, yielding a value of 2.2×10^7 s^{-1} for k_{PET}. In contrast, the lifetime of the lower energy phen-based excited state in the complex is indistinguishable from that observed for the $[(phen)(Cl)Os(dppe)(bpa)]^+$ parent monomer (3800 ns at 77 K). From this results, the authors have concluded that

quenching of the bpy excited state occurs via reductive electron transfer from the [Os(phen)(dppe)Cl] centre to the $[(bpy)_2(CO)Os(bpa)]$ emitting centre.

3.4.2 Driving force for Photoinduced Electron Transfer

As it has been shown that electron transfer is the most likely quenching mechanism in the trimer, it is of interest to determine whether the excited state located at the $[(bpy)_2Os(bpe)_2]$ centre is quenched via oxidative or reductive electron transfer from one of the $[(bpy)_2Os(bpe)Cl]$ centres. An estimation of the thermodynamic driving force for the respective electron transfer allows the most energetically favourable electron transfer process to be identified. If the Coulombic stabilisation energy of the products is negligible (typically less than 0.1 eV in polar solvents), then the thermodynamic driving force for electron transfer, $\Delta G°$, can be estimated from the Rehm-Weller equation[45] and the relevant formal potentials:

$$\Delta G° = e[E°(Donor) - E°(Acceptor)] - E^{0-0} \qquad (3.2)$$

where E°(Donor) and E°(Acceptor) are the formal potentials are associated with the donor and acceptor, respectively, and E^{0-0} is the energy difference between the lowest vibrational levels of the ground and excited states. The value of E^{0-0}, as obtained from the wavelength of maximum emission of the trimer at cryogenic temperatures (737 nm) is 1.68 eV. As the reactant and product in the trimer are linked together by the bpe ligand bridge, Equation 3.3 does not need to contain a term which takes into account the work required for the reactants and products to diffuse together to form an association complex. The Rehm-Weller equation can be adapted to determine the redox potentials of the electronically excited states of a complex via the following equations:[46,47]

$$E^{o}_{Ox}{}^{*} = E^{o}_{Ox} - E^{0-0} \qquad (3.4)$$

$$E^{o}_{Red}{}^{*} = E^{o}_{Red} + E^{0-0} \qquad (3.5)$$

where E^{o}_{Red} and E^{o}_{Ox} are the potentials for the first reduction and oxidation, respectively. Equations 3.4 and 3.5 assume that all the spectroscopic energy of the excited state (E^{0-0}) can be used as free energy in the redox process.[46]

The electronically excited state located at the $[Os(bpy)_2\ (bpe)_2]$ centre could be quenched by electron donation from (reductive quenching), or to (oxidative quenching), the $[Os(bpy)_2\ bpe\ Cl]^+$ moiety. In oxidative quenching, the $[Os(bpy)_2\ (bpe)_2]^{2+*}$ moiety acts as the donor while the central $[Os(bpy)_2\ bpe\ Cl]^+$ unit acts as the acceptor:

$$\{(bpy)(bpy^{\bullet-})Os^{III}\text{-}[(bpe)\text{-}Os^{II}(bpy)_2Cl]_2\}^{4+*} \longrightarrow \{(bpy)(bpy)Os^{III}\text{-}[(bpe)\text{-}Os^{I}(bpy)_2Cl]_2\}^{4+}$$

This product then relaxes via charge recombination to give the ground state complex $\{(bpy)_2Os^{II}\text{-}[(bpe)\text{-}Os^{II}(bpy)_2Cl]_2\}^{4+}$.

In order to calculate $\Delta G°$, $E°_{Ox}$ and $E°_{Red}$ must be known for the $[Os(bpy)_2(bpe)_2]^{2+}$ and $[Os(bpy)_2\ bpe\ Cl]^+$ complexes, respectively. Figure 3.7 illustrates a solution phase cyclic voltammogram of the trimer complex, $\{[Os(bpy)_2(bpe)_2][Os(bpy)_2Cl]_2\}^{4+}$, overlaid with that of $[Os(bpy)_2(bpe)_2]^{2+}$. $[Os(bpy)_2(bpe)_2]^{2+}$ demonstrates one reversible metal-based oxidation at 0.830 V, consistent with an osmium complex containing six N-donor ligands.[48,49] $\{[Os(bpy)_2(bpe)_2][Os(bpy)_2Cl]_2\}^{4+}$ exhibits two oxidations at 0.427 and 0.838 V. The redox peak at 0.427 V has approximately twice the area of the peak at 0.838 V, indicating that the two $[Os(bpy)_2Cl]^+$ centres are the first to be oxidised. This is expected on the basis of the known strong σ-donating properties of the chloride ligand.

It is interesting to note that the formal potential of the $[Os(bpy)_2(bpe)_2]^{2+}$ oxidation is not significantly changed upon binding to the two $[Os(bpy)_2Cl]^+$ centres in the trimer complex, indicating that minimal electrostatic interactions exist within the complex.[7,24] If there was strong electronic communication between the $[Os(bpy)_2(bpe)_2]^{2+}$ and $[Os(bpy)_2Cl]^+$ centres through the bpe bridge, the formal potential of the $[Os(bpy)_2(bpe)_2]^{2+}$ metal centre would be expected to shift in a negative potential direction due to the presence of the electron-donating chloro ligand on the $[Os(bpy)_2Cl]^+$. The lack of a significant shift, in conjunction with the UV-vis spectroscopic results detailed earlier, indicates that the osmium centres in this complex are not strongly coupled.

Knowledge of the formal potentials of the osmium centres within the complexes allows $\Delta G°$ for oxidative quenching to be calculated according to Equation 3.3. As shown in Table 3.2, the first reduction potential of the $[Os(bpy)_2\ bpe\ Cl]^+$ complex is at –1.52 V corresponding to the bpy/bpy$^{\bullet -}$ couple. Therefore, according to Equation 3.2, $\Delta G°_{Ox}$ is approximately +0.68 eV. The observation that oxidation of the $[Os(bpy)_2\ (bpe)_2]^{2+*}$ centre is highly endergonic makes this quenching pathway unlikely.

In reductive quenching, the $[Os(bpy)_2\ bpe\ Cl]^+$ moiety acts as the donor while the central $[Os(bpy)_2\ (bpe)_2]^{2+*}$ unit acts as the acceptor:

$$\{(bpy)(bpy^{\bullet -})Os^{III}\text{-}[(bpe)\text{-}Os^{II}(bpy)_2Cl]_2\}^{4+*} \longrightarrow \{(bpy)(bpy)Os^{II}\text{-}[(bpe)\text{-}Os^{III}(bpy)_2Cl]_2\}^{4+}$$

Figure 3.7 and Table 3.2 show that $E°_{Ox}$ for the $[Os(bpy)_2\ bpe\ Cl]^+$ fragment within the trimer is +0.427 V. While the voltammetric response corresponding to reduction of the bipyridyl ligands of the trimer is less well defined than the oxidation response illustrated in Figure 3.7, these voltammograms reveal that $E°_{Red}$ for the trimer is approximately –0.950 V. In conjunction with Equation 3.2, these values yield a $\Delta G°_{Red}$ value of approximately -0.3 eV.

The observation that oxidative quenching is thermodynamically uphill by approximately 0.68 eV, while reductive quenching is exergonic by approximately 0.3 eV, suggests that the electronically excited state is quenched by electron transfer from the $[Os(bpy)_2\ Cl]^+$ moiety across the bpe bridge to the electronically excited $[Os(bpy)_2\ (bpe)_2]^{2+*}$ centre. As stated in the previous section, the conclusion that reductive electron transfer is responsible for the observed quenching of the $[Os(bpy)_2(bpe)_2]^{2+*}$ electronically excited state, is consistent with previous reports describing electron transfer quenching in osmium and ruthenium dimers linked by similar polypyridyl bridging ligands.[13,14] Beyond providing an insight into the quenching mechanism, knowledge of the driving force for photoinduced electron transfer allows the electron transfer rate constants for optically and electrochemically driven processes to be compared. This will be described in later in this chapter.

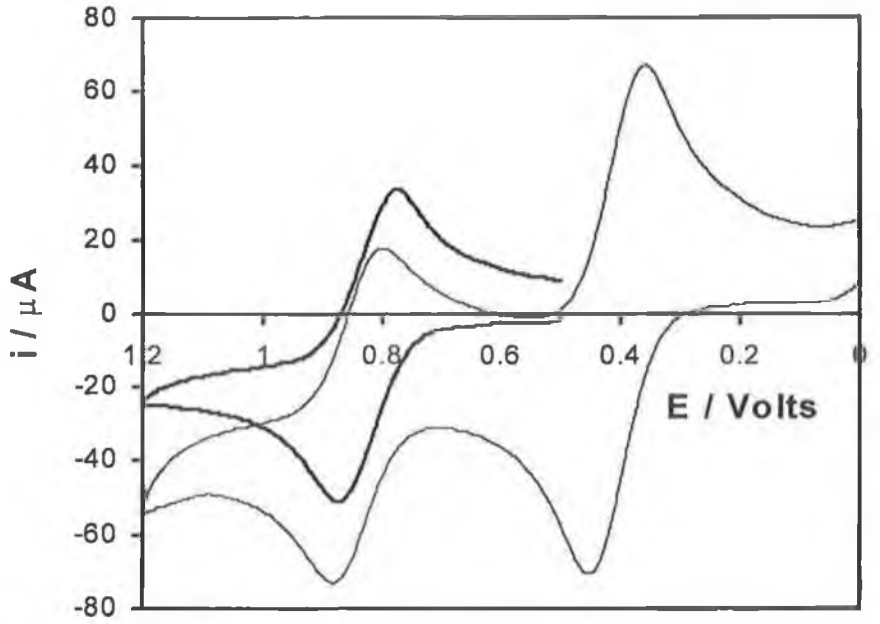

Figure 3.7 Cyclic voltammograms of 5 mM $[Os(bpy)_2(bpe)_2]^{2+}$ (thick line) and $\{[Os(bpy)_2(bpe)_2][Os(bpy)_2Cl_2]\}^{4+}$ (thin line) in de-aerated acetonitrile/ 0.1 M $TBABF_4$. Potentials are versus Ag/AgCl. The working electrode is a 2 mm diameter platinum disc. The scan rate is 0.1 V s^{-1}.

Table 3.2 Formal potentials for monomeric and trimeric complexes.[a]

Complex	$E^{\circ\prime}_{Ox}$ / V[b]	$E^{\circ\prime}_{Red}$ / V[c]	E°_{Ox} */ V[d]	E°_{Red} */ V[d]
$\{[Os(bpy)_2(bpe)_2][Os(bpy)_2Cl]_2\}^{4+}$	+0.427	-0.950	-1.253	+0.730
	+0.838		-0.842	
$[Os(bpy)_2(bpe)_2](PF_6)_2$	+0.830	-1.480	-0.850	+0.200
$[Os(bpy)_2$ bpe Cl$]PF_6$	+0.310	-1.520		

[a] All measurements were made in anhydrous acetonitrile containing 0.1 M $TBABF_4$ as supporting electrolyte. Potentials are quoted versus an Ag/AgCl reference electrode.

[b] Formal potentials are reproducible to within ±10 mV.

[c] Voltammograms show evidence of adsorption and formal potentials are typically reproducible to within ±30 mV.

[d] Calculated from Equations 3.3 and 3.4 with $E^{0\text{-}0}$ = 1.68 eV, as determined from low-temperature emission spectroscopy.

3.4.3 Ground State Electron Transfer

Previous investigations have demonstrated that complexes containing ligands with two pyridine groups, one of which is bound to the metal complex with the other being available for adsorption, form stable monolayers with nearly ideal electrochemical responses.[8,50,51,52] As illustrated in Scheme 3.1, both $[Os(bpy)_2(bpe)_2]^{2+}$ and $[Os(bpy)_2$ bpe pyridine$]^{2+}$ make useful analogues of the trimer that can be used to probe the dynamics and energetics of electron transfer across the bpe bridge in the ground state. This is because the bpe bridging ligand which links the osmium centre to the electrode, is identical to the bridging ligand which links the osmium centres in the $\{[Os(bpy)_2(bpe)_2][Os(bpy)_2Cl]_2\}^{4+}$ trimer. Figures 3.9 and 3.10 show representative background corrected cyclic voltammograms for spontaneously adsorbed monolayers of both $[Os(bpy)_2(bpe)_2]^{2+}$ and $[Os(bpy)_2$ bpe pyridine$]^{2+}$. For comparison purposes, Figure 3.8 shows the cyclic voltammograms for the $[Os(bpy)_2(bpe)_2]^{2+}$ monolayers uncorrected for background capacitive current. The supporting electrolyte in all cases is aqueous 1.0 M $LiClO_4$.

The voltammetric peak heights change by less than 10% when the monolayer is repeatedly cycled for periods up to 5 hours in blank electrolyte solutions. The observation that these monolayers are stable towards voltammetric cycling is consistent with behaviour previously reported for [Os(bpy)2 bpe Cl]$^{2+}$ monolayers.[62] These voltammograms are consistent with those expected for an electrochemically reversible reaction involving a surface-confined species.[53,54] The peak shape is independent of scan rate, ν, for $0.01 \leq \nu \leq 100$ Vs^{-1} and the peak height increases linearly with increasing scan rate, rather than the $\nu^{1/2}$ dependence observed for solution phase species.[55] However, nonzero peak-to-peak splitting (ΔE_p) is demonstrated even at low scan rates ($\Delta E_p = 35 \pm 3$ mV for $0.01 \leq \nu \leq 100$ Vs^{-1}), in contrast with the zero ΔE_p expected for the situation where there are no lateral interactions between adsorbates.[53,54,55] This behaviour has been previously reported for structurally related systems.[6] These have been interpreted by Feldberg and Rubenstein[56] as unusual quasi-reversibility (UQR), or apparent nonkinetic hysteresis in CVs, in terms of N-shaped free energy curves, as opposed to parabolic energy curves usually used in electron transfer models.[57] In their interpretation, hysteretic UQR arises because of rate processes which are slow in comparison to the experimental timescale, resulting in a finite ΔE_p. It is important to

note that ΔE_p does not increase with increasing scan rate for $0.1 \leq v \leq 100$ Vs^{-1}, which suggests that slow heterogeneous electron transfer is not responsible for the observed non-ideal behaviour. If the rate of electron transfer was slow, ΔE_p would be expected to increase with increasing scan rate,[58] and not remain constant for $0.1 \leq v \leq 100$ Vs^{-1} as observed experimentally.

Where there are no lateral interactions between surface confined redox centres, a FWHM of 90.6 mV is expected for a one-electron transfer.[53,54,55] For the $[Os(bpy)_2(bpe)_2]^{2+}$ monolayers, for $0.1 \leq v \leq 100$ Vs^{-1} the FWHM values are between 100 and 120 mV indicating that only very weak lateral interactions (e.g., electrostatic repulsion between the positively charged osmium centres) exist between adsorbates within the monolayers. In contrast, the monolayers of $[Os(bpy)_2$ bpe pyridine$]^{2+}$ exhibit slightly lower FWHM of between 90 and 110 mV, indicating that the effect of lateral interactions between adsorbates is more significant for the $[Os(bpy)_2(bpe)_2]^{2+}$ species. The reasons for this are not immediately apparent, but may arise from different packing densities or differences in hydrophobic interactions.

For both monolayers, the surface coverage obtained from the Faradaic charge measured from the background corrected voltammograms at a scan rate of 0.1 mV s^{-1} is $1.0 \pm 0.1 \times 10^{-10}$ mol cm^{-2} corresponding to an area of occupation of 166 ± 14 $Å^2$. This surface coverage is consistent with that expected for a close packed monolayer on the basis of structurally related systems and crystallographic data[59,60] which indicate that the radii of osmium and ruthenium polypyridyl complexes are of the order of 6.7 Å.

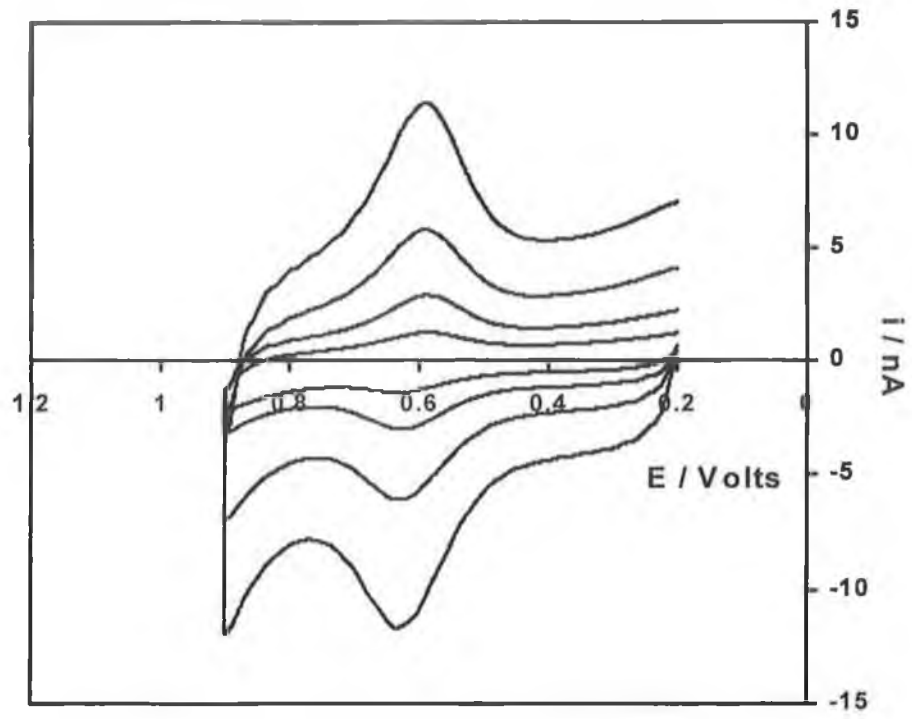

Figure 3.8 Cyclic voltammograms for a spontaneously adsorbed $[Os(bpy)_2(bpe)_2]^{2+}$ monolayer on a 25 μm radius platinum microdisk electrode. The supporting electrolyte is aqueous 1.0 M $LiClO_4$. The scan rates from top to bottom are 2.0, 1.0, 0.5 and 0.2 V s^{-1}. The surface coverage is 1.0×10^{-10} mol cm^{-2}.

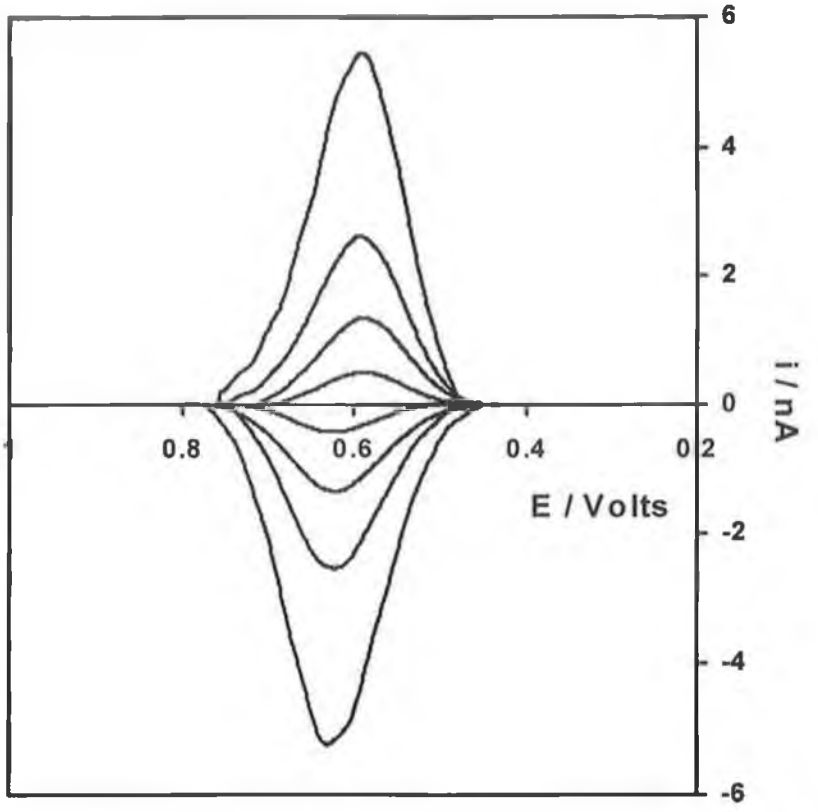

Figure 3.9 Background corrected cyclic voltammograms for a spontaneously adsorbed $[Os(bpy)_2(bpe)_2]^{2+}$ monolayer on a 25 μm radius platinum microdisk electrode. The supporting electrolyte is aqueous 1.0 M $LiClO_4$. The scan rates from top to bottom are 2.0, 1.0, 0.5 and 0.2 V s^{-1}. The surface coverage is 1.0×10^{-10} mol cm^{-2}.

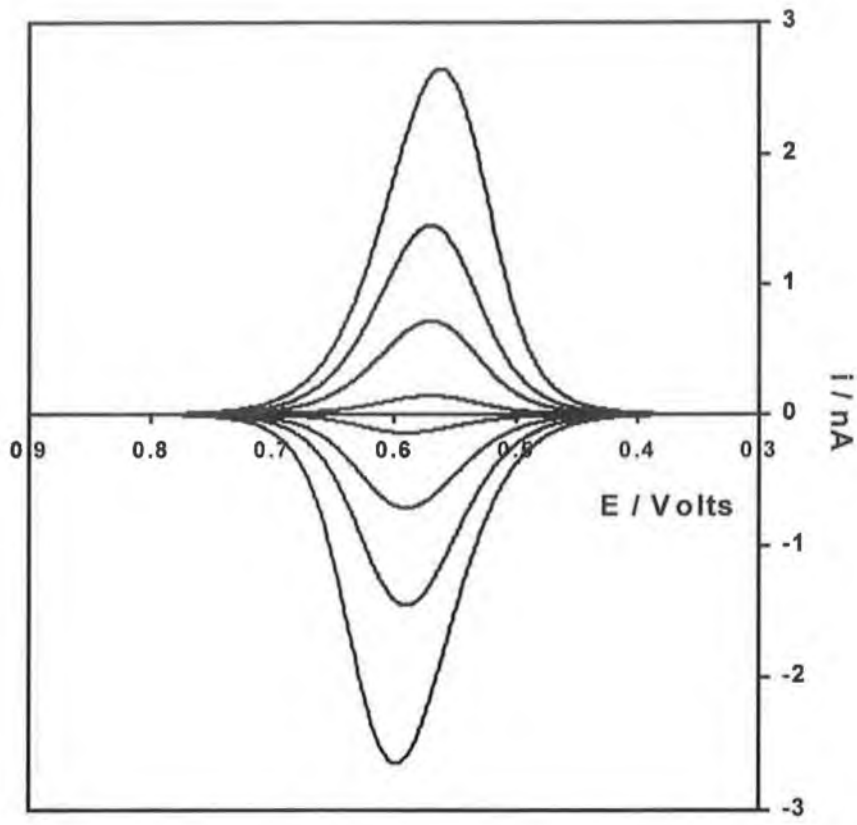

Figure 3.10 Background corrected cyclic voltammograms for a spontaneously adsorbed $[Os(bpy)_2$ bpe pyridine$]^{2+}$ monolayer on a 5 μm radius platinum microdisk electrode. The supporting electrolyte is aqueous 1.0 M $LiClO_4$. The scan rates from top to bottom are 2.0, 1.0, 0.5 and 0.1 V s^{-1}. The surface coverage is 1.0×10^{-10} mol cm^{-2}.

3.4.4 Effect of scan rate on the voltammetric response

As described in Chapter 1, for both functionalised alkane-thiol[29,30,61] and osmium polypyridyl monolayers, [9,51,62] cyclic voltammetry can provide a powerful insight into the rate of heterogeneous electron transfer across the electrode / monolayer interface. When the time constants for the voltammetric experiment and heterogeneous electron transfer become comparable, the peak-to-peak splitting, ΔE_p, between the anodic, E_{pa}, and cathodic, E_{pc}, peak potentials increases.[30,62] Notably, this increase in ΔE_p at scan rates $\geq$ 1000 V s^{-1} has been observed for monolayers of $[Os(bpy)_2(bpe)Cl]^+$ adsorbed on platinum microelectrodes,[62] where the metal centre is linked to the electrode via the same bpe bridging ligand as described here. Figure 3.12 illustrates how the voltammetric response associated with the $Os^{2+/3+}$ redox reaction in $[Os(bpy)_2(bpe)_2]^{2+}$ changes as the scan rate, ν, is increased from 5,000 to 20,000 V s^{-1}. Significantly, at these relatively high scan rates, the peak-to-peak separation is no longer close to zero and ΔE_p increases from 160 to 320 mV on going from 5,000 to 20,000 V s^{-1}. Figure 3.13 shows that A similar response is seen for the monolayers of $[Os(bpy)_2$ bpe pyridine$]^{2+}$ with ΔE_p increasing from 140 to 270 mV on going from 5,000 to 20,000 Vs^{-1}.

Uncompensated cell resistance could contribute to the observed behaviour. Where the working electrode is a 5 μm radius microelectrode, the uncompensated resistance as measured using potential step chronoamperometry, is 18.5±1.8 kΩ in 1 M $LiClO_4$ (Figure 3.11). Taken in conjunction with the maximum peak current of approximately 1750 nA, this cell resistance leads to an iR drop of approximately 32 mV. This ohmic loss is negligible compared to the peak-to-peak separation of 270 mV observed at a scan rate of 20,000 Vs^{-1}. Therefore, it appears that at high scan rates the dynamics of electron transfer across the electrode/monolayer influence the voltammetric response.

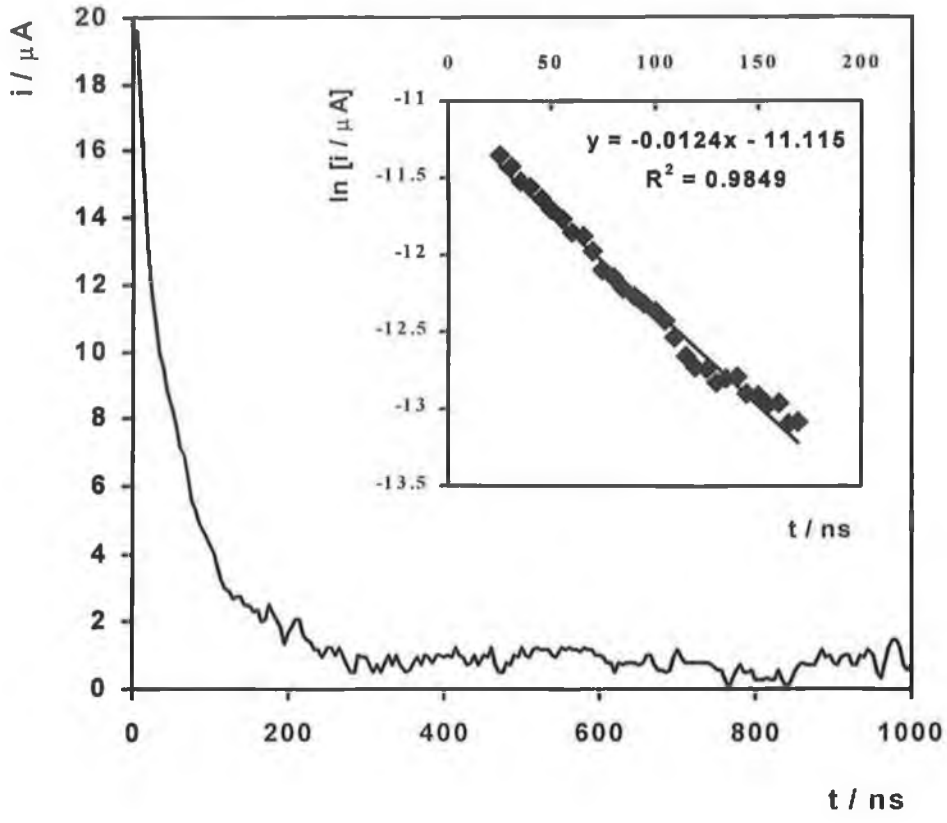

Figure 3.11 Current transient obtained following the application of a 250 mV potential step (50 to 300 mV) to a clean 5 μm radius platinum microelectrode. The supporting electrolyte is 1 M $LiClO_4$. Inset: semilog plot of the decay.

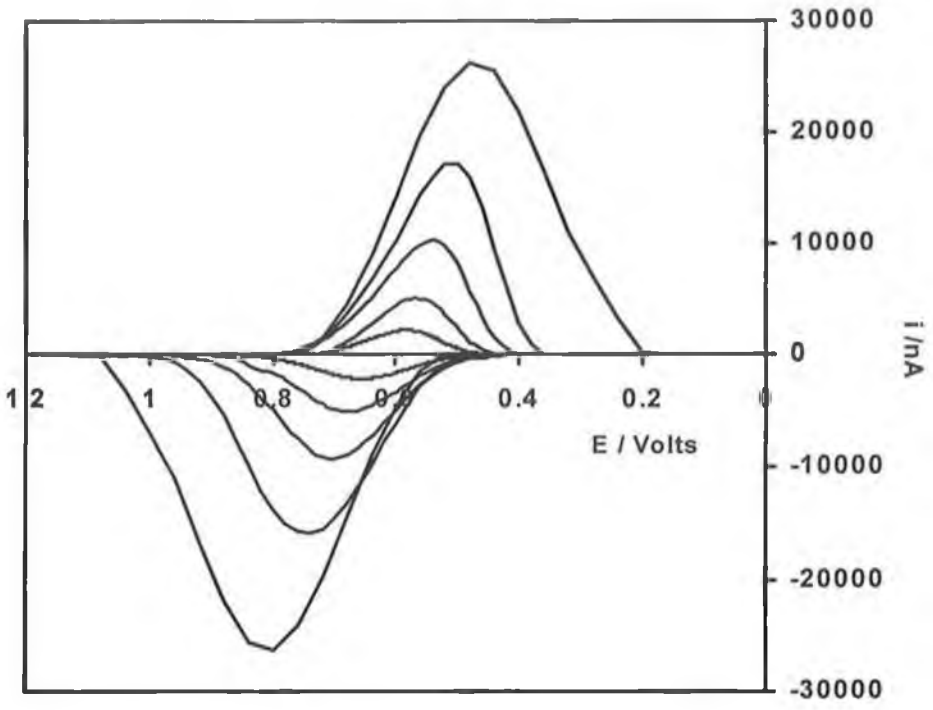

Figure 3.12 Background corrected cyclic voltammograms for a spontaneously adsorbed $[Os(bpy)_2(bpe)_2]^{2+}$ monolayer on a 25 μm radius platinum microdisk electrode. The supporting electrolyte is aqueous 0.1 M $LiClO_4$. The scan rates from top to bottom are 20,000, 10,000, 5000, 2500 and 1000 V s^{-1}. The surface coverage is 1.0×10^{-10} mol cm^{-2}.

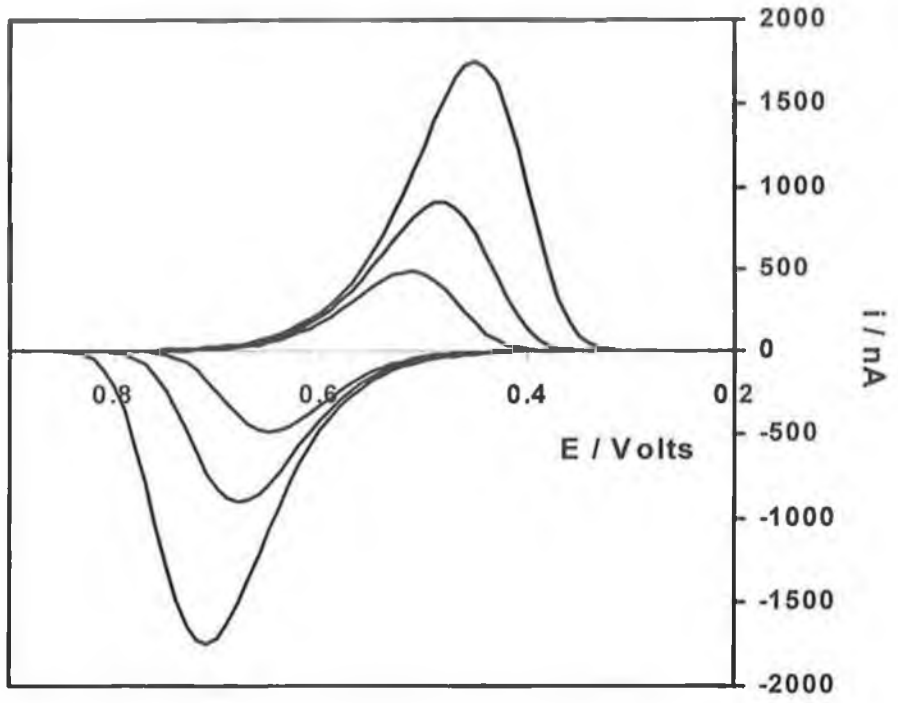

Figure 3.13 Background corrected cyclic voltammograms for a spontaneously adsorbed $[Os(bpy)_2$ bpe pyridine$]^{2+}$ monolayer on a 5 μm radius platinum microdisk electrode. The supporting electrolyte is aqueous 0.1 M $LiClO_4$. The scan rates from top to bottom are 20,000, 10,000 and 5000 V s^{-1}. The surface coverage is 1.0×10^{-10} mol cm^{-2}.

As discussed in Section 1.2 of Chapter 1,[63,64,65] the standard heterogeneous electron transfer rate constant, k^o depends on both a frequency factor and a Franck-Condon barrier and is described by:

$$k^o = A_{ET}\exp\left(-\Delta G^{\neq}/RT\right) \qquad (3.6)$$

where A_{et} is the pre-exponential factor and $\Delta G^{\neq}$ is the electrochemical free energy of activation.[66] For an adiabatic reaction, the prefactor is the product of κ_{el} the electronic transmission coefficient (equal to unity for an adiabatic reaction) and ν_n a frequency factor dictated either by nuclear or solvent motion. In contrast, for a non-adiabatic reaction where the reactants are weakly coupled κ_{el} is significantly less than unity and the prefactor is dictated by the electron hopping frequency in the activated complex, ν_{el}.

As demonstrated by Chidsey,[29] Creager[61] and Murray,[30], the voltammetric response can be modelled according to a non-adiabatic electron transfer response to extract standard heterogeneous electron transfer rate constants and reorganization energies. Following Chidsey,[29] the potential dependent rate constants for monolayer reduction, $k_{Red,\eta}$ and oxidation, $k_{Ox,\eta}$, are given by

$$k_{Red,\eta} = \kappa_{el}\,\rho\,k_B T\int_{-\infty}^{\infty}\frac{\exp\left\{-(x-(\lambda+\eta)/k_B T)^2/(k_B T/4\lambda/\right\}}{1+\exp(x)}\,dx \qquad (3.7)$$

$$k_{Ox,\eta} = \kappa_{el}\,\rho\,k_B T\int_{-\infty}^{\infty}\frac{\exp\left\{-(x-(\lambda-\eta)/k_B T)^2/(k_B T/4\lambda/\right\}}{1+\exp(x)}\,dx \qquad (3.8)$$

where x is the electron energy relative to the Fermi level, κ_{el} is the distance dependent electronic coupling between the electrode and the redox sites, ρ is the density of electronic states in the metal electrode, k_B is the Boltzmann constant, T the absolute temperature, and λ is the reorganization energy (defined as the change in Gibbs energy if the reactant state were to distort to the equilibrium configuration of the product state without transfer of the electron[67]).

The voltammetric current for the reaction of an immobilized redox centre following first order kinetics is given by:[30]

$$i_F = nFA(k_{Ox,\eta}\,\Gamma_{Red,\,\eta} - k_{Red,\eta}\,\Gamma_{Ox,\,\eta}) \qquad (3.9)$$

where $\Gamma_{Red,\,\eta}$ and $\Gamma_{Ox,\,\eta}$ are the instantaneous surface coverages of the oxidized and reduced species. Energy minimized molecular modelling indicates that the electron transfer distance is approximately 10 Å. Therefore, in using Equation 3.9 to model the voltammetric response, there are only two freely adjustable parameters for each redox centre, k° and $\Delta G^{\neq}$ (= λ / 4).

To fit the experimental voltammograms, a computer simulation program described previously has been used.[68] This program uses the electron transfer models described above to generate theoretical voltammograms for the electron transfer process. This is achieved by providing certain parameters from the experiment, e.g., the radius of the microelectrode (μm), the temperature (K), the scan rate (V s^{-1}), the overpotential range for the simulation (V), the formal potential (V), the distance from the redox centre to the electrode (Å) and the resolution (the interval of overpotential used in the calculation of individual currents in the simulation (V)). The independent variables are k° and λ and the program provides random values of k° and λ at the start of every independent simulation. The model fits the data by finding the values of k° and λ that minimise the sum square residuals between the theoretical and experimental currents observed in the linear sweep voltammograms. This minimisation is carried out using the Nelder and Mead Simplex[69] algorithm and is coded into the model by means of a Microsoft Excel macro. The simplex method was used by Creager[61] to fit peak potential vs. log (scan rate) data to predictions from theory as a means of analysing experimental voltammograms. Similar to this model, the independent variables were k° and λ. However, in the model developed by Forster and co-workers,[68] the simplex is used to match the full experimental cyclic voltammogram as opposed to the peak potential vs. log (scan rate). Using the entire curve should allow the shape of the experimental curve to influence the result of the simplex and therefore provide a more accurate estimate of the cyclic voltammetric data. For example, this model has been used successfully to determine k° and $\Delta G^{\neq}$ (= λ/4) for a number of osmium polypyridyl monolayers,[9,51,62] including monolayers of $[Os(bpy)_2(bpe)Cl]^+$ adsorbed on platinum microelectrodes,[62] where values of $9.4\pm0.9 \times 10^3$ s^{-1} and 11.4 ± 0.8 kJ mol^{-1} were obtained for k° and $\Delta G^{\neq}$, respectively (λ = 0.47 eV).

Figure 3.14 shows the attempt to fit the anodic branch of the monolayers shown in Figure 3.12 ($[Os(bpy)_2(bpe)_2]^{2+}$) to the model described above. While there is good correlation between the experimental peak potentials and those predicted by the model, the experimental peaks are considerably broader. One explanation for this lies in the fact that the model assumes a FWHM of 90.6 mV, while the FWHM values observed for this monolayer are between 100 and 120 mV, as discussed earlier. Broad monolayer peaks have also been observed for other systems and, beyond the effect of lateral interactions discussed earlier, can be attributed to a distribution of formal potentials within the monolayer caused by differences in the local microenvironment.[70] The model yields a value for k° of $2.7\pm0.2 \times 10^4$ s^{-1}, which is of the order of heterogeneous electron transfer rate constants previously observed for osmium polypyridyl monolayers of this type.[6,62,71] It is slightly higher than the value of $9.4\pm0.9 \times 10^3$ s^{-1} determined for electron transfer across the same bpe bridge in monolayers of $[Os(bpy)_2(bpe)Cl]^+$.[62] However, the values of λ obtained are not reliable, as the value increases with increasing scan rate, i.e., λ is 0.2 eV at 2500 V s^{-1} and is 9 eV at 10,000 V s^{-1}! If the model can accurately model the data, it should yield the same value of λ at all scan rates, within a reasonable experimental error, say $\pm$ 5 - 10 %. Also, the values at high scan rate are extremely high when compared to typical values of $0.1 \leq \lambda \leq 1.0$ eV obtained for both functionalised alkane-thiols[29,30,61] and osmium polypyridyl monolayers.[9,51,62]

In an attempt to obtain a better fit between the experimental and theoretical voltammograms, the computer simulation program was modified to include a square distribution of formal potentials and to search for values of k°, λ and a distribution of formal potentials within the monolayer which would accurately fit the experimental peaks. The result is shown in Figure 3.15. As with the previous model, the agreement of experimental and theoretical peak potentials is quite good, but again, this model does not accurately predict the observed experimental peak shape. A closer examination of the anodic peaks highlights the difference between the experimental and theoretical voltammograms. Including a distribution of formal potentials has resulted in a theoretical CV that has a similar peak shape to the left hand side of the anodic experimental peak, but is not the same shape as the right hand side of the experimental peak. This problem may be due to the assumption of a square distribution of formal potentials, when a Gaussian distribution is more likely.[53] This modified computer

simulation yields best-fit values of $2.2\pm0.5 \times 10^4$ s^{-1} and 0.33 ± 0.3 eV for k° and λ, respectively. The value of k° is similar to that obtained with the previous simulation ($2.7\pm0.2 \times 10^4$ s^{-1}) and again compares favourably with heterogeneous electron transfer rate constants previously observed for osmium polypyridyl monolayers of this type.[6,62,71] The value of λ is within the range of values obtained by modelling the voltammetry of a range of monolayer systems using the electron transfer theory described above ($0.1 \leq \lambda \leq 1.0$ eV).[6,9,29,30,61,62,71] These results demonstrate that the peak shape has little effect on the value of k° obtained, but has a marked effect on the value of λ returned by the computer simulation. This indicates that, as expected, modelling the entire voltammetric curve, as opposed to peak potential vs. log (scan rate) as reported by Creager,[61] allows the shape of the experimental curve to influence the result of the simplex and therefore provide a more accurate estimate of k° and $\Delta G^{\neq}$. Unfortunately, this means that if the experimental voltammograms obtained are not fully "ideal", e.g., do not exhibit FWHM values of 90.6 mV, this will have an adverse effect on the accuracy of the simulation.

In contrast, Figure 3.16 shows that the theoretical values predicted by the nonadiabatic model with no potential distribution modification satisfactorily fits the voltammograms obtained at 5,000 and 10,000 Vs^{-1} for the $[Os(bpy)_2$ bpe pyridine$]^{2+}$ monolayers and yields a value of $3.1\pm0.2 \times 10^4$ s^{-1} for k^o. The reorganization energy is 0.4 eV, but a similar quality fit is obtained for $0.3\leq\lambda\leq0.5$ eV. However, for the highest scan rate investigated, 20,000 Vs^{-1}, the theoretical response agrees less well with that found experimentally. Thus, while the theoretical and experimental peak potentials agree to within experiment error, the experimental peak currents are approximately 20 % larger than theory predicts. This observation suggests that there may be a small population of redox centres within the monolayer that can undergo more rapid heterogeneous electron transfer than the majority of the population. Behaviour of this kind has been found for related systems[31] and most likely arises because of an imperfect monolayer structure, e.g., because of surface roughness or flexibility of the bridge. The observation that these monolayers may be adequately fit to the Marcus model, when the corresponding $[Os(bpy)_2(bpe)_2]^{2+}$ monolayers are fit less well, is most likely due to the lower FWHM values of the $[Os(bpy)_2$ bpe pyridine$]^{2+}$ monolayers. At 90 – 110 mV, they are closer to the theoretical value of 90.6 mV predicted for a monolayer which obeys Langmuir isotherm conditions, i.e., no lateral interactions between redox sites,[55] than the 100 –

120 mV FWHM values observed for the $[Os(bpy)_2(bpe)_2]^{2+}$ monolayers. When lateral interactions exist between oxidised (O) and reduced (R) sites in monolayer, the shape of the CV peak depends on the energies of the interactions between O with O, R with R and O with R.[55] Perhaps the substitution of the second bpe ligand on the $[Os(bpy)_2(bpe)_2]^{2+}$ complex by the pyridine ligand in the $[Os(bpy)_2$ bpe pyridine$]^{2+}$ complex affects the interactions between adsorbed redox sites. This would account for the observed difference in peak widths and therefore FWHM values.

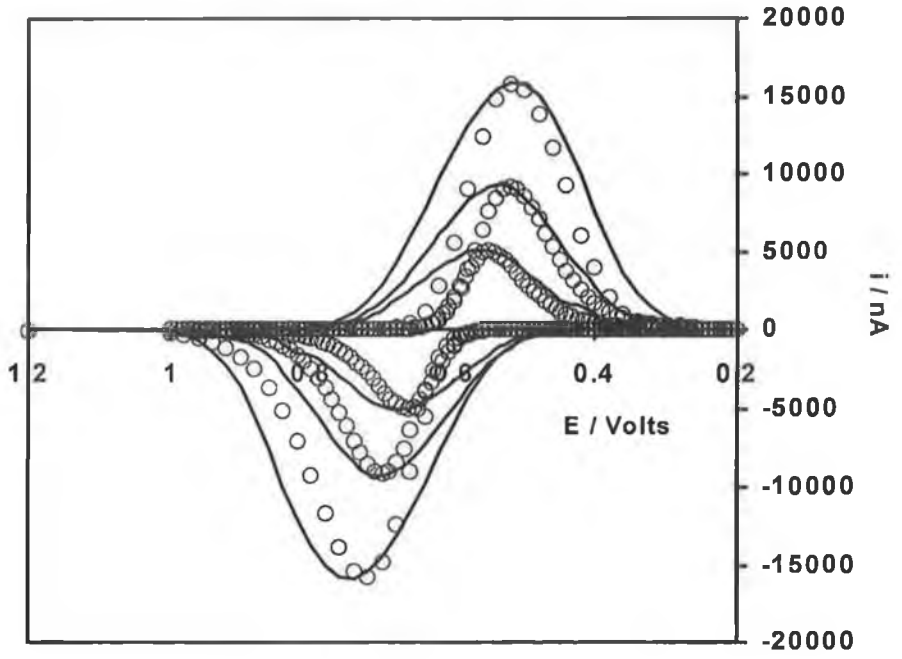

Figure 3.14 Background corrected cyclic voltammograms for a spontaneously adsorbed monolayer of $[Os(bpy)_2(bpe)_2]^{2+}$ on a 25 μm radius microelectrode (thick line). Overlaid are the theoretical currents obtained using the nonadiabatic tunneling model (open circles). The scan rates from top to bottom are 10,000, 5000 and 2500 V s^{-1}. The supporting electrolyte is aqueous 1.0 M $LiClO_4$. The surface coverage is 1.0×10^{-10} mol cm^{-2}.

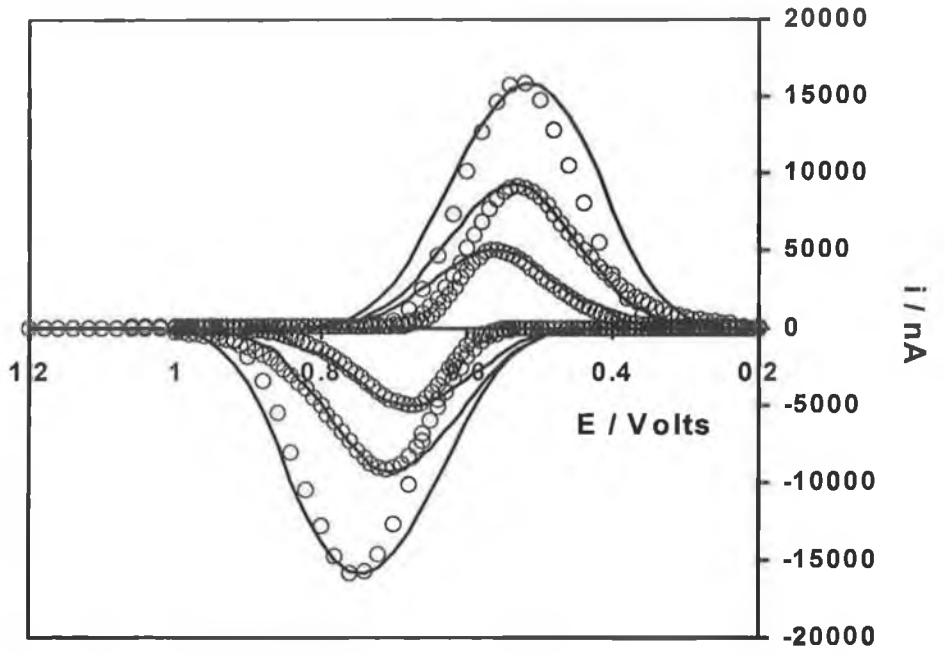

Figure 3.15 Background corrected cyclic voltammograms for a spontaneously adsorbed monolayer of $[Os(bpy)_2(bpe)_2]^{2+}$on a 25 μm radius microelectrode (thick line). Overlaid are the theoretical currents obtained using the adiabatic model with the square formal potential distribution included(open circles). The scan rates from top to bottom are 10,000, 5000 and 2500 V s^{-1}. The supporting electrolyte is aqueous 1.0 M $LiClO_4$. The surface coverage is 1.0×10^{-10} mol cm^{-2}.

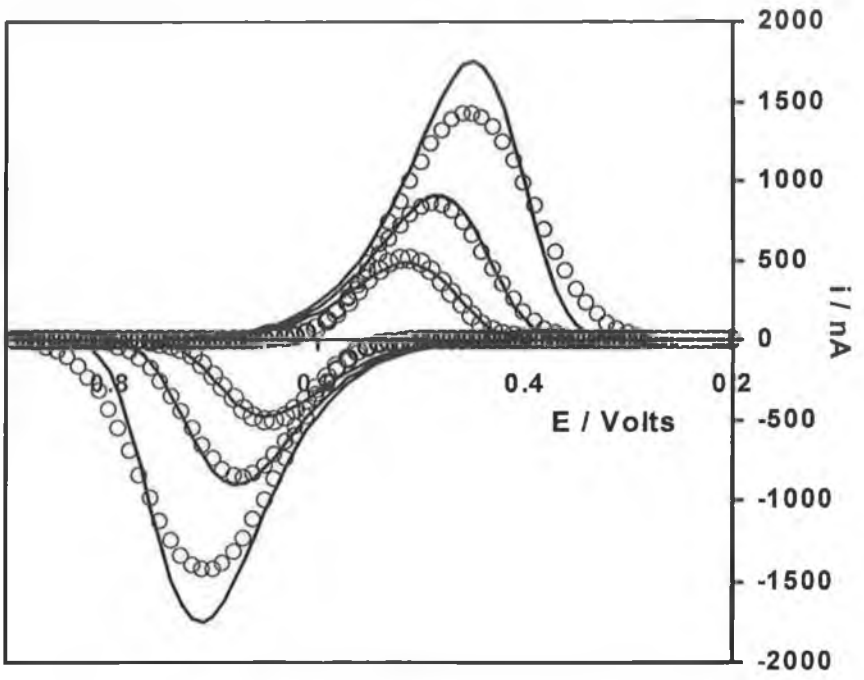

Figure 3.16 Background corrected cyclic voltammograms for a spontaneously adsorbed monolayer of $[Os(bpy)_2$ bpe pyridine$]^{2+}$on a 5 μm radius microelectrode (thick line). Overlaid are the theoretical currents obtained using the nonadiabatic tunneling model (open circles). The scan rates from top to bottom are 5000, 10000 and 20000 V s^{-1}. The supporting electrolyte is aqueous 1.0 M $LiClO_4$. The surface coverage is 1.0×10^{-10} mol cm^{-2}.

3.4.5 Comparison of Optically and Electrochemically Driven Electron Transfer.

In section 3.4.2, the driving force found for the photochemically induced electron transfer (reductive quenching) is -0.3 eV. The non-adiabatic electron transfer model outlined in Equations 3.7 and 3.8 indicates that for this driving force, the heterogeneous electron transfer rate constant is $2.0\pm0.2 \times 10^6$ s^{-1}. The fact that this value is substantially lower than the predicted by the Butler-Volmer formalism, 1.0×10^7 s^{-1}, reflects the ability of the Marcus approach to correctly predict the experimental observation that the rate constant becomes less sensitive to the driving force for large values of overpotential. The most striking result of this analysis is that even under conditions of identical driving forces, the photoinduced electron transfer rate constant is almost two orders of magnitude larger, $1.3\pm0.1 \times 10^8$ s^{-1}, than that of the electrochemically driven heterogeneous electron transfer, $2.0\pm0.2 \times 10^6$ s^{-1}.

Given the large differences between k_{hetero} and k_{PET}, it is of interest to determine whether the strength of donor/acceptor coupling across the *trans*-1,2-bis-(4-pyridyl)ethylene bridge is weaker for the delocalised metallic states of an electrode compared to the localized redox states of the trimer. For the photoinduced electron transfer reaction, this can be achieved via the Marcus-Hush theory of homogeneous electron transfer, as detailed in Chapter 1 of this thesis. As described by Marcus,[63,64,66] in the case of the photoinduced electron transfer reaction, the rate constant for electron cross-exchange between the two osmium sites, k_{PET}, depends on the difference in the redox potentials of the two reactants, $\Delta G°$, and the reorganisation energy, λ:

$$k_{PET} = A_{ET} \exp\left[-\frac{(\lambda + \Delta G°)^2}{4\lambda RT}\right] \qquad (3.10)$$

Theoretical modelling of the monolayer voltammetric response at high scan rates show that the best fits to the experimental data of Figure 3.16 indicate that λ is approximately 42 kJ mol^{-1}. Using the standard prediction from Marcus theory[55] that $\lambda_{PET} = 2\lambda_{hetero}$, yields a value of 82 kJ mol^{-1} for λ_{PET}.

The driving force for the photoinduced reaction, $\Delta G°$, is determined from the difference in the redox potentials of the two reactants as provided by the electrochemical data in

Section 3.4.2. The reduction and oxidation potentials for $[Os(bpy)_2\ (bpe)_2]^{2+*}$ (acceptor) and $[Os(bpy)_2$ bpe $Cl]^+$ (donor) are +0.200 and +0.427 V, respectively. This indicates that $\Delta G°$ is approximately 21.9 kJ mol^{-1} (0.227 eV). Substituting these values of λ and $\Delta G°$ into Equation 3.10 indicates that the pre-exponential factor, A_{ET}, for the PET process is approximately 9×10^{13} s^{-1}.

The pre-exponential factor for ground state electron transfer can be calculated using Equation 3.6. Using the experimental values of $3.1 \pm 0.2 \times 10^4$ s^{-1} and 10.5 kJ mol^{-1} for $k°$ and $\Delta G^{\neq}$ ($\lambda/4$), respectively, obtained from the computer simulation of the monolayer voltammograms in Figure 3.16, this equation yields a value of approximately 2×10^6 s^{-1} for A_{ET} for the ground state process. A_{ET} values may be used to compare the strength of electronic coupling in an electron transfer reaction, as for a nonadiabatic reaction such as described here, A_{ET} is equal to ν_{el}, the electron hopping frequency in the complex. The magnitude of ν_{el} depends on H_{rp}, a factor describing the electronic coupling energy between the electron donor and acceptor (c.f. Equation 1.2.10). As the pre-exponential factor is dramatically smaller (by more than seven orders of magnitude) for the monolayers than for the trimer, this suggests that the extent of electronic communication across the *trans*-1,2-bis-(4-pyridyl)ethylene bridge is much weaker when linking a metal electrode surface and a metal complex compared to when it bridges molecular components.

Forster and Keyes have demonstrated the same weaker electronic coupling across a 3,6-bis(4-pyridyl)-1,2,4,5-tetrazine bridge (4-tet) when it links an osmium centre to a platinum microelectrode, compared to the situation when it bridges two metal centres in a dimer.[18] They have used the same method to determine k_{PET} as described here, i.e., the emission lifetime of the bpy-based excited state in $[Os(bpy)_2$ p0p 4-tet$]^{2+}$ (p0p is 4,4'-dipyridyl and bpy is 2,2'-dipyridyl) is determined in the presence and absence of a linked quencher, $[Os(bpy)_2\ Cl]^+$. This measurement has provided an estimate of 1.6×10^7 s^{-1} for k_{PET}. However, the authors have pointed out that it is possible that the $[Os(bpy)_2\ Cl]^+$ moieties within the dimer create a favourable vibronic deactivation pathway in the PET experiments, causing the photoinduced electron transfer rate constant to be overestimated.[18] This is also possible in the measurements of k_{PET} in the trimer described here and would cause a concomitant overestimation of A_{ET} for the photoinduced reaction.

Meyer et al. have suggested that estimations of intramolecular electron transfer rate constants can be complicated by the presence of rotational orientations in the ligand bridge.[10,13] For example, in an osmium-osmium dimer linked by a 1,2-bis(4-pyridyl)ethane (p2p) bridge, the rate of intramolecular electron transfer quenching is estimated to be 2.2×10^7 s^{-1} at 77 K.[13] Quenching in the dimer yields a charge-separated state $[(L)(bpy^{\bullet-})Os^{II}\text{-}p2p\text{-}Os^{III}(L')(L'')Cl]^{3+}$, where the electron-hole pair is separated by the intervening Os^{II} centre and the p2p ligand. Rotational reorientations at the CH_2-CH_2 link in the p2p bridge could allow through-space contact between the $bpy^{\bullet-}$ and Os^{III} sites and decay by outer-sphere electron transfer. This nonradiative decay would lessen the observed lifetime of the dimer and would cause k_{PET}, as estimated via Equation 3.1, to be overestimated.[13] However, due to the rigid nature of the double bond link in the bpe ligand bridge in the trimer, rotational transitions of this kind are unlikely to significantly interfere with the estimation of k_{PET} in this instance.

3.5 Conclusions

Chapter 1 has demonstrated that there is widespread interest in investigating the factors which affect electron transfer, in both ground and electronically excited states. To date, the investigation of heterogeneous electron transfer has focused on the use of adsorbed monolayers on microelectrodes.[6,9,29,30,31,61,62,71] Excited state (photoinduced) electron transfer has generally been probed using di- and tri-metallic transition metal complexes.[13,14,16,17,22] These experimental methods have proved to be powerful model systems by which to investigate the parameters which govern electron transfer, including inter-reactant distance, the role of the solvent medium and the strength of electronic coupling between the donor and acceptor moieties. However, few reports have compared ground and photoinduced electron transfer by combining measurements of photoinduced electron transfer in di- or tri-metallic complexes with ground state measurements of heterogeneous electron transfer across a metal/monolayer interface.[18] Combining these techniques allows the comparison of electronic coupling across a bridge linking two metal centres compared with the same bridge linking remote redox centres to a metal surface.

To achieve this aim, a novel trimer of the form $\{[Os(bpy)_2(bpe)_2][Os(bpy)_2Cl]_2\}^{4+}$ has been synthesised, characterised and used to probe the dynamics of photoinduced electron transfer between metal centres across rigid bridges. Transient emission spectroscopy and time-correlated single photon counting have been used to determine the emission lifetime of the trimer and its parent monomer complex, $[Os(bpy)_2(bpe)_2]^{2+}$. The lifetime of the emitting $[Os(bpy)_2(bpe)_2]$ centre in the trimer (6.5 ± 1.4 ns) is significantly shorter than that of the monomer complex (42.2 ± 0.6 ns), indicating that the emission is quenched by the $[Os(bpy)_2Cl]$ centres linked to the emitting centre in the trimer via the bpe bridge. The rate constant for this intramolecular quenching, k_{PET}, is $1.3\pm0.1 \times 10^8$ s^{-1}. In common with related systems,[13,18,44] Förster energy transfer is discounted as the quenching mechanism, as the overlap of the emission and absorbance spectra for the $[Os(bpy)_2(bpe)_2]^{2+}$ and $[Os(bpy)_2$ bpe $Cl]^+$ complexes is very weak, given that $\lambda_{max,em}$ and $\lambda_{max,abs}$ are approximately 750 and 450 nm, respectively.

Using electrochemical data for the complexes, the driving forces for oxidative and reductive electron transfer quenching of the excited state have been calculated using the

Rehm-Weller equation. The observation that a reductive electron transfer process is exergonic (-0.3 V), while oxidative electron transfer is endoergonic (+ 0.68 V), indicates that quenching of the excited state involves electron donation from the $[(bpe)Os(bpy)_2\ Cl]^+$ moiety to the electronically excited $[Os(bpy)_2\ (bpe)_2]^{2+*}$ centre.

Ground state heterogeneous electron transfer has been probed using monolayers of $[Os(bpy)_2(bpe)_2]^{2+}$ and $[Os(bpy)_2$ bpe pyridine$]^{2+}$ immobilised on platinum microelectrodes. These complexes make useful analogues of the trimer, as the bridging ligand that binds the redox centre to the electrode (bpe) is identical to that which links the $[Os(bpy)_2Cl]$ centres to the $[Os(bpy)_2(bpe)_2]$ centre in the trimer. Computer simulation of the cyclic voltammograms obtained at high scan rates, where the rate of heterogeneous electron transfer controls the observed response, has been carried out. The simulation is based on the Marcus model of heterogeneous electron transfer. A fitting algorithm minimises the difference between the experimental and theoretical voltammograms and yields values of k^o, the rate constant for heterogeneous electron transfer and λ, the reorganisation energy. The experimental voltammograms for $[Os(bpy)_2$ bpe pyridine$]^{2+}$ are more adequately fit by the computer simulation than those for $[Os(bpy)_2(bpe)_2]^{2+}$, i.e., the values of k^o and λ obtained are within expected values for this type of monolayer. This is most likely due to the fact that the $[Os(bpy)_2$ bpe pyridine$]^{2+}$ monolayers exhibit FWHM values closer to the ideal of 90.6 mV for a monolayer with no lateral interactions between adsorbates.[55] This observation demonstrates the marked effect that simulating the entire peak has on the estimates of k^o and λ obtained, and indicates that including the peak shape in a simulation provides more accurate estimates of k^o and λ. The simulation yields values of $3.1\pm0.2 \times 10^4\ s^{-1}$ for k^o and approximately 0.4 eV for λ.

Comparing the ground and photoinduced electron transfers shows that the rate constant for the photoinduced electron transfer process is $1.3\pm0.1 \times 10^8\ s^{-1}$ compared to $2.0\pm0.2 \times 10^6\ s^{-1}$ for the ground state process with the same driving force (-0.3 eV). This result suggests that the proximity of donor/acceptor and bridge states, i.e., the achievement of resonance (where the energy of the donor and acceptor states are identical) in the PET reaction, dramatically enhances the rate of electron transfer. The values of k^o, λ and driving force for the photoinduced, $\Delta G°$, and heterogeneous, $\Delta G^{\neq}$, electron transfer reactions, have been used to calculate the experimental pre-exponential factors, A_{ET}, for

both the ground and photoinduced electron transfers. These calculations show that A_{ET} is 9×10^{13} s^{-1} and 2×10^{6} s^{-1} for the photoinduced and heterogeneous electron transfers, respectively. Significantly, this result reveals that the strength of electronic coupling across the *trans*-1,2-bis-(4-pyridyl)ethylene bridge is significantly higher when it links two metal complexes compared the situation where it acts as a bridge between a metal centre and an electrode. This result suggests that the tunnelling junction between the bulk metal and an adsorbed bridge can significantly influence heterogeneous electron transfer rates. These results represent some of the first where electron transfer and in particular, electronic coupling, across a ligand bridge has been investigated by combining excited state measurements on a trimetallic complex and ground state measurements on adsorbed monolayers.

REFERENCES

(1) Fox, M. A.; Chanon, M. "Photoinduced Electron Transfer", Elsevier, Amsterdam, **1988**.

(2) O'Regan, B.; Gratzel, M. *Nature* **1991**, *353*, 737.

(3) Hopfield, J. J.; Onuchic, J. N.; Beratan, D. N. *J. Phys. Chem.* **1989**, *93*, 6350.

(4) Knox, R. S. *Photosynth. Res.* **1996**, *48*, 35.

(5) Bard, A. J.; Fox, M. A. *Acc. Chem. Res.* **1995**, *28*, 141.

(6) Forster, R. J.; Faulkner, L. R. *J. Am. Chem. Soc.* **1994**, *116*, 5444.

(7) Balzani, V.; Juris, A.; Venturi, M.; Campagna, S.; Serroni, S. *Chem. Rev.* **1996**, *96*, 759.

(8) Acevedo, D.; Abruña, H.D. *J. Phys. Chem.* **1991**, *95*, 9590.

(9) Forster, R. J.; Loughman, P.; Keyes, T. E. *J. Am. Chem. Soc.* **2000**, *122*, 11948.

(10) Schanze, K. S.; Meyer, T. J. *Inorg. Chem.* **1985**, *24*, 2123.

(11) De Cola, L.; Belser, P. *Coord. Chem. Rev.* **1998**, *177*, 301.

(12) Ward, M. D. *Chem. Soc. Rev.* **1995**, *24*, 121.

(13) Schanze. K. S.; Neyhart, G. A.; Meyer, T. J. *J. Phys. Chem.* **1986**, *90*, 2182.

(14) Powers, M. J.; Meyer, T. J. *J. Am. Chem. Soc.* **1980**, *102*, 1289.

(15) Curtis, J. C.; Bernstein, J. S.; Meyer, T. J. *Inorg. Chem.* **1985**, *24*, 385.

(16) De Cola, L.; Balzani, V.; Barigelletti, F.; Flamigni, L.; Belser, P.; von Zelewsky, A.; Frank, M.; Vogtle, F. *Inorg. Chem.* **1993**, *32*, 5228.

(17) Balzani, V.; Barigelletti, F.; Belser, P.; Bernhard, S.; De Cola, L.; Flamigni, L. *J. Phys. Chem.* **1996**, *100*, 16786.

(18) Forster, R. J.; Keyes, T. E. *J. Phys. Chem.* **2001**, *105*, 8829.

(19) Zahavy, E.; Fox, M. A. *Chem. Eur. J.* **1998**, *4*, 1647.

(20) Richter, M.M.; Brewer, K.J. *Inorg. Chem.* **1993**, *32*, 5762.

(21) Brauns, E.; Jones, S. W.; Clark, J. A.; Molnar, S. M.; Kawanishi, Y.; Brewer, K. J. *Inorg. Chem.* **1997**, *36*, 2861.

(22) Molnar, S. M.; Nallas, G.; Bridgewater, J. S.; Brewer, K. J. *J. Am. Chem. Soc.* **1994**, *116*, 5206.

(23) Nallas, G. N. A.; Brewer, K. J. *Inorg. Chim. Acta.* **1996**, *253*, 7.

(24) Arana, C. R.; Abruña, H. D. *Inorg. Chem.* **1993**, *32*, 194.

(25) Diamond, D.; Hanratty, V. C. A. "Spreadsheet Applications in Chemistry using Microsoft Excel", Wiley, New York, 1997.

(26) O'Hanlon D. P., Ph.D. Thesis, Dublin City University, **1999**.

(27) Trasatti, S.; Petrii, O. A. *J. Electroanal. Chem.* **1992**, *327*, 354.

(28) Tirado, J. G.; Abruña, H. D. *J. Phys. Chem* **1996**, *100*, 4556.

(29) Chidsey, C. E. D. *Science* **1991**, *251*, 919.

(30) Tender, L.; Carter, M. T.; Murray, R. W. *Anal. Chem.* **1994**, *66*, 3173.

(31) Finklea, H. O.; Hanshew, D. D. *J. Am. Chem. Soc.* **1992**, *114*, 3173.

(32) Meyer, T. J. *Acc. Chem. Res.* **1978**, *11*, 94.

(33) Kalyanasundaram, K. *Coord. Chem. Rev.* **1982**, *46*, 159.

(34) Powers, M. J.; Callahan, R. W.; Salmon, D. J.; Meyer, T. J. *Inorg. Chem.* **1976**, *15*, 894.

(35) Robin, M.B.; Day, P. *Adv. Inorg. Chem. Radiochem.* **1967**, *10*, 247.

(36) Dubicki, L.; Ferguson, J; Krausz, E. R.; Lay, P. A.; Maeder, M.; Magnuson, R. H.; Taube, H. *J. Am. Chem. Soc.* **1985**, *107*, 2167.

(37) Barigelletti, F.; Flamigni, L.; Balzani, V.; Collin, J-P.; Sauvage, J-P.; Sour A.; Constable, E. D.; Thompson, J. *J. Am. Chem. Soc.* **1994**, *116*, 7692.

(38) Atkins, P. W., "Physical Chemistry", 1st Ed., Oxford University Press, London, 1978.

(39) Barigelletti, F.; Belser, P.; Von Zelewsky, A.; Juris, A.; Balzani, V.; *J. Phys. Chem.* **1985**, *89*, 3680.

(40) Aldrich Catalogue Handbook of Fine Chemicals, **2000 – 2001**, Aldrich Chemical Company, United Kingdom.

(41) Lakowicz, J. R. "Principles of Fluorescence Spectroscopy", 2nd Ed., Kluwer Academic / Plenum Publishers, New York, **1999**.

(42) Denti, G.; Campagna, S.; Serroni, S.; Ciano, M.; Balzani, V. *J. Am. Chem. Soc.* **1992**, *114*, 2944.

(43) Balzani, V.; Scandola, F. in "Comprehensive Supramolecular Technology", Vol. 10 – Supramolecular Technology, Eds. Atwood, J. L.; Davies, E. D. D.; MacNicol, D. D.; Vöglte, F., Pergamon Press, London, **1996**.

(44) Wang, P.-W.; Fox, M. A. *Inorg. Chem.* **1995**, *34*, 36.

(45) Rehm, D.;Weller, A. *Israel J. Chem.*, **1970**, *8*, 259.

(46) Ballardini, R.; Varani, G.; Indelli, M. T.; Scandola, F.; Balzani, V. *J. Am. Chem. Soc.* **1978**, *100*, 7219.

(47) Bock, C. R.; Connor, J. A.; Guiterrez, A. R.; Meyer, T. J.; Whitten, D. G.; Sullivan, B. P.; Nagle, J. K. *J. Am. Chem. Soc.* **1979**, *101*, 4815.

(48) Forster, R.J.; *Inorg. Chem.* **1996**, *35*, 3394.

(49) Sauvage, J.-P.; Collin, J.-P.; Chambron, J.-C.; Guillerez, S.; Coudret, C.; Balzani, V.; Barigelletti, F.; De Cola, L.; Flamigni, L. *Chem. Rev.* **1994**, *94*, 993.

(50) Acevedo, D.; Bretz, R. L.; Tirado, J. D.; Abruña, H. D. *Langmuir*, **1994**, *10*, 1300.

(51) Walsh, D. A.; Keyes, T. E.; Hogan, C. F.; Forster, R. J. *J. Phys. Chem.*, **2001**, *105*, 2792.

(52) Forster, R. J.; O'Kelly, J. P. *J. Electrochem. Soc.*, **2001**, *148*, E31.

(53) Laviron, E. *J. Electroanal. Chem.* **1974**, *52*, 395.

(54) Brown, A. P.; Anson, F. C. *Anal. Chem.*, **1977**, *49*, 1589.

(55) Bard, A. J.; Faulkner, L. R. "Electrochemical Methods: Fundamentals and Applications", 2nd Ed., Wiley, New York, **2001**.

(56) Feldberg, S. W.; Rubenstein, I. *J. Electroanal. Chem.* **1988**, *240*, 1.

(57) Marcus, R. A. *Angew. Chem. Int. Ed. Eng.* **1993**, *32*, 1111.

(58) Laviron, E. *J. Electronanal. Chem.* **1979**, *101*, 19.

(59) Goodwin, H. A.; Kepert, D. L.; Patrick, J. M.; Skelton, B. W.; White, H. *Aust. J. Chem.*, **1984**, *37*, 1817.

(60) Ferguson, J. E.; Love, J. L.; Robinson, W. T. *Inorg. Chem.*, **1972**, *11*, 1662.

(61) Weber, K.; Creager, S. E. *Anal. Chem.* **1994**, *66*, 3164.

(62) Forster, R. J.; Figgermeier, E.; Loughman, P.; Lees, A.; Hjelm, J.; Vos, J. G. *Langmuir* **2000**, *16*, 7871.

(63) Bagchi, B. *Ann. Rev. Phys. Chem.*, **1989**, *40*, 115.

(64) Sutin, N. *Acc. Chem. Res.*, **1982**, *15*, 275.

(65) Li, T. T.; Guyer, K. L.; Barr, S. W.; Weaver, M .J. *J. Electroanal. Chem.*, **1984**, *164*, 27.

(66) Brunschwig, B. S.; Sutin, N. *Coord. Chem. Rev.* **1999**, *187*, 223.

(67) Bolton, J. R.; Archer, M. D. in "ET in Inorganic, Organic, and Biological Systems", Eds. Bolton, J. R.; Mataga, N.; McLendon, G., American Chemical Society, Washington D.C., **1999**.

(68) Loughman, J. P. Ph.D. Thesis, Dublin City University, 2001.

(69) Ebert, K.; Ederer, H.; Isenhour, T. L. "Computer Applications in Chemistry: An Introduction for PC Users", VCH Publishers: New York, **1989**.

(70) Forster, R. J.; Keyes, T. E.; Vos. J. G. "Interfacial Supramolecular Assemblies: Electrochemical and Photophysical Properties", Wiley, New York, 2002.

(71) Forster, R. J.; Faulkner, L. R. *J. Am. Chem. Soc.* **1994**, *116*, 5453.

Chapter 4

The Effect of Laser Light on Unmodified Electrodes

"There is one thing even more vital to science than intelligent methods; and that is, the sincere desire to find out the truth, whatever it may be"

Charles Sander Pierce

4.1 Introduction

The excited state electrochemistry experiment proposed in Chapter 1 requires laser pulses to promote a monolayer of a ruthenium complex, immobilised on a microelectrode, into an electronically excited state. High-speed voltammetry will allow the excited state redox potentials to be measured before the complex decays back to the ground state. An important control experiment is to investigate the effect of these laser pulses on unmodified electrode surfaces. This chapter details the results of experiments carried out to quantify the effect of pulses from the third harmonic (355 nm) of a 10 Hz, 9 ns Nd:YAG laser on gold macroelectrodes.

As described in Section 1.6 of Chapter 1, many of the previous investigations of the interaction of laser light and electrode surfaces have focused on its impact on electroanalysis, mainly the perspective of generating surfaces that are activated towards electron transfer. For example, McCreery and co-workers have used high intensity (10 – 80 MW cm^{-2}) pulses of 1064 nm light to activate the surface of glassy carbon,[1,2,3] highly-ordered pyrolytic graphite (HOPG)[4] and platinum[5] electrodes. The laser activation results in increased heterogeneous electron transfer rates to solution phase redox probes, by removing adsorbed contaminants and by restructuring the electrode material. Related experiments by Strein and Ewing,[6] have shown that the reversibility of cyclic voltammetry of a series of biological amines at carbon fibre microelectrodes can be significantly improved by treatment with pulses from a nitrogen laser prior to the voltammetric sweep. Watanabe and co-workers[7] have carried out a more aggressive laser treatment on gold electrode surfaces. High – intensity pulses (≈ 360 MW cm^{-2}) of infrared laser light have been used to produce clean electrode surfaces by periodically ablating the top layer of a gold electrode surface during the voltammetric sweep. This approach, known as *laser ablation voltammetry*, can cause significant damage to the electrode surface, limiting the lifetime of the electrode. Compton et al.[8] have adapted this method and used lower-intensity 532 nm light during a potential sweep which causes less damage to the electrode surface. Using this *laser activation voltammetry* technique, they have obtained reproducible steady-state voltammograms at gold and platinum electrodes for analytes which are difficult to analyse by traditional electrochemical means. The technique also allows electrochemistry to take place in passivating media, as the laser pulse periodically removes any material deposited on the electrode during electrochemical experiments.[9]

Beyond these electroanalytical applications, pulsed laser sources have been used to elucidate the structure of the electrode/solution interface, e.g., to study the electrical double layer at mercury[10,11] and gold[12] and platinum[13] single crystal electrodes. The current or potential transients obtained upon laser illumination are typically interpreted as arising from restoration of the double layer and adsorbed ions following perturbation by the laser. Most reports have focused on the dependence of the observed transients on applied potential and on identifying the similarity of the potential of zero response, i.e., the applied potential at which a transient of zero amplitude is observed, with the potential of zero charge of the electrode.

Feldberg and co-workers[14,15] have developed an Indirect Laser Induced Temperature jump method (ILIT) that involves indirect irradiation of the electrode, i.e., the laser pulse impinges on the "back face" or non-electrolyte electrode surface. In this method, some of the incident photons are adsorbed by the thin foil or film electrode and thermalise virtually instantaneously causing a rapid rise in the interfacial temperature. This process changes the open-circuit potential as the system attempts to re-establish equilibrium under the new conditions. This method has been used to probe the electrode kinetics of fast reactions.[15,16]

In this chapter, the effect of nanosecond pulsewidth 355 nm laser pulses of 3 – 11 MW cm^{-2} intensity on the surface and electrochemical properties of gold electrodes is presented. Scanning electron microscopy is used to probe the extent to which laser irradiation triggers structural changes of the electrode surface. When taken in conjunction with measurements of double layer capacitance, open circuit potential and the electron transfer kinetics of a solution phase redox probe, an insight into the mechanism of laser activation has been obtained. Also detailed is the investigation of laser-induced current transients and the origin of this transient response is discussed in terms of models of double-layer structure and thermal properties of interfaces.

4.2 Apparatus and Materials

Potassium ferricyanide (III) and lithium perchlorate were purchased from Aldrich and were used without further purification.

Electrochemical cells were of conventional design. All potentials are quoted with respect to a CH Instruments Ag/AgCl reference electrode which had a potential of +0.190 V with respect to the NHE. Cyclic voltammetry, potential step chronoamperometry and open circuit potential measurements were performed using a CH Instruments Model 660 Electrochemical Workstation and a conventional three-electrode cell, with a platinum flag functioning as counter electrode. The working electrode was a 2 mm diameter gold macrodisc (CH Instruments) and was polished using a slurry of 0.05 μm alumina and water on a felt pad before use. All solutions were degassed using nitrogen.

The light source used in these experiments was a Spectron Lasers Q-switched Nd:YAG laser with a 9 ns pulse width and 10 Hz repetition rate. The laser output is set to the third harmonic at 355 nm. At this wavelength the laser is capable of a power intensity output of between 3.19 and 11.01 MW cm^{-2}. Laser intensities were measured using a Spectron Instruments Triple diode energy monitor No. 23 coupled to a Hewlett Packard 54510A 250 MHz Digitising Oscilloscope.

Laser activation was carried out in air using a Safelab thermometer adapter (Aldrich) as an electrode holder and clamping it in a fixed position in front of the laser. The electrode may be easily positioned inside the adaptor and removed following laser activation.

The capacitance of gold macrodisc electrodes was determined by recording the current decay following the application of a 20 mV potential step across the electrode in a region where there are no faradaic currents present. The decay transients were analysed in Microsoft Excel and the capacitance of the electrode was obtained from the slope and intercept of the linearised current decay. The peak-to-peak separation of potassium ferricyanide(III) cyclic voltammograms (ΔE_p) were determined using the CHI 660 software and the results analysed using Microsoft Excel. Heterogeneous electron transfer rate constants (k^o) were calculated from ΔE_p values using the method of

Nicholson[17] and a Microsoft Excel Solver model. Open circuit potential values were measured using the "open circuit potential" tool in the CH Instruments 660 potentiostat software.

The effect of laser radiation on the capacitance, open circuit potential and electron transfer kinetics of a gold macrodisc electrode was monitored as follows: after 10 minutes polishing, the electrode was placed in a conventional electrochemical cell and the parameter of interest was recorded. The electrode was then removed from the electrochemical cell and placed in the laser activation cell. Approximately 3000 laser pulses were applied to the electrode surface. The electrode was then removed from the laser cell and returned to the electrochemical cell, where the parameter of interest was recorded for the second time.

In-situ laser activation measurements were carried out in the cell depicted in Figure 4.1. The cell was manufactured by drilling an electrode diameter – sized hole in one wall of a polymethylmethacrylate disposable cuvette (Kartell). A watertight seal was achieved by fixing an o-ring over the hole in the cuvette wall with epoxy resin (Radionics) and surrounding the join with silicone sealant (Radionics). The cell was fixed in position in front of the laser by the use of a conventional stand and clamp arrangement. It was filled with the solution of interest, e.g., in the investigation of ferricyanide kinetics, 5 mM solution of $Fe(CN)_6$ in 0.1 M $LiClO_4$, and both electrochemical measurements and laser activation were carried out in the laser cell. The reference and counter electrodes were placed directly in the laser cell.

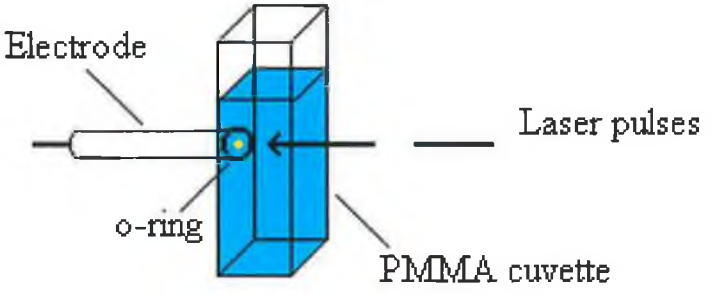

Figure 4.1 Schematic diagram of the cell used for *in-situ* laser activation.

In the measurement of laser current transients, a Hewlett Packard HP8003A Pulse Generator was used to repetitively trigger the application of a fixed potential from a custom-built function generator-potentiostat to a two-electrode cell. A Stanford Research Instruments Model DG535 Four Channel Digital Pulse Generator / Delay Generator was used as controller to simultaneously trigger the laser pulse and a Hewlett Packard 54201A digitising oscilloscope, which was used to monitor the applied potential and capture the current transients. The data was transferred to a PC using a National Instruments GPIB-232CT controller and was analysed in Microsoft Excel. A Pt flag and an Ag/AgCl reference electrode were combined to form a counter electrode. The flag lowered the resistance and provided a high frequency path. The supporting electrolyte throughout was 0.1 M $LiClO_4$.

Scanning electron microscope images were obtained using a Hitachi S3000N Scanning Electron Microscope. All images were obtained using an accelerating voltage of 10 kHz.

Digital Camera images were obtained using a Nikon Coolpix 950 digital camera. Images were uploaded into Microsoft Photo Editor for processing.

4.3 Results and Discussion

4.3.1 Heterogeneous Electron Transfer Dynamics of Potassium Ferricyanide

The ferri/ferrocyanide couple is one of the most extensively investigated outer-sphere electron transfer reactions.[18] However, recent investigations have shown that the electron transfer mechanism is not as simple as previously thought and many authors have observed slow heterogeneous kinetics for potassium ferricyanide at both glassy carbon[19] and metal electrodes.[20,21] These slow kinetics have been attributed to the formation of a Prussian Blue-like passivating film during cyclic voltammetry[22,23] coupled with the general cleanliness of the electrode surface.[19,24] Laser activation has previously been shown to produce fast heterogeneous electron transfer rates for ferricyanide[2,8] but these studies have been restricted to the use of 1064 and 532 nm light for activation. Therefore, ferricyanide has been used here as a redox probe to investigate the effect of 355 nm light at varying power densities on the heterogeneous electron transfer kinetics of a redox reaction and to provide insights as to the mechanism of electrode activation by the laser.

Figure 4.2 shows representative cyclic voltammograms of 5 mM ferricyanide before and after laser activation. Note the improvement in peak shape and the decrease in the peak-to-peak potential separation (ΔEp) effected by the action of the laser. These ΔEp values can be used to calculate the heterogeneous electron transfer rate constant (k^o) for the redox process using the following equation developed by Nicholson:[17]

$$k^{o} = \psi\sqrt{\pi a D_O} \qquad (4.1)$$

where

$$a = \frac{nFv}{RT} \qquad (4.2)$$

k^o is the heterogeneous electron transfer rate constant (cm s^{-1}), D_0 is the diffusion coefficient of ferricyanide (6.30 x 10^{-6} cm^2 s^{-1}),[4] v is the scan rate (V s^{-1}), ψ is a dimensionless parameter relating ΔE_p to the charge transfer rate constant, and n, F, R and T have their usual significance. The accuracy of k^o values determined using this equation was maximized by the use of a Microsoft Excel Solver model to fit the ΔEp

values to Nicholson's working curve of ΔEp vs. ψ. Due to the need for extrapolation of this curve for ΔEp greater than 200 mV, k^o values below 10^{-4} cm s^{-1} are considered to be estimates.

Using these equations to analyse the data presented in Figure 4.2 reveals that k^o for the redox reaction increases from approximately 9.19×10^{-5} to 2.40×10^{-3} cm s^{-1} following laser activation. To verify the accuracy of using Nicholson's method of rate constant determination in these experiments, a series of simulated voltammograms were generated using the simulation tool in the CH Instruments 660A potentiostat software. The heterogeneous electron transfer rate constant determined experimentally using Nicholson's model was entered into the simulation mechanism and the other parameters for the simulation were matched to the experimental conditions. The simulated voltammograms generated using this method were found to compare favorably with the experimental voltammograms. Figures 4.3 and 4.4 demonstrate the fit between the experimental data shown in Figure 4.2 and the corresponding simulated voltammograms. At higher values of ΔEp (Figure 4.4), the fit is less accurate than at lower values of ΔEp (Figure 4.3), due to the aforementioned need to extrapolate Nicholson's working curve. Nevertheless, the figure illustrates that, under these experimental conditions, the Nicholson's theory model is valid for rapidly obtaining estimates of the heterogeneous electron transfer rate constant of a solution phase redox reaction.

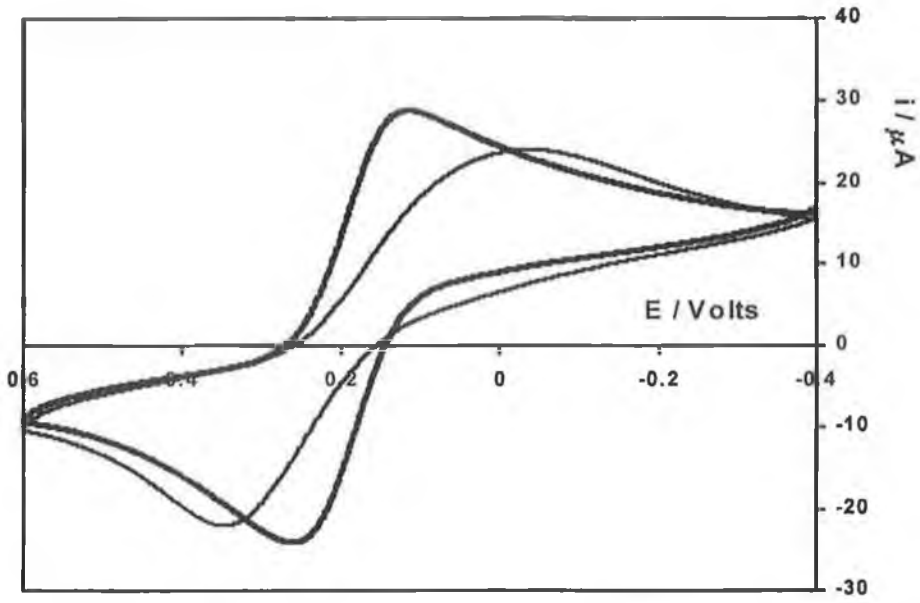

Figure 4.2 Cyclic voltammograms of 5 mM potassium ferricyanide (III) recorded before (thin line) and after (thick line) 3000 pulses of 355 nm, 11 MW cm^{-2} intensity laser activation in water. The scan rate is 0.1 V s^{-1}. The working electrode is a 2 mm diameter gold macrodisk. Potentials are versus Ag/AgCl. The supporting electrolyte is 0.1 M $LiClO_4$.

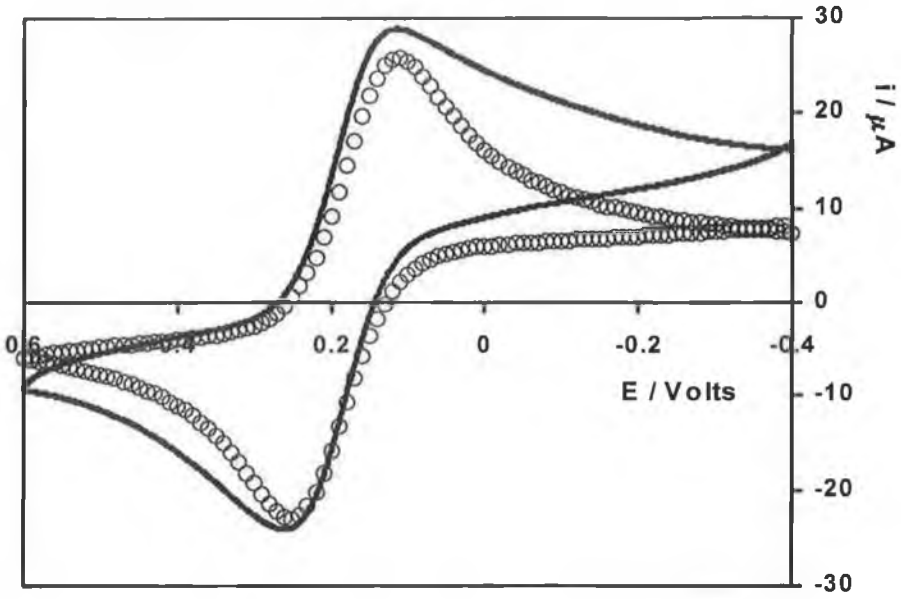

Figure 4.3 Cyclic voltammograms of 5 mM potassium ferricyanide (III) recorded after 3000 pulses of 355 nm, 11 MW cm^{-2} intensity laser activation in water. Thick lines represent experimental data. Open circles represent CVs generated using the CH Instruments 660A simulation software, using parameters identical to experimental conditions. A k° value was determined from the experimental data using the method of Nicholson.[17] Experimental conditions are as for Figure 4.2

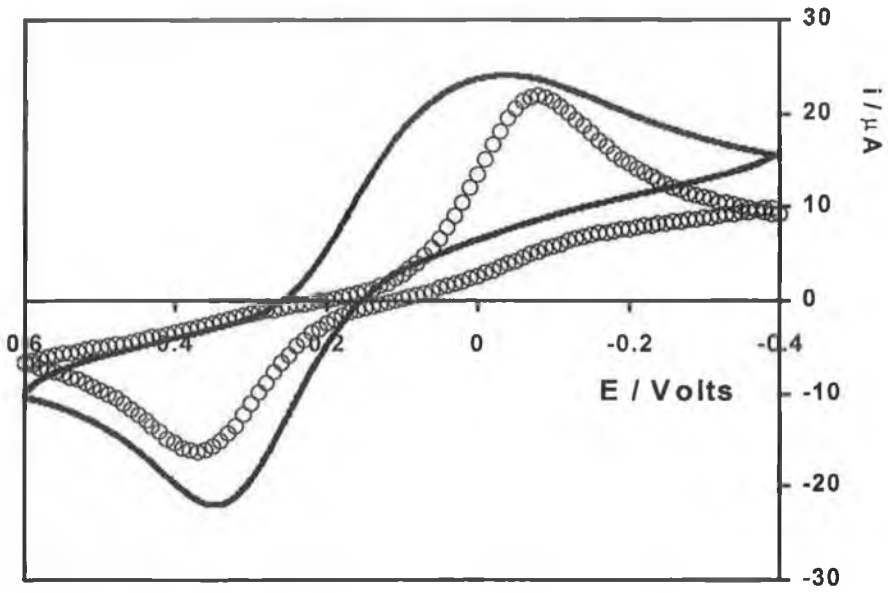

Figure 4.4 Cyclic voltammograms of 5 mM potassium ferricyanide (III) recorded after 10 minutes of conventional polishing with 0.05 μm alumina. Thick lines represent experimental data. Open circles represent CVs generated using the CH Instruments 660A simulation software, using parameters identical to experimental conditions. A k° value was determined from the experimental data using the method of Nicholson.[17] Experimental conditions are as for Figure 4.2

Figure 4.5 details the data obtained from a series of voltammograms obtained following laser activation at increasing intensity. It shows clearly that as the intensity of the laser radiation is sequentially increased, ΔE_p is decreased indicating that k^o for the reaction is increased. The data presented in Figure 4.5 is the average of two replicate experiments, which shows the reproducibility of the trend seen in the graph between experiments. The full data for one experiment is displayed in Table 4.1.

In order to accurately probe the effect of laser pulse intensity on the electron transfer dynamics, it is essential to reproduce similar electrode surface conditions by polishing between activation steps. Figure 4.6 capably illustrates that fast heterogeneous kinetics obtained following laser activation are removed by ten minutes of conventional polishing on a felt pad with a slurry of 0.05 μm alumina and deionised water, following laser activation at all intensities.

As stated previously, this improvement in the electron transfer kinetics of the ferri/ferrocyanide redox system has been previously documented using many types of solid electrodes.[2,4,5,25,26] However, in all these cases, the intensity of the laser radiation used was considerably higher than the intensities used here (10 – 100 MW cm^{-2} as compared to 3 – 11 MW cm^{-2}) and it is interesting to note that the use of laser radiation of comparatively low intensity can still result in a similar improvement in electron transfer kinetics. Also, as will be illustrated later by SEM images before and after laser activation, the damage to the surface of the electrode effected by the laser is minimal, in comparison to similar work such as that reported by Hinoue et al. on ferricyanide kinetics at gold electrodes,[26] where the laser intensity used (350 MW cm^{-2}) causes substantial damage to the electrode surface and hence limits its useful lifetime.

To investigate whether increasing the activation time at constant laser intensity has an effect on the values of k^o obtained, a series of experiments were performed where the laser intensity remained constant while the activation time was varied. Laser activation was carried out in water for 1, 2, 5, 10, 15, 20 and 25 minutes each at intensities of 3, 9 and 11 MW cm^{-2}. Figure 4.7 illustrates the result of these experiments and shows that at all three intensities studied, a longer activation time results in a faster k^o for the redox reaction. However, from the data presented, it can clearly be concluded that an activation time of five to ten minutes is sufficient to achieve the maximum rate constant.

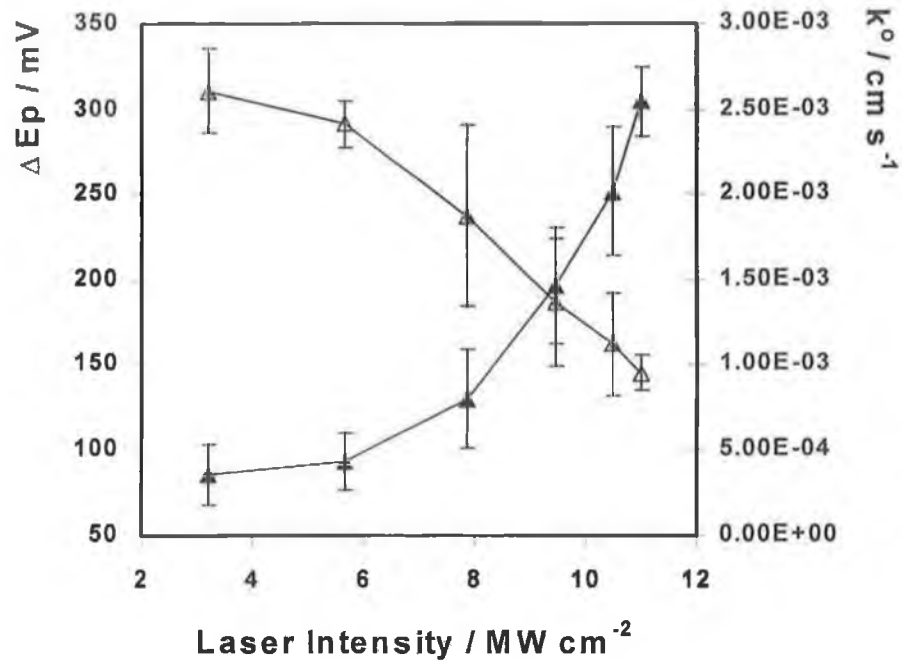

Figure 4.5 Effect of 355 nm laser pulses of increasing intensity on the peak-to-peak separation (open triangles) and heterogeneous electron transfer rate constant (closed triangles) for 5mM potassium ferricyanide (III). 3000 laser pulses were applied to the electrode surface. k° values were determined from the experimental data using the method of Nicholson.[17] Experimental conditions are as for Figure 4.2.

Table 4.1 Electron transfer kinetics for $Fe(CN)_6$[a] achieved with laser activated gold electrodes as a function of increasing laser intensity. Approximately 3000 laser pulses applied to the electrode in aqueous solution.

Laser Intensity [MW cm^{-2}]	$(E_p)_c$ [b] [mV]	$(E_p)_a$ [b] [mV]	ΔE_p [mV]	k^{o} [c] [cm s^{-1}]
3.2	50	344	294	4.75×10^{-4}
5.7	63	344	281	5.47×10^{-4}
7.9	69	344	275	5.90×10^{-4}
9.5	108	321	213	1.22×10^{-3}
10.5	131	315	183	1.75×10^{-3}
11.0	160	313	152	2.69×10^{-3}

[a] 5 mM aqueous potassium ferricyanide. Supporting electrolyte is 0.1 M $LiClO_4$.

[b] Peak potential values determined using CHI 660 software. The error on the value of the peak potential is $\pm$ 2 mV.

[c] k° values were determined from the experimental data using the method of Nicholson.[17] The error on the value of k° is $\pm 2 \times 10^{-6}$ cm s^{-1}.

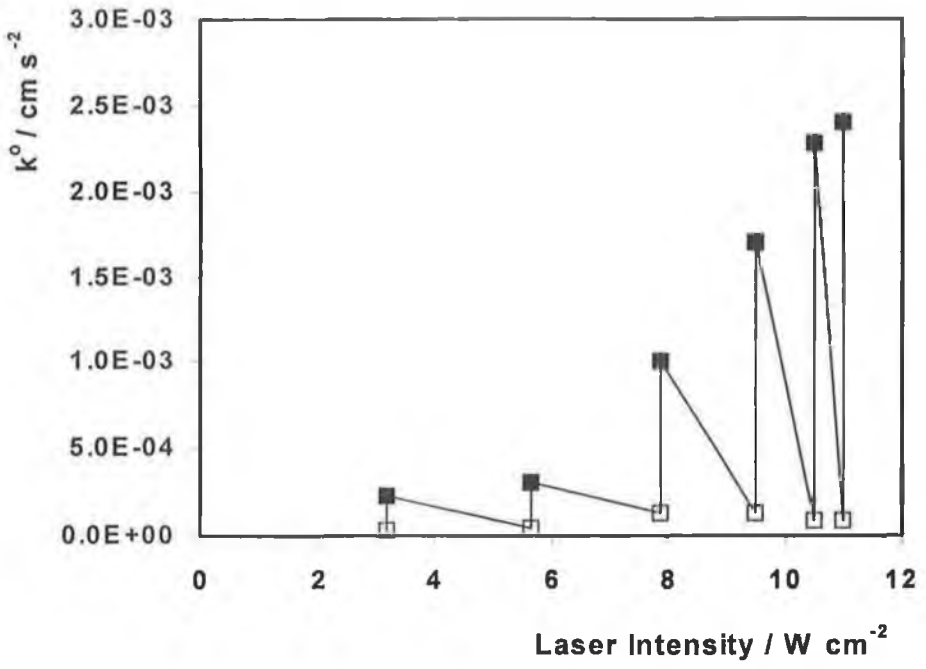

Figure 4.6 Change in k° effected by five minutes of 355 nm laser activation at increasing intensities (closed squares) and by conventional polishing on a felt pad with 0.05 μm alumina between the activation steps (open squares). 3000 laser pulses were applied to the electrode surface. k° values were determined from the experimental data using the method of Nicholson.[17] Experimental conditions are as for Figure 4.2.

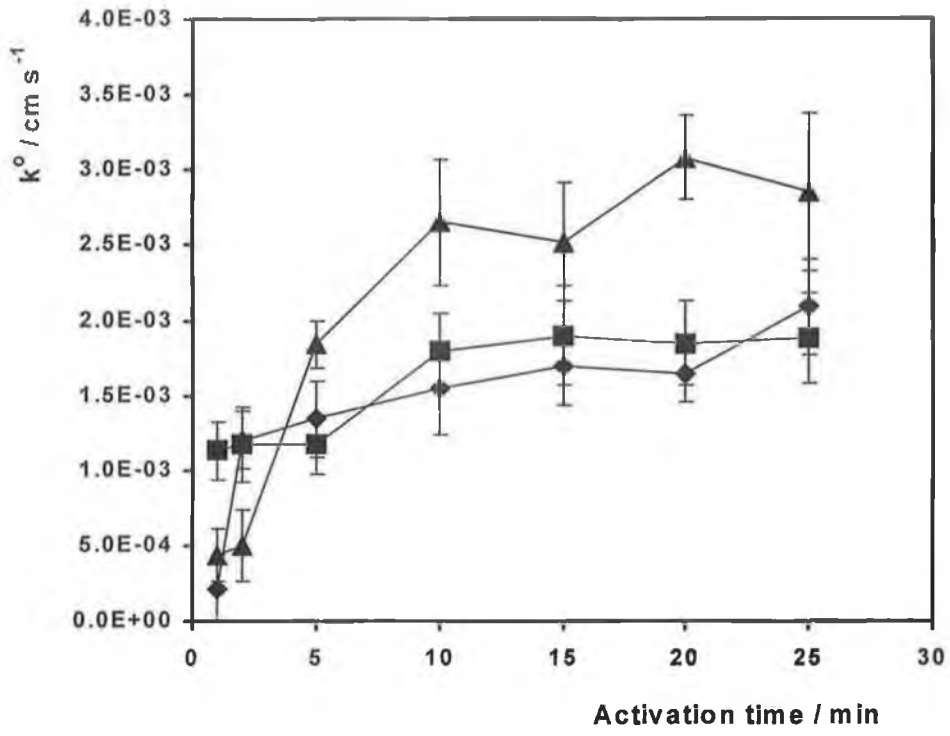

Figure 4.7 Effect of increasing activation time on the k° measured following 355 nm laser activation at 3 MW cm^{-2} (diamonds), 9 MW cm^{-2} (squares) and 11 MW cm^{-2} (triangles) intensity. k° values were determined from the experimental data using the method of Nicholson.[17] Experimental conditions are as for Figure 4.2.

4.3.2 Effect of Laser Activation on Interfacial Properties

In previous reports, two possible mechanisms have been suggested to account for the activation of heterogeneous kinetics seen following laser action which has been detailed in Section 4.3.1. The first suggests that the laser is removing adsorbed particles and electrode material from the electrode surface, which has been used by many authors to explain laser activation of kinetics.[2,25] In order to investigate if the laser light is changing the composition of the electrode surface, the capacitance and open circuit potential (OCP) of the electrode, two parameters which are known to be sensitive to the surface composition of an electrode,[27] were monitored before and after laser activation, with respect to increasing laser intensity. Such electrochemical measurements can provide a rapid and sensitive insight into the properties of the electrode surface. For example, the double layer capacitance, C_{dl}, is extremely sensitive to the composition and structure of the interfacial region and, being an extensive property, depends on the electrode area. Therefore, monitoring C_{dl} before and after laser activation provides an insight into changes in the interfacial structure and electrode area due to laser ablation. In contrast, the open circuit potential, OCP, of the electrode, is an intensive property and is sensitive to the physico-chemical properties, e.g., ablation, of the electrode surface.

In the Gouy-Chapman-Stern (GCS) model of the double–layer at the electrode-solution interface, the differential capacitance is defined as the ability of the interface to store charge in response to a change in potential.[29] The double layer capacitance for a disc-shaped electrode depends on the area of the electrode and is given by:

$$C = \pi r^2 C^o \qquad (4.3)$$

where r is the radius of the electrode and C^o is the specific double layer capacitance of the electrode.[28] Therefore, if laser activation increases the area of the electrode, e.g., by desorbing impurities, then the interfacial capacitance, C, should increase. However, the GCS model of the double layer is based on the mercury-electrolyte interface, whose surface is homogeneous and atomically smooth.[29] For solid electrodes such as gold, platinum and glassy carbon, the surface is not atomically smooth and may be rough at the atomic lengthscale.[29,30] A recent report suggest that the properties of the double layer at solid electrodes are strongly dependent on the crystallographic structure of the

metal surface and that variations in surface structure can have a significant effect on measurements of capacitance.[27] The capacitance of a solid electrode may also be affected by the presence of adsorbed material and polishing debris.[30]

Figure 4.8 illustrates the data obtained for an experiment where the interfacial capacitance of the unmodified electrode was measured following laser activation at increasing intensity. The electrode was polished for 10 minutes between changes of laser intensity. The capacitance was determined by potential step chronoamperometry as described in Section 4.2 of this document. The decays were linear to 1.5 times the RC time constant of the electrode. A linearised decay of 3 times the RC value is normally used for this kind of measurement,[29] but due to the imperfect cleanliness of the electrode surface in these experiments, it was difficult to achieve this degree of linearity. However, the values obtained are sufficient to demonstrate the trend observed in Figure 4.8, which clearly illustrates that as the intensity of the laser light used for activation is increased, the interfacial capacitance of the electrode is increased accordingly.

The effect demonstrated in Figure 4.8 can be explained in terms of the laser effecting either a change in the surface composition of the electrode by removing adsorbed material, or the microscopic surface area of the electrode, or a combination of both. To confirm the theory that the laser light is removing adsorbed material, measurements of the open circuit potential (OCP) of the electrode before and after laser activation were carried out in tandem with the capacitance measurements. As the open circuit potential is an electrode property which depends strongly on the condition of the electrode surface, these measurements should confirm the desorption of material by the laser treatment.

Included in Figure 4.8 is the change in open circuit potential of the unmodified gold electrode effected by laser activation at various intensities. The overall conclusion to be made from these measurements is that the laser is consistently causing a change in OCP measured before and after laser activation, regardless of the laser intensity applied. This result, combined with the measurements of interfacial capacitance detailed earlier, leads to the conclusion that the laser is quite likely desorbing material from the surface of the electrode.

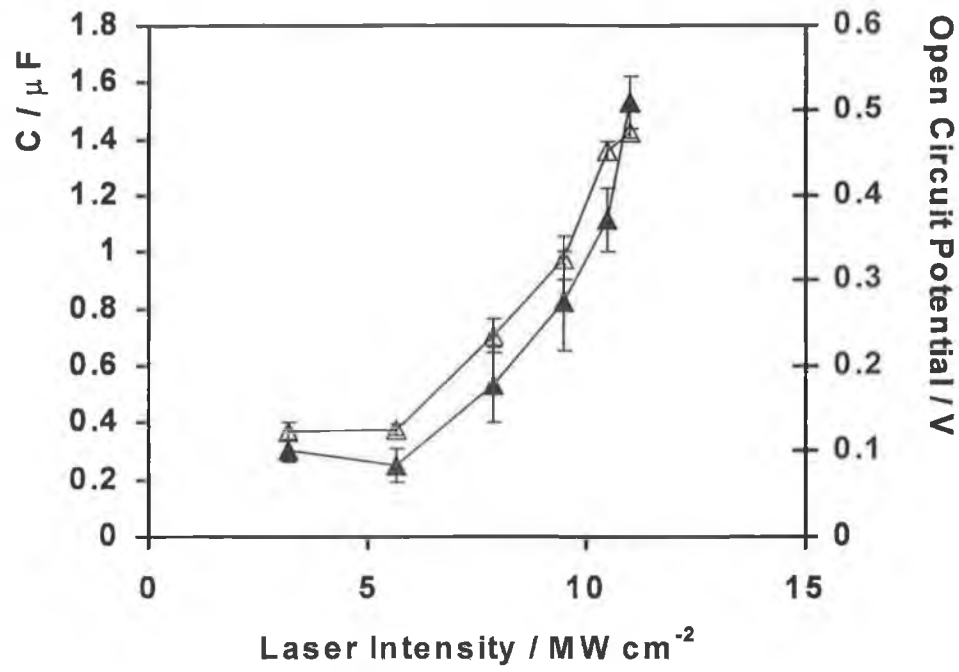

Figure 4.8 Effect of 355 nm laser pulses of increasing intensity on the interfacial capacitance (closed triangles) and open circuit potential (open triangles) of an unmodified 2 mm diameter gold macroelectrode. 3000 laser pulses were applied to the electrode surface. Potentials are versus Ag/AgCl. The supporting electrolyte is 0.1 M $LiClO_4$.

While the open circuit potential measurements support the theory that the laser is desorbing impurities from the electrode surface, the interfacial capacitance results presented earlier may also indicate that the laser light is resulting in a change in the microscopic surface area of the electrode. Presented on the following pages is a set of Scanning Electron Micrographs of the 2 mm diameter gold electrode surface, obtained after polishing and laser activation at three different intensities. The electrode was polished for 10 minutes between activations. To allow the same area of the electrode to be imaged following activation at different intensities, a set of crosshairs were scratched into the surface of the electrode using a scalpel. These had the effect of dividing the electrode into four "quadrants" and allowed for easier comparison of images. Images were obtained of all four quadrants following 10 minutes conventional polishing and laser activation at intensities of 5.7, 9.1 and 11.0 MW cm^{-2}. Following test images using 5, 10, and 15 kV, an accelerating voltage of 10 kV was chosen, as it provided the best compromise between topography and resolution for this surface. Images with magnifications of × 90, × 500 and × 1000 were obtained, however, inspection of these revealed that a magnification of × 500 is sufficient to show the topography of the surface and is presented in Figures 4.9 to 4.12.

Clearly visible in the images presented in are scratches, pits and raised spots caused by the polishing procedure employed. A close examination of each of the images obtained following laser activation reveals minimal differences in the surface topography, suggesting that the laser causes unsubstantial damage to the electrode surface. This observation allows us to confirm that the changes in OCP and capacitance observed are caused primarily by the removal of adsorbed impurities.

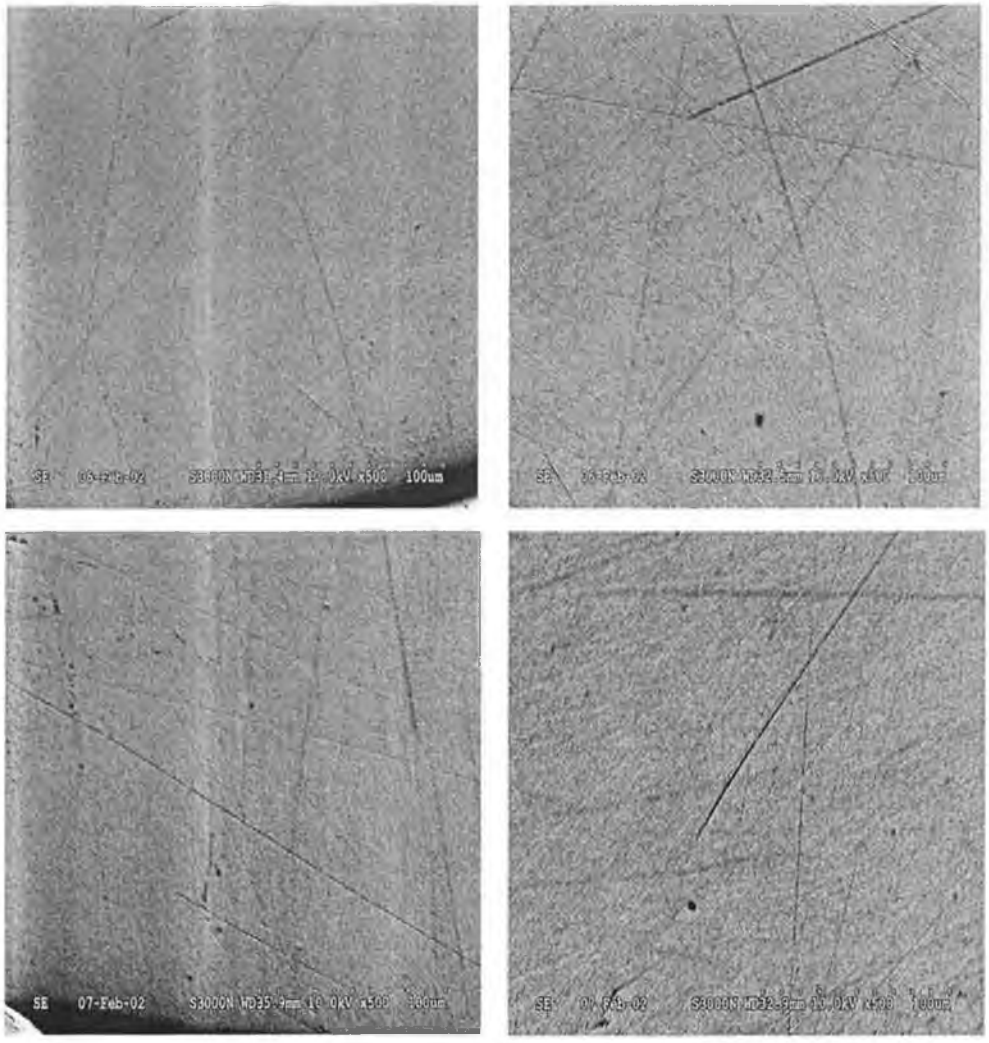

Figure 4.9 Scanning electron micrographs of Quadrant 1 of the surface of a 2mm diameter gold disk electrode following, clockwise from top left, 10 minutes of conventional polishing with 0.05 μm alumina on a felt pad, and activation with 3000 pulses of 355 nm laser radiation of 5.7, 9.1 and 11.0 MW cm^{-2} intensity, respectively. The electrode was polished for 10 minutes in-between laser activations. The magnification used was × 500 and the accelerating voltage was 10 kV.

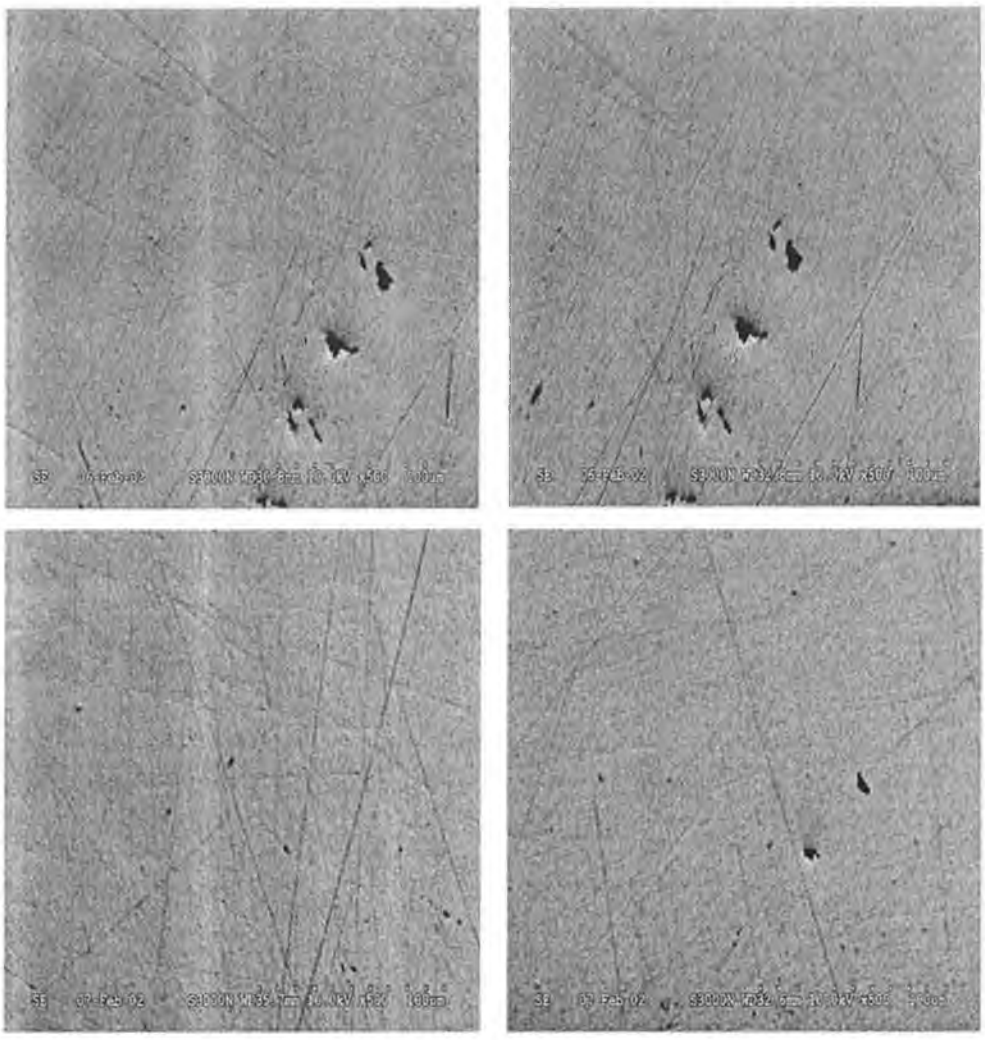

Figure 4.10 Scanning electron micrographs of Quadrant 2 of the surface of a 2mm diameter gold disk electrode following, clockwise from top left, 10 minutes of conventional polishing with 0.05 μm alumina on a felt pad, and activation with 3000 pulses of 355 nm laser radiation of 5.7, 9.1 and 11.0 MW cm^{-2} intensity, respectively. The electrode was polished for 10 minutes in-between laser activations. The magnification used was × 500 and the accelerating voltage was 10 kV.

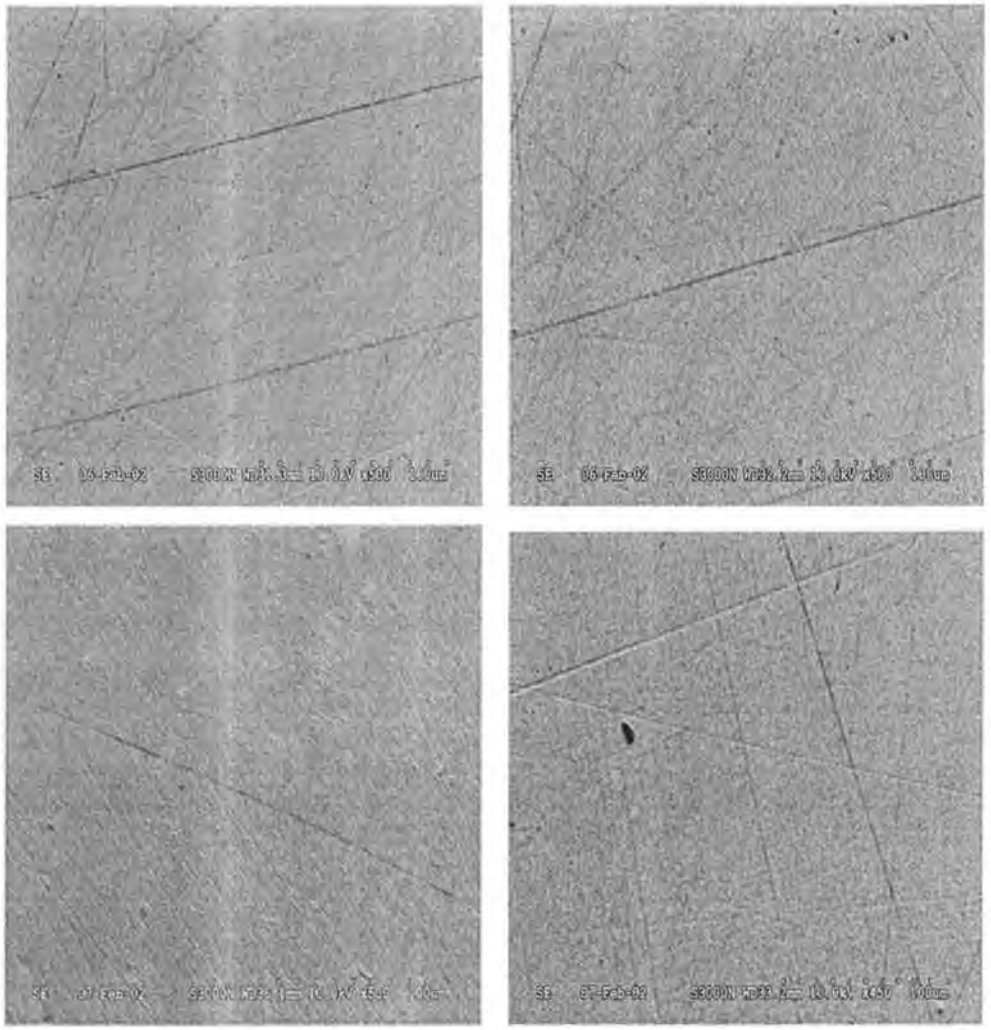

Figure 4.11 Scanning electron micrographs of Quadrant 3 of the surface of a 2mm diameter gold disk electrode following, clockwise from top left, 10 minutes of conventional polishing with 0.05 μm alumina on a felt pad, and activation with 3000 pulses of 355 nm laser radiation of 5.7, 9.1 and 11.0 MW cm^{-2} intensity, respectively. The electrode was polished for 10 minutes in-between laser activations. The magnification used was × 500 and the filament accelerating voltage was 10 kV.

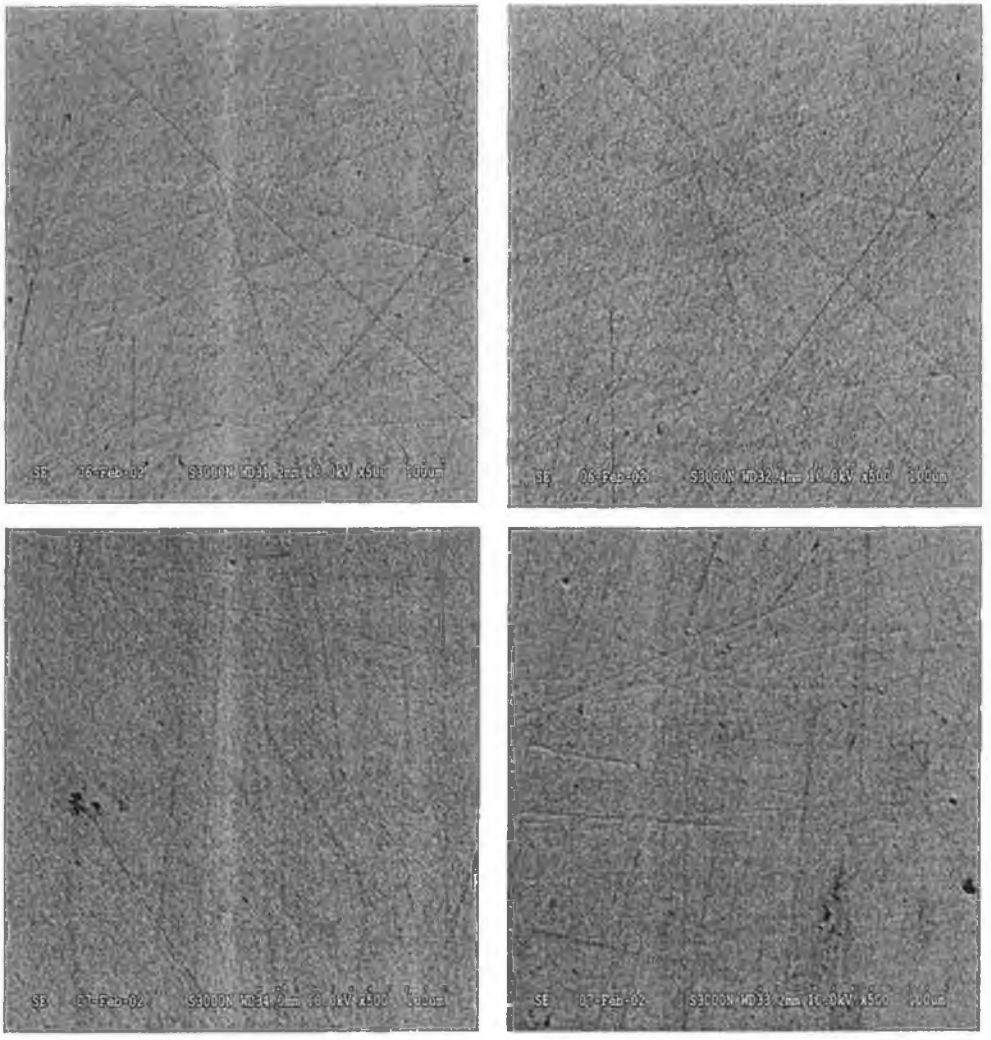

Figure 4.12 Scanning electron micrographs of Quadrant 4 of the surface of a 2mm diameter gold disk electrode following, clockwise from top left, 10 minutes of conventional polishing with 0.05 μm alumina on a felt pad, and activation with 3000 pulses of 355 nm laser radiation of 5.7, 9.1 and 11.0 MW cm^{-2} intensity, respectively. All laser activation was carried out in 0.1 M $LiClO_4$. The electrode was polished for 10 minutes in-between laser activations. The magnification used was × 500 and the filament accelerating voltage was 10 kV.

4.3.3 Thermal Activation Mechanism

While the results in the previous section have shown that the primary mode of activation of the laser treatment is the cleaning of the surface by the removal of adsorbed impurities such as polishing debris, a second mechanism which has been proposed to explain laser activation of heterogeneous kinetics is the heating of the electrode by the laser action. According to the Arrhenius equation,[31] an increase in the temperature of the electrode would cause an increase in the kinetics of the reaction. This heating of the electrode has previously been suggested for the enhancement of the kinetics of metal dissolution and hydrogen evolution at a range of solid electrodes during laser treatment.[32,33] To test the validity of this argument, it is necessary to calculate if a temperature change is effected in the gold electrode by the laser action. This may be achieved using an equation developed by Benderskii et al.,[34] which states that when a metal surface is heated with a laser pulse, the following temperature increase will be attained at the metal surface:

$$\Delta T_m = \frac{2(1-R)q}{\sqrt{\pi \kappa c d} + \sqrt{\pi \kappa_{Soln} c_{Soln} d_{Soln}}} \sqrt{t_0} \qquad (4.3)$$

where κ, c and d and κ_{Soln}, c_{Soln}, and d_{soln} are the thermal conductivity, thermal capacity and density of gold and the aqueous electrolyte solution, respectively, q is the power density of the laser at the surface, which, is assumed to be reduced from the actual laser power density by the reflectivity of the gold surface at 355 nm, (R = 0.387) and t_0 is the laser pulsewidth, 10 ns. The results show that a single laser pulse can heat the surface of the gold electrode by up to 250 K, depending on the intensity of the laser pulse used.

The following equation is used to describe the temperature decay following the laser pulse:[11,32]

$$\Delta T(t) = \frac{1}{2} \Delta T_m \sqrt{\frac{t_o}{t}} \qquad (4.4)$$

where t is the time after the application of the laser pulse, ΔT_m is the temperature change after the laser pulse and ΔT is the temperature change following a time, t, after

the laser pulse has been applied. The results of this model are also tabulated in Table 4.2 and show clearly that the change in surface temperature drops to between 0 and 2 K after 10^{-4} s, depending on the laser pulse intensity.

The results presented in Table 4.2 imply that over the course of a typical laser activation experiment, in which 3000 laser pulses are applied to the electrode surface, the surface temperature of the electrode is repeatedly increasing and decreasing with each laser pulse and will return to its equilibrium value after laser action has stopped. For this heating to increase the heterogeneous kinetics of the ferricyanide redox reaction via an Arrhenius effect, it would have to persist for at least five minutes following laser action, to allow time for the removal of the electrode from the cell and the recording of a CV. This is demonstrated by the model to be clearly impossible and is more likely that the heating of the electrode is assisting in the desorption of impurities from the electrode surface, and it is this cleaning that is responsible for the observed increase in ferricyanide kinetics.

Table 4.2 Temperature increases affected in a gold electrode by a pulse of 355 nm light at various intensities, ΔT_m, and the temperature 10^{-4} s after the laser pulse, $\Delta T(t = 10^{-4}$ s).

Laser Intensity [MW cm^{-2}]	**ΔT_m [K]**	**$\Delta T(t = 10^{-4}$ s) [K]**
3.2	72.2	0.34
5.7	127.7	0.61
7.9	178.0	0.84
9.1	205.8	0.98
9.5	214.5	1.02
10.5	237.4	1.03
11.0	249.1	1.18

4.3.4 *In-situ* Laser Activation of Heterogeneous Electron Transfer Kinetics

In the preceding experiments, the electrochemical investigations were made in a separate electrochemical cell before the electrode was transferred to a laser cell for activation. Following activation, the electrode was returned to the electrochemical cell and the post activation electrochemical measurement recorded. In contrast, the following experiments were carried out entirely in the laser cell, i.e., for the measurement of the heterogeneous kinetics of the ferricyanide redox reaction, the cell was filled with 5 mM $Fe(CN)_6$ in 0.1M $LiClO_4$ electrolyte solution and activation was carried out in this medium instead of air. The purpose of these experiments is to explore the use of laser activation as an *in-situ* pre-treatment procedure for electroanalytical applications.

Figure 4.13 illustrates the results of two replicate experiments where the electrochemical measurements and laser activation were carried out in the laser cell shown in Figure 4.1. The three electrodes remain connected to the potentiostat during laser treatment, but are not kept under potential control. Between changes of laser intensity the electrode is removed from the cell and polished for 10 minutes. The laser cell was refilled with a fresh aliquot of 5 mM $Fe(CN)_6^{3-/4-}$ solution each time the electrode was replaced following polishing. It is clear from Figure 4.13 that the *in-situ* activation results in a similar increase in the heterogeneous rate constant demonstrated for the *ex-situ* measurements in Section 4.3.1. However, it appears that the *in-situ* activation is more effective than the *ex-situ* procedure, as even at the lowest light intensity employed, the k^o value achieved after *in-situ* activation is approximately 2.5 times that achieved following *ex-situ* activation. A full comparison of the *in-* and *ex-situ* results is presented in Table 4.3. The fact that *in-situ* activation is more effective than *ex-situ* may be due to the re-passivation of the electrode by adventitious impurities during transfer from the laser cell to the electrochemical cell in the *ex-situ* procedure. Overall, these results indicate the potential of this *in-situ* activation procedure as a method of electrode cleaning for electroanalytical applications. This approach has been utilised by a number of authors to clean electrodes for use in passivating media and to electrochemically analyse species which are traditionally difficult to detect in a conventional electrochemical set-up.[7,8,9,35]

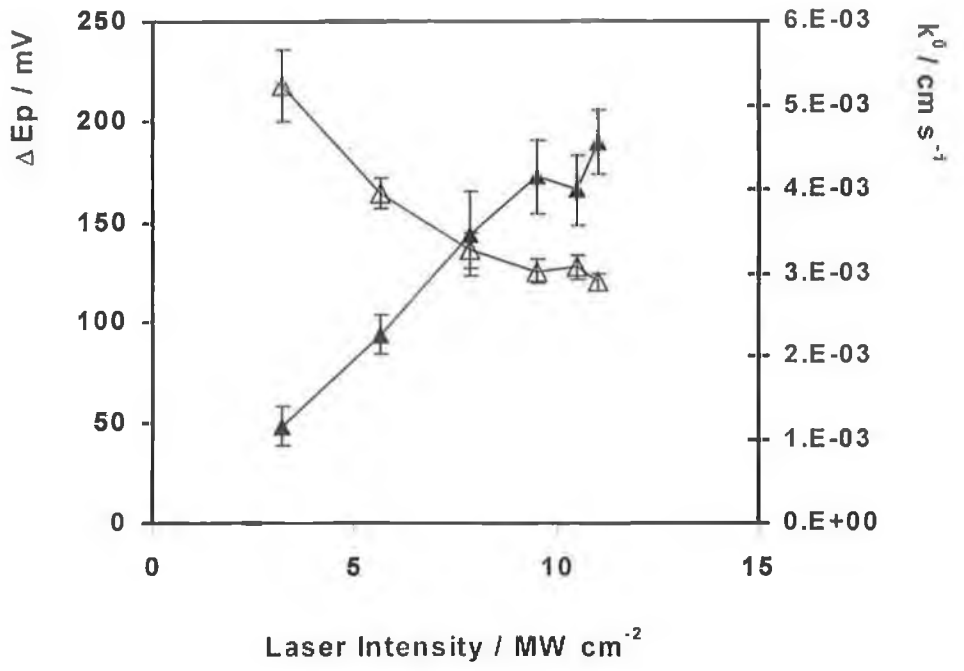

Figure 4.13 Effect of 355 nm laser pulses of increasing intensity on the peak-to-peak separation (open triangles) and heterogeneous electron transfer rate constant (closed triangles) for 5 mM potassium ferricyanide (III). 3000 laser pulses were applied to the electrode in a solution of 5 mM $Fe(CN)_6$ in 0.1 M $LiClO_4$. k° values were determined from the experimental data using the method of Nicholson.[17] Experimental conditions are as for Figure 4.2.

Table 4.3 Comparison of *in-* and *ex-situ* laser $Fe(CN)_6$[a] heterogeneous kinetics laser activation experiments. Approximately 3000 laser pulses applied to the electrode in aqueous solution.

Laser Intensity [MW cm^{-2}]	*ex-situ* ΔEp [b] [mV]	*in-situ* ΔEp [mV]	*ex-situ* k^{o} [c] [cm s^{-1}]	*in-situ* k^{o} [cm s^{-1}]
3.2	294	218	4.75×10^{-4}	1.15×10^{-3}
5.7	281	165	5.47×10^{-4}	2.26×10^{-3}
7.9	275	136	5.90×10^{-4}	3.47×10^{-3}
9.5	213	126	1.22×10^{-3}	4.15×10^{-3}
10.5	183	128	1.75×10^{-3}	3.99×10^{-3}
11.0	152	121	2.69×10^{-3}	4.46×10^{-3}

[a] 5 mM aqueous potassium ferricyanide. Supporting electrolyte is 0.1 M $LiClO_4$.

[b] Peak potential values determined using CHI 660 software. The error on the values is $\pm$ 2 mV.

[c] k^{o} values were determined from the experimental data using the method of Nicholson.[17] The error on the value of k^{o} is $\pm 2 \times 10^{-6}$ cm s^{-1}.

4.3.5 *In-situ* Measurements of Interfacial Capacitance

Following the success of the *in-situ* laser activation method in improving the heterogeneous electron transfer kinetics of the ferricyanide redox reaction, attempts were made to analyse the effects of the laser activation on the interfacial capacitance *in-situ* in the same manner, to determine if the effects seen in the *ex-situ* experiments would be duplicated *in-situ*. As in Section 4.3.4, the electrochemical measurements were carried out in the laser cell, with the counter and reference electrodes placed directly into the cell. The supporting electrolyte material was aqueous 0.1 M $LiClO_4$ and as previously, electrodes were polished for 10 minutes between changes of laser intensity applied.

Figure 4.14 depicts the results of two replicate experiments to test the effect of increasing the intensity of the laser radiation applied on the interfacial capacitance of the electrode. In contrast to the *ex-situ* experiment, these results do not follow an obvious pattern. The first four data points seem to indicate a trend of increased capacitance with increasing applied laser intensity, but the two highest intensities applied yield *lower* values of capacitance than the lower intensities analysed. In particular, for the highest laser intensity, the small error bars indicate the reliability of the capacitance value obtained. To further explore this result, the experiment was repeated without removing the electrode and polishing it between changes of laser intensity. The result of four replicate experiments is also detailed in Figure 4.14 and again the first four intensities yield sequentially increasing values of capacitance, while for the two highest intensities lower values than expected are obtained.

Close observation of the electrode during and after laser activation revealed the presence of small bubbles of liquid on the Teflon body of the electrode and as the intensity of the laser radiation reaches its threshold value, on the surface of the gold itself. To confirm if the presence of these bubbles is interfering with the experiment by disrupting the normal double layer configuration at the electrode solution interface, a digital camera was employed to capture images of the electrode surface while the experiment described above was repeated. These images are detailed in Figure 4.15, while the corresponding capacitance values obtained at increasing laser intensity are depicted in Figure 4.16. The data follows the expected pattern of increasing capacitance with increasing laser intensity until 11 MW cm^{-2}, where the value

decreases with respect to the previous intensity. An inspection of the digital camera images illustrate that this corresponds to the appearance of a significant amount of bubbles on the electrode surface. These will likely disrupt the structure of the double layer at the electrode/solution interface, resulting in values for the interfacial capacitance which deviate from what is expected on the basis of the earlier *ex-situ* measurements. So while we are unable to form any conclusions as the effect of the laser activation on the interfacial capacitance of an unmodified electrode from these *in-situ* measurements, they do support the theory of electrode heating presented in Section 4.3.3, as heating of the electrode surface to the temperatures calculated using the thermal model would likely result in localised boiling of the solution at the electrode/solution interface, particularly at the higher laser intensities employed.

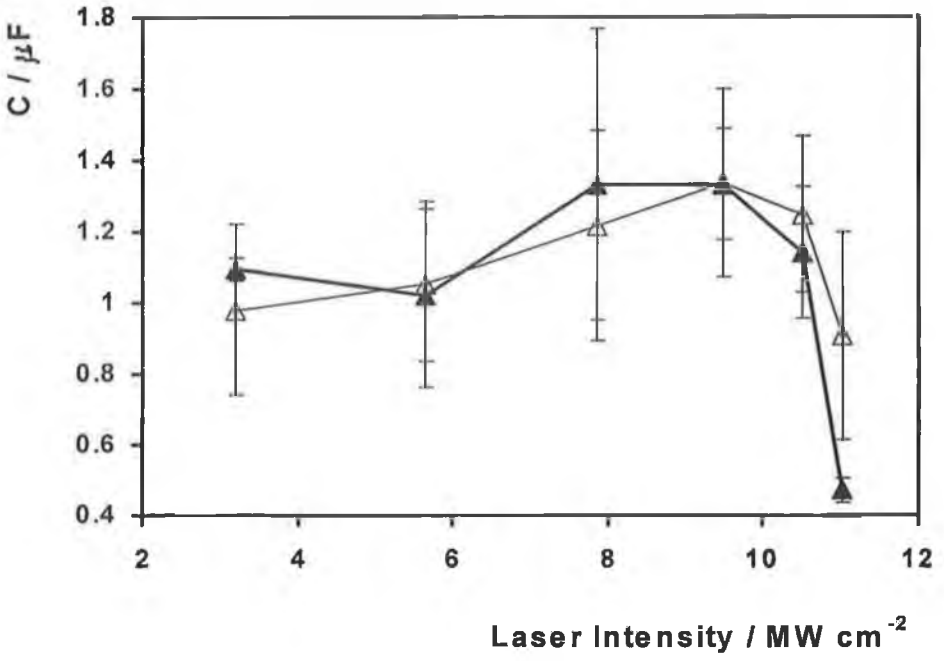

Figure 4.14 Effect of 355 nm laser pulses of increasing intensity on the interfacial capacitance of an unmodified 2 mm diameter gold macroelectrode. Closed triangles indicate data where the electrode was polished for 10 minutes in-between changes of laser intensity. Open triangles indicate data where the electrode was not polished in-between changes of laser intensity. Potentials are versus Ag/AgCl.

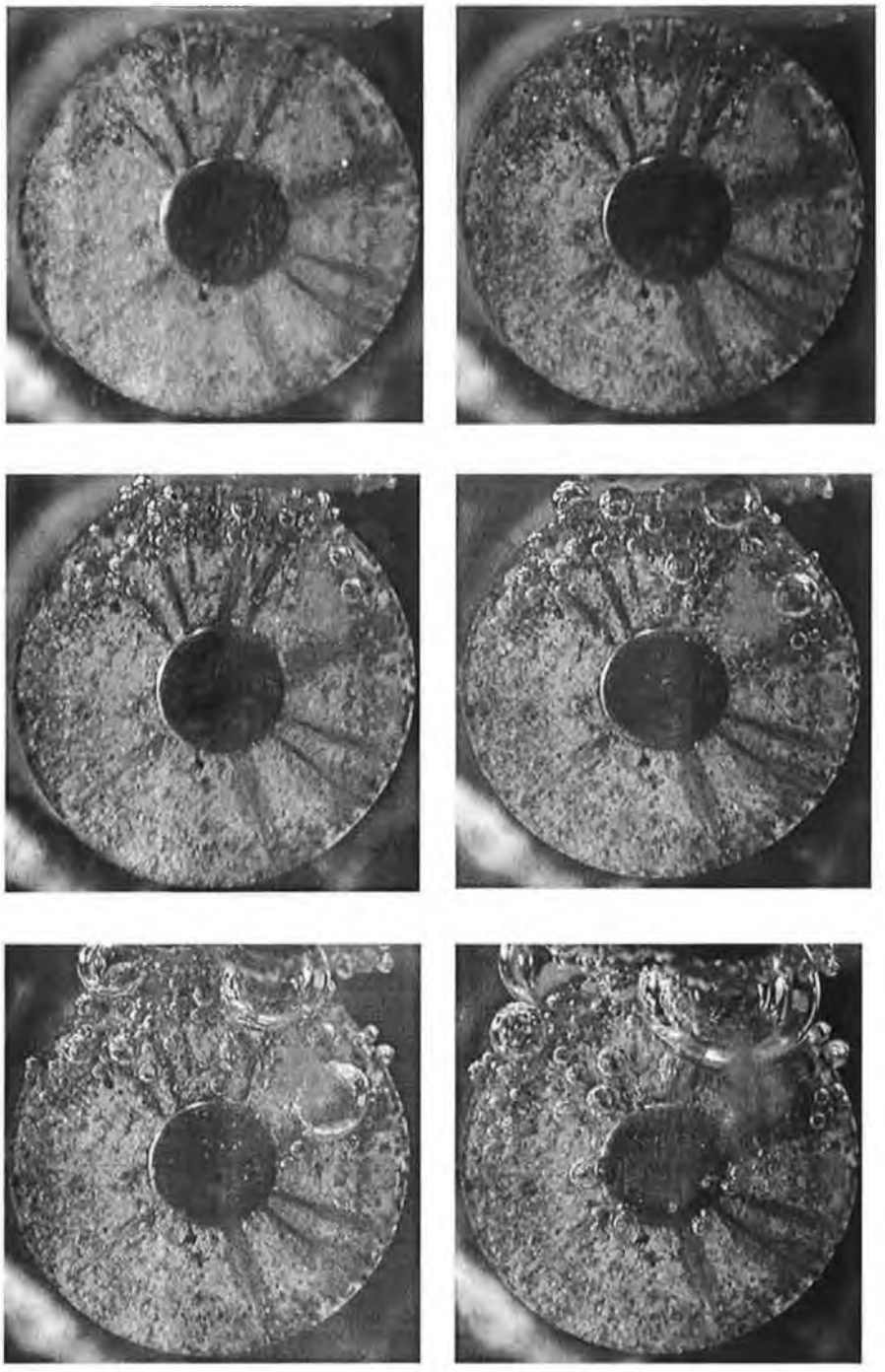

Figure 4.15 Digital camera images detailing bubbles formed on the surface of an unmodified 2 mm diameter gold macroelectrode during laser activation with increasing intensities of 355 nm laser light. Laser activation is carried out for five minutes in aqueous 0.1 M $LiClO_4$. Intensities applied are (left to right, top to bottom) 3.2, 5.6, 7.9, 9.5, 10.5 and 11.0 MW cm^{-2}.

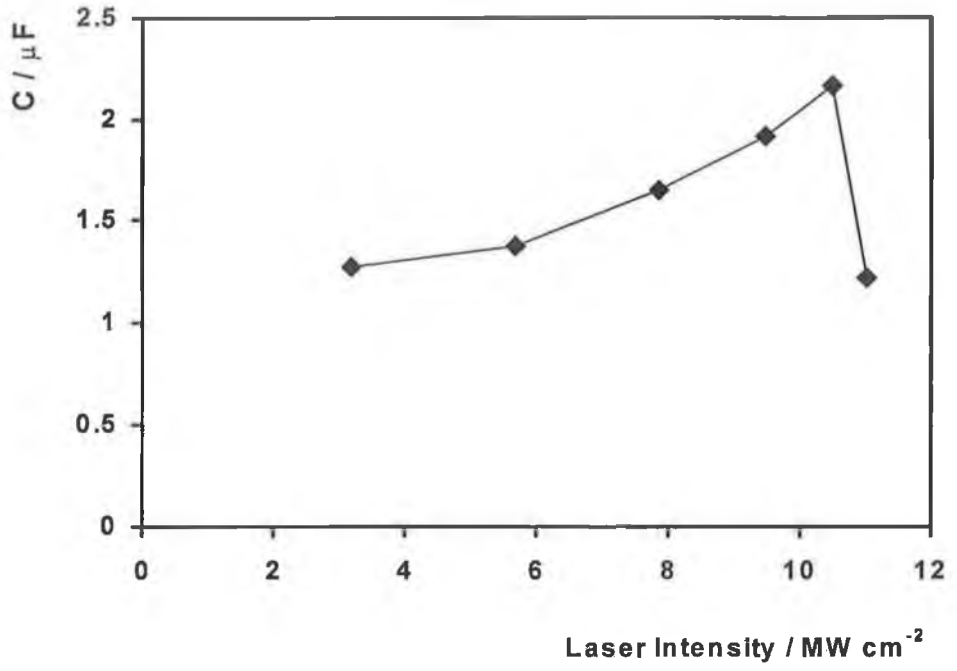

Figure 4.16 Effect of 355 nm laser pulses of increasing intensity on the interfacial capacitance of an unmodified 2 mm diameter gold macroelectrode measured in tandem with the digital camera images in Figure 4.15. The electrode was not polished during changes of laser intensity. Potentials are versus Ag/AgCl.

4.3.6 Laser – Induced Current Transients

Figure 4.17 illustrates voltammograms for a 2 mm diameter gold electrode immersed in aqueous 0.1 M $LiClO_4$ solution measured during laser activation of increasing intensity. The data reveals the presence of small current "spikes" on the normally smooth current of the background cyclic voltammogram. These spikes increase in amplitude as the applied laser intensity is increased, and appear to have the same frequency, regardless of the applied laser intensity. It is interesting to note that the amplitude of the spikes also varies with the potential applied to the electrode, being more significant for large values of the absolute applied potential.

Theory and experiment have demonstrated that impinging a laser pulse causes the electrode surface to heat rapidly, e.g., Table 4.2 shows that ΔT_m is up to 250 K within 9 ns for the highest laser power considered here. Therefore, to accurately record the current-time response associated with both rapid electrode heating and slower cooling, high speed electrochemical instrumentation capable of accurately measuring current responses at nanosecond timescale, has been used. A full description of the experimental set-up may be found in Section 4.2. Laser current transients were obtained as a function of applied potential for a range of potentials from +700 to –700 mV and a selection of the transients are displayed in Figure 4.18. In this system, cathodic currents are positive and anodic currents are negative. The largest transient is obtained at – 700 mV applied potential and the transients decrease in size as the applied potential is made more positive, eventually reaching zero amplitude at + 200 mV and changing to a negative amplitude at potentials from + 200 mV up to a maximum of + 700 mV.

The behaviour of these transients can provide insights as to the structure of the double layer at differing applied potentials. The potential where no transient is observed (+ 200 mV), has been designated as the *potential of zero response* (pzr) by previous authors who have observed this phenomena at glassy carbon,[3] and mercury electrodes.[10,11] The result is also consistent with previous investigations by Compton et al. on polycrystalline gold in contact with $HClO_4$ as the supporting electrolyte.[12] The pzr is analogous to the *potential of zero charge* (pzc) of an electrode, the potential where the charge excesses at the double layer change sign.[29] At potentials positive of the pzr, the observed transient is anodic, suggesting that anions are adsorbed in excess

of cations in the double layer at the electrode/solution interface. The transients obtained at potentials negative of the pzr are cathodic, suggesting that cations are absorbed in excess of anions. This observation is consistent with theory,[29] which states that at positive applied potentials there is a positive excess charge on the electrode surface, and accordingly, at negative potentials there is a negative excess charge. Simple electrostatics predicts that at positive potentials, to balance the excess positive charge, anions will be adsorbed in excess over cations at the electrode surface, and vice versa.

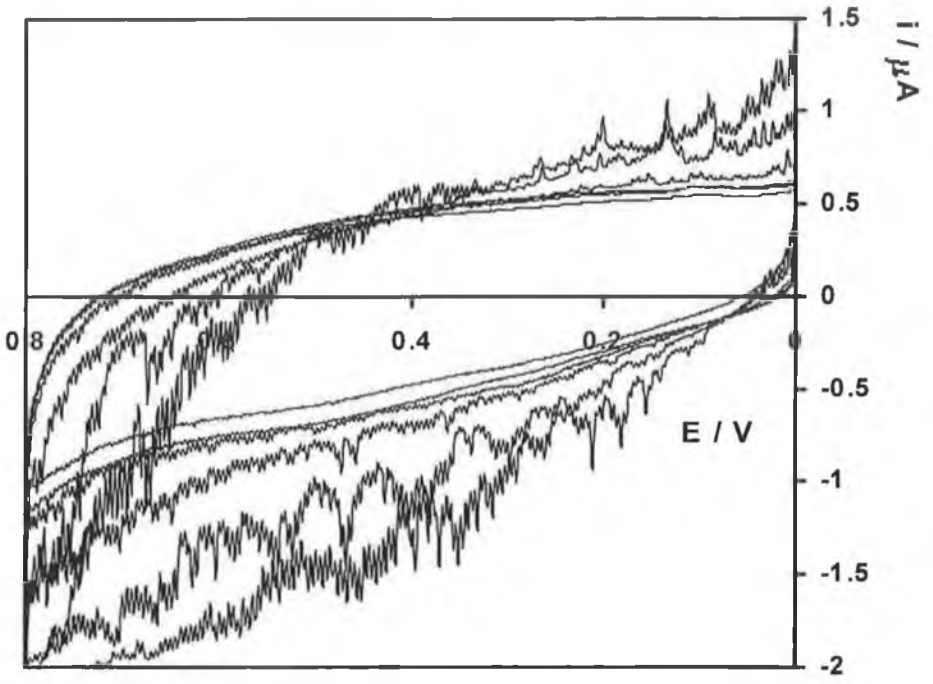

Figure 4.17 Cyclic voltammograms for an unmodified 2 mm diameter gold electrode recorded during the application of laser pulses of increasing intensity. The innermost CV is for the minimum laser intensity and the outermost CV is for the maximum intensity. Cathodic currents are up and anodic currents are down. Potentials are versus Ag/AgCl. The scan rate is 50 mV s^{-1}.

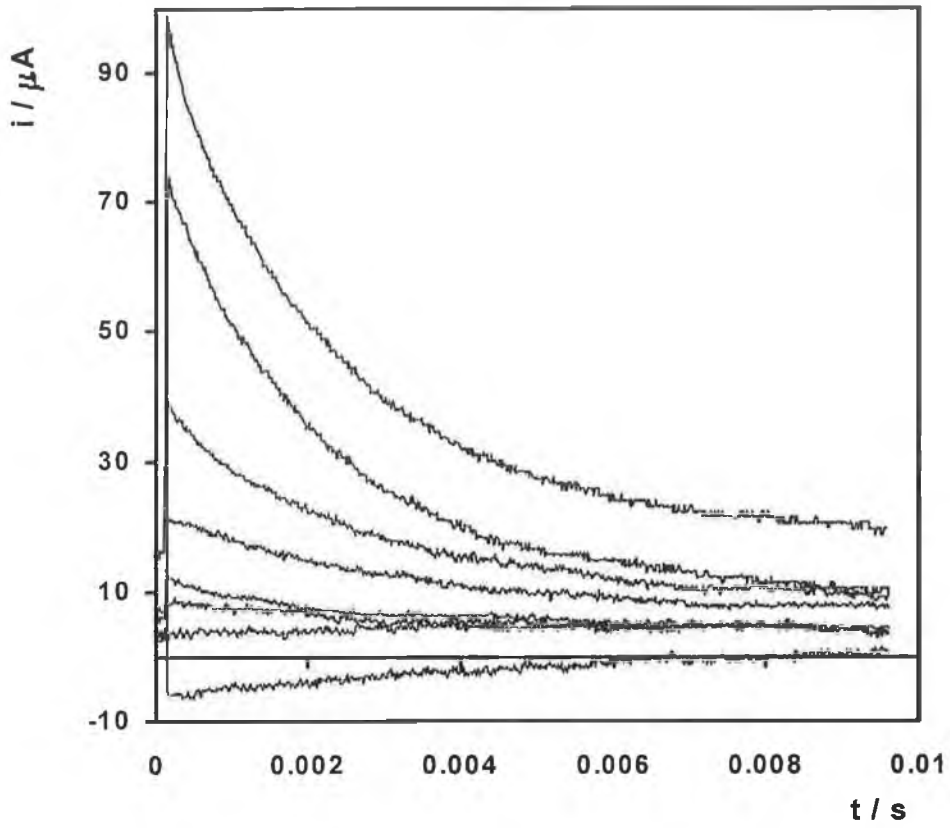

Figure 4.18 Laser-induced current transients observed following the application of a 355nm, 11 MW cm^{-2} intensity laser pulse to a 2mm diameter gold disk electrode in 0.1 M $LiClO_4$, as a function of applied potential. From top to bottom, the applied potential is –700, -400, -200, -100, 0, 100, 200, 600 mV. Cathodic currents are up and anodic currents are down. Potentials are versus Ag/AgCl.

As described in Section 4.3.3, impinging a laser pulse on an electrode causes rapid heating of the surface, followed by a relatively slower cooling process. This rapid change in the interfacial temperature has been described by Benderskii and co-workers. Recalling Equation 4.3, the temperature increase may be calculated as follows:[34]

$$\Delta T_m = \frac{2(1-R)q}{\sqrt{\pi\kappa c d} + \sqrt{\pi\kappa_{Soln} c_{Soln} d_{Soln}}}\sqrt{t_0} \qquad (4.3)$$

where κ, c and d and κ_{Soln}, c_{Soln}, and d_{soln} are the thermal conductivity, thermal capacity and density of gold and the aqueous electrolyte solution, respectively, q is the power density of the laser at the surface, which, is assumed to be reduced from the actual laser power density by the reflectivity of the gold surface at 355 nm, (R = 0.387) and t_0 is the laser pulsewidth, 9 ns.

As expressed within the Gouy-Chapman-Stern model of the electrochemical double layer,[29] the double layer capacitance, C, is expected to *decrease* with an *increase* in the interfacial temperature. Therefore, one might expect that the short timescale current response would be dominated by capacitive current, $i_c(t)$, arising from the virtually instantaneous thermally driven restructuring of the double layer. Under these circumstances, the current-time response can be analysed according to:[29]

$$i_c(t) = \Delta E/R \exp\left(-\frac{t}{RC}\right) \qquad (4.5)$$

where ΔE is the thermally driven change in the interfacial potential and R is the total cell resistance.

The change in the interfacial potential is related to the interfacial entropy of formation of the interface, ΔS_{Form}, according to the electrocapillary equation:

$$\frac{\partial E}{\partial T} = -\left(\frac{\partial \Delta S_{Form}}{q}\right)_T \qquad (4.6)$$

where q is the double-layer charge.

The longer timescale current decay then corresponds to the relatively slower cooling response and is given by:[11]

$$\Delta T_m = \frac{2(1-R)q}{\sqrt{\pi\kappa c d} + \sqrt{\pi\kappa_{Soln} c_{Soln} d_{Soln}}}\left[\sqrt{t-\sqrt{t-t_0}}\right] \qquad (4.7)$$

Therefore, by combining Equations 4.5 and 4.7, it should be possible to fit the complete current-time transient. Analysis of this kind is important for the following reasons. First, it can provide an insight into the mechanism of laser activation of electrodes towards heterogeneous electron transfer that is useful for electroanalysis. Second, an insight into double layer structure can be obtained. Third, the potential dependence of the thermal conductivity and capacity of metals can be probed by investigating the dependence of the laser induced current transients on the applied potential.

Figure 4.19 illustrates the best fits to the experimental data obtained by combining Equations 4.5 and 4.7 where κ, c, ΔE, R and C are freely adjustable parameters. The quality of the fit is excellent with the combination model accurately reproducing the current-time transients. A similar quality fit is obtained for all values of the applied potential investigated. An important test of the validity of this approach is to probe whether it accurately predicts the expected decrease in C at higher temperatures, as well as the potential dependence of C and R. Figure 4.20 illustrates the potential dependence of C and R extracted using the combination model. For all potentials investigated, the interfacial capacitance is approximately 50% lower than that determined using conventional potential step chronoamperometry at room temperature. This decrease in C is consistent with the predictions of Equation 4.3, which predicts an increase in the interfacial temperature of approximately 250 K immediately after the 9 ns laser pulse with a power density of 11 $MWcm^{-2}$. Moreover, consistent with theory, and experimental measurements, a minimum C value (pzr) is observed at approximately +0.2 V.[36] Also, the total cell resistance is independent of the applied potential, 135±14 Ω, and is consistent with that found using small amplitude potential step chronoamperometry, 150±10 Ω. As shown in Table 4.4, the change in the interfacial potential induced by the laser pulse, ΔE, depends on the applied potential with values between 8 and 1 mV being observed at –0.700 and +0.600 V. These values are entirely consistent with those reported by Compton for single crystal gold and platinum using a coulostatic potential transient approach[13,37] further supporting the use

of Equations 4.5 and 4.7 to model the current transients. The absolute magnitude of C and R as well as their potential dependences, strongly suggest that it is appropriate to model the short time scale current response according to Equation 4.5 and that laser induced current transients can provide an insight into the properties of interfaces at temperatures that are not accessible using other approaches.

Figure 4.21 shows the potential dependence of the metal thermal conductivity and thermal capacity. It is important to note that despite the fact that κ and c are freely adjustable variables within the model, the best fit is obtained with values that are close to literature values for gold at room temperature, 3.15 J cm^{-1} K^{-1} and 0.129 J g^{-1} K^{-1}, respectively. This close agreement suggests that Equation 4.7 provides an appropriate description of the longer timescale current decay and arises in part because of changes in the thermal and electronic properties of the gold electrode, as well as thermally driven double layer restructuring as the electrode cools. Figure 4.21 provides an insight into the potential dependence of the thermal properties of the metal side of the gold/solution interface. Both κ and c show marked potential dependence with the maximum values being observed at approximately +0.1 V with lower values being observed for more positive or negative potentials. Potential dependent changes in the reflectivity of the electrode surface would cause the temperature change induced by the laser pulse to depend on the applied potential which would make κ and c appear to be potential dependent. However, given that κ is expected to decrease with increasing temperature while c is expected to increase, the observation in Figure 4.21 that the potential dependence of κ and c is indistinguishable strongly suggests that potential dependent changes in electrode reflectivity are not the origin of the observed behaviour.

Significantly, as illustrated in Figure 4.22, the thermal diffusion coefficient depends approximately linearly on the applied potential. It is perhaps important to note that the experimentally determined thermal diffusion coefficients are all smaller than that of gold at 298 K, i.e., 1.314 cm^2s^{-1}, which, given that D_T decreases with increasing temperature, is consistent with heating of the interface. The thermal diffusion coefficient obtained at the potential of zero response, 1.264 cm^2s^{-1}, has been used to estimate the interfacial temperature as approximately 490 K immediately following the 9 ns laser pulse. The thermal diffusion coefficient is known to decrease with increasing temperatures and these literature data can be used to estimate the interfacial temperature as approximately 490 K immediately following the 9 ns laser pulse. An

important test of internal consistency is to compare this value with that predicted by the Benderskii model.[11] Equation 4.3 predicts that for a 9 ns laser pulse with a laser power density of 11 $MWcm^{-2}$ the interfacial temperature will rise to approximately 550 K. Given the approximations involved in both of these approaches, the agreement between the predicted interfacial temperatures is satisfactory. However, while this data does not allow this potential dependent reflectance possibility to be discounted, the potential dependence of κ and c discussed above suggest that it is not appropriate. There are several factors that are likely to contribute to the observed potential dependence of D_T including changes in the electron density of the metal and the Fermi electron drift velocity as the voltage and hence the electric field within the metal is changed.

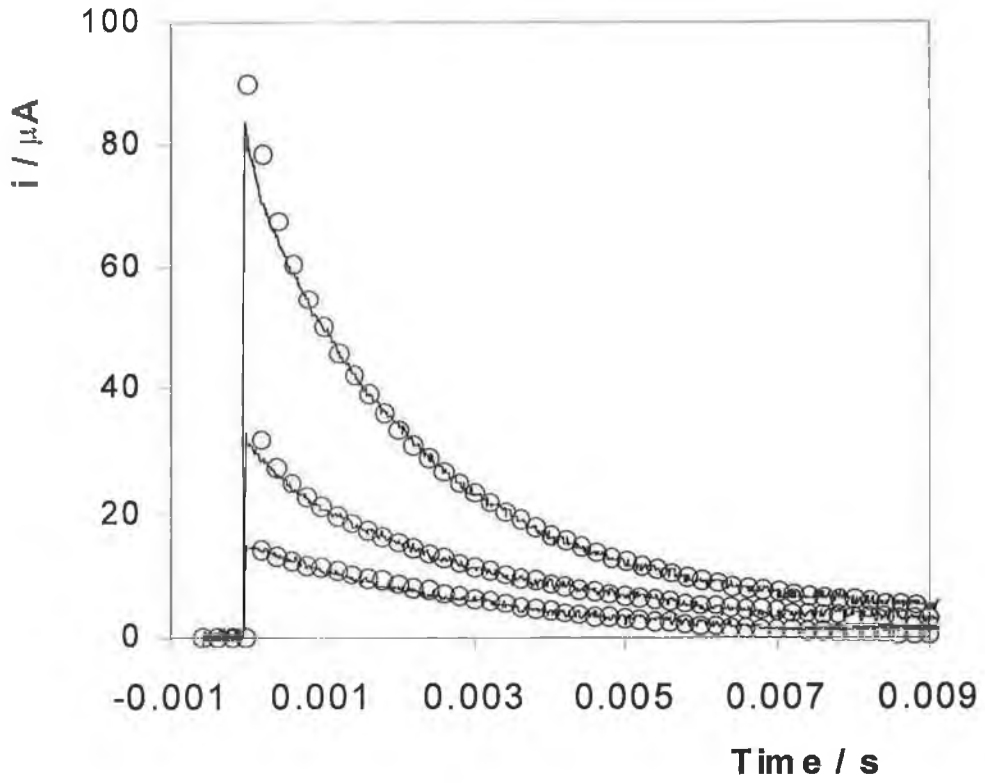

Figure 4.19 Laser-induced current transients observed following the application of a 355 nm, 11 MW cm^{-2} intensity laser pulse to a 2 mm diameter gold disk electrode in aqueous 0.1 M $LiClO_4$, as a function of applied potential. From top to bottom, the applied potential was –700, -200, and -100 mV, respectively. The open circles are the best fits of the experimental data to Equations 4.5 and 4.7 that models the current-time transient in terms of double layer charging at short times and a slower cooling response at longer times.

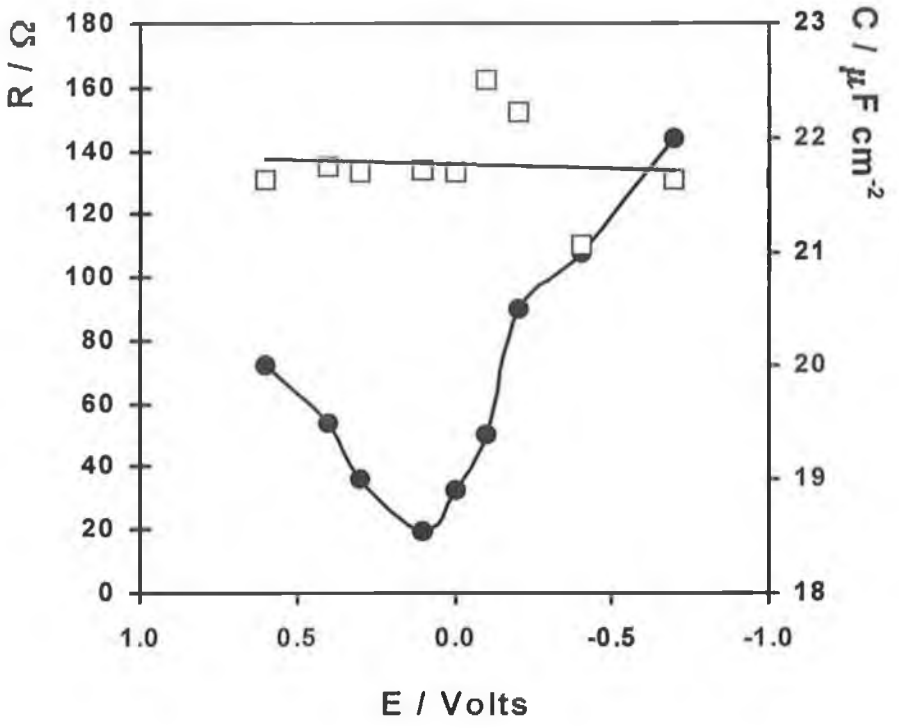

Figure 4.20 Potential dependence of the resistance, R, (open squares) and capacitance, C, (solid circles) of a 2 mm diameter gold disc electrode. Data was extracted from the laser-induced current transients using the combination model described in the text.

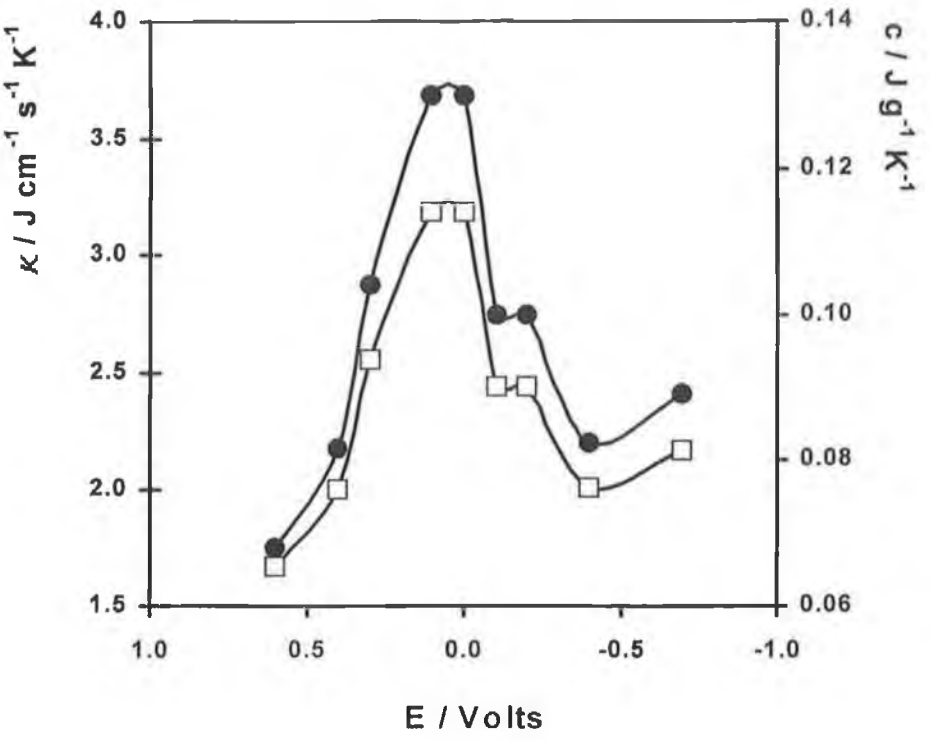

Figure 4.21 Potential dependence of the thermal conductivity, κ, (open squares) and heat capacity, c, (solid circles) of a 2 mm diameter gold disc electrode. Data was extracted from the laser-induced current transients using the combination model described in the text.

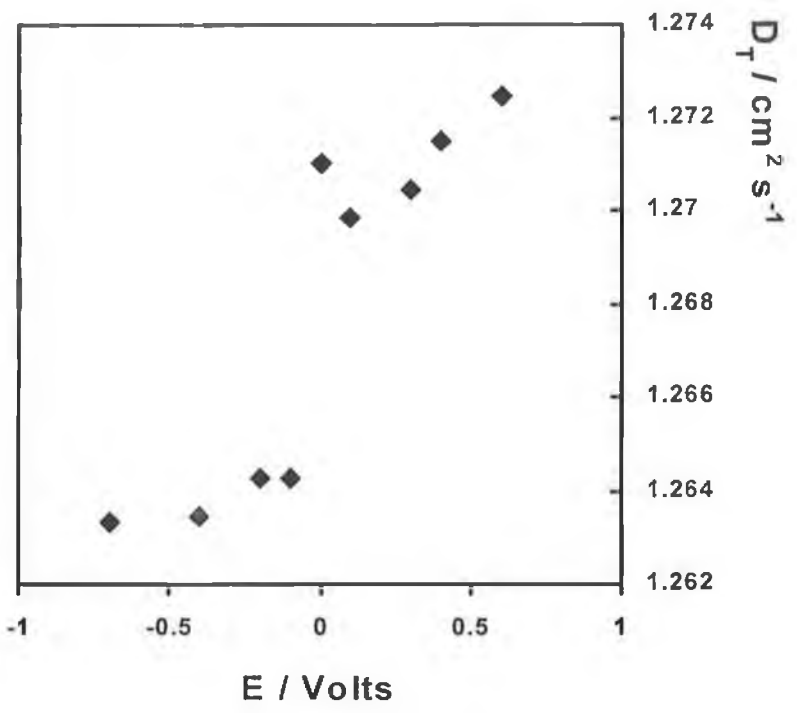

Figure 4.22 Potential dependence of the thermal diffusion coefficient, D_T, for gold as determined by modeling the long time scale response of the laser induced current transient induced by a 9 ns pulse of 355 nm laser light at a power density of 11 MW cm^{-2}.

Table 4.4 Table of electrode-solution parameters obtained from the combination model described in the text.

E [V]	ΔE [mV]	R [Ω]	C [μF cm^{-2}]	κ [J cm^{-1} s^{-1} K^{-1}]	c [J g^{-1} K^{-1}]	D_T [cm^2 s^{-1}]
-0.7	7.9	131	22.0	2.17	0.09	1.263
-0.4	5.3	110	21.0	2.01	0.08	1.263
-0.2	3.3	152	20.5	2.44	0.10	1.264
-0.1	3.2	162	19.4	2.44	0.10	1.264
0.0	1.3	133	18.9	3.19	0.13	1.267
0.1	1.3	134	18.6	3.19	0.13	1.267
0.3	1.2	133	19.0	2.55	0.10	1.270
0.4	1.2	135	19.5	2.00	0.08	1.271
0.6	1.2	131	20.0	1.67	0.07	1.272

4.4 Conclusions

The results presented in this chapter have shown that the application of MW cm^{-2} laser pulses to an unmodified gold macrodisc electrode affects the rate of heterogeneous electron transfer for a solution phase redox probe. The rate of electron transfer can be significantly improved, with the extent of the improvement related to the intensity of the laser pulses applied. This improvement is removed by conventional polishing with a slurry of alumina and water on a felt pad, indicating the superiority of laser treatment over polishing for electrode preparation. The mode of action of the laser, determined using measurements of capacitance, open circuit potential and SEM images of the electrode surface, was determined to be the removal of adsorbed particles which inhibit electron transfer. The model presented in Section 4.3.3 has shown that the rapid heating of the electrode by the laser pulse thermally assists this removal of debris. The effect on heterogeneous electron transfer rates is more marked when the activation is carried out *in-situ*, indicating that this method is very suitable as an electrode pre-treatment procedure for electroanalytical applications.

Laser-induced current transients which occur following the application of a single laser pulse to a gold electrode in blank electrolyte solution have been recorded using a high-speed electrochemical system. The transients depend on applied potential. Anodic transients are obtained at applied potentials positive of + 200 mV, the potential of zero response, and cathodic transients at potentials negative of this value. The transients have been fit using a model which describes the current-time transient in terms of double layer charging at short times and a slower cooling response at longer times. The results of the model with respect to capacitance are consistent with the predictions of Gouy-Chapman-Stern theory. The fit of the model to the longer timescale data has provided an insight into the potential dependence of the thermal properties of the metal side of the electrode/solution interface. Significantly, the model predicts a potential dependence of the thermal diffusion coefficient and heat capacity of the gold metal, which is not explained by an electroreflectance effect. The thermal diffusion coefficient of the gold metal also displays a potential dependence. The values of D_T obtained are all smaller than that for gold at 298 K, and as the thermal diffusion coefficient is expected to decrease with increasing temperature, this further reinforces the theory of electrode heating by the laser pulses.

The main conclusion to be drawn from this investigation is that laser pulses can have a significant effect on the electron transfer, interfacial and thermal properties of a gold macrodisc electrode. However, for the lowest laser intensity studied, 3 MW cm^{-2}, the effect on these properties is significantly smaller when compared to the highest intensity, 11 MW cm^{-2}. This has important ramifications for the excited state electrochemistry experiment, where laser pulses will be applied to an adsorbed monolayer on a microelectrode during a high-speed potential sweep, as it indicates that the laser pulses applied must be of low intensity, in order to avoid significant damage to an adsorbed monolayer.

REFERENCES

(1) Hershenhart, E.; McCreery, R. L.; Knight, R. D. *Anal. Chem.* **1984**, *56*, 2256.

(2) Rice, R. J.; Pontikos, N. M.; McCreery, R. L. *J. Am. Chem. Soc.* **1990**, *112*, 4617.

(3) Jaworski, R. K.; McCreery, R. L. *J. Electrochem. Soc.* **1993**, *140*, 1360.

(4) Bowling, R. J.; Packard, R. T.; McCreery, R. L. *J. Am. Chem. Soc.* **1989**, *111*, 1217.

(5) Huang, W.; McCreery, R. L. *J. Electroanal. Chem.* **1992**, *326*, 1.

(6) Strein, T. G.; Ewing, A. G. *Anal. Chem.* **1991**, *63*, 194.

(7) Hinoue, T.; Kuwamoto, N.; Watanabe, I. *Journal of Electroanal. Chem.* **1999**, *466*, 31.

(8) Akkermans, R. P.; Suárez, M. F.; Roberts, S. L.; Fulian, Q.; Compton, R. G. *Electroanalysis* **1999**, *11*, 1192.

(9) Fulian, Q.; Compton, R.G. *Anal. Chem.* **2000**, *72*, 1830.

(10) Barker, G. C.; Cloke, G. *J. Electroanal. Chem.* **1974**, *52*, 468.

(11) Benderskii, V. A.; Velichko, G. I. *J. Electroanal. Chem.* **1982**, *140*, 1.

(12) Climent, V.; Coles, B. A.; Compton, R. G. *J. Phys. Chem. B* **2001**, *105*, 10669.

(13) Climent, V.; Coles, B. A.; Compton, R. G. *J. Phys. Chem. B* **2002**, *106*, 5258.

(14) Smalley, J. F.; Krishnan, C. V.; Goldman, M.; Feldberg, S. W.; Ruzic, I. *J. Electroanal. Chem.* **1988**, *248*, 255.

(15) Smalley, J.F.; Feldberg, S.W.; Chidsey, C.D.; Linford, M.R.; Newton, M.D.; Liu, Y.P. *J. Phys. Chem.* **1995**, *99*, 13141.

(16) Sachs, S. B.; Dudek, S. P.; Hsung, R. P.; Sita, L. R.; Smalley, J. F.; Newton, M. D.; Feldberg, S. W.; Chidsey, C. E. D. *J. Am. Chem. Soc.* **1997**, *119*, 10563.

(17) Nicholson, R. S. *Anal. Chem.* **1965**, *37*, 1351.

(18) Peter, L. M.; Durr, W.; Bindra, P.; Gerischer, H. *J. Electroanal. Chem* **1976**, *71*, 31.

(19) Wrightman, R. M.; Deakin, M. R.; Kovach, P. M.; Kuhr, W. G.; Stutts, K. J. *J. Electrochem. Soc.* **1984**, *131*, 1579.

(20) Winkler, K. *J. Electronanal. Chem* **1995**, *388*, 151.

(21) Iwasaki, Y.; Horiuchi, T.; Morita, M.; Niwa, O. *Surf. Sci.***1999**, *427-428*, 195.

(22) Wieckowski, A.; Szklarczyk, M. *J. Electroanal. Chem.* **1982**, *142*, 157.

(23) Kawaik, J.; Kulesza, P. J.; Galus, Z. *J. Electroanal. Chem.* **1987**, *226*, 305.

(24) Goldstein, E. L.; Van de Mark, M. R. *Electrochimica Acta* **1982**, *27*, 1079.

(25) Poon, M.; McCreery, R. L. *Anal. Chem.* **1986**, *58*, 2745.

(26) Hinoue, T.; Watanabe, I.; Watari, H. *Chem. Letts.* **1996**, 329.

(27) Parsons, R. *Chem. Rev.*, **1990**, *90*, 813.

(28) Forster, R. J. "Ultrafast Electrochemical Techniques" in "The Encyclopaedia of Analytical Chemistry", Wiley, New York, 2000.

(29) Bard, A. J.; Faulkner, L. R. "Electrochemical Methods – Fundamentals and Applications", 2nd Ed., Wiley, New York, 2001.

(30) Adams, R. N. "Electrochemistry at Solid Electrodes", Marcel Dekker, New York, 1969.

(31) Atkins, P. W. "Physical Chemistry", Oxford University Press, Oxford, U.K., 1979.

(32) Efimov, I. O.; Krivenko, A. G.; Benderskii, V. A. *Russ. J. Electrochem.* **1989**, *24*, 1097.

(33) Rice, R. J.; McCreery, R. L. *J. Electroanal. Chem.* **1991**, *310*, 127.

(34) Benderskii, V. A.; Efimov, I. O.; Krivenko, A. G. *J. Electroanal. Chem.* **1991**, *315*, 29.

(35) Poon, M.; McCreery, R. L. *Anal. Chem.* **1987**, *59*, 1615.

(36) O'Kelly, J.P. PhD Thesis, Dublin City University, 1998.

(37) Climent, V.; Coles, B. A.; Compton, R. G. *J. Phys. Chem.* **2002**, *106*, 5988.

Chapter 5

$[Ru(dpp)_2(Qbpy)]^{2+}$: Ground and Excited State Redox Properties

"The only way to discover the limits of the possible is to go beyond them into the impossible"

Arthur C. Clarke

5.1 Introduction

Chapter 1 highlighted the important role that electronically excited states play in areas as diverse as semiconductors for solar energy conversion, to photosynthesis.[1,2] Photoexcited reactants have been used extensively to study electron transfer because excited states, created upon absorption of a photon, are simultaneously better electron donors and acceptors than their ground-state precursors.[3] However, as discussed in Chapter 1, while the understanding of heterogeneous electron transfer in the ground state has evolved to a high degree on both theoretical and experimental fronts, there have been few reports on heterogeneous electron transfer to and from the electronically excited state or the *direct* measurement of excited state redox potentials.[4,5] This lack of experimental data is due to the simple fact that electronically excited states are transient species and typically have short, i.e., micro- or nanosecond lifetimes. Hence, traditional electrochemical methods cannot provide a means to analyse excited states since these are restricted to millisecond, or longer, timescales.[6] However, with the advent of ultrafast electrochemical techniques and microelectrodes, it is now possible to directly probe the properties of species having sub-microsecond lifetimes.[7]

While Fox and co-workers (Section 1.4) have demonstrated that it is possible to directly measure the excited-state redox potentials for a solution-phase species with lifetimes on the order of hundreds of nanoseconds,[4] the slow time-scale of diffusion prevents the measurement of dynamic parameters. Forster and Keyes have shown that this diffusion limitation may be overcome by forming a spontaneously adsorbed monolayer.[5] As discussed in Section 1.4, they have carried out ultrafast cyclic voltammetry on monolayers of $Ru(bpy)_2(Qbpy)]^{2+}$, where bpy is 2,2'-dipyridyl and Qby is 2,2';4,4';4',4''-quarterpyridyl, during electronic excitation of the monolayers using a nanosecond laser pulse. They describe the observation of fluorescence from the monolayer, which is explained by weak electronic coupling between the metal centre in the monolayer and the electrode and the use of nonmirror finish microelectrodes, which combine to impede the expected radiationless deactivation of the monolayer excited state by the metal electrode surface. High scan-rate cyclic voltammograms are presented which contain responses consistent with the oxidation of the Ru^{2+*} excited state. These represent the first reported cyclic voltammograms of an excited-state species.

This chapter details the results of the spectroscopic and electrochemical evaluation of $[Ru(dpp)_2(Qbpy)]^{2+}$, where dpp is 4,7-diphenyl-1,10-phenanthroline and Qbpy is 2,2';4,4'';4',4''-Quarterpyridyl, as a suitable test species for the *direct* determination of excited-state redox potentials.

Scheme 1 Schematic representation of $[Ru(dpp)_2(Qbpy)](PF_6)_2$, where dpp is 4,7-diphenyl-1,10-phenanthroline and Qbpy is 2,2';4,4'';4',4''-Quarterpyridyl.

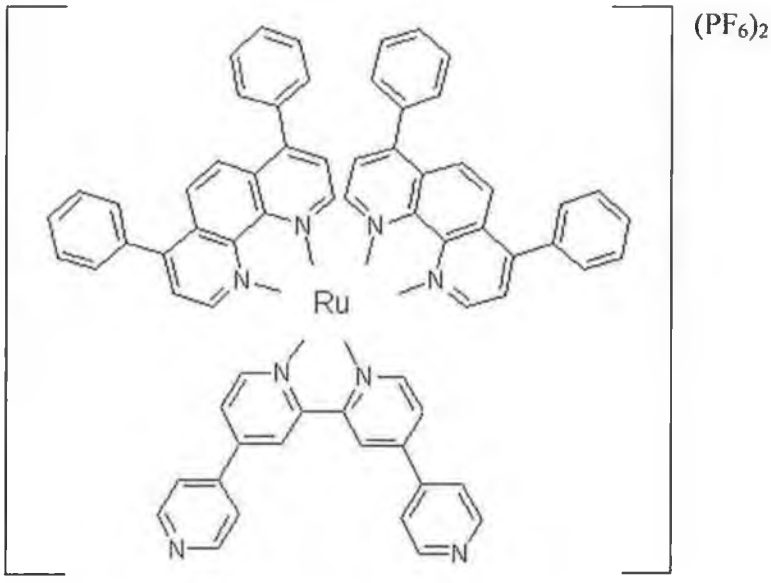

$[Ru(dpp)_2Qbpy](PF_6)_2$

5.2 Apparatus

Ultraviolet-visible spectra were recorded using a Shimadzu UV-3100 diode array spectrometer. For pK_a determinations, approximately 1 mg of the ruthenium complex dissolved in 1 cm^3 acetone was added to 100 cm^3 of Britton-Robinson buffer (0.04 M boric acid, 0.04 M acetic acid, 0.04 M phosphoric acid). The pH was changed by adding concentrated H_2SO_4 or NaOH and measured using a Corning 240 digital pH meter.[8] Room temperature emission spectra were recorded using a Perkin Elmer LS50 B luminescence spectrometer, equipped with a red sensitive Hamamatsu R928 detector. Samples were prepared at concentrations of 10^{-5} to 10^{-6} M in spectroscopic grade butyronitrile. For room temperature measurements, 1 cm quartz cells were used. The excitation and emission slits were 2 nm for all experiments.

Luminescent lifetimes and low temperature emission spectra for the monomeric complex were measured using the third harmonic (355 nm) of a Spectron Q-switched Nd-YAG laser for excitation. Emission was detected in a right-angled configuration to the laser using an Oriel model IS520 gated intensified CCD coupled to an Oriel model MS125 spectrograph. With suitable signal averaging, this configuration allows a complete emission spectrum (spectral range 250 nm) to be obtained within times as short as 10 ns. The emission spectra were typically recorded using the average of twenty laser shots. The gatewidth, i.e., the exposure time of the CCD, was never more than 5% of the excited state lifetime. The step size, i.e., the time between the acquisition of discrete spectra, was typically 5 % of the excited state lifetime.

Dilute solutions of the complex in butyronitrile (10^{-5} to 10^{-6} M) were de-aerated for 20 minutes under nitrogen prior to use. Low temperature emission lifetime studies were carried out using an Oxford Instruments gas-exchange cryostat equipped with an ITC502 temperature controller. Standard iterative techniques were employed to determine the lifetimes of emission.[9]

Cyclic voltammetry was performed using a CH Instruments Model 660A Electrochemical Workstation and a conventional three-electrode cell. All solutions were deoxygenated thoroughly using argon, and a blanket of argon was maintained over the solution during all experiments. Potentials are quoted with respect to a CH Instruments Ag/AgCl reference electrode filled with saturated KCl which had a

potential of +0.190 V with respect to the normal hydrogen electrode. The potential of the ferrocene/ferrocenium couple at this electrode was 0.340 V. All experiments were performed at room temperature (22±3 °C).

In high- speed electrochemical measurements, a custom-built function generator-potentiostat, with a rise time of less than 10 ns, was used to apply potential steps (chronoamperometry) or triangular waveforms (cyclic voltammetry), of variable pulse width and amplitude directly to a two-electrode cell.[10] A Pt flag and an Ag/AgCl reference electrode were combined to form a counter electrode. The flag lowered the resistance and provided a high-frequency path. A Hewlett Packard 54201A digitising oscilloscope was used to monitor the applied waveform and capture the resulting voltammogram. The data was transferred to a PC using a National Instruments GPIB-232CT controller and was analysed in Microsoft Excel. In studies of the voltammetry of electronically excited species, the application of the potential sweep was triggered using the Q-switch sync output on the front panel of the Spectron Q-switched Nd-YAG laser.

Microelectrodes were fabricated from platinum microwires of radii between 5 and 25 μm (Goodfellows Metals Ltd.) by sealing them in soft glass using a procedure described previously.[11] Microdisk electrodes were exposed by removing excess glass using 600 grit emery paper, followed by succesive polishing with 12.5, 5, 1, 0.3 and 0.05 μm alumina. The polishing material was removed between changes of particle size by sonicating the electrodes in deionised water for at least 1 minute. Electrochemical cleaning of the electrodes was carried out by cycling in 0.1 M H_2SO_4 between potential limits chosen to initially oxidize and then reduce the surface of the platinum electrode. Excessive cycling was avoided in order to minimize the extent of surface roughening. The real surface area of the electrodes was determined by calculating the charge under the platinum oxide reduction peak.[12] Typically surface roughness values were between 1.3 and 1.6. Determining the real, as opposed to the geometric area of the electrodes is important if the area of occupation of the adsorbate is to be accurately determined. The final step in the cleaning procedure was repetitive cycling between – 0.2 and + 1.0 V in 0.1 M $LiClO_4$ until hydrogen desorption was complete and a flat background was obtained.[13]

Spontaneously adsorbed monolayers of $[Ru(dpp)_2(Qbpy)]^{2+}$ were formed by immersing a microelectrode, cleaned as described above, in a 1 mM solution of the complex in 50:50 (v/v) acetone:water for up to 30 min. The electrode was removed from the deposition solution, rinsed with 50:50 (v/v) acetone:water and placed in deoxygenated 1.0 M $LiClO_4$ containing 50 μM of the complex for analysis. A low concentration of the surface-active complex in solution minimizes the diffusional contribution to the overall current in chronoamperometry or cyclic voltammetry and improves the stability of the monolayers. The complex is stable towards aerial oxidation and no precautions were taken to exclude atmospheric oxygen during monolayer formation.

5.3 Materials

The synthesis of $[Ru(dpp)_2(Qbpy)]^{2+}$ is described in Chapter 2. Electrochemical and spectroscopic measurements carried out on $[Ru(dpp)_3]^{2+}$ were available from another study and were kindly provided by Robert Forster.

5.4 Results and Discussion

5.4.1 UV-Vis Absorption Spectroscopy

The recording of an ultraviolet-visible spectrum of a complex provides insights into the electronic transitions within the complex. Figure 5.1 illustrates the UV-Vis spectra of $[Ru(dpp)_2(Qbpy)]^{2+}$ dissolved in spectroscopic grade acetonitrile. The compound exhibits intense bands representing ligand-based $\pi \rightarrow \pi^*$ transitions in the high-energy near - UV region of the spectrum[14] (200-380 nm) and spin-allowed metal-to-ligand charge transfer (MLCT) bands in the low-energy visible region[14] (380-780 nm). These absorption bands are typical of the UV-Vis spectra of osmium and ruthenium polypyridyl complexes.[15,16]

For $[Ru(dpp)_2(Qbpy)]^{2+}$ the visible region $d\pi(Ru^{II}) \rightarrow \pi^*(dpp)$ and $d\pi(Ru^{II}) \rightarrow \pi^*(Qbpy)$ metal-to ligand charge transfer (MLCT) bands are seen in a broad region at approximately 430-460 nm, while the shoulder at approximately 310 nm most likely corresponds to metal-centered (MC) transitions.[17] Comparison to published results for $[Ru(bpy)_2(Qbpy)]^{2+}$, an analogous complex where the dpp ligand is replaced by 2,2'-dipyridyl, and its derivative, $[Ru(bpy)_2(Qbpy\text{-}me)]^{2+}$, containing a methylated Qbpy ligand,[18] indicate that the broad absorption at 430-460 nm can be resolved into two bands centred at 432 and 465 nm, corresponding to $d\pi(Ru^{II}) \rightarrow \pi^*(dpp)$ and $d\pi(Ru^{II}) \rightarrow \pi^*(Qbpy)$, respectively. A strong MLCT band is also seen at 275 nm, while the other bands between 200 and 300 nm correspond to ligand-centered $\pi \rightarrow \pi^*$ transitions.[17]

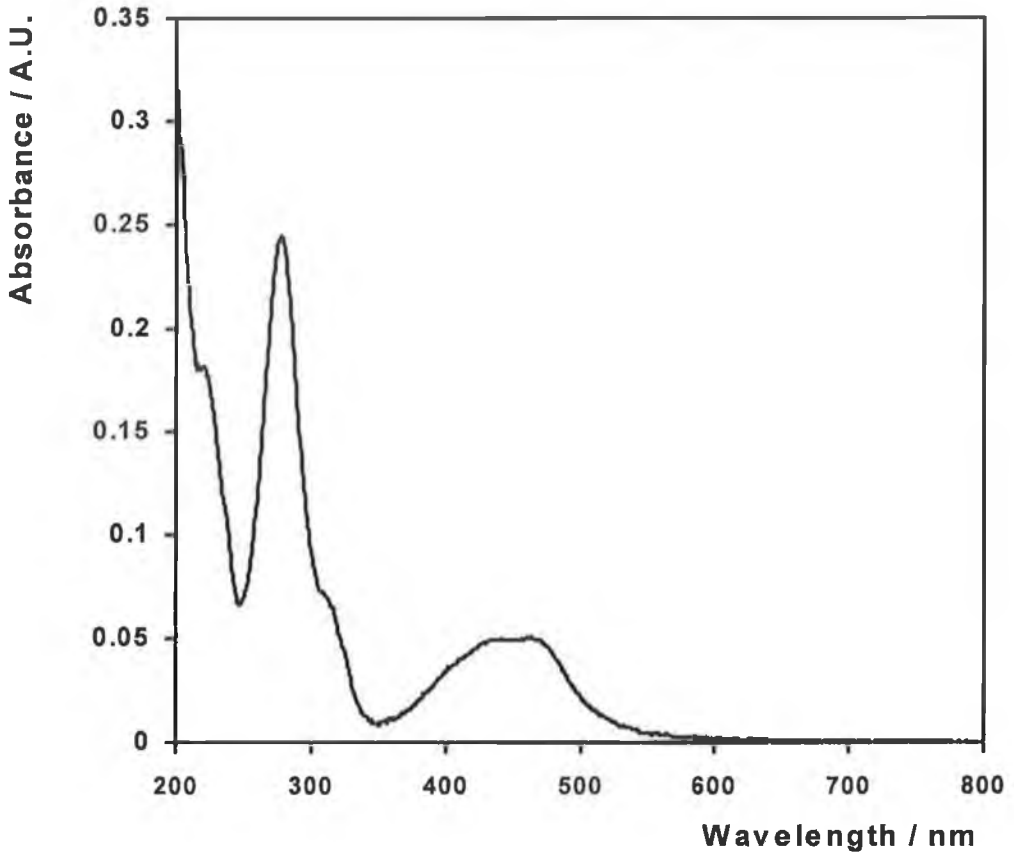

Figure 5.1 UV-Vis absorbance spectra of 2×10^{-6} M $[Ru(dpp)_2Qbpy]^{2+}$. The solvent is deoxygenated acetonitrile.

5.4.2 pK_a Determination

It may be observed from Scheme 5.1, that the $[Ru(dpp)_2(Qbpy)]^{2+}$ complex contains two pendant nitrogens, which will allow it to bind to metal surfaces such as gold or platinum. In low pH solutions, one or both of these nitrogens will be protonated, which is likely to prevent the complex from binding to a surface. Therefore, the determination of pK_a values for this complex is useful in terms of evaluating the optimum pH for monolayer formation. pK_a values are determined by obtaining UV-VIS spectra of a complex dissolved in Britton-Robinson buffer. Protonating the quarterpyridyl will change the electron density on the ligand and may alter the intensity of the MLCT bands. The pK_a values of the complex may be determined from a plot of the percentage change in absorbance vs. pH. In this experiment, the pH was adjusted stepwise from pH 1.0 to pH 8.0 by addition of concentrated NaOH solution with negligible change in the volume of the test solution.

Figure 5.2 is an overlay of a selection of the spectra obtained, which shows the change in intensity of the MLCT bands in both the UV and visible regions of the spectrum. If two species of a chemical equilibrium absorb, and if there is some overlap of their absorption curves, the wavelength at which this happens is an isosbestic point, and the molar extinction coefficient of both species is the same. The existence of an isosbestic point is a necessary condition to prove that there are only two absorbing species in equilibrium with overlapping absorption bands.[14] The data in Figure 5.2 do not display an isosbestic point, indicating that the protonation of $[Ru(dpp)_2(Qbpy)]^{2+}$ is not governed by a simple equilibrium such as described below in Equation 5.1.

$$HA_2 \overset{K_a1}{\longleftrightarrow} HA^- \overset{K_a2}{\longleftrightarrow} A^{2-} \qquad (5.1)$$

Figure 5.3 is a plot of the percentage change in absorbance at 263 nm vs the pH of the solution. The MLCT band in the UV region of the spectrum was chosen, as the changes in band intensity are more marked at this wavelength, compared to the band in the visible region. This graph clearly shows that the transition region from the fully protonated to the fully deprotonated form of $[Ru(dpp)_2(Qbpy)]^{2+}$ does not contain two well-defined pK_as for the equilibrium described in Equation 5.1. However, Figures 5.2

and 5.3 show that protonating the quaternary nitrogens on the Qbpy ligand of the complex can have a marked effect on the intensity of the MLCT bands of the UV-Vis spectrum. Protonating one of the nitrogens may cause a change in the local electrostatic environment and/or a change in the electron density of the ligand. These changes may be responsible for the observed affect of changing pH on the MLCT bands in the spectrum.

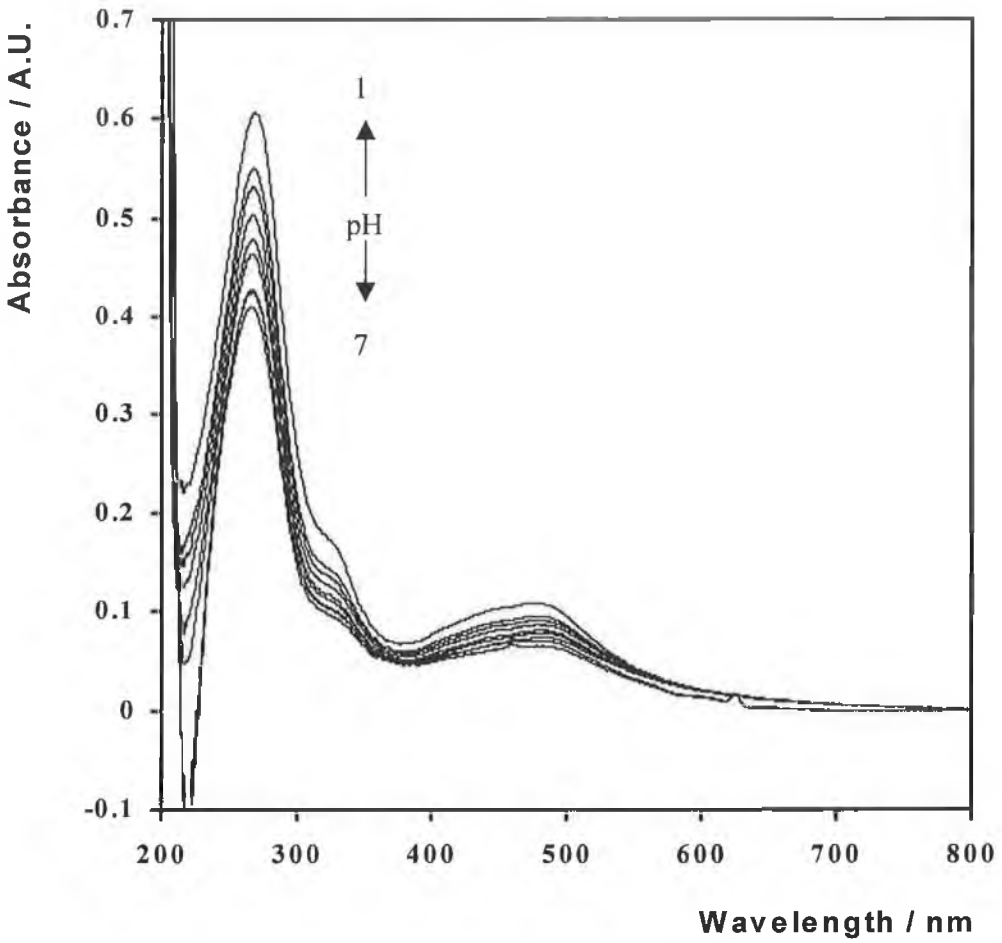

Figure 5.2 Overlay of a selection of UV-VIS spectra of $[Ru(dpp)_2(Qbpy)]^{2+}$ in Britton-Robinson buffer at 298 K, recorded over the pH range 1.0 to 8.0, illustrating the decrease in intensity of the MLCT bands with increasing pH. The pH was adjusted by adding concentrated NaOH.

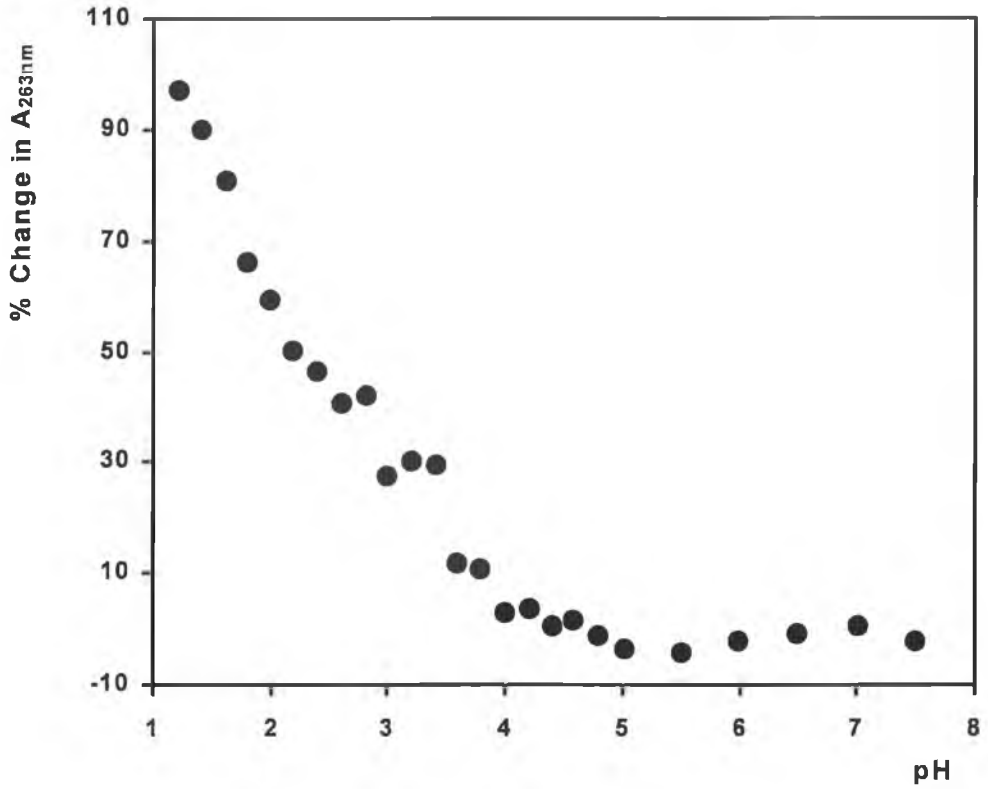

Figure 5.3 Percent change in absorbance at 263 nm with pH for $[Ru(dpp)_2(Qbpy)]^{2+}$.

5.4.3 Emission Spectroscopy

In the excited-state electrochemistry experiment reported later in this chapter, a potential sweep across a monolayer of an emitting species is used in an attempt to detect the redox potentials of the excited state. A suitable probe species for these experiments should exhibit a long radiative lifetime for two main reasons: (1) to ensure that the potential sweep may be carried out in full before the excited state has fully decayed to the ground state and (2) to ensure that the lifetime exceeds the minimum response time of the microelectrode - typically between nano- and micro-seconds, depending on the size of the electrode.[7] The $[Ru(dpp)_2(Qbpy)]^{2+}$ complex has been investigated in terms of its emission lifetime and therefore feasibility for use as a probe in excited state electrochemistry experiments. Emission data on the complex is also required for the Rehm-Weller calculation of excited state redox potentials as described in Section 1.4.[19]

The emission spectrum of the quarterpyridyl complex in acetonitrile at 298 K is presented in Figure 5.4. The complex exhibits an emission maximum at approximately 615 nm, at slightly lower energy than $[Ru(bpy)_3]^{2+}$, which emits at 605 nm in acetonitrile.[20] A comparison spectrum of $[Ru(dpp)_3]^{2+}$ (not shown) exhibited the same emission maximum. Figure 5.5 illustrates the low-temperature emission spectrum of the complex at 77 K in butyronitrile glass. The emission at low temperature is of a very broad nature and exhibits a shoulder at 680 nm, indicative of the vibrational fine structure in the spectrum. This vibrational structure is assigned to a perturbed skeletal vibration of the dpp aromatic ring, due to the removal of the π^* electron and is only visible at low temperatures.[21] This shoulder is poorly-resolved when compared to that previously reported for $[Ru(bpy)_3]^{2+}$ in a rigid ethanol-methanol glass.[17]

The fluorescence lifetime of a substance represents the average amount of time the species remains in the excited state prior to its return to the ground state. Fluorescence is typically a unimolecular process and therefore the excited state population established by an impulse of exciting light will generally decay exponentially according to first order kinetics.[22] In these experiments, the lifetime of the complex is estimated by monitoring the decay of emission as a function of time and plotting the natural log of emission versus time. The lifetime, τ, may be determined from the slope as follows:

$$\ln(I/I_O) = -kt \qquad (5.2)$$

$$k = 1/\tau \qquad (5.3)$$

To fully investigate the emission properties of $[Ru(dpp)_2(Qbpy)]^{2+}$, the emission lifetime in butyronitrile has been determined over a range of temperatures from 77 to 300 K. As illustrated in Figure 5.6, the decays seen for the complex were single exponentials with lifetimes of the order of microseconds. The emission lifetimes at each temperature, calculated from the slope of these transients, are detailed in Table 5.1 along with the maximum emission wavelength at each temperature.

The data in Table 5.1 demonstrates that as temperature increases, the emission lifetime decreases and that the maximum emission wavelength is shifted to longer wavelengths, i.e., lower energy. These changes may be attributed to either (a) a thermally activated surface crossing to another excited state (usually from ^{3}MLCT to ^{3}MC) or (b) the role of vibrational modes that favour radiationless decay.[23] These vibrational modes are prevented at low temperature because of the frozen molecular environment. The plot of lifetime vs. temperature shown in Figure 5.7 clearly illustrates an abrupt change in lifetime between 100 – 200 K. A change in the maximum wavelength of emission is also seen in Table 5.1. These changes occur in the region of the melting point of the butyronitrile solvent[24] at 161 K.

The fact that this complex exhibits long-lived emission at both room temperature and in glass matrix is advantageous for the excited state redox experiments. Monolayers of the complex on platinum microelectrodes will be utilised for the excited-state electrochemistry experiment. According to the literature presented in Section 1.4 and 1.5, monolayers of a fluorescing species immobilised near a metal surface can exhibit efficient emission despite being located near to a metal centre.[5,25] If the complex immobilised on a platinum microelectrode, can exhibit a similar lifetime to that observed in solution, this indicates that the potential sweep applied to the electrode must be in the kV s^{-1} range, so as to allow the potential sweep to be completed before the excited state decays to the ground state.

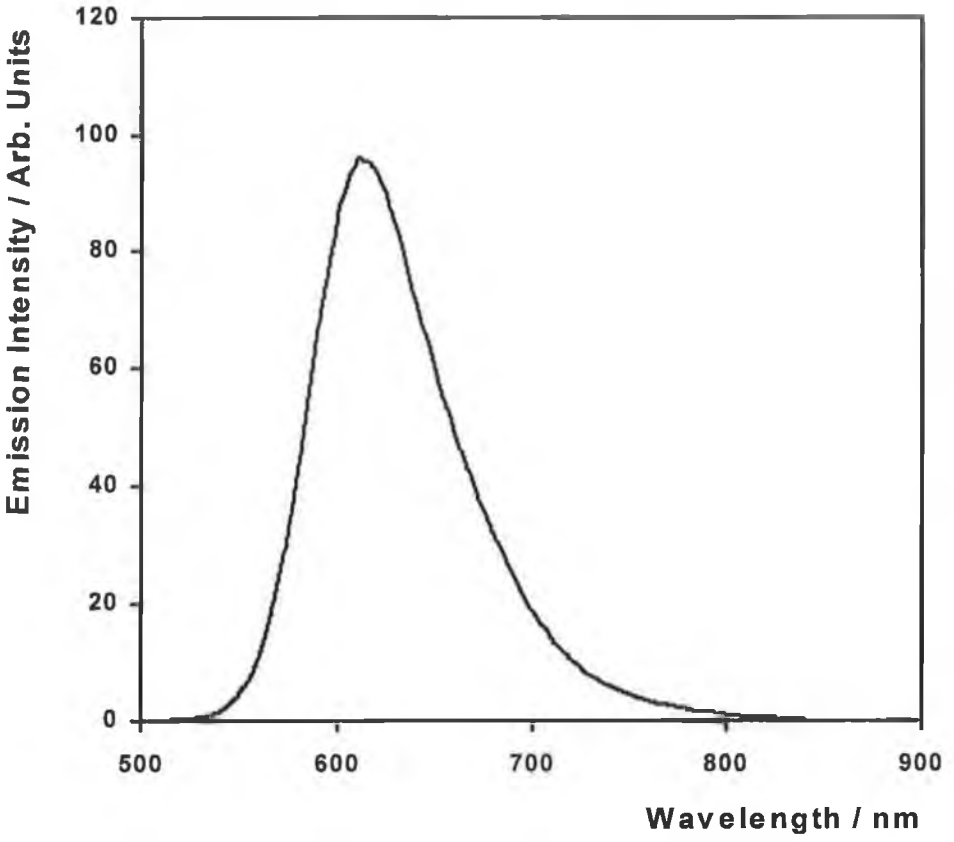

Figure 5.4 Emission spectrum of 1×10^{-5} M $[Ru(dpp)_2(Qbpy)]^{2+}$ at 298 K in deoxygenated acetonitrile.

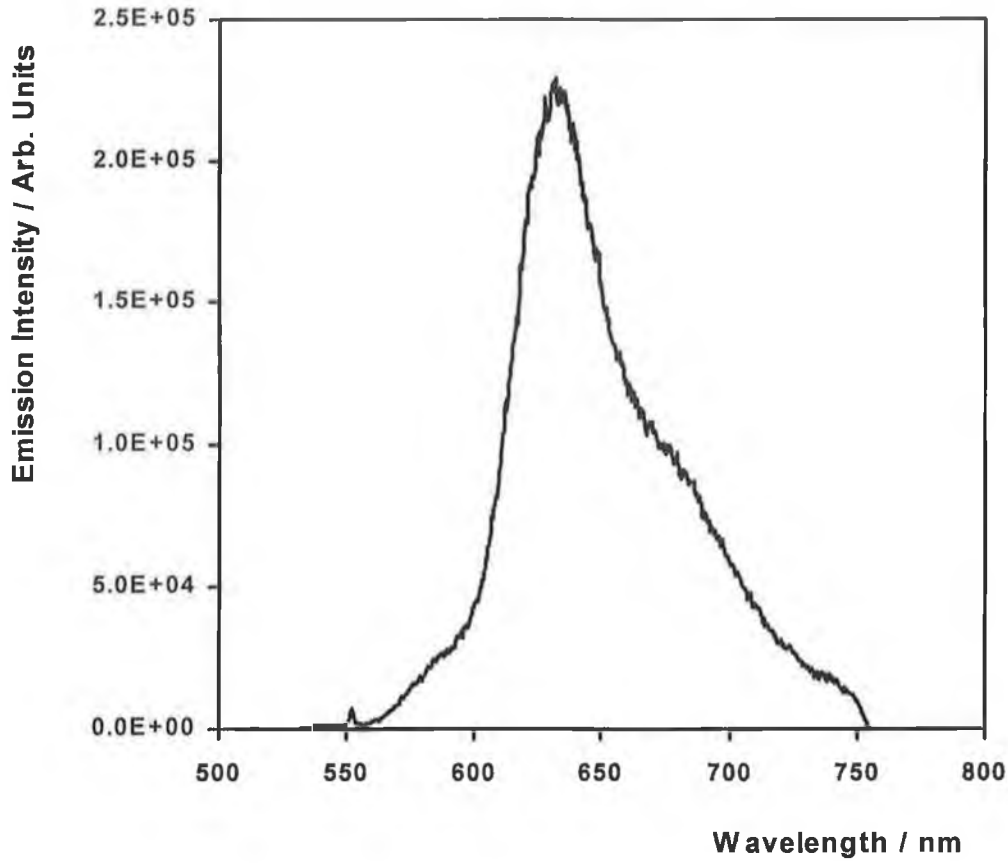

Figure 5.5 Emission spectrum of 1×10^{-5} M $[Ru(dpp)_2(Qbpy)]^{2+}$ at 77 K in deoxygenated butyronitrile.

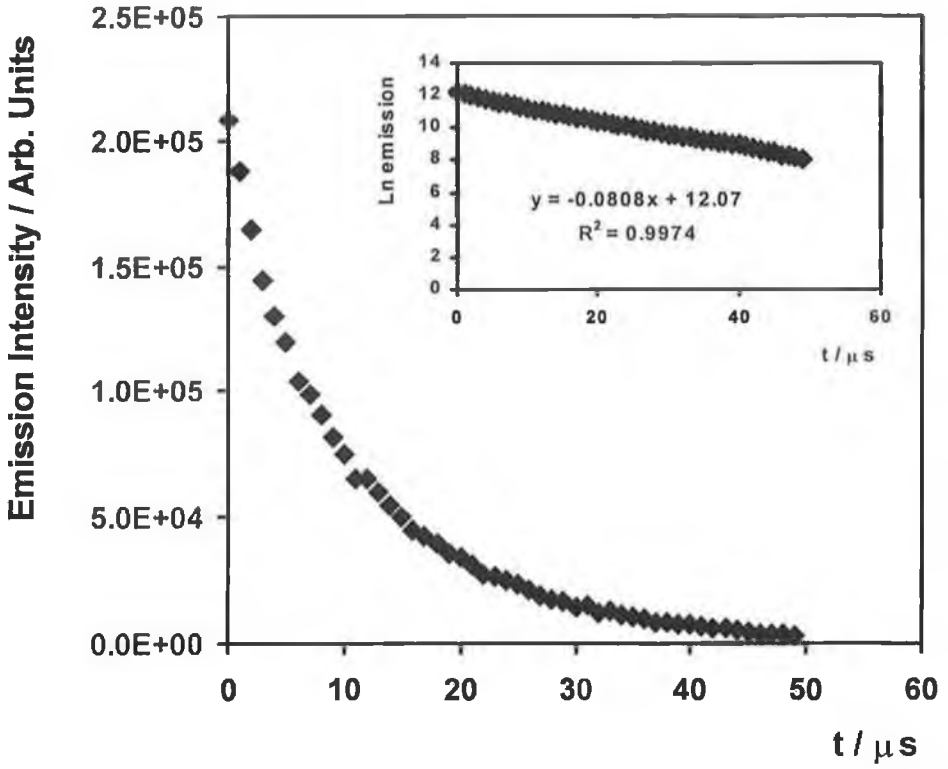

Figure 5.6 Emission transients for a solution of 1×10^{-5} M $[Ru(dpp)_2(Qbpy)]^{2+}$ in deoxygenated butyronitrile at 77K. The inset shows a semilog plot of the response.

Table 5.1 Excited state lifetime and maximum emission wavelength versus temperature for 1×10^{-5} M $[Ru(dpp)_2(Qbpy)]^{2+}$ in deoxygenated butyronitrile.

Temperature / K	Lifetime / μs	Wavelength / nm [a]
77	12.4 ± 1.9	631
90	11.5 ± 1.5	632
95	11.3 ± 1.4	634
105	11.3 ± 1.3	635
115	10.6 ± 1.3	634
125	10.6 ± 1.2	635
140	10.4 ± 1.3	635
160	7.2 ± 0.3	658
180	2.8 ± 0.2	658
200	0.8 ± 0.1	663
225	0.5 ± 0.1	666
250	0.4 ± 0.1	669
275	0.4 ± 0.1	671
300	0.4 ± 0.1	671

[a] The error on the emission wavelength is typically ± 0.34 nm.

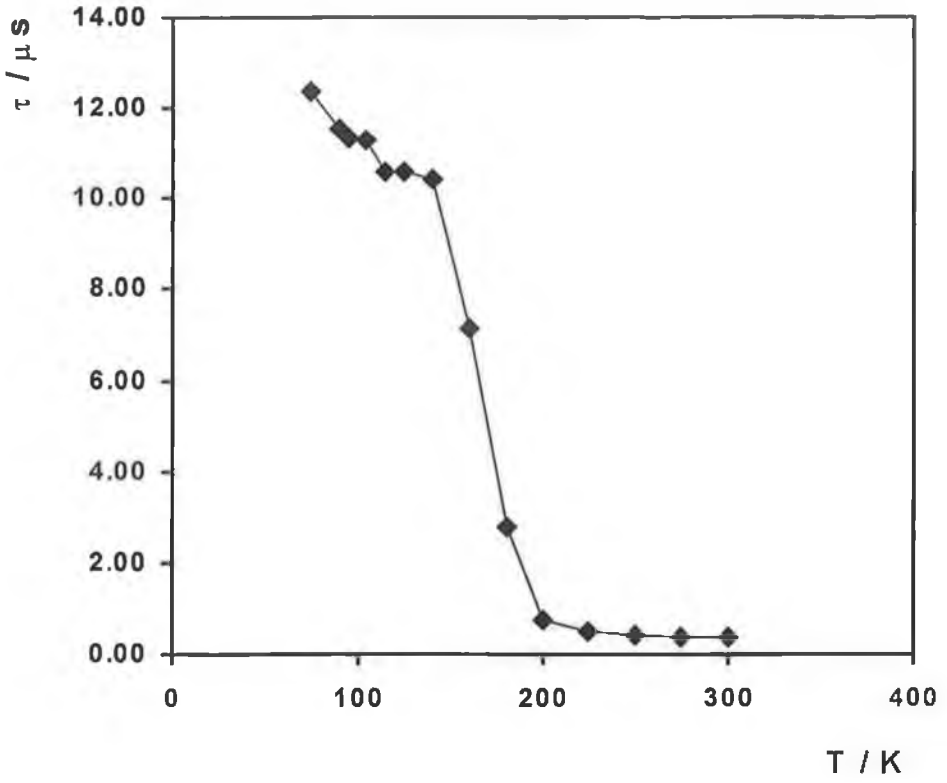

Figure 5.7 Plot of the excited state lifetime vs. temperature for a 1×10^{-5} M solution of $[Ru(dpp)_2(Qbpy)]^{2+}$ in deoxygenated butyronitrile over the temperature range 77 – 300 K.

5.4.4 General Electrochemical Properties

Ruthenium complexes are well known for the reversibility of their metal based redox processes in the ground state and a wealth of information is now available on the electrochemical behaviour of ruthenium - polypyridine complexes.[16] Figure 5.8 illustrates a voltammogram of $[Ru(dpp)_2(Qbpy)]^{2+}$, showing the oxidation and reduction processes within the complex. The formal potential for the $Ru^{2+/3+}$ redox process is 1.23 V vs. Ag/AgCl.

Reduction of Ru(II) complexes may in principle involve either a metal-centered or a ligand-centered orbital, depending on the relative energy ordering. When the ligand field is sufficiently strong, and/or the ligands can be easily reduced, reduction takes place on a ligand π^* orbital. This is the commonly observed behaviour of Ru(II) polypyridine complexes.[17,26] The added electron appears to be localised on a single ligand and several reduction steps can often be observed in the accessible potential range. The identity of the first excited state of a complex can often be inferred from the potential of the first reduction wave, if, as described by Koopman's theorem,[26] the π_L^* orbital involved in the reduction process is the same as that involved in the MLCT transitions.

Figure 5.8 illustrates a voltammogram of $[Ru(dpp)_2(Qbpy)]^{2+}$, showing both the metal-centered oxidations and the ligand reductions of the complex. The sharp peak observed at – 1.28 V suggests that at negative potentials, the complex is absorbed onto the electrode. This phenomenon is commonly observed in the ligand reduction potentials of surface-active transition metal polypyridyl complexes.[27] However, the voltammogram is sufficiently well resolved to estimate the potentials of the first three reductions. They are observed at –0.95, -1.20 and –1.38 V. Comparison with previous work carried out on $[Ru(bpy)_2(Qbpy)]^{2+}$, an analogue of the complex detailed here where the dpp ligands are replaced by 2,2'-bypyridine ligands,[5,18] indicates that the reduction at –0.95 V is based on the quarterpyridyl ligand. The remaining reductions at –1.20 and –1.38 V are assigned to the diphenylphenanthroline ligands.

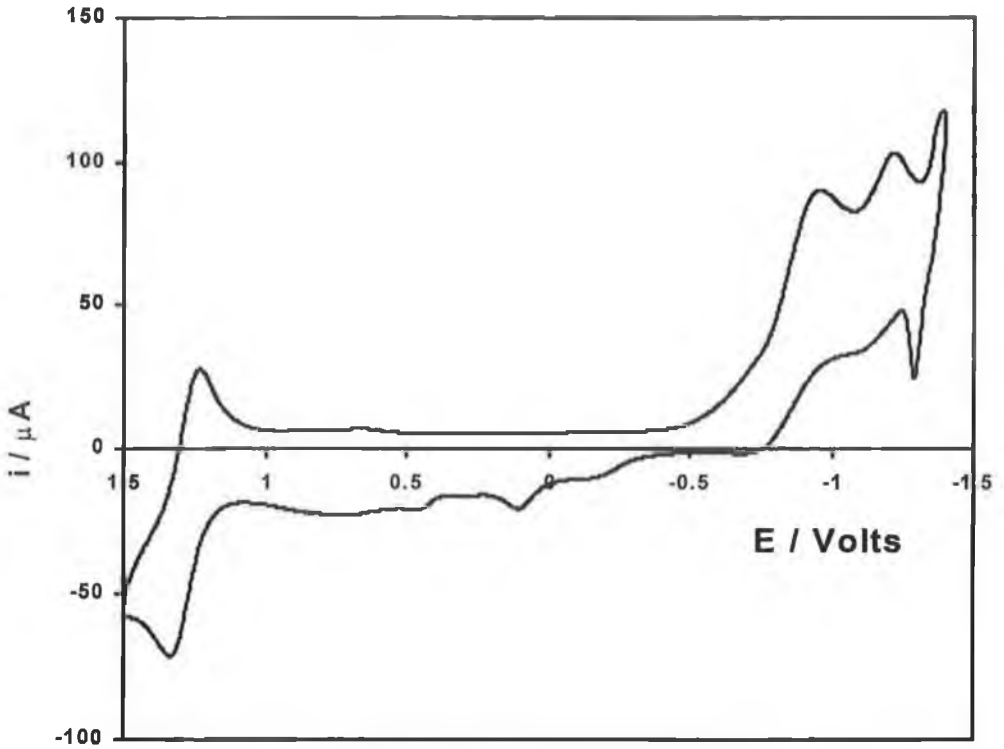

Figure 5.8 Segments 5 and 6 of a cyclic voltammogram of 5 mM $[Ru(dpp)_2Qbpy]^{2+}$ in deoxygenated acetonitrile/ 0.1 M $TBABF_4$. Potentials are versus Ag/AgCl. The working electrode is a 3 mm diameter glassy carbon disc. The scan rate is 0.1 V s^{-1} and the initial potential is 0.0 V.

5.4.5 Calculation of Excited State Redox Potentials

The spectroscopic and electrochemical parameters of $[Ru(dpp)_2(Qbpy)]^{2+}$ reported in this chapter may be used to calculate the excited state redox potentials of the complex. As detailed in Section 1.4, excited state redox potentials are traditionally calculated by the method of Rehm and Weller,[19] using the excited state energy $E^{0\text{-}0}$ to correct the ground-state redox potentials:

$$E^{\circ}{}_{Ox}{}^{*} = E^{\circ\prime}{}_{Ox} - E^{0-0} \qquad (5.4)$$

$$E^{\circ}{}_{Red}{}^{*} = E^{\circ\prime}{}_{Red} + E^{0-0} \qquad (5.5)$$

where $E^{\circ\prime}{}_{Red}$ and $E^{\circ\prime}{}_{Ox}$ are the potentials for the first reduction and oxidation respectively and $E^{0\text{-}0}$ is the energy gap between the zeroth vibrational levels of the ground and excited states, estimated from emission spectra obtained at cryogenic temperatures. Equations 5.4 and 5.5 assume that all the spectroscopic energy of the excited state ($E^{0\text{-}0}$) can be used as free energy in the redox process.[28] The oxidation and reduction potentials, i.e., $E^{\circ\prime}{}_{Ox}$ and $E^{\circ\prime}{}_{Red}$, used in this calculation were obtained from Figure 5.8. $E^{0\text{-}0}$ is obtained from the maximum emission wavelength at 77 K (630 nm), and yields a value of 1.968 eV.

Given that $E^{\circ}{}_{Ox} = 1.289$ V : $\quad E^{\circ}{}_{Ox}{}^{*} = 1.289\text{ V} - 1.968\text{ V}$

$$= \mathbf{-0.679\text{ V}}$$

Given that $E^{\circ}{}_{Red} = -0.948$ V : $\quad E^{\circ}{}_{Red}{}^{*} = -0.948\text{ V} + 1.968\text{ V}$

$$= \mathbf{+1.020\text{ V}}$$

It is important to note that in the excited state, the reduction potential is *positive* of the excited state oxidation potential, which contrasts with ground state electrochemistry, in which the reduction potential is typically at a lower potential than the oxidation potential. The values calculated here provide a useful guide as to where on the potential axis the excited state response might be expected, while the emission lifetime will dictate the experimental timescale.

5.4.6 Ground State Heterogeneous Electron Transfer

In attempting to investigate electron transfer from the electronically excited state, it is important to first examine the kinetics of ground state electron transfer to provide an estimate of the rate of the heterogeneous electron transfer. Previous investigations have demonstrated that complexes containing ligands with two pyridine groups, one of which is bound to the metal complex with the other being available for adsorption, form stable monolayers with nearly ideal electrochemical responses.[29,30,31,32] As described in Section 1.3, spontaneously adsorbed monolayers are excellent model systems to probe heterogeneous electron transfer kinetics.

Figure 5.9 shows representative background corrected cyclic voltammograms for spontaneously adsorbed monolayers of $[Ru(dpp)_2(Qbpy)]^{2+}$ where the supporting electrolyte is aqueous 1.0 M $LiClO_4$. The experimental voltammetric response observed for the monolayer demonstrates all of the characteristics of a redox system confined to an electrode surface.[6] For example, the peak shapes are symmetrical and independent of scan rate, ν, at least over the range 1 to 100 V s^{-1}, and the peak height scales linearly with scan rate, unlike the $\nu^{1/2}$ dependence expected for a freely diffusing species. However, non-zero peak-to-peak splitting, ΔE_p, is demonstrated even at low scan rates, which contrasts with the zero ΔE_p expected for the situation where there are no lateral interactions between adsorbates.[6,33,34] This behaviour has been previously reported for structurally related systems.[31] Similar nonideal responses have been interpreted by Feldberg and Rubenstein[35] as unusual quasi-reversibility (UQR), or apparent nonkinetic hysteresis in cyclic voltammetry, in terms of N-shaped free energy curves, as opposed to the parabolic energy curves usually used in electron transfer models.[36] In their interpretation, hysteretic UQR arises because of rate processes which are slow in comparison to the experimental timescale, resulting in a finite ΔE_p. It is important to note that ΔE_p does not increase with increasing scan rate for $0.1 \leq \nu \leq 100$ Vs^{-1}, which suggests that slow heterogeneous electron transfer is not responsible for the observed non-ideal behaviour. If the rate of electron transfer was slow, at relatively slow scan rates, ΔE_p would increase with increasing scan rate,[37] and not remain constant for $0.1 \leq \nu \leq 100$ Vs^{-1} as observed here.

Where there are no lateral interactions between surface confined redox centres, a FWHM of 90.6 mV is expected for a one-electron transfer.[6,33,34] In these monolayers, for $0.1 \leq \nu \leq 100$ Vs^{-1} the FWHM values are between 100 and 120 mV indicating that only very weak destabilizing interactions, e.g., electrostatic repulsion between the positively charged osmium centres, exist within the monolayers.

The surface coverage obtained from the Faradaic charge measured from the background corrected voltammograms at a scan rate of 0.1 mV s^{-1} is $1.0 \pm 0.1 \times 10^{-10}$ mol cm^{-2} corresponding to an area of occupation of 166 ± 14 $Å^2$. This surface coverage is consistent with that expected for a close packed monolayer on the basis of structurally related systems and crystallographic data[38,39] which indicate that the radii of osmium and ruthenium polypyridyl complexes are of the order of 6.7 Å.

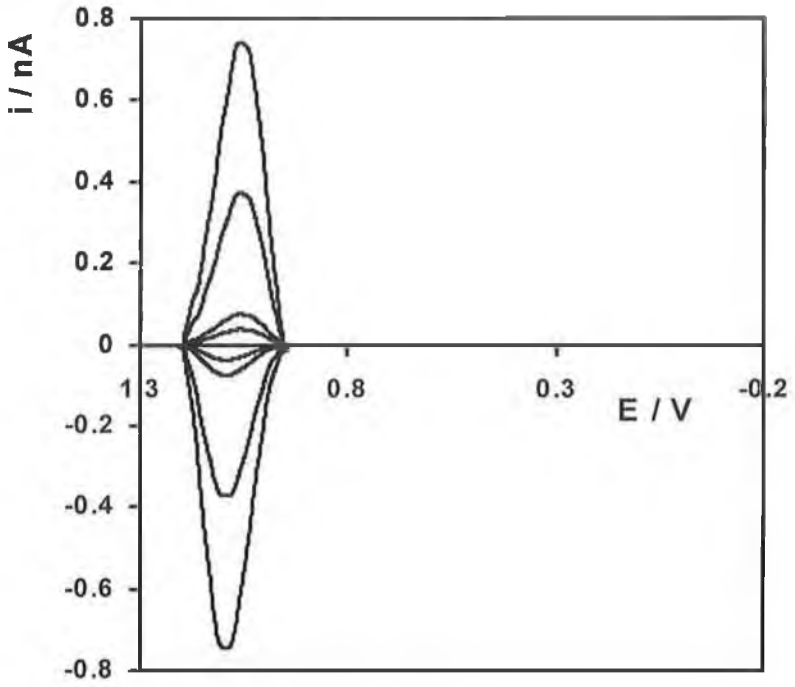

Figure 5.9 Background corrected cyclic voltammograms for a spontaneously adsorbed $[Ru(dpp)_2(Qbpy)]^{2+}$ monolayer on a 5 μm radius platinum microdisk electrode. The supporting electrolyte is aqueous 1.0 M $LiClO_4$. The scan rates from top to bottom are 10.0, 5.0, 1.0 and 0.5 V s^{-1}. The surface coverage is $1.0\pm0.1 \times 10^{-10}$ mol cm^{-2}.

For an ideal electrochemical reaction following a surface-bound species, the Faradaic current following a potential step that changes the redox composition of the monolayer exhibits a single-exponential decay in time according to:[40,42,43]

$$i_F(t) = kQ\exp(-kt) \qquad (5.6)$$

where k is the apparent rate constant for the overall reaction for a given overpotential, η, ($\eta = E - E°$) and Q is the total charge passed in the redox transformation.

Figure 5.10 illustrates typical examples of the chronoamperometric response observed for the $Ru^{3+} + e^- \rightarrow Ru^{2+}$ redox reaction of a $[Ru(dpp)_2(Qbpy)]^{2+}$ monolayer formed on a 5 μm radius microelectrode, where the electrolyte is 1.0 M $LiClO_4$. In these experiments, the potential was stepped from 1.100 V to potentials, E, that were 150 and 300 mV more negative than the formal potential, E°'. Closer observation of these transients shows that on a low microsecond time domain, two current decays are observed. These responses correspond to double-layer charging and the Faradaic reaction, respectively, and are time resolved because the time constant for double-layer charging is more rapid than electron transfer.

In carrying out these measurements, it is important to consider the effect of ohmic drop on the observed response.[6,40] Ohmic drop is caused when currents flow through a solution generating a potential that weakens the applied potential by an amount iR, where i is the total current flow in the solution and R is the solution resistance.[7] This ohmic drop can lead to distortions of the experimental response and inaccurate measurements of the heterogeneous rate constant. The effects of ohmic drop have been minimised in these experiments by using a high supporting electrolyte concentration (1.0 M), by using electrodes of small radius which yield small experimental currents and where possible, by analysing data relatively late in the lifetime of the transient, where currents are smaller and therefore iR is reduced. By analysing the initial decays due to charging current to estimate the solution resistance (approx. 20,000 Ω) and multiplying this by the experimental current, the average iR drop is estimated to be less than 75 mV. At high overpotentials, the Faradaic response is very convoluted with the double layer response, resulting in the requirement to analyse data relatively early in the lifetime of the transient to obtain the estimate of k. Unfortunately, the effects of iR

drop will be more significant at these early timescales. Nevertheless, the small electrodes used minimise even these effects, e.g., the maximum ohmic loss observed at the highest overpotential applied here is reduced from approximately 2500 mV to 195 mV on going from a 12.5 μm radius electrode to one of radius 5 μm.

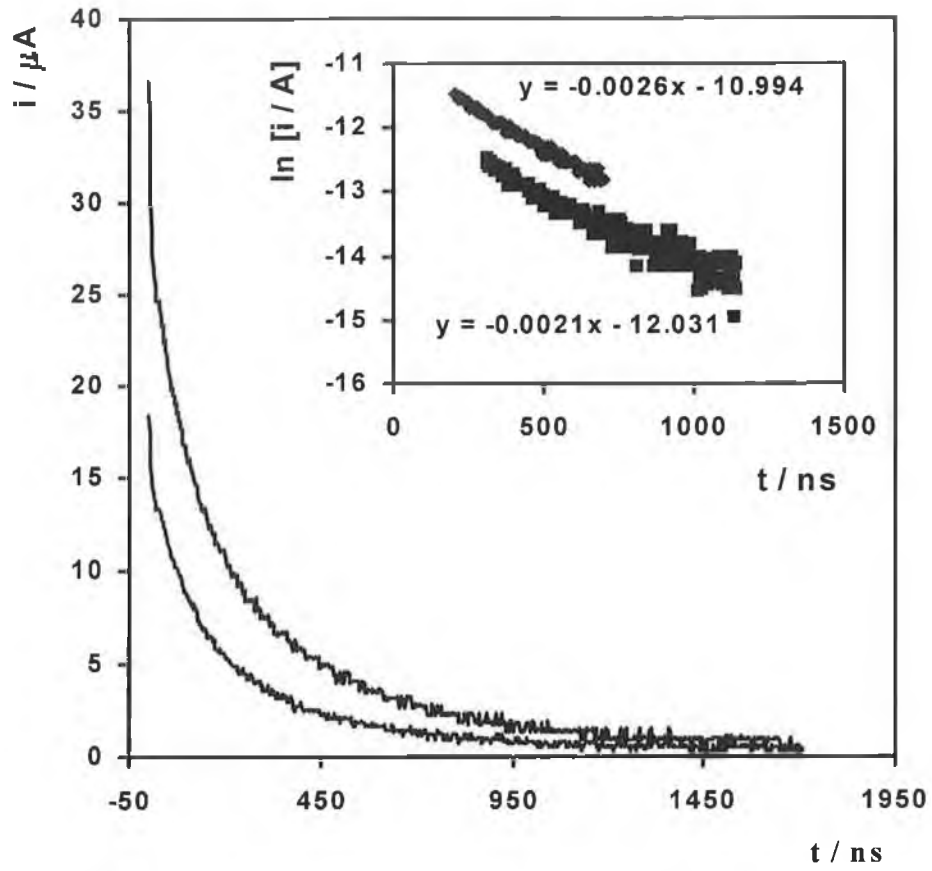

Figure 5.10 Current response for reduction of the Ru^{3+} redox centre occurring within a $[Ru(dpp)_2(Qbpy)]^{2+}$ monolayer formed on a 5 µm platinum microelectrode. From top to bottom on the left hand side, the overpotentials, η, are 300 mV and 150 mV, respectively. The supporting electrolyte is aqueous 1 M $LiClO_4$. The inset shows corresponding semilog plots of the response for the Faradaic reactions. From top to bottom on the right hand side, the overpotentials, η, are 300 and 150 mV, respectively.

5.4.6.1 Potential Dependence of k

One advantage of using redox-active monolayers as model systems for understanding the factors that affect electron transfer rates, is the ability to control the driving force for the reaction.[6] Butler Volmer kinetics predicts an exponential dependence of k, the heterogeneous electron transfer rate, on the overpotential, η. Equation 5.7 describes the situation for a one – electron reduction:[6]

$$k = k^{\circ} \exp\left[- \alpha_c nF\eta / RT \right] \qquad (5.7)$$

where k° is the standard heterogeneous rate constant, α_c is the cathodic transfer coefficient, and n, F, R and T have their usual significance. A Tafel plot of ln k vs. overpotential is predicted to be linear with a slope of $-\alpha_c nF/RT$ for the cathodic step and $(1-\alpha_a)nF/RT$ for the anodic step. Extrapolating either branch to zero overpotential allows k° to be estimated.[6,40] Figure 5.11 illustrates a Tafel plot of ln k vs. overpotential for the reduction of Ru^{3+} to Ru^{2+}. It is not possible to obtain Tafel plots for the corresponding oxidation, since this would require carrying out chronoamperometric steps that would trigger oxidation of the Pt electrode.

The Tafel plot shows that ln k depends approximately linearly on overpotential in the range $60 \leq \eta \leq 175$ mV. At higher overpotentials, k begins to plateau off and there is some curvature visible in the plot at these overpotentials. Such curvature has been previously observed in Tafel plots for other monolayer systems.[40,41,42] This behaviour is consistent with the Marcus electron transfer theory and indicates that, at high driving force, Butler Volmer theory does not accurately predict the potential dependence of k.[40,43]

Using the data in the linear portion of the graph and extrapolating it to zero overpotential allows the standard heterogeneous electron transfer rate constant, k°, to be estimated. This analysis yields a value of 9.1×10^5 s^{-1}. However, the Tafel slope of this plot yields an α_c value of 0.2, lower than the expected value of 0.5 for a reversible electron transfer. This low slope may be in part attributed to the adverse effects of ohmic drop on the current –time responses obtained. Despite this drawback, the Tafel

plot provides an estimate of k° and shows that it is of the order of 10^5 s^{-1} making it a rapid process. This result is in agreement with the value previously reported[5] for this bridging ligand, $5.1\pm0.3 \times 10^5$ s.

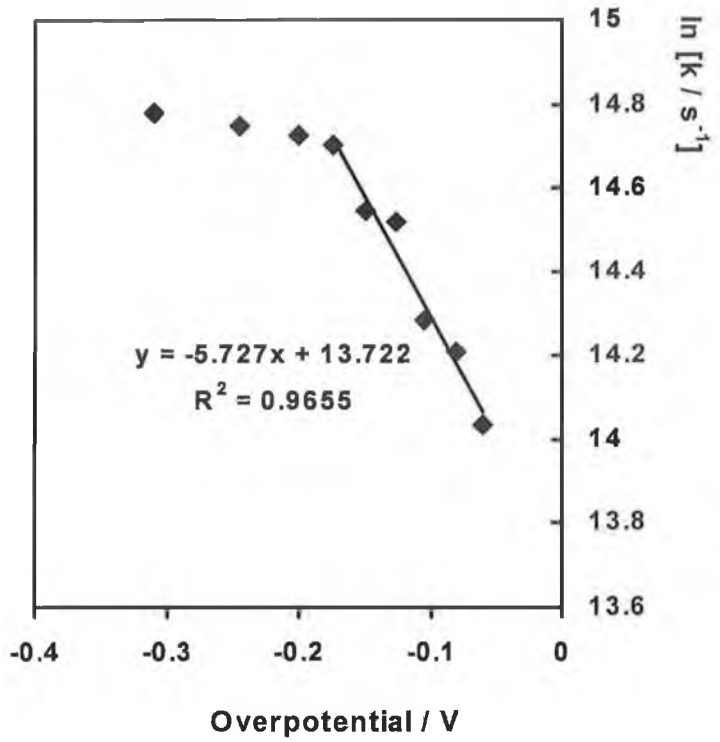

Figure 5.11 Tafel plot for the $Ru^{3+} + e^- \rightarrow Ru^{2+}$ redox reaction occurring within a $[Ru(dpp)_2(Qbpy)]^{2+}$ monolayer formed on a 5 μm platinum microelectrode. The supporting electrolye is aqueous 1.0 M $LiClO_4$.

5.4.7 Laser Effects on the Cyclic Voltammetry of Unmodified Microelectrodes.

As demonstrated in Chapter 4, recording a cyclic voltammogram of a clean gold macroelectrode in blank electrolyte solution while laser pulses are being applied to the electrode surface results in small current spikes overlaid on the voltammogram. To determine if applying laser radiation during the potential sweep affects the observed cyclic voltammetry at microelectrodes, a series of voltammograms at low (0.05 V s^{-1}) and high (1000 V s^{-1}) scan rate were recorded for unmodified 5 μm platinum and gold microelectrodes where 3 MW cm^{-2} intensity laser pulses are applied to the electrode surface during the potential sweep. The effect of laser pulses on high scan rate (90,000 V s^{-1}) voltammograms obtained using the high-speed electrochemistry apparatus was also investigated for the platinum and gold electrodes. Testing both gold and platinum microelectrodes allows us to investigate if the laser pulses have the same effect on the voltammetry observed using both metals. This control experiment is important, as it must be demonstrated that the laser pulses do not cause any artefacts in the cyclic voltammograms, so that any redox peaks detected can be identified as Faradaic responses due to excited state redox processes occurring within the monolayer.

Figures 5.12 illustrates slow scan rate cyclic voltammograms for 5 μm radius gold and platinum electrodes recorded with and without the application of laser pulses to the electrode surface. The expansion of the data in the potential region 0.6 to 0.8 V presented in Figure 5.13 shows the presence of small current spikes in the voltammogram of the gold electrode. This is in agreement with the results presented in Chapter 4 for gold macroelectrodes. Surprisingly, the voltammetry of the platinum electrode remains relatively unperturbed by the laser light. In Chapter 4, the effect of rapid heating of the gold metal by the laser pulse has been shown to manifest itself as laser-induced current transients. The observed decay was successfully modelled as firstly, the response of the double layer and secondly, the thermal response of the gold metal, caused by the heating triggered by the laser pulse. The thermal diffusion coefficient for platinum (0.250 cm^2 s^{-1}) is considerably smaller than that for gold (1.272 cm^2 s^{-1}), indicating that any temperature increase achieved at the electrode surface by the laser pulse will spread more slowly through platinum than through gold. It is possible that this slow dissipation of heat through the platinum electrode results in a less rapid restructuring of the double layer responsible for the current transients at gold

electrodes and this may explain the lack of significant laser-induced current transients observed at platinum electrodes.

Figure 5.14 shows that at high scan rates (1000 V s^{-1}) applied using a conventional potentiostat, the current transients visible at slow scan rates, are not visible in the voltammetry obtained at this fast timescale. Using the high-speed electrochemical apparatus, scan rates of 90,000 V s^{-1} were achieved. Figure 5.15 shows that there is no difference between the voltammograms obtained with and without laser pulses. Therefore, it may be concluded that laser-induced current responses are not detectable in the cyclic voltammograms obtained at scan rates $\geq$ 1000 V s^{-1}.

(a)

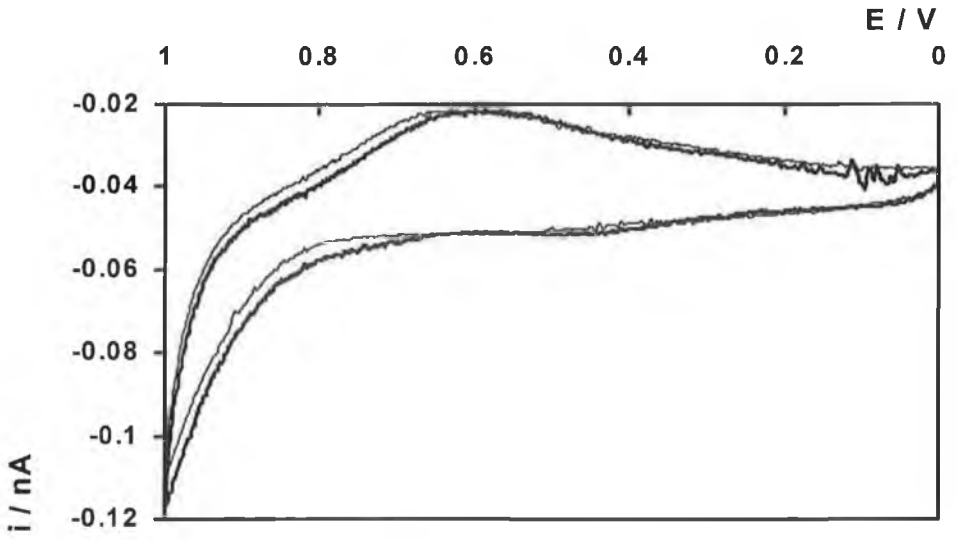

(b)

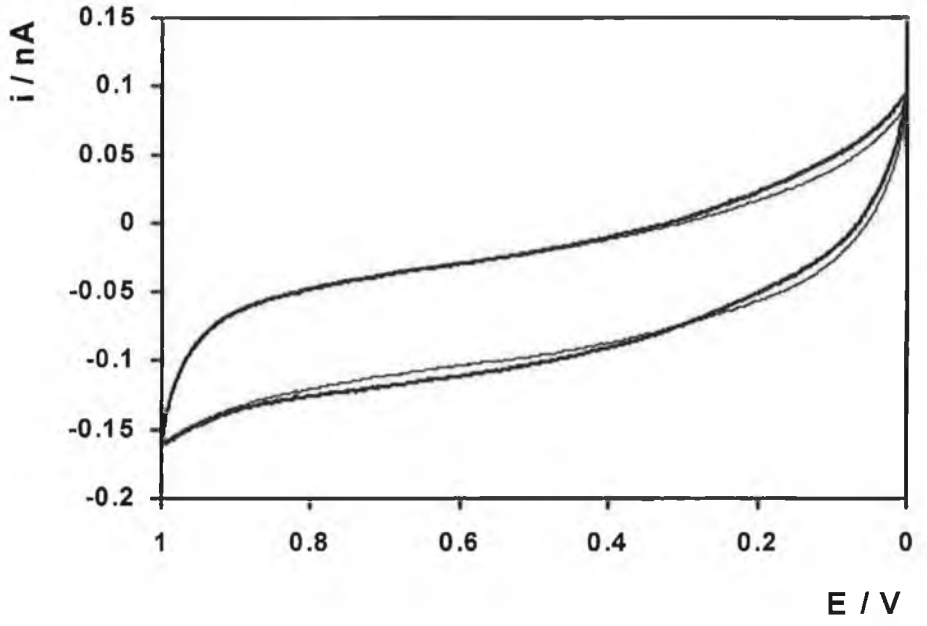

Figure 5.12 Effect of 3 MW cm^{-2} intensity 355 nm laser pulses on the cyclic voltammogram of a 5 μm radius (a) gold and (b) platinum microelectrode. The thick line indicates data for the case where laser pulses are applied during the potential sweep. The thin line indicates data for the case where no pulses are applied during the potential sweep. The supporting electrolyte is 1.0 M $LiClO_4$. Potentials are vs. Ag/AgCl. The scan rate is 0.05 V s^{-1} and the initial potential is 0.000 V.

(a)

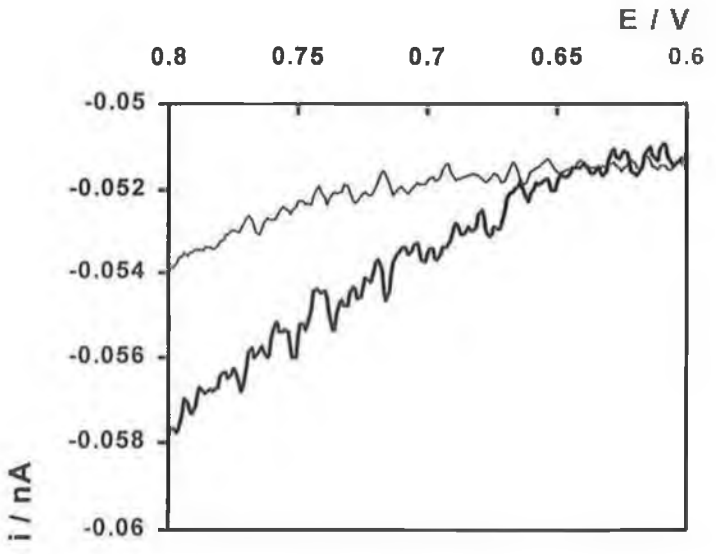

(b)

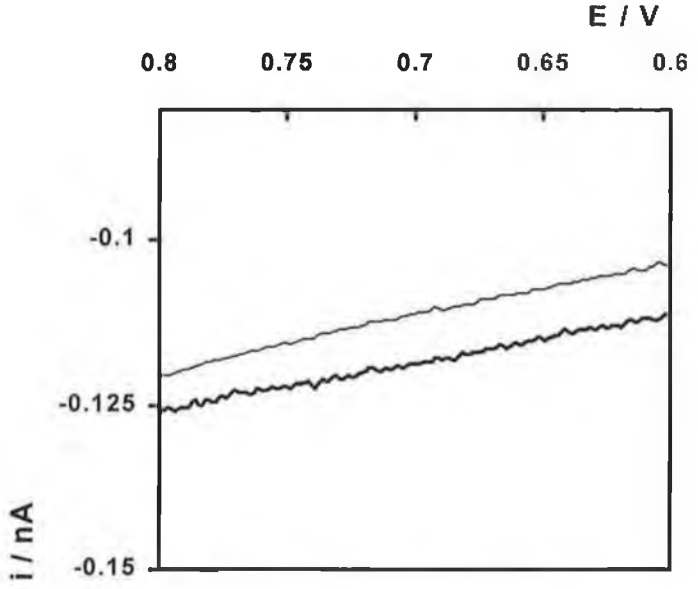

Figure 5.13 Expansion of Figure 5.13 anodic current in the potential region 0.6 to 0.8 V. (a) 5 μm radius gold and (b) 5 μm radius platinum microelectrode. The thick line indicates data for the case where 3 MW cm^{-2} laser pulses are applied during the potential sweep. The thin line indicates data for the case where no pulses are applied during the potential sweep. The supporting electrolyte is 1.0 M $LiClO_4$. Potentials are vs. Ag/AgCl. The scan rate is 0.05 V s^{-1} and the initial potential is 0 V.

(a)

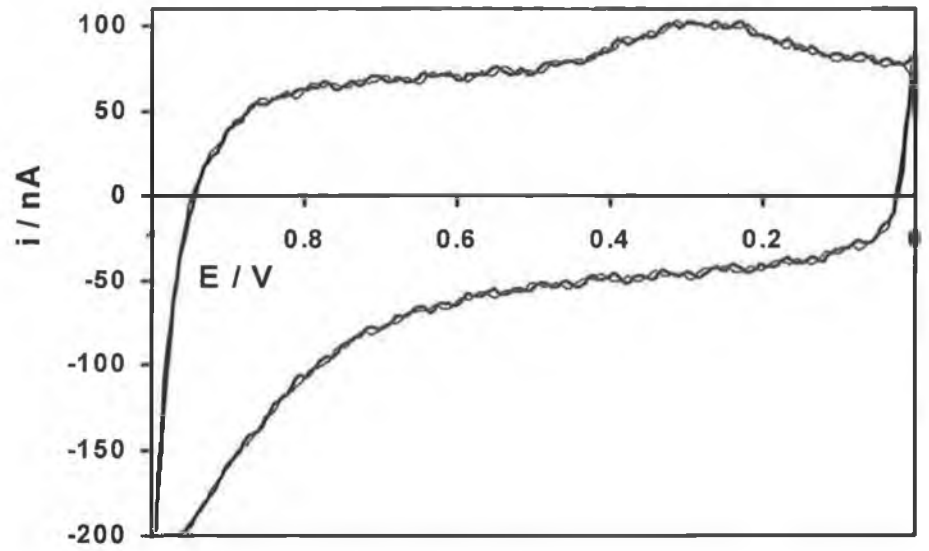

(b)

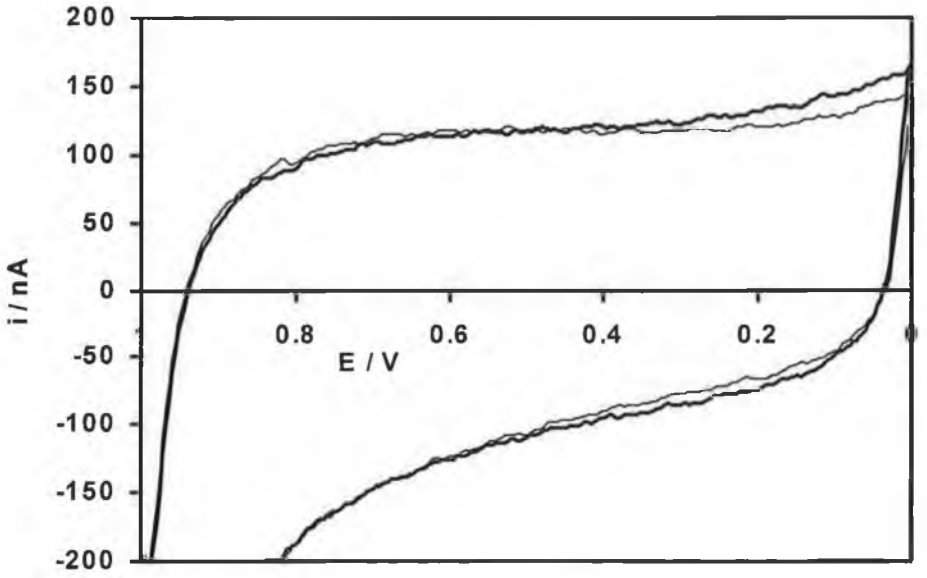

Figure 5.14 Effect of 3 MW cm^{-2} intensity 355 nm laser pulses on the cyclic voltammogram of a 5 μm radius (a) gold and (b) platinum microelectrode. The thick line indicates data for the case where laser pulses are applied during the potential sweep. The thin line indicates data for the case where no pulses are applied during the potential sweep. The supporting electrolyte is 1.0 M $LiClO_4$. Potentials are vs. Ag/AgCl. The scan rate is 1000 V s^{-1} and the initial potential is 0.000 V.

(a)

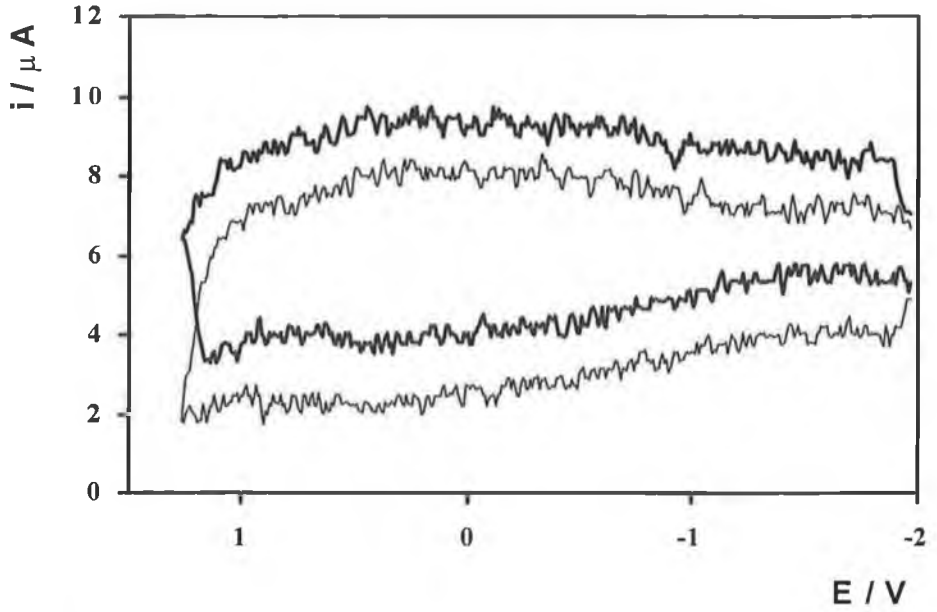

(b)

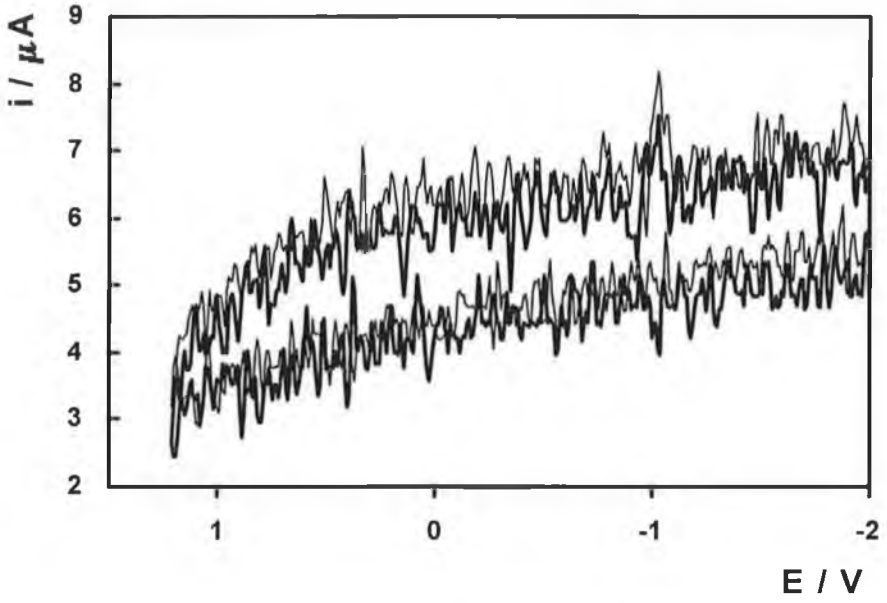

Figure 5.15 Effect of 3 MW cm^{-2} intensity 355 nm laser pulses on the cyclic voltammogram of a 5 μm radius (a) gold and (b) platinum microelectrode recorded using the high-speed electrochemistry apparatus. The thick line indicates data for the case where laser pulses are applied during the potential sweep. The thin line indicates data for the case where no pulses are applied during the potential sweep. The supporting electrolyte is 1.0 M $LiClO_4$. Potentials are vs. Ag/AgCl. The scan rate is 90,000 V s^{-1} and the initial potential is 0 V.

5.4.8 Monolayer Stability Under Laser Irradiation

In using laser light to electronically excite a monolayer of the ruthenium complex immobilised on a platinum microelectrode, it is essential that the monolayer remains attached to the electrode following the application of the laser pulse. The results presented in Chapter 4 have shown that laser light from a 355 nm, 10 Hz Nd:YAG laser has the ability to clean the surface of gold macroelectrodes and activate them towards fast heterogeneous electron transfer. However, for the lowest laser intensity studied, 3 MW cm^{-2}, the effects on the heterogeneous kinetics of a solution phase redox probe and on the interfacial properties of the electrode were found to be minimal. While the Chapter 4 experiments are based on gold electrode surfaces, the formation of stable monolayers of $[Ru(dpp)_2(Qbpy)]^{2+}$ requires platinum electrodes.

In this section, the stability of $[Ru(dpp)_2(Qbpy)]^{2+}$ monolayers on platinum electrodes to laser irradiation is presented. Monolayers were formed in the usual manner and the electrode was placed in the cell detailed in Figure 4.1 of Chapter 4. The supporting electrolyte was aqueous 1.0 M $LiClO_4$, containing 50 μM of the complex to improve the stability of the monolayer. The surface coverage was determined by cyclic voltammetry prior to application of the laser light. A series of sets of approximately 10 pulses of 3 MW cm^{-2} intensity were applied to the electrode surface. Following each set of 10 pulses, the surface coverage was determined again.

Figure 5.16 illustrates a plot of surface coverage of $[Ru(dpp)_2(Qbpy)]^{2+}$ vs. number of pulses for three replicate experiments. The graph shows that the surface coverage drops from $1.13\pm0.1 \times 10^{-10}$ mol cm^{-2} to $1.06\pm0.2 \times 10^{-10}$ mol cm^{-2} after the application of the first ten pulses. The surface coverage drops further with the application of 10 more pulses, finally reaching low sub-monolayer coverage after the application of 5 sets of 10 pulses. The conclusion to be drawn from this graph is that a monolayer is stable to one application of 10 laser pulses and for this reason, in further experiments where laser pulses are applied to a monolayer, only 10 pulses are applied.

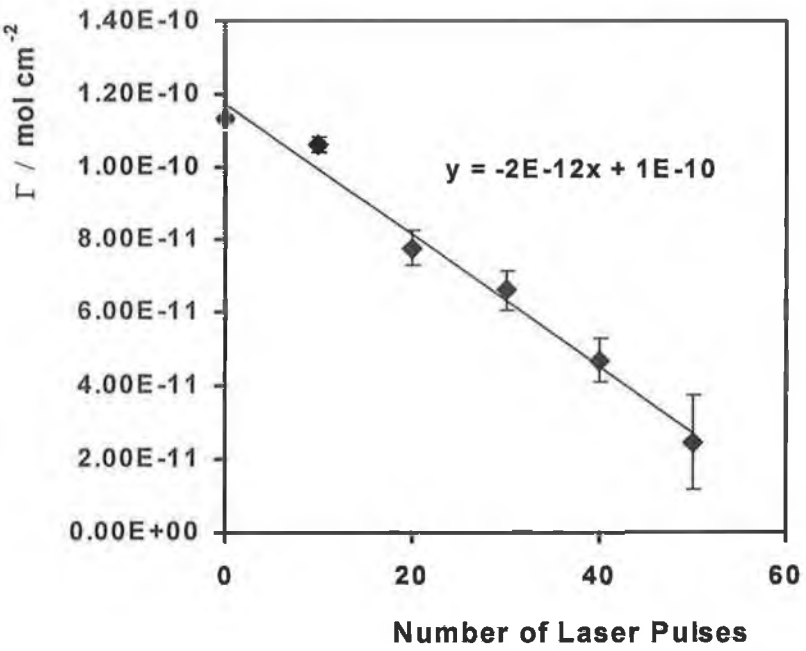

Figure 5.16 Surface coverage obtained from cyclic voltammograms of a monolayer of $[Ru(dpp)_2(Qbpy)]^{2+}$ immobilised on a platinum microelectrode following the application of sets of 10 pulses of 355 nm, 9ns, 10 Hz laser light, of 3MW cm^{-2} intensity. The supporting electrolyte is 1.0 M $LiClO_4$.

5.4.9 High-Speed Cyclic Voltammetry

The high scan rates required to detect the oxidation or reduction of a transient species such as the electronically excited state are achievable using the high-speed electrochemistry apparatus described in Section 5.2 of this chapter. Figure 5.17 is a cyclic voltammogram of a 5 μm radius platinum microelectrode, modified with a monolayer of $[Ru(dpp)_2(Qbpy)]^{2+}$ at a scan rate of 22,000 V s^{-1}. This scan rate yields an experimental timescale of 1.2 μs, slightly longer than the lifetime of the complex, 0.37 μs, and therefore will allow for the detection of the excited state response before it decays to the ground state. The CV is the average of 256 separate experiments. The presence of the monolayer was confirmed before the high-speed measurement with cyclic voltammetry using lower scan rates of 0.1 V s^{-1}. The high-speed CV in Figure 5.17 shows no trace of the monolayer peaks and resembles that obtained for a clean, unmodified electrode surface. A CV recorded at slow scan rates (0.1 V s^{-1}) confirms that the monolayer is still present and has not been removed by the high-speed measurement. The absence of the redox peaks in the high-speed CV appears to originate from the poor signal-to-noise ratio of the fastscan instrumentation. The expected faradaic current for the monolayer redox reaction, i_F, may be calculated using Equation 5.8:

$$i_F = \frac{n^2 F^2 A \Gamma \nu}{4RT} \qquad (5.8)$$

where n is the number of electrons transferred in the redox process, A is the area of the electrode (7.85×10^{-7} cm^{-2}), Γ is the surface coverage of the monolayer (1.0×10^{-10} mol cm^{-2}), ν is the scan rate (V s^{-1}) and F, R and T have their usual significance.[6] At a scan rate of 22,000 V s^{-1}, i_F expected to be 1.86 μA, which is approximately only 7 % of a full-scale deflection even under the most sensitive conditions. At a scan rate of 22,000 V s^{-1}, the ratio of capacitive current to faradaic current is approximately 3:1, indicating that under ideal experimental conditions, the faradaic peaks should be resolvable from the background capacitive current.

Despite this result, an attempt was made to carry out the excited state electrochemistry experiment as proposed in the introduction to this chapter. In this experiment, a rapid potential sweep is applied to a monolayer-modified electrode during the application of

laser pulses to the monolayer. The laser pulses will promote the monolayer molecules into the electronically excited state, and if the potential sweep is rapid enough, it should allow the detection of the excited state redox potentials of the $[Ru(dpp)_2(Qbpy)]^{2+}$ complex. The noise problem encountered in the preceding experiment may not affect the observation of excited state redox peaks, as it has been shown previously[5] that the $Ru^{2+*/3+}$ redox process exhibits a larger current than the corresponding $Ru^{2+/3+}$ process, due to the larger rate constant of the $Ru^{2+*/3+}$ electron transfer reaction. The signal for the excited state redox reactions is therefore likely to be larger than the ground state reaction and may be observable under these experimental conditions.

The application of the high scan rate potential sweep (22,000 V s^{-1}) was triggered using the Q-switch sync output of the laser power supply. This output allows for synchronous triggering of other equipment with firing of the laser pulses. In this set-up, every time a laser pulse is fired, a potential sweep is applied to the electrode. The laser does not have a single-shot facility, so the laser pulses are applied by rapid manual opening and closing of the shutter. This is to ensure that only 10 pulses are applied to the monolayer/electrode surface. As the laser pulses were applied for a short time only ($\approx$ 1 s), the CV obtained consists of one store and not the average of 256 stores as in Figure 5.17. If more than one store is obtained, the stores recorded at later times would correspond to data where no laser pulses are applied and so the excited state redox response, if present, would be "averaged out".

Figure 5.18 is the result of the experiment described above. The thin line corresponds to one store obtained where no laser pulses were applied to the monolayer-modified electrode. The thick line corresponds to one store obtained where approximately 10 laser pulses of 3 MW cm^{-2} intensity were applied. The signal obtained for both situations is extremely noisy, as it is impossible, under the experimental conditions, to average a number of stores to produce a smoothed signal. Therefore, it is difficult to tell if any faradaic response due to either the ground or electronically excited state has been detected. Performing a number of repetitive experiments and averaging the single stores obtained in Microsoft Excel could overcome this problem. However, the lack of observation of any Faradaic peaks in the ground state CV indicates that, using the current experimental set-up, it is difficult to detect any Faradaic responses. Unfortunately, this experiment has not resulted in the successful electrochemical

detection of the redox response of the electronically excited state of $[Ru(dpp)_2(Qbpy)]^{2+}$ complex.

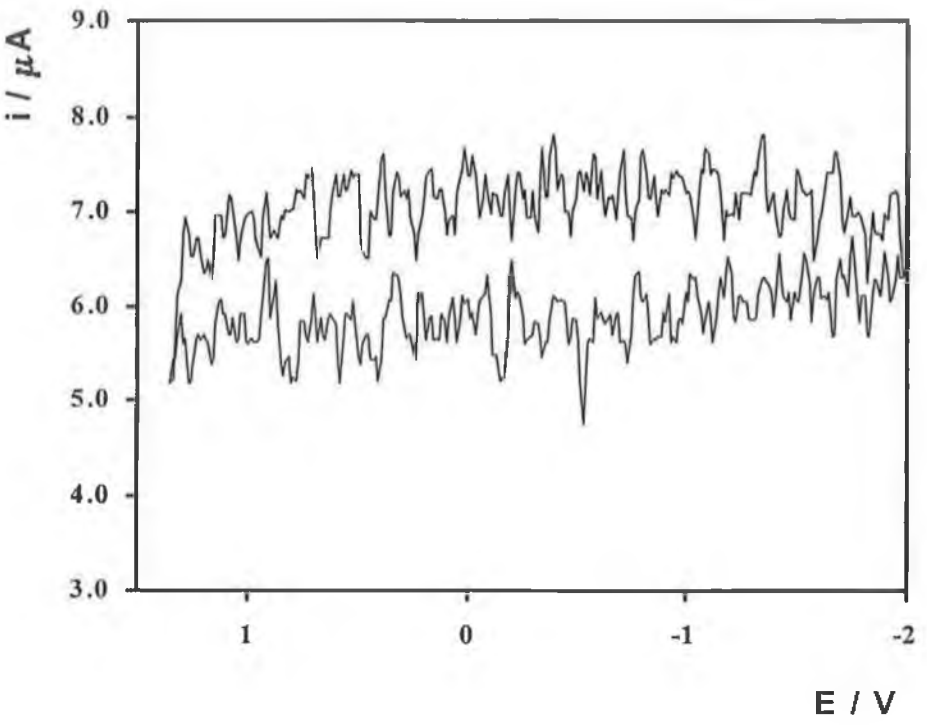

Figure 5.17 Cyclic voltammogram of a spontaneously adsorbed $[Ru(dpp)_2(Qbpy)]^{2+}$ monolayer on a 5 μm radius platinum microdisk electrode obtained using the high-speed electrochemistry apparatus. The supporting electrolyte is aqueous 1.0 M $LiClO_4$. The scan rate is 22,000 V s^{-1}. The surface coverage is $1.0\pm0.1 \times 10^{-10}$ mol cm^{-2}. This CV is the average of 256 stores recorded on the oscilloscope.

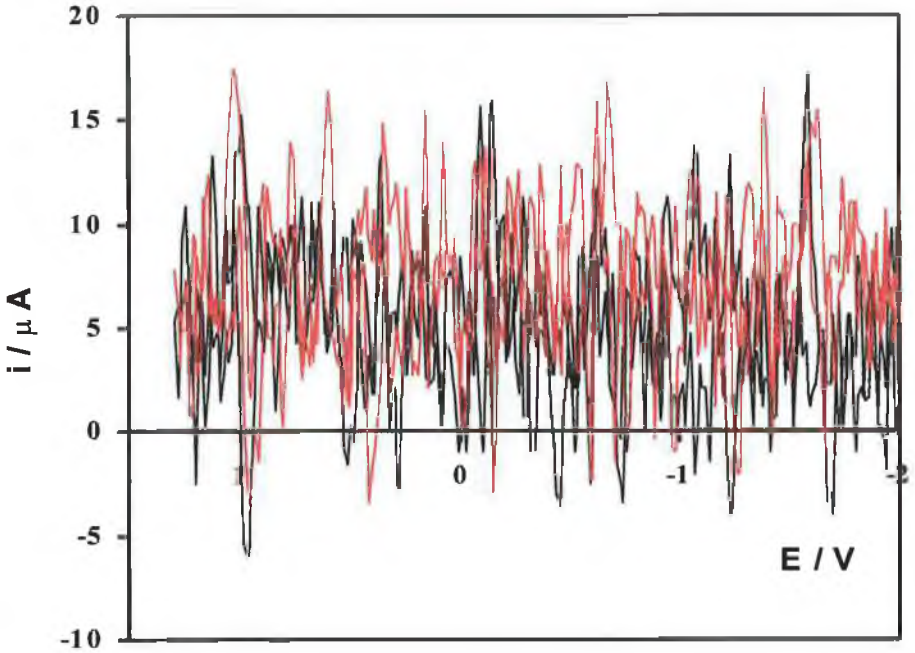

Figure 5.18 Cyclic voltammogram of a spontaneously adsorbed $[Ru(dpp)_2(Qbpy)]^{2+}$ monolayer on a 5 μm radius platinum microdisk electrode obtained using the high-speed electrochemistry apparatus. Black line – without laser pulses, red line – with ≈ 10 laser pulses. The supporting electrolyte is aqueous 1.0 M $LiClO_4$. The scan rate is 22,000 V s^{-1}. The surface coverage is $1.0\pm0.1 \times 10^{-10}$ mol cm^{-2}. This CV is the result of one store recorded on the oscilloscope.

There are many reasons for the failure of this experiment. The first is the small size of the currents resulting from the application of the potential sweep to the electrode when they are converted to a voltage signal and recorded on the oscilloscope. These small currents result in a small signal being registered on the oscilloscope (even at the lowest voltage range of 40 mV) and therefore a low signal-to-noise ratio. This makes distinguishing any faradaic responses from the observed noise a difficult task. Electrodes with a larger geometric area, such as one constructed using a 25 μm radius wire, yield larger currents and smoother voltammograms. However, larger electrodes will not have the short response time, i.e., RC time constant, that is needed to measure a rapid redox process like the oxidation or reduction of the electronically excited state. This precludes the use of larger electrodes for this measurement. The simplest solution to the problem of small currents may be to utilise an i - E converter with a larger resistance. For example, increasing the resistance of the converter five-fold from 1470 to 7350 Ω would cause the faradaic signal seen on the oscilloscope to increase five-fold from 2.7 mV to 13.5 mV. This would be detectable, even using the smallest voltage range of 40 mV. The capacitive current would also increase, increasing the size of the observed signal.

The experimental set-up for the detection of excited state redox processes could also be improved in the manner that the laser pulses, the application of the potential sweep and the recording of the voltammogram are timed. A suggestion for improving this lies in the use of a low–power Nd:YAG laser recently acquired by this laboratory. This laser has a single shot facility and a Q-switch "sync out" port which could be used to trigger the potential sweep and the oscilloscope data acquisition. The single shot would allow the application of one sweep and the acquisition of a single un-averaged voltammogram by the oscilloscope, concomitant with the application of a single laser pulse. Applying only one pulse would also minimise laser damage to the monolayer. Unfortunately, time constraints have not allowed the experiment to be carried out in this manner, which was used by Forster and Keyes in a previous excited state electrochemistry experiment.[5]

Another issue which may affect this experiment, is the possibility of efficient quenching of the electronically excited state by electron and/or energy transfer from the metal surface. If the excited state is not as long-lived when immobilised on the platinum surface as it is in fluid solution (372 ns), then it will be impossible to detect

the redox processes of the excited state using cyclic voltammetry, even at the ultrafast scan rates possible with the high-speed electrochemistry apparatus. Forster and Keyes have detected long-lived emission (6.2 μs) from monolayers of $[Ru(bpy)_2(Qbpy)]^{2+}$ on platinum microelectrodes.[5] They have determined that ground state heterogeneous electron transfer proceeds via a nonadiabatic mechanism, indicating weak electronic coupling between the monolayer and the electrode. This weak electronic coupling means that quenching of the excited state via energy transfer from the platinum electrode is unlikely to be an efficient process. These results suggest that for fluorescence to be observed from a monolayer, in conjunction with weak electronic coupling, the excited state lifetime must be long, i.e., of microsecond order, to enable the emission process to "out-live" any electron transfer quenching processes. In contrast, some reports detailed in Section 1.5 of Chapter 1 state that for the observation of efficient fluorescence from monolayers immobilised on metal electrodes, a short fluorescence lifetime is necessary, as the emission process is then competitive with quenching via energy and electron transfer.[44,45,46] It may be that the latter theory is more accurate and therefore, a redox probe with a short lifetime e.g., low nanosecond order, such as the $[Os(bpy)_2(bpe)_2]^{2+}$ complex described in Chapter 3, would be more suitable for the detection of excited state redox processes via a combination of laser excitation and ultrafast scan-rate cyclic voltammetry.

5.5 Conclusions

As discussed in the introduction to this chapter, electron transfer involving electronically excited states is of considerable interest. While considerable effort has been expended in the theoretical and experimental probing of ground state heterogeneous electron transfer, few reports have probed heterogeneous electron transfer to and from electronically excited states. Moreover, there have been few experimental methods to achieve the *direct* measurement of the excited state redox potentials. As electronically excited states are transient species, the development of electrochemical methods to probe these states requires the use of high-speed instrumentation, and microelectrodes, which have short response times and allow the accurate investigation of rapid processes such as fast electron transfer ($k^\circ = 10^3 - 10^5$ s $^{-1}$). One successful method has involved recording a high-speed cyclic voltammogram of a ruthenium complex immobilised on a platinum microelectrode, during the electronic excitation of the ruthenium centres by the application of laser pulses.[5] The use of ultrafast scan rates (kV - MV s^{-1}) and microelectrodes allowed the investigation of electrochemical properties of the electronically excited state of a ruthenium complex and the *direct* measurement of the excited state oxidation potential of the complex.

This chapter has presented the evaluation of a ruthenium polypyridyl complex, $[Ru(dpp)_2(Qbpy)]^{2+}$, where dpp is 4,7-diphenyl-1,10-phenanthroline and Qbpy is 2,2';4,4'';4',4''-quarterpyridyl, as a suitable probe species for the *direct* measurement of excited state redox potentials. To be suitable for this measurement, the complex must be redox-active, have an emissive lifetime of microsecond order and be capable of forming a monolayer on a microelectrode surface. Spectroscopic and electrochemical investigations have shown that $[Ru(dpp)_2(Qbpy)]^{2+}$ is redox-active and has an emission lifetime of 372 ns at 298 K. The excited state redox potentials of the complex, as calculated from the Rehm-Weller approximation, are –0.679 and +1.020 V for oxidation and reduction, respectively.

Spontaneously adsorbed monolayers of the complex have been formed on platinum microelectrodes. High-speed potential step chronoamperometry has been used to probe the heterogeneous kinetics of the $Ru^{2+/3+}$ redox reaction. A Tafel plot of ln k vs.

overpotential has yielded a value of 9.1×10^5 s^{-1} for k°, the standard heterogeneous electron transfer rate constant.

In developing the excited state electrochemistry experiment, it is important to show that the laser pulses applied do not cause significant damage to the monolayer. It is equally important that the laser pulses do not cause any artefacts in the voltammetry observed, at least at the fast scan rates employed here. The results presented have shown that a monolayer of $[Ru(dpp)_2(Qbpy)]^{2+}$ is capable of withstanding 10 pulses of 3 MW cm^{-2}, 355 nm laser light (the minimum amount possible with the laser employed). Therefore, the amount of laser pulses applied during the excited state electrochemistry experiment must be restricted to 10 pulses. Studies of the effect of applying laser pulses to an unmodified microelectrode during a potential sweep have demonstrated that laser effects, i.e., the laser-induced current transients discussed in Chapter 4, are absent at fast scan rates $\geq$ 1000 V s^{-1}.

High-speed cyclic voltammetry (22,000 V s^{-1}) of a platinum microelectrode modified with a monolayer of $[Ru(dpp)_2(Qbpy)]^{2+}$ has proved to yield disappointing results. Due to instrumental limitations, it is difficult for the faradaic response of the monolayer redox processes to be detected with the system described here. High levels of noise in the signal, coupled with the inherent small size of the signal itself, are the origin of this difficulty. Similarly, it proved impossible to detect the redox processes of the electronically excited state. A number of improvements to the instrumentation and experimental set-up have been proposed. The issue of quenching of the excited state by the metal electrode has also been discussed.

REFERENCES

(1) Nazeeruddin, M. K.; Kay, A.; Rodicio, I.; Humphry-Baker, R.; Müller, E.; Liska, P.; Vlachpoulos, N. Grätzel, M. *J. Am. Chem. Soc.* **1993**, *115*, 6382.

(2) Knox, R. S. *Photosynth. Res.* **1996**, *48*, 35.

(3) Ward, M. D. *Chem. Soc. Rev.* **1997**, *26*, 365.

(4) Jones, W. E.; Fox, M. A. *J. Phys. Chem.* **1994**, *98*, 5095.

(5) Forster, R. J.; Keyes, T. E. *J. Phys. Chem. B* **1998**, *102*, 10004.

(6) Bard, A. J.; Faulkner, L. R. "Electrochemical Methods: Fundamentals and Applications", 2nd Ed., Wiley and Sons, New York, 2001.

(7) Forster, R. J. "Ultrafast Electrochemical Techniques" in "The Encyclopaedia of Analytical Chemistry", Wiley and Sons, New York, 1998.

(8) Weldon, F., Ph.D. Thesis, Dublin City University, 1998.

(9) Diamond, D.; Hanratty, V. C. A. "Spreadsheet Applications in Chemistry using Microsoft Excel", Wiley, New York, 1997.

(10) Xu, C. PhD Thesis, University of Illinois at Urbana-Champaign, 1992.

(11) O'Hanlon D. P., Ph.D. Thesis, Dublin City University, **1999**.

(12) Trasatti, S.; Petrii, O. A. *J. Electroanal. Chem.* **1992**, *327*, 354.

(13) Tirado, J. G.; Abruña, H. D. *J. Phys. Chem* **1996**, *100*, 4556.

(14) Christian, G. D. "Analytical Chemistry", 5th Ed., Wiley, New York, 1994.

(15) Kalyanasundaram, K. *Coord. Chem. Rev.* **1982**, *46*, 159.

(16) Balzani, V.; Juris, A.; Venturi, M.; Campagna, S.; Serroni, S. *Chem. Rev.* **1996**, *96*, 759.

(17) Juris, A.; Balzani, V.; Barigelletti, F.; Campagna, S.; Belser, P.; Von Zelewsky, A. *Coord. Chem. Rev.* **1988**, *84*, 85.

(18) Bierig, K.; Morgan, R. J.; Tysoe, S.; Gafney, H. D.; Strekas, T. C.; Baker, A. D. *Inorg. Chem.* **1991**, *30*, 4898.

(19) Rehm, D., Weller, A., *Isr. J. Chem.* **1970**, *8*, 259.

(20) Durham, B.; Caspar, J. V.; Nagle, J. K.; Meyer, T. J. *J. Am. Chem. Soc.* **1982**, *104*, 4803.

(21) Seddon, E. A.; Seddon, K. R. "The Chemistry of Ruthenium", Elsevier, New York, 1984.

(22) Atkins, P. W., "Physical Chemistry", 1st Ed., Oxford University Press, London, 1978.

(23) Barigelletti, F.; Belser, P.; Von Zelewsky, A.; Juris, A.; Balzani, V. *J. Phys. Chem.* **1985**, *89*, 3680.

(24) Aldrich Catalogue Handbook of Fine Chemicals, Aldrich, United Kingdom, 1996 – 1997.

(25) Weitz, D. A.; Garoff, S.; Gersten, J. I.; Nitzan, A. *J. Chem. Phys.* **1983**, *78*, 5234.

(26) De Armond, M. K.; Carlin, C. M. *Coord. Chem. Rev.* **1981**, *36*, 325.

(27) Nallas, G. N. A.; Jones, S. W.; Brewer, K. J. *Inorg. Chem.* **1996**, *35*, 6974.

(28) Ballardini, R.; Varani, G.; Indelli, M. T.; Scandola, F.; Balzani, V. *J. Am. Chem. Soc.* **1978**, *100*, 7219.

(29) Acevedo, D.; Abruña, H. D. *J. Phys. Chem.* **1991**, *95*, 9590.

(30) Acevedo, D.; Bretz, R. L.; Tirado, J. D.; Abruña, H. D. *Langmuir*, **1994**, *10*, 1300.

(31) Walsh, D. A.; Keyes, T. E.; Hogan, C. F.; Forster, R. J. *J. Phys. Chem.*, **2001**, *105*, 2792.

(32) Forster, R. J.; O'Kelly, J. P. *J. Electrochem. Soc.*, **2001**, *148*, E31.

(33) Laviron, E. *J. Electroanal. Chem.* **1974**, *52*, 395.

(34) Brown, A. P.; Anson, F. C. *Anal. Chem.*, **1977**, *49*, 1589.

(35) Feldberg, S. W.; Rubenstein, I. *J. Electroanal. Chem.* **1988**, *240*, 1.

(36) Marcus, R. A. *Angew. Chem. Int. Ed. Eng.* **1993**, *32*, 1111.

(37) Laviron, E. *J. Electronanal. Chem.* **1979**, *101*, 19.

(38) Goodwin, H. A.; Kepert, D. L.; Patrick, J. M.; Skelton, B. W.; White, H. *Aust. J. Chem.*, **1984**, *37*, 1817.

(39) Ferguson, J. E.; Love, J. L.; Robinson, W. T. *Inorg. Chem.*, **1972**, *11*, 1662.

(40) Forster, R. J.; Faulkner, L. R. *J. Am. Chem. Soc.* **1994**, *116*, 5444.

(41) Forster, R. J. *Inorg. Chem.* **1996**, *35*, 3394.

(42) Forster, R. J.; O'Kelly, J. P. *J. Phys. Chem.* **1996**, *100*, 3695.

(43) Chidsey, C. E. D. *Science* **1991**, *251*, 919.

(44) Chen, S. H.; Frank, C. W. *Langmuir* **1991**, 7, 1719.

(45) Pope, J. M.; Buttry, D. A. *J. Electroanal. Chem.* **2001**, *498*, 75.

(46) Fox, M. A.; Li, W.; Wooten, M.; McKerrow, A.; Whitesell, J. K. *Thin Solid Films* **1998**, *329*, 477.

ABBREVIATIONS AND SYMBOLS

ABBREVIATIONS

A	acceptor
D	donor
BF	basic fuschin
BL	bridging ligand
DNA	deoxyribonucleic acid
ECL	electrogenerated chemiluminescence
EDL	electrical double layer
ET	electron transfer
HOPG	highly ordered pyrolytic graphite
ILIT	indirect laser-induced temperature jump
ITO	indium-doped tin oxide
Ir	iridium
L	ligand bridge
Os	osmium
Ox	oxidised species
P	product
PET	photoinduced electron transfer
PMV	phase modulated voltammetry
Pt	platinum
pzc	potential of zero charge
pzr	potential of zero response
R	reactant
Red	reduced species
R6G	rhodamine 6G
Ru	ruthenium
QE	quantum efficiency
$TBABF_4$	tetrabutylammonium tetrafluoroborate
TBAP	tetrabutylammonium perchlorate

LIGAND ABBREVIATIONS

4-tet	3,6-bis(4-pyridyl)-1,2,4,5-tetrazine
bpe	*trans*-1,2-(4-pyridyl)ethylene
bpy	2,2'-dipyridyl
bpy'	4-methyl-(dodecyl-1-thiol)-2,2'-bipyridine
dpb	2,3-bis(2-pyridyl)benzoquinoxaline
dppe	cis-$Ph_2PCH{=}CHPPh_2$
Ome-bpy	4,4'-dimethyoxy-2,2'-bipyridyl
phen	1'10'-phenanthroline
p0p	4,4'-bipyridyl
p2p	1,2-bis(4-pyridyl)ethane
p3p	4,4'-trimethylenedipyridine
Qbpy	2,2':4,4'':4',4''-quarterpyridyl
tppz	tetra-2-pyridyl-1,4-pyrazine
tpy	2,2';6',2''-terpyridine

ENGLISH SYMBOLS

A_{et}	pre-exponential factor
c	thermal (heat) capacity
d	inter-reactant centre-to-centre separation distance, density
d_0	inter-reactant centre-to-centre separation at Van der Waals distance
$D_{OX}(\varepsilon)$	distribution of acceptor states in a monolayer
E_{abs}	absorption maximum
E_B	barrier height
E_p	peak potential
E^o	formal potential
$E^{0\text{-}0}$	excited state energy
$E_{1/2}{}^{red}$	oxidation potential
$E_{1/2}{}^{ox}$	reduction potential
ΔE_e	threshold energy for photoemission
f_0	threshold frequency for photoelectron emission
f^r_j	j^{th} normal mode force constant in the reactant species
f^p_j	j^{th} normal mode force constant in the product species

ΔG_{OS}	outer sphere component of the Gibbs free energy of activation
$\Delta G°$	difference in Gibbs energy between the equilibrium configurations of the product and reactant states.
$\Delta G^{\neq}$	Gibbs free energy of activation for forward electron transfer
h	Planck's constant
H_{rp}	electronic coupling energy
$\Delta H^{\ddagger}$	electrochemical enthalpy
k_B	Boltzmann constant
k_{ET}	first order rate constant for electron transfer
k^o	standard heterogeneous electron transfer rate constant
$k_{Ox}(\eta)$	heterogeneous rate constant for oxidation at a given overpotential, η
$k_{red}(\eta)$	heterogeneous rate constant for reduction at a given overpotential, η
k_q	rate constant for electron transfer quenching by an organic quencher
$n(\varepsilon)$	Fermi function for a metal
$P(\varepsilon)$	probability factor describing electron tunnelling at a given energy
q	laser intensity
Δq_j	equilibrium displacement of the j^{th} normal coordinate
r	molecular radius
R	general gas constant, reflection coefficient of a metal
r_P	radii of the products
r_R	radii of the reactants
$\Delta S_{rc}°$	reaction entropy
ΔS^{σ}	specific surface entropy
t_0	laser pulse length
T	temperature
T_{in}	temperature change following a laser pulse
T(t)	temperature change at time, t, following a laser pulse
V_h	open circuit potential response to electrode heating
V_e^0	potential of the lowest free electron in the electrolyte
ΔV	applied voltage

GREEK SYMBOLS

β	tunnelling parameter
ε_F	Fermi level
ε_{max}	molar extinction coefficient
ε_0	permittivity of free space
ε_{op}	optical dielectric constant of the solvent
ε_s	static dielectric constants of the solvent
ϕ	work function of a metal
$\Gamma_{Red,\,\eta}$	instantaneous surface coverage of an oxidised species
$\Gamma_{Ox,\,\eta}$	instantaneous surface coverage of a reduced species
η	overpotential
φ	applied potential
κ	thermal conductivity
κ_{el}	electronic transmission coefficient
λ	total reorganisation energy
λ_{in}	inner reorganisation energy
λ_{out}	outer reorganisation energy
λ_{th}	threshold wavelength of electron emission
ν	cyclic voltammetric scan rate
ν_{el}	electron hopping frequency
ν_n	nuclear frequency factor
ρ	density of electronic states in a metal electrode
$\Delta\upsilon_{1/2}$	bandwidth at half-height

Appendix A

121/23

Ground *vs.* excited state electron transfer: Adsorbed monolayers and trimers in solution

Jennifer L. Brennan, Michael Howlett and Robert J. Forster*

National Centre for Sensor Research, School of Chemical Sciences, Dublin City University, Dublin 9, Ireland

Received 29th November 2001, Accepted 4th February 2002

Transient emission spectroscopy has been used to probe the rate of photoinduced electron transfer between metal centres within a novel trimeric complex $\{[Os(bpy)_2(bpe)_2][Os(bpy)_2Cl]_2\}^{4+}$, where bpy is 2,2′-bipyridyl and bpe is *trans*-1,2-bis-(4-pyridyl)ethylene. Transient emission experiments on the trimer, and on $[Os(bpy)_2\ (bpe)_2]^{2+}$ in which the $[Os(bpy)_2\ Cl]^+$ quenching moieties are absent, reveal that the rate of photoinduced electron transfer (PET) across the bpe bridge is $1.3 \pm 0.1 \times 10^8\ s^{-1}$. Investigations into the driving forces for oxidation and reduction of the electronically excited state within the trimer indicate that quenching of the $[Os(bpy)_2\ (bpe)_2]^{2+*}$ centre within the trimer involves electron transfer from the $[bpe\ Os(bpy)_2\ Cl]^+$ centres to the electronically excited state with a driving force of −0.3 eV. Monolayers of the complex, $[Os(bpy)_2\ bpe\ pyridine]^{2+}$, have been formed by spontaneous adsorption onto platinum microelectrodes and used to probe the dynamics of electron transfer across the *trans*-1,2-bis-(4-pyridyl)ethylene bridge in the ground state. These monolayers are stable and exhibit well defined voltammetric responses for the $Os^{2+/3+}$ redox reaction. Cyclic voltammograms recorded at high scan rates can be accurately modelled according to a non-adiabatic electron transfer model based on the Marcus theory using a standard heterogeneous electron transfer rate constant, k°, of $3.1 \pm 0.2 \times 10^4\ s^{-1}$ and a reorganization energy of 0.4 ± 0.1 eV. This rate constant is a factor of approximately two orders of magnitude smaller than that found for photoinduced electron transfer across the same bpe bridge for identical driving forces. This significant difference is interpreted in terms of both the nature of the orbitals involved in electrochemically and optically driven electron transfer, as well as the strength of electronic coupling between two molecular components as opposed to a molecular component and a metal electrode.

Introduction

Controlling the dynamics and energetics of electron transfer in molecular electronic systems continues to be of intense interest.[1,2] This interest is driven in part by the pivotal role that electron transfer reactions play in diverse areas including dye sensitisation for solar energy conversion,[3] information storage[4] and artificial photosynthesis.[5,6] Multinuclear ruthenium and osmium polypyridyl complexes in which the metal centres are linked by suitable coordinating bridges are well suited for probing redox processes in both the ground and excited states.[7] These polypyridyl complexes exhibit facile, reversible electrochemical responses as well as useful photophysical properties, *e.g.*, long lived excited states.[8] Moreover, by choosing appropriate bridging ligands, the

internuclear separation and perhaps orientation can be controlled. Significant investigations into electron transfer between metal centres have been carried out utilising both dimeric homo- and hetero-metallic complexes of osmium, ruthenium and other metals such as rhenium, iridium and rhodium.[2,9,10] In particular, Meyer and coworkers have probed the electron transfer properties of homo-metallic dimers of osmium[8,11] and ruthenium,[12,13] bridged using polypyridyl-type ligands. Balzani and co-workers have also performed pre-eminent work on electron transfer in ruthenium and osmium dimers[2,14,15] and their research has shown that the electrochemical and photophysical properties of these dimers depend heavily on the type of bridging ligand used.

Recent literature reports have shown that trimetallic complexes of osmium and ruthenium can function as useful photonic molecular devices. For example, Zahavy and Fox have reported on the use of an osmium-nickel-palladium complex as an electro-switchable-photoinduced-electron-transfer device (ESPET).[16] Brewer and co-workers have extensively investigated the properties of trimeric hetero-metallic osmium, ruthenium and iridium polypyridyl complexes.[17,18] They have synthesised a ruthenium-iridium-ruthenium complex which functions as a device for photoinitiated electron collection, whereby the bridging ligands linking the two ruthenium centres to the iridium core are photoreduced by one electron and the electrons are delivered to a substrate.[19] This complex has been shown to act as a catalyst for the reduction of carbon dioxide to formate.[20] Abruña and coworkers have reported on a series of trimetallic complexes of ruthenium and osmium bridged with the ligand tetra-2-pyridyl-1,4-pyrazine (tppz). The tppz ligand is synthetically flexible and gives rise to a number of complexes with electronic properties that are attractive for constructing molecular wires.[21]

While many of these investigations have probed the electron transfer mechanisms between metal centres in a trimer complex, there have been relatively few reports on the dynamics and energetics of electron transfer. Moreover, the differences between electrochemically (ground) *vs.* optically (excited state) driven electron transfer has not been extensively considered. Information about processes of this kind is especially important for molecular electronics applications ranging from information storage to the production of antennae complexes suitable for solar energy conversion.[22,23] In this contribution, we present an investigation into the electrochemistry, photophysics and the rates of photoinduced electron transfer within a novel osmium trimer complex, $\{[Os(bpy)_2(bpe)_2][Os(bpy)_2Cl]_2\}^{4+}$, where bpy is 2,2′-bipyridyl and bpe is *trans* -1,2-bis-(4-pyridyl)-ethylene. Moreover, spontaneously adsorbed monolayers of $[Os(bpy)_2$ bpe pyridine$]^+$ have been formed. These monolayers exhibit nearly ideal voltammetric responses and the dynamics and energetics of heterogeneous electron transfer have been probed by modelling fast scan rate voltammetry according to a non-adiabatic electron transfer model based on the Marcus theory. By comparing the heterogeneous electron transfer rate across the bpe with that found for photo induced electron transfer, an insight has been obtained into the differences between ground and excited state electron transfer processes. Finally, the strength of electronic coupling across the *trans*-1,2-bis-(4-pyridyl)ethylene bridge is compared for two metal centres as opposed to a metal electrode and a metal complex.

Experimental

Materials

$[Os(bpy)_2$ bpe Cl$]^+$ and $[Os(bpy)_2$ bpe pyridine$]^{2+}$ were synthesized using approaches similar to those described previously.[24]

$[Os(bpy)_2(bpe)_2]$. 172 mg (0.3 mmol) of $[Os(bpy)_2Cl_2]$ was placed in 40 cm^3 of methanol and refluxed for 10 min to ensure complete dissolution. A solution of 55 mg (0.3 mmol) of *trans*-1,2-bis-(4-pyridyl)ethylene dissolved in 10 cm^3 of methanol was added, together with 40 cm^3 of water and the solution was refluxed for 15 h. The progress of the reaction was monitored using high performance liquid chromatography (HPLC) and cyclic voltammetry. After the reaction was complete, the volume was reduced to 5 cm^3 by rotary evaporation. Ammonium hexafluorophosphate (95+%, Aldrich) was then added, and the dark green-black product was collected by filtration and washed with diethyl ether. The product was recrystallised from aqueous methanol to give dark green-black crystals, yield 295 mg, 85%. Elemental analysis: Calculated for $C_{44}H_{36}N_8OsP_2F_{12}$,

C:45.67%, H:3.11%, N:9.68%. Found C:45.43%, H:3.20%, N:9.62%. The complex was further characterized using IR, UV-Vis, NMR and cyclic voltammetry.

$\{[Os(bpy)_2(bpe)_2][Os(bpy)_2Cl]_2\}^{4+}$. $[Os(bpy)_2Cl_2]$ (99.2 mg, 0.173 mmol) and $[Os(bpy)_2(bpe)_2](PF_6)_2$ (100 mg, 0.0865 mmol) were dissolved in 30 cm^3 ethanol. The mixture was then refluxed for 72 h. The solvent was removed to a volume of 10 cm^3, and was added dropwise with constant stirring to a solution of concentrated aqueous NH_4PF_6. The resulting black solid was collected by filtration and recrystallised from acetone/water (2/1 v/v) by slow evaporation. Elemental analysis (Calc[d]. For $Os_3C_{84}H_{68}N_{16}P_4F_{18}Cl$; C, 40.0%; H, 2.71%; N, 8.88%. Found: C, 38.38%; H, 2.43%; N, 8.18%. The complex was further characterized using IR, UV-Vis, NMR and cyclic voltammetry.

Instrumentation

In high speed chronoamperometry,[25] a custom-built function generator-potentiostat, with a rise time of less than 2 ns, was used to apply potential steps of variable pulsewidth and amplitude directly to a two-electrode cell. A Pt foil and an Ag/AgCl reference electrode were combined to form a counter electrode. The foil lowered the resistance and provided a high frequency path.

Cyclic voltammetry was performed using a CH Instruments Model 660 Electrochemical Workstation and a conventional three-electrode cell. All solutions were degassed thoroughly using nitrogen, and a blanket of nitrogen was maintained over the solution during all experiments. Potentials are quoted with respect to a CH Instruments Ag/AgCl reference electrode filled with saturated KCl which had a potential of +0.190 V with respect to the normal hydrogen electrode. All experiments were performed at room temperature (22 ± 3 °C).

Microelectrodes were prepared using platinum microwires of radii between 2.5 and 50 (m sealed in a glass shroud. They were mechanically polished as described previously.[26] Electrochemical cleaning of the electrodes was carried out by cycling in 0.1 M H_2SO_4 between potential limits chosen to initially oxidize and then reduce the surface of the platinum electrode. Excessive cycling was avoided in order to minimize the extent of surface roughening. The real surface area of the electrodes was determined by calculating the charge under the platinum oxide reduction peak. Typically surface roughness values were between 1.6 and 2.0. Determining the real, as opposed to the geometric area of the electrodes is important if the area of occupation of the adsorbate is to be accurately determined.

Spontaneously adsorbed monolayers were formed by immersing the microelectrodes in micromolar solutions of $[Os(bpy)_2$ bpe pyridine$]^{2+}$ in acetone/water (50/50, v/v) for periods up to 12 h. The complex is stable towards aerial oxidation and no precautions were taken to exclude atmospheric oxygen during monolayer formation. Before electrochemical measurements were made, the electrodes were rinsed with 50/50 acetone/water, Milli-Q water and the electrolyte to remove any unbound material. Subsequent measurements were performed in blank electrolyte.

Ultraviolet-visible spectra were recorded using a Shimadzu UV-3100 diode array spectrometer. Room temperature emission spectra were recorded using a Perkin Elmer LS50 B luminescence spectrometer, equipped with a red sensitive Hamamatsu R928 detector. Samples were prepared at concentrations of 10^{-4} to 10^{-5} M in spectroscopic grade butyronitrile. For room temperature measurements, 1 cm quartz cells were used. The excitation and emission slits were 2 nm for all experiments.

Luminescent lifetimes for the monomeric complexes were measured using the third harmonic (355 nm) of a Spectron Q-switched Nd-YAG laser for excitation. Emission was detected in a right angled configuration to the laser using an Oriel model IS520 gated intensified CCD coupled to an Oriel model MS125 spectrograph. With suitable signal averaging, this configuration allows a complete emission spectrum (spectral range 250 nm) to be obtained within times as short as 10 ns. The emission spectra were typically recorded using the average of twenty laser shots. The gate-width, *i.e.*, the exposure time of the CCD, was never more than 5% of the excited state lifetime. The step size, *i.e.*, the time between the acquisition of discrete spectra, was typically 5% of the excited state half life.

The excited state lifetime of the trimer was determined using an Edinburgh Analytical Instruments Single Photon Counter in a T setting using J-ya monochromators. The light source in this system is an nF 900 nanosecond flashlamp filled with nitrogen, with a profile of 1 ns. The detector

is a Single Photon Photomultiplier Detection system, Model S300, with a Norland N5000 MCA card and a Cd900 serial PC interface. The program used for the data correlation and manipulation is an F900 program, Version 5.13. The excitation wavelength was 337 nm and the lifetimes were collected determined by analysing the emission decay at λ_{max}.

Dilute solutions of the complex in acetonitrile (RT) or ethanol/methanol 4/1 (77 K) (10^{-4} to 10^{-5} M) were deaerated for 20 min under nitrogen prior to use. Low temperature emission lifetime studies were carried out using an Oxford Instruments gas-exchange cryostat equipped with a Thor 3030 temperature controller. Standard iterative techniques were employed to determine the lifetimes of emission.

Results and discussion

Photoinduced charge transfer

Spontaneously adsorbed and self-assembled monolayers that incorporate redox active centres provide important insights into the energetics and dynamics of electron transfer. In particular, tunnelling across an organic bridge, *e.g.*, an alkane chain, that links the continuum of states in the electrode and the localised molecular orbitals of the redox centres, has been investigated in considerable detail. However, relatively few studies have compared this situation with the dynamics of photoinduced electron transfer between two molecular components across the same bridge. For example, by comparing the rates of photochemically and electrochemically triggered electron transfer across the *trans*-1,2-bis-(4-pyridyl)ethylene bridge, insight can be obtained into the effect of swapping an electronically localized redox centre for an electronically delocalized metal electrode on the strength of electronic coupling. Here, we probe this issue by considering photo induced charge transfer within a trimeric metal complex, $\{[Os(bpy)_2(bpe)_2][Os(bpy)_2Cl]_2\}^{4+}$.

Fig. 1 shows that the trimeric complex, $\{[Os(bpy)_2(bpe)_2][Os(bpy)_2Cl]_2\}^{4+}$, exhibits a weak emission at 760 nm at room temperature. It also illustrates the emission spectrum for a model monomeric complex $[Os(bpy)_2(bpe)_2]$, and shows that while the wavelengths of maximum emission are indistinguishable for the two complexes, the intensity of the trimer emission is only about 2% of that found for the monomer. The observation that the $[Os(bpy)_2(bpe)_2]^{2+}$ complex is highly luminescent is entirely consistent with the known photophysical properties of $[Os(N)_6]^{2+}$ complexes, where N represents a nitrogen donor such as pyridine or bpy. In contrast to the luminescence observed for these two complexes, $[Os(bpy)_2\ bpe\ Cl]^+$ emits only very weakly even at liquid nitrogen temperatures. This behaviour is typical of that found for $[Os(N)_5\ Cl]^+$ complexes where vibrational relaxation provides a fast non-radiative decay pathway.[27] The observation that the

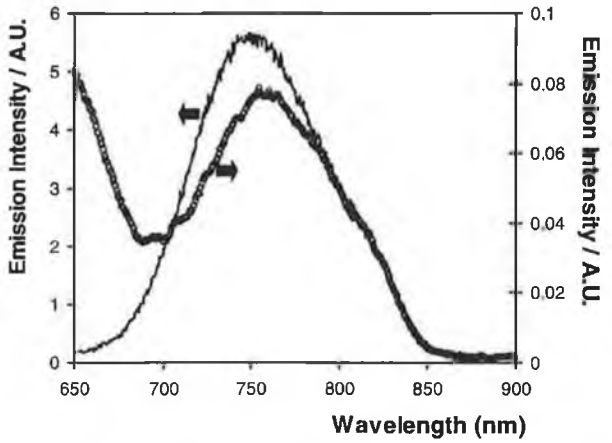

Fig. 1 Emission spectra at 298 K of $[Os(bpy)_2(bpe)_2]^{2+}$ (solid line) and $\{[Os(bpy)_2(bpe)_2][Os(bpy)_2Cl_2]\}^{4+}$ (open circles). In both cases the solvent is deoxygenated butyronitrile. Both spectra were processed using a 5-point moving average smooth.

emission intensity is dramatically lower for the trimer than the model $[Os(bpy)_2\ (bpe)_2]^{2+}$ complex suggests that the [bpe $Os(bpy)_2Cl]+$ centres play an important role in quenching the luminescence of the electronically excited $[Os(bpy)_2\ (bpe)_2]^{2+*}$ centre within the trimer.

Energy or electron transfer are possible quenching mechanisms in a system of this kind. However, efficient Förster energy transfer through dipole-dipole coupling requires significant overlap of the absorption and emission spectra of the two species. Fig. 2 depicts the absorption spectra of the $[Os(bpy)_2$ bpe $Cl]^+$, $[Os(bpy)_2(bpe)_2]^{2+}$ and $\{[Os(bpy)_2(bpe)_2][Os(bpy)_2Cl]\}^{4+}$ complexes. Typical of osmium polypyridyl complexes,[2] all of the complexes exhibit intense bands originating from ligand based $\pi \rightarrow \pi^*$ transitions in the high-energy UV region of the spectrum as well as metal-to-ligand charge transfer bands (MLCT) in the visible region. The trimer spectrum is simply a composite of the absorption bands of the component monomer complexes and does not exhibit any significant new spectral features. This observation indicates that the $[Os(bpy)_2\ (bpe)_2]^{2+}$ and $[Os(bpy)_2\ Cl]^+$ moieties interact only weakly across the bpe bridge in the trimer.[8,11] However, Fig. 1 and 2 are revealing from the perspective of Förster energy transfer. The overlap of the emission and absorbance spectra for the $[Os(bpy)_2\ (bpe)_2]^{2+}$ and $[Os(bpy)_2$ bpe $Cl]^+$species is very weak given that $\lambda_{max,em}$ and $\lambda_{max,abs}$ are approximately 750 and 450 nm, respectively. Therefore, in common with related systems,[28] it appears that Förster *energy* transfer involving dipolar coupling is not the dominant quenching mechanism in the trimer. In contrast, *electron* transfer to or from the $[Os(bpy)_2\ Cl]^+$ moiety to the $[Os(bpy)_2\ (bpe)_2]^{2+*}$ excited state is the more likely mechanism.

Rate of photoinduced electron transfer

The photoinduced electron transfer rate constant, k_{PET}, can be estimated using eqn. (1):

$$k_{PET} = \frac{1}{\tau} - \frac{1}{\tau^o} \tag{1}$$

where τ and τ° are the luminescence lifetimes in the presence and absence of a linked quencher. Fig. 3 illustrates emission transients for both the trimer and the structurally analogous monomeric complex, $[Os(bpy)_2\ (bpe)_2]^{2+}$, that does not include the quenching moiety. These data reveal that the excited state lifetime of the dimer is significantly shorter (6.5 ± 1.4 ns) than that of the monomer (42.4 ± 0.6 ns). This result indicates that the $[Os(bpy)_2\ Cl]^+$ moiety quenches the excited $[Os(bpy)_2\ (bpe)_2]^{2+*}$ centre. The rate constant for this charge transfer process is $1.3 \pm 0.1 \times 10^8\ s^{-1}$ at 298 K suggesting that quenching takes place efficiently across the 10 Å *trans*-1,2-bis-(4-pyridyl)ethylene bridge.

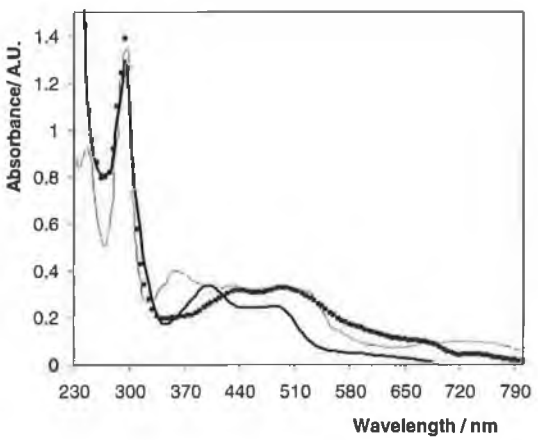

Fig. 2 Overlaid UV-vis spectra of $[Os(bpy)_2$ bpe $Cl]+$ (solid squares), $[Os(bpy)_2(bpe)_2]^{2+}$ (thick line), and $\{[Os(bpy)_2(bpe)_2][Os(bpy)_2Cl_2]\}^{4+}$ (thin line). In all cases the solvent is deoxygenated butyronitrile.

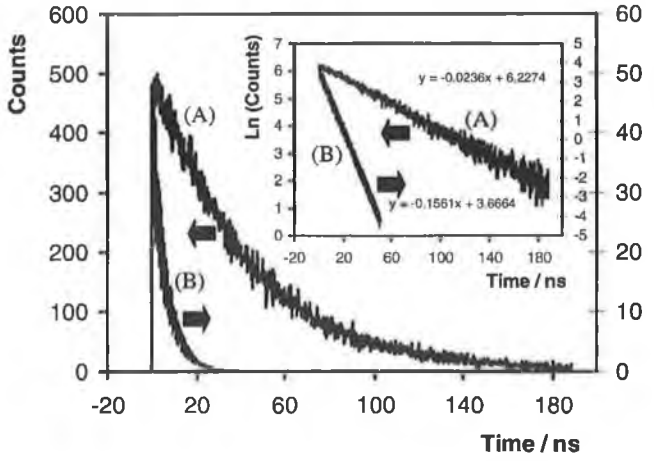

Fig. 3 Emission transients for $[Os(bpy)_2(bpe)_2]^{2+}$ (A) and $\{[Os(bpy)_2(bpe)_2][Os(bpy)_2Cl_2]\}^{4+}$ (B) recorded using a pulsed YAG laser and time correlated single photon counting (TCSPC) approaches, respectively. In the case of the TCSPC approach, the experimental data after correction for the lamp profile are illustrated. The insets show the corresponding semi-log intensity *vs.* time plots.

Driving force for PET

One of our objectives is to probe whether there are differences between the photo- and electrochemically induced electron transfer processes.[28] If the Coulombic stabilisation energy of the products is negligible (typically less than 0.1 eV in polar solvents), then the thermodynamic driving force for electron transfer, ΔG°, can be estimated from the Rehm–Weller equation[29] and the relevant formal potentials:

$$\Delta G^\circ = e[E^\circ(\text{Donor}) - E^\circ(\text{Acceptor})] - E^{\circ\circ} \quad (2)$$

where E°(Donor) and E°(Acceptor) are the formal potentials associated with the donor and acceptor, respectively, and $E^{\circ\circ}$ is the energy difference between the lowest vibrational levels of the ground and excited states. Low temperature emission spectroscopy provides a convenient approach to measuring $E^{\circ\circ}$. Fig. 4 illustrates the emission spectrum for the trimer and $[Os(bpy)_2(bpe)_2]^{2+}$ monomer within an ethanol:methanol glass at 77 K. The value of $E^{\circ\circ}$, as obtained from the wavelength of maximum emission of the trimer at cryogenic temperatures (737 nm) is 1.68 eV.

The electronically excited state could be quenched by electron donation from (reductive quenching), or to (oxidative quenching), the $[Os(bpy)_2\ bpe\ Cl]^+$ moiety. In oxidative quenching, the $[Os(bpy)_2(bpe)_2]^{2+*}$ moiety acts as the donor while the central $[Os(bpy)_2\ bpe\ Cl]^+$ unit acts as the acceptor. Therefore, in order to calculate ΔG°, E°_{Ox} and E°_{Red} must be known for the $[Os(bpy)_2(bpe)_2]^{2+}$ and $[Os(bpy)_2\ bpe\ Cl]^+$ complexes, respectively. Fig. 5 illustrates the solution phase cyclic voltammogram for the trimer dissolved in acetonitrile obtained at a scan rate of 0.2 V s^{-1} where the supporting electrolyte is 0.1 M $TBABF_4$. This voltammogram shows that the peak currents for the couple centred at +0.427 V, is approximately twice that found for couple centred at +0.838 V. This result is consistent with the two $[Os(bpy)_2\ bpe\ Cl]^+$ moieties being easier to oxidise because of the strong σ-donor properties of the chloride ligand. Therefore, consistent with an osmium complex containing six pyridine N-donor ligands, E°_{Ox} is +0.838 V for the $[Os(bpy)_2(bpe)_2]^{2+}$ moiety within the trimer. As shown in Table 1, the first reduction potential of the $[Os(bpy)_2\ bpe\ Cl]^+$ complex is at −1.52 V corresponding to the bpy/bpy$^{\bullet-}$ couple. Therefore, according to eqn. (2), ΔG°_{Ox} is approximately +0.68 eV. The observation that oxidation of the $[Os(bpy)_2(bpe)_2]^{2+*}$ centre is highly endergonic makes this quenching pathway unlikely.

In reductive quenching, the $[Os(bpy)_2\ bpe\ Cl]^+$ moiety acts as the donor while the central $[Os(bpy)_2(bpe)_2]^{2+*}$ unit acts as the acceptor. Fig. 5 and Table 1 show that E°_{Ox} for the $[Os(bpy)_2\ bpe\ Cl]^+$ fragment within the trimer is +0.427. While the voltammetric response corresponding to

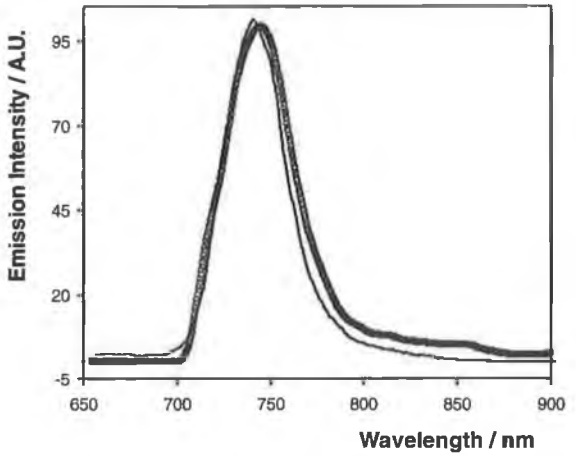

Fig. 4 Emission spectra at 77 K in an ethanol : methanol glass of $[Os(bpy)_2(bpe)_2]^{2+}$ (solid line) and $\{[Os(bpy)_2(bpe)_2][Os(bpy)_2Cl_2]\}^{4+}$ (open circles). In both cases the solvent is deoxygenated butyronitrile. Both spectra were processed using a 5-point moving average smooth. In both cases, the emission is normalised to 100% at λ_{max}.

reduction of the bipyridyl ligands of the trimer is less well defined than the oxidation response illustrated in Fig. 5, these voltammograms reveal that E°_{Red} is approximately −0.950 V. In conjunction with eqn. (2), these values yield a ΔG°_{Red} value of approximately −0.3 eV.

The observation that oxidative quenching is thermodynamically uphill by approximately 0.68 eV, while reductive quenching is exergonic by approximately 0.3 eV, suggests that the electronically excited state is quenched by electron transfer from the $[Os(bpy)_2\,Cl]^+$ moiety across the bpe bridge to the electronically excited $[Os(bpy)_2\,(bpe)_2]^{2+*}$ centre. Beyond providing an insight into the quenching mechanism, knowledge of the driving force for photoinduced electron transfer allows the electron transfer rate constants for optically and electrochemically driven processes to be compared.

Ground state electron transfer

Previous investigations by us and others have demonstrated that complexes containing ligands with two pyridine groups, one of which is bound to the metal complex with the other being available for

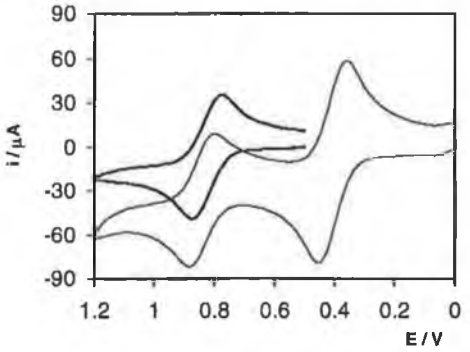

Fig. 5 Voltammograms for 3 mM solutions of $\{[Os(bpy)_2(bpe)_2][Os(bpy)_2Cl]_2\}^{4+}$ (thin line) and $[Os(bpy)_2(bpe)_2]^{2+}$ (thick line) dissolved in acetonitrile where the supporting electrolyte is 0.1 M $TBABF_4$. The scan rate is 0.2 V s^{-1} and the working electrode is a 3 mm diameter glassy carbon disk. Cathodic currents are up, anodic currents are down.

Table 1 Formal potentials for monomeric and trimeric metal complexes[a]

Complex	$E^{\circ}_{Os^{2+/3+}}/V^{b}$	$E^{\circ}_{bpy/bpy^{-}}/V^{c}$
$\{[Os(bpy)_2(bpe)_2][Os(bpy)_2Cl]_2\}^{4+}$	0.427, +0.838	−0.950
$[Os(bpy)_2(bpe)_2](PF_6)_2$	0.630	−1.480
$[Os(bpy)_2$ bpe Cl$]PF_6$	0.310	−1.520
$[Os(bpy)_2$ bpe pyridine$](PF_6)_2$	0.620	−1.450

[a] All measurements were made in acetonitrile containing 0.1 M $TBABF_4$ as supporting electrolyte. [b] Formal potentials are reproducible to within ±10 mV. [c] Voltammograms show evidence of adsorption and formal potentials are typically reproducible to within ±30 mV.

adsorption, form stable monolayers with nearly ideal electrochemical responses.[30–33] As illustrated in Scheme 1, the $[Os(bpy)_2$ bpe pyridine$]^{2+}$ makes a useful monomeric analogue of the trimer that can be used to probe the dynamics and energetics of electron transfer across the bpe bridge in the ground state. Fig. 6 shows representative background corrected cyclic voltammograms for a spontaneously adsorbed $[Os(bpy)_2$ bpe pyridine$]^{2+}$ monolayer where the supporting electrolyte is aqueous 1.0 M $LiClO_4$. The voltammetric peak heights change by less than 10% when the monolayer is repeatedly cycled for periods up to 5 h in blank electrolyte solutions. The observation that these monolayers are stable towards voltammetric cycling over prolonged periods is entirely consistent with the behaviour previously reported for $[Os(bpy)_2$ bpe Cl$]^{+}$ monolayers.[34] These voltammograms are consistent with those expected for an electrochemically reversible reaction involving a surface-confined species.[35,36] The peak shape is independent of scan rate, ν, for $0.05 \leq \nu \leq 50$ V s^{-1} and the peak height increases linearly with increasing scan rate, rather than the $\nu^{1/2}$ dependence observed for the complex in solution. The FWHM values are between 90 and 110 mV indicating that only very weak destabilizing interactions exist within the monolayers.

The formal potential for the $Os^{2+/3+}$ couple shifts by approximately 40 mV in a negative potential direction upon surface confinement indicating that the reduced form is more strongly adsorbed. It is perhaps important to note that E° for the $Os^{2+/3+}$ couple within the $[Os(bpy)_2$ bpe py$]^{2+}$ complex is less positive by approximately 250 mV compared to the same moiety within the trimer, suggesting that the two [Os(bpy)2 bpe Cl]+ moieties decrease the electron density on the central $[Os(bpy)_2$ $(bpe)_2]^{2+}$ unit of the trimer. The surface coverage obtained from the Faradaic

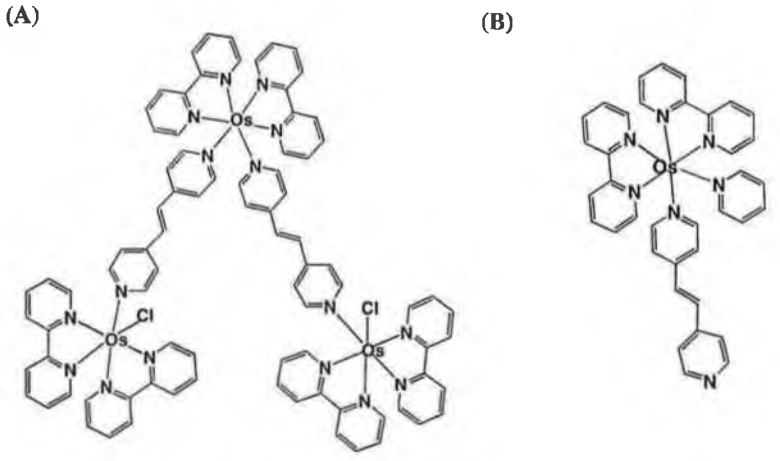

Scheme 1 Structures of the trimeric (A) and monomeric (B) metal complexes used to investigate photoinduced electron transfer and form spontaneously adsorbed monolayers, respectively.

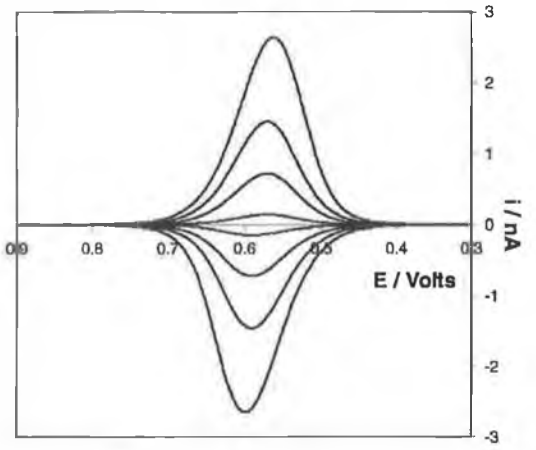

Fig. 6 Background corrected cyclic voltammograms for a spontaneously adsorbed $[Os(bpy)_2$ bpe pyridine$]^{2+}$ monolayer on a 25 μm radius platinum microdisk electrode. The supporting electrolyte is aqueous 0.1 M LiClO4. The scan rates from top to bottom are 2.0, 1.0, 0.5 and 0.1 V s^{-1}. The surface coverage is 1.0×10^{-10} mol cm^{-2}.

charge measured from this background corrected voltammogram is $1.0 \pm 0.1 \times 10^{-10}$ mol cm^{-2} corresponding to an area of occupation of 166 ± 14 Å^2. This surface coverage is consistent with that expected for a close packed monolayer on the basis of structurally related systems and crystallographic data[37,38] which indicate that the radii of osmium and ruthenium polypyridyl complexes are of the order of 6.7 Å.

Effect of scan rate on the voltammetric response

Voltammetry can provide a powerful insight into the rate of heterogeneous electron transfer across the electrode/monolayer interface. When the time constants for the voltammetric experiment and heterogeneous electron transfer become comparable, the peak-to-peak splitting, ΔE_p, between the anodic, E_{pa}, and cathodic, E_{pc}, peak potentials increases. Fig. 7 illustrates how the voltammetric response associated with the $Os^{2+/3+}$ redox reaction changes as the scan rate, ν, is increased from 5000 to 20 000 V s^{-1}. Significantly, at these relatively high scan rates, the peak-to-peak separation is no longer close to zero and ΔE_p increases from 140 to 270 mV on going from 5000 to 20 000 V s^{-1}.

Uncompensated cell resistance and slow heterogeneous electron transfer could contribute to the observed behaviour. Where the working electrode is a 5 μm radius microelectrode, the uncompensated resistance as measured using potential step chronoamperometry is 7630 ± 332 Ω. Taken in conjunction with the maximum peak current of approximately 1750 nA, this cell resistance leads to an iR drop of approximately 13 mV. This ohmic loss is negligible compared to the peak-to-peak separation of 270 mV observed at a scan rate of 20 000 V s^{-1}. Therefore, it appears that at high scan rates the dynamics of electron transfer across the bpe bridge influence the voltammetric response.

As discussed elsewhere,[39-41] the standard heterogeneous electron transfer rate constant, k° depends on both a frequency factor and a Franck-Condon barrier and is described by:

$$k^\circ = A_{el} \exp(-\Delta G^{\neq}/RT) \quad (3)$$

where A_{el} is the pre-exponential factor and $\Delta G^{\neq}$ is the electrochemical Gibbs energy of activation.[42] For an adiabatic reaction, the prefactor is the product of κ_{el} the electronic transmission coefficient (equal to unity for an adiabatic reaction) and ν_n a frequency factor dictated either by nuclear or solvent motion. In contrast, for a non-adiabatic reaction where the reactants are weakly coupled κ_{el} is significantly less than unity and the prefactor is dictated by the electron hopping frequency in the activated complex, ν_{el}.

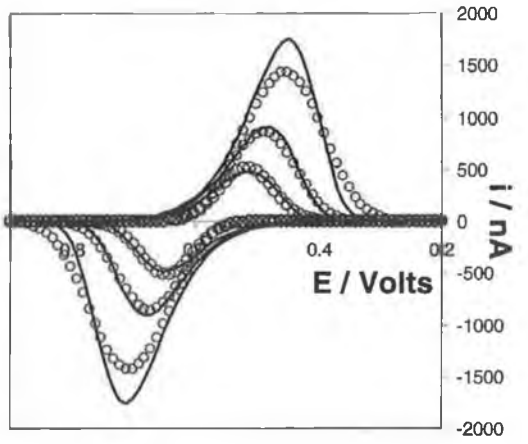

Fig. 7 Effect of the scan rate on the voltammetry of an $[Os(bpy)_2(bpe)_2]^{2+}$ monolayer. The surface coverage is 1.0×10^{-10} mol cm^{-2} and the platinum microdisk radius is 5 μm. The scan rates from top to bottom are 20 000, 10 000, 5000 and 2000 V s^{-1}. The open circles represent the theoretical fit obtained from the non-adiabatic tunnelling model where k° is 3.1×10^4 s^{-1} and λ is 0.4 eV. The supporting electrolyte is aqueous 1.0 M $LiClO_4$.

As discussed by Chidsey,[43] Creager[44] and Murray,[45] the voltammetric response can be modelled according to a non-adiabatic electron transfer response to extract standard heterogeneous electron transfer rate constants and reorganization energies. Following Chidsey, the potential dependent rate constants for monolayer reduction, $k_{\text{red},\eta}$ and oxidation, $k_{\text{ox},\eta}$, are given by

$$k_{\text{Red},\eta} = \kappa_{\text{el}}\ \rho\ k_{\text{B}}T \int_{-\infty}^{\infty} \frac{\exp\left\{-(x-(\lambda+\eta)/k_{\text{B}}T)^2(k_{\text{B}}T/4\lambda)\right\}}{1+\exp(x)}\ \text{d}x \tag{4}$$

$$k_{\text{Ox},\eta} = \kappa_{\text{el}}\ \rho\ k_{\text{B}}T \int_{-\infty}^{\infty} \frac{\exp\left\{-(x-(\lambda-\eta)/k_{\text{B}}T)^2(k_{\text{B}}T/4\lambda)\right\}}{1+\exp(x)}\ \text{d}x \tag{5}$$

where x is the electron energy relative to the Fermi level, κ_{el} is the distance dependent electronic coupling between the electrode and the redox sites, ρ is the density of electronic states in the metal electrode, k_{B} is the Boltzmann constant, T the absolute temperature, and λ is the reorganization energy.

The voltammetric current for the reaction of an immobilized redox centre following first order kinetics is given by:

$$i_{\text{F}} = nFA(k_{\text{Ox},\eta}\Gamma_{\text{Red},\eta} - k_{\text{Red},\eta}\Gamma_{\text{Ox},\eta}) \tag{6}$$

where $\Gamma_{\text{Red},\eta}$ and $\Gamma_{\text{Ox},\eta}$ are the instantaneous surface coverages of the oxidized and reduced species. Energy minimized molecular modelling indicates that the electron transfer distance is approximately 10 Å. Therefore, in using eqn. (6) to model the voltammetric response, there are only two freely adjustable parameters for each redox centre, k° and $\Delta G^{\neq}$ ($= \lambda/4$). To fit the experimental voltammograms, we have used the Nelder and Mead Simplex[46] algorithm to find the values of k° and $\Delta G^{\neq}$ that minimize the sum square residuals between the theoretical and experimental currents observed in anodic branches of the linear sweep voltammograms. Fig. 7 shows that the theory satisfactorily fits the voltammograms obtained at 5000 and 10 000 V s^{-1} for the $[Os(bpy)_2$ bpe pyridine$]^{2+}$ monolayers where k° is 3.1×10^6 s^{-1}. The reorganization energy is 0.6 eV, but a similar quality fit is obtained for $0.5 \leq \lambda \leq 0.7$ eV. However, for the highest scan rate investigated, 20 000 V s^{-1}, the theoretical response agrees less well with that found experimentally. Thus, while the theoretical and experimental peak potentials agree to within experiment error, the experimental peak currents are approximately 20% larger than theory predicts. This observation suggests that there may be a small population of redox centres within the monolayer that can

undergo more rapid heterogeneous electron transfer than the majority of the population. Behaviour of this kind has been found for related systems[47] and most likely arise because of an imperfect monolayer structure, *e.g.*, because of surface roughness or flexibility of the bridge.

Comparison of optically and electrochemically driven electron transfer

The driving force found for the photochemically induced electron transfer is −0.3 eV. The non-adiabatic electron transfer model outlined in eqn. (4) and (5) indicates that for this driving force, the heterogeneous electron transfer rate constant is 2.0×10^6 s^{-1}. The fact that this value is substantially lower than the predicted by the Butler–Volmer formalism, 1.0×10^7 s^{-1}, reflects the ability of the Marcus approach to correctly predict the experimental observation that the rate constant becomes less sensitive to the driving force for large values of overpotential. The most striking result of this analysis is that even under conditions of identical driving forces, the photoinduced electron transfer rate constant is almost two orders of magnitude larger, 1.3×10^8 s^{-1}, than that of the electrochemically driven heterogeneous electron transfer, 2.0×10^6 s^{-1}.

It is possible that the [bpe Os(bpy)$_2$ Cl]$^+$ moieties within the trimer create a favourable vibronic deactivation pathway in the PET experiments causing the photoinduced electron transfer rate constant to be overestimated. However, it is important to determine whether the D/A coupling across the *trans*-1,2-bis-(4-pyridyl)ethylene bridge is weaker for the delocalised metallic states of an electrode compared to the localized redox states of the trimer.

As described by Marcus,[39,40,42] in the case of the photoinduced electron transfer reaction, the rate constant for electron cross-exchange between the two osmium sites, k_{PET}, depends on the difference in the redox potentials of the two reactants, ΔG°, and the reorganization energy, λ. Consistent with results found for related systems using both temperature dependent measurements of k_{PET} and theoretical modelling of the voltammetric response, the best fits to the experimental data of Fig. 7 indicate that λ is approximately 42 kJ mol^{-1}.

$$k_{PET} = A_{ET} \exp\left[-\frac{(\lambda + \Delta G^\circ)^2}{4\lambda RT}\right] \tag{7}$$

The reduction and oxidation potentials for [Os(bpy)$_2$ (bpe)$_2$]$^{2+*}$ and [Os(bpy)$_2$ bpe Cl]$^+$ are +0.360 and +0.427 V, respectively, indicating that ΔG° is approximately 6.5 kJ mol^{-1}. Thus, eqn. (7) indicates that A_{ET} for the PET process is approximately, 4×10^{10} s^{-1}. In contrast, using the experimental values of $3.1 \pm 0.2 \times 10^4$ s^{-1} and 10.5 kJ mol^{-1} for k° and $\Delta G^{\neq}$, respectively, eqn. (6) yields a value of approximately 2×10^6 s^{-1} for A_{ET} for the ground state process. The observation that the pre-exponential factor is dramatically smaller (by more than four orders of magnitude) for the monolayers than for the trimer is highly significant. It suggests that the extent of electronic communication across the *trans*-1,2-bis-(4-pyridyl)ethylene bridge is much weaker when linking a metal electrode surface and a metal complex compared to when it bridges molecular components.

Conclusions

Novel trimers of the form {[Os(bpy)$_2$(bpe)$_2$][Os(bpy)$_2$Cl]$_2$}$^{4+}$ have been synthesised, characterised and used to probe the dynamics of photoinduced electron transfer between metal centres across rigid bridges. Analysis of the driving forces for oxidative and reductive electron transfer quenching of the excited state as calculated using the Rehm–Weller equation indicates that quenching of the excited state involves electron donation from the [bpe Os(bpy)$_2$ Cl]$^+$ moiety to the electronically excited [Os(bpy)$_2$ (bpe)$_2$]$^{2+*}$ centre. The rate constant for the photoinduced electron transfer process is $1.3 \pm 0.1 \times 10^8$ s^{-1} compared to $2.0 \pm 0.2 \times 10^6$ s^{-1} for the ground state process with the same driving force. This result suggests that the proximity of donor/acceptor and bridge states, *i.e.*, the achievement of resonance in the PET reaction, dramatically enhances the rate of electron transfer. These investigations into trimeric monolayers also reveal that the strength of electronic coupling across the *trans*-1,2-bis-(4-pyridyl)ethylene bridge is significantly higher when it links two metal complexes compared with the situation where it acts as a bridge between a metal centre and

an electrode. This result suggests that the tunnelling junction between the bulk metal and an adsorbed bridge can significantly influence heterogeneous electron transfer rates.

Acknowledgement

Financial support from Enterprise Ireland, the Irish Science and Technology Agency, under the Basic Research Programme is gratefully acknowledged. The assistance of Dr. Marco Duati of Dublin City University with the collection and analysis of the TCSPC measurements is deeply appreciated. We acknowledge the generous loan of potassium hexachloroosmate(IV) by Johnson Matthey under the loan scheme.

References

1 R. J. Forster and L. R. Faulkner, *J. Am. Chem. Soc.*, 1994, **116**, 5444.
2 V. Balzani, A. Juris, M. Venturi, S. Campagna and S. Serroni, *Chem. Rev.*, 1996, **96**, 759.
3 B. O'Regan and M. Gratzel, *Nature*, 1991, **353**, 737.
4 J. J. Hopfield, J. N. Onuchic and D. N. Beratan, *J. Phys. Chem.*, 1989, **93**, 6350.
5 R. S. Knox, *Photosynth. Res.*, 1996, **48**, 35.
6 A. J. Bard and M. A. Fox, *Acc. Chem. Res.*, 1995, **28**, 141.
7 T. E. Keyes, R. J. Forster, P. M. Jayaweera, C. G. Coates, J. J. McGarvey and J. G. Vos, *Inorg. Chem.*, 1998, **22**, 5925.
8 K. S. Schanze and T. J. Meyer, *Inorg. Chem.*, 1985, **24**, 2123.
9 L. De Cola and P. Belser, *Coord. Chem. Rev.*, 1998, **177**, 301.
10 M. D. Ward, *Chem. Soc. Rev.*, 1995, **24**, 121.
11 K. S. Schanze, G. A. Neyhart and T. J. Meyer, *J. Phys. Chem.*, 1986, **90**, 2182.
12 M. J. Powers and T. J. Meyer, *J. Am. Chem. Soc.*, 1980, **102**, 1289.
13 J. C. Curtis, J. S. Bernstein and T. J. Meyer, *Inorg. Chem.*, 1985, **24**, 385.
14 L. De Cola, V. Balzani, F. Barigelletti, L. Flamigni, P. Belser, A. von Zelewsky, M. Frank and F. Vogtle, *Inorg. Chem.*, 1993, **32**, 5228.
15 V. Balzani, F. Barigelletti, P. Belser, S. Bernhard, L. De Cola and L. Flamigni, *J. Phys. Chem.*, 1996, **100**, 16786.
16 E. Zahavy and M. A. Fox, *Chem. Eur. J.*, 1998, **4**, 1647.
17 M. M. Richter and K. J. Brewer, *Inorg. Chem.*, 1993, **32**, 5762.
18 E. Brauns, S. W. Jones, J. A. Clark, S. M. Molnar, Y. Kawanishi and K. J. Brewer, *Inorg. Chem.*, 1997, **36**, 2861.
19 S. M. Molnar, G. Nallas, J. S. Bridgewater and K. J. Brewer, *J. Am. Chem. Soc.*, 1994, **116**, 5206.
20 G. N. A. Nallas and K. J. Brewer, *Inorg. Chim. Acta.*, 1996, **253**, 7.
21 C. R. Arana and H. D. Abruña, *Inorg. Chem.*, 1993, **32**, 194.
22 C. P. Collier, E. W. Wong, M. Belohradsky, F. M. Raymo, J. F. Stoddart, P. J. Kuekes, R. S. Williams and J. R. Heath, *Science*, 1999, **285**, 391.
23 J. Chen, M. A. Reed, A. M. Rawlett and J. M. Tour, *Science*, 1999, **286**, 1550.
24 R. J. Forster, E. Figgemeier, A. C. Lees, J. Hjelm and J. G. Vos, *Langmuir*, 2000, **16**, 7867.
25 C. Xu, Ph.D. Thesis, University of Illinois at Urbana-Champaign, 1992
26 R. J. Forster, *Inorg. Chem.*, 1996, **35**, 3394.
27 F. Barigelletti, L. Flamigni, V. Balzani, J. P. Collin, J. P. Sauvage, A. Sour, E. D. Constable and J. Thompson, *J. Am. Chem. Soc.*, 1994, **116**, 7692.
28 R. J. Forster and T. E. Keyes, *J. Phys. Chem. B.*, 2001, **105**, 8829.
29 D. Rehm and A. Weller, *Israel J. Chem.*, 1970, **8**, 259.
30 D. Acevedo and H. D. Abrûna, *J. Phys. Chem.*, 1991, **95**, 9590.
31 D. Acevedo, R. L. Bretz, J. D. Tirado and H. D. Abrûna, *Langmuir*, 1994, **10**, 1300.
32 D. A. Walsh, T. E. Keyes, C. F. Hogan and R. J. Forster, *J. Phys. Chem.*, 2001, **105**, 2792.
33 R. J. Forster and J. P. O'Kelly, *J. Electrochem. Soc.*, 2001, **148**, E31.
34 R. J. Forster, P. J. Loughman, E. Figgemeier, A. C. Lees, J. Hjelm and J. G. Vos, *Langmuir*, 2000, **16**, 7871.
35 E. Laviron, *J. Electroanal. Chem.*, 1974, **52**, 395.
36 A. P. Brown and F. C. Anson, *Anal. Chem.*, 1977, **49**, 1589.
37 H. A. Goodwin, D. L. Kepert, J. M. Patrick, B. W. Skelton and H. White, *Aust. J. Chem.*, 1984, **37**, 1817.
38 J. E. Ferguson, J. L. Love and W. T. Robinson, *Inorg. Chem.*, 1972, **11**, 1662.
39 G. Bagchi, *Annu. Rev. Chem.*, 1989, **40**, 115.
40 N. Sutin, *Acc. Chem. Res.*, 1982, **15**, 275.
41 T.-T. Li, K. L Guyer, S. W. Barr and M. J. Weaver, *J. Electroanal. Chem.*, 1984, **164**, 27.
42 N. Sutin and B. S. Brunschwig, *ACS Symp. Ser.*, 1982, **198**, 105.

43 C. E. D. Chidsey, *Science*, 1991, **251**, 919.
44 K. Weber and S. E. Creager, *Anal. Chem.*, 1994, **66**, 3164.
45 L. Tender, M. T. Carter and R. W. Murray, *Anal. Chem.*, 1994, **66**, 3173.
46 K. Ebert, H. Ederer and T. L. Isenhour, *Computer Applications in Chemistry: An Introduction for PC Users*, VCH, New York, 1989
47 H. O. Finklea and D. D. Hanshew, *J. Am. Chem. Soc.*, 1992, **114**, 3173.